



Enhancement of Bone Healing through Mechanical Stimulation

Natacha Rosa

Dissertation submitted to Faculdade de Engenharia da Universidade do Porto
to obtain the degree of

Doctor of Philosophy in Mechanical Engineer

Supervisor: Professor Dr. António Torres Marques
Co-Supervisors: Professor Dr. Fernão Domingos de Magalhães
Professor Dr. Ricardo João Ferreira Simões

2016

FCT
Fundação para a Ciência e a Tecnologia
Ministério da Ciência, Tecnologia e Inovação

U. PORTO
FEUP FACULDADE DE ENGENHARIA
UNIVERSIDADE DO PORTO

 **Laeta**
laboratório associado

 **lepabe**
Laboratory for Process Engineering,
Environment, Biotechnology and Energy

*This thesis is dedicated to
mom, sis, dad and Ivo*

Acknowledgments

The completion of this thesis could not be possible without the participation and assistance of a number of people whose names may not all be enumerated. However, their support has been crucial along the way and I'm very grateful to each and every person.

I would like to express my gratitude to my supervisor and co-supervisors, Professor Antonio Torres Marques, Professor Fernão Domingos de Magalhães and Professor Ricardo Simões, for their always constructive critique and encouragement, which helped me to conceptualize and accomplish my PhD thesis.

I would like to thank José Dias and Vladimiro Fernandes from *Artur Salgado S.A.* for providing the intramedullary nails and the respective instrumentation. Their contribution was essential for my work.

I would like to thank Professor Maria Helena, Professor Pedro Gomes, José Carlos and Liliana Grenho from the Laboratory of Bone Metabolism and Regeneration at the Faculty of Dental Medicine of the University of Porto, for helping me with the cytocompatibility evaluation and for allowing me to use their facilities and materials. It was an honor and pleasure to know them, to work and to learn with them.

I would like to thank all my colleagues from the Mechanical Department for guidance and support over the years, both professionally and personally, and for making me feel so welcome.

At last, but definitely not least, my sincere gratitude to the constant support, encouragement and unconditional love of my family, boyfriend and friends.

This PhD thesis was funded by the Foundation for Science and Technology (FCT) through the research grant SFRH/BD/87089/2012.

This work was financially supported by projects POCI-01-0145-FEDER-006939 - Laboratory for Process Engineering, Environment, Biotechnology and Energy – LEPABE and NORTE-01-0145-FEDER-000005 – LEPABE-2-ECO-INNOVATION, funded by FEDER funds through COMPETE2020 - Programa Operacional Competitividade e Internacionalização (POCI) and Programa Operacional Regional do Norte (NORTE2020), by the project UID/CTM/50025/2013 and by national funds through FCT - Fundação para a Ciência e a Tecnologia.



Publications

Articles:

Rosa, N., Simoes, R., Magalhães F. D. and Marques, A. T., *From mechanical stimulus to bone formation: A review*. Medical Engineering & Physics, 2015. **37**(8): 719-28.

Rosa, N., Marta, M., Vaz, M., Tavares, S., Simoes, R., Magalhães, F. D. and Marques, A.T., *The Biomechanical Perspective of the Intramedullary Nailing Evolution*. Submitted (2016).

Rosa, N., Marta, M., Vaz, M., Tavares, S., Simoes, R., Magalhães, F. D. and Marques, A.T., *The Biomechanical History of Intramedullary Nailing*. Submitted (2016).

Rosa, N., Magalhães F. D., Simoes, R. and Marques, A.T., *Bone an Outstanding Composite Material*. To be submitted (2016).

Rosa, N., Tavares, S., Vaz, M., Tavares, S., Monteiro, J., Tavares, P. J., Carbas, R. J. C., Simoes, R., Magalhães, F. D. and Marques, A.T., *Composite Tibia Stiffness concept study: Experimental validation of a finite element model*. To be submitted (2017).

Presentations at national and international conferences:

Rosa, N. and Marques, A. T. *The effect of cement bone-interface on the behaviour of hip arthroplasty replacement* in *Materiais2013*. 2013. Coimbra, Portugal

Rosa, N. and Marques, A. T. *A Perspective on Bone-Cement Interface Loosening in Hip Implants* in *5th Portuguese Congress on Biomechanics*. 2013. Espinho, Portugal

Rosa, N., Magalhães, F. D., Simoes, R. and Marques, A.T. *Enhanced bone healing through mechanical stimulation by implanted piezoelectric actuators* in *International Joint Conference on Biomedical Engineering Systems and Technology (BIOSTEC)*. 2014. Angers, France

Rosa, N., Magalhães, F. D., Simoes, R. and Marques, A.T. *Intramedullary Nailing Stability in the Bone Healing Process* in *1st Doctoral Congress in Engineering*. 2015. Porto, Portugal

Rosa, N., Magalhães, F. D., Simoes, R. and Marques, A.T. *Nailing Stability during Tibia Fracture Early Healing Process: A Biomechanical Study* in *International Conference and Expo on Biomechanics and Implant Design*. 2015. Florida, USA.

*“Take small steps so that you do not fall, bring the best
out of you and be driven by a passion to be better”*

Dr. Vijay Eswaran

Abstract

Long bone fractures are one of the most common serious musculoskeletal system injuries, and for which intramedullary nail is the recommended method to enable healing and injured site mobility and function recovery. Despite the high rate of success ensured by this stabilization technique, tibia shaft fractures are still associated with a prolonged healing time. This limitation represents a substantial burden to society and patients. The main goal of this thesis is, by taking advantage of the potentialities given by intramedullary nail fixation method and not interfering with its normal functioning, propose an innovative device which by applying additional well-aimed and well-timed low-magnitude high-frequency interfragmentary mechanical stimulus at the early healing stage will enhance the recovery process quality and progress. The understanding that the mechanical environment at bone fracture site, and more importantly the interfragmentary movements, strongly influence the rate and quality of the callus formation, was complemented with a study of the bone-implant stability concept. Through this analysis a strategy was proposed, considering both finite element analysis and mechanical tests under simple and reproducible conditions, while reflecting physiological load and bone orientation. In this study, a stable bone-implant construct demonstrated that, despite the system's high stiffness, the interfragmentary site will always be subjected to some motion, and that during early healing phase the nail will support a significant portion of the load applied on the lower limb. Based on the acquired knowledge, and considering the thesis goal, ferrite was chosen as the actuator material. Ferrite's displacement can be induced by a magnetic field, giving the device an additional advantages over conventional wired actuators, such as higher safety and operating life. The affinity of MG-63 cells for selected ferrite samples was also evaluated, as well as the influence of the removal of the static magnetic field on their adhesion and proliferation. Both ferrite materials tested, $Ni_{0.27}Cu_{0.14}Zn_{0.6}$ and Sr-Ca, showed strong evidences of being cytocompatible. Considering the material potential for not being toxic to the human body, it was possible to advance the idea into the development of a demonstration model where the principle of a ferromagnetic actuator coupled to the fixation device and controlled through a magnetic field can be easily perceived. The demonstration model showed that this new approach for enhancing fracture healing was able to reflect clinicians' needs and at the same time respect the human body's biological processes. As such, the goal outlined in this thesis was successfully achieved.

Resumo

As fraturas dos ossos longos são umas das lesões mais comuns e graves do sistema músculo-esquelético e cuja cicatrização e recuperação da mobilidade e funcionamento é garantido pela aplicação de cavilhas intramedulares, sendo que, esta é considerada a intervenção preferencial para o efeito. Apesar da elevada taxa de sucesso providenciada por esta técnica de estabilização óssea, as fraturas diafisárias da tíbia continuam associadas a um tempo de recuperação demasiado longo. Esta limitação representa uma sobrecarga considerável para a sociedade e para os pacientes. Considerando as potencialidades conferidas pelo método de fixação com cavilhas intramedulares e sem interferir com o seu normal funcionamento, o principal objetivo desta tese consistiu em propor um dispositivo inovador que através da aplicação correta de estímulos mecânicos de baixa magnitude e elevada frequência durante a fase de recuperação óssea inicial, seja capaz de melhorar a qualidade e a progressão do processo de recuperação óssea. A compreensão sobre a forte influencia que ambiente mecânico tem na fratura em recuperação, e principalmente os movimentos interfragmentários presentes, têm sobre a velocidade de formação e a qualidade do calo ósseo obtido, foi complementada com um estudo sobre o conceito de estabilidade osso-implante. Através deste estudo foi proposta uma estratégia que considera a análise em elementos finitos assim como ensaios mecânicos em condições simples e reprodutíveis, e refletindo a orientação e aplicação de cargas ósseas fisiológicas. Neste estudo, foi demonstrado a ocorrência de movimentos interfragmentários da fratura perante uma construção osso-implante estável mesmo tratando-se de um sistema rígido. Foi também demonstrado que durante a fase inicial de recuperação óssea é a cavilha intramedular que suporta grande porção da carga aplicada nos membros inferiores. Baseado no conhecimento adquirido e tendo em consideração o objetivo principal da tese, a ferrite foi selecionada como material base para o atuador. O movimento da ferrite pode ser induzido pelo campo magnético, o que garante uma vantagem adicional ao dispositivo quando comparado com os atuadores convencionalmente conectados por fios tanto ao nível de segurança como em termos de período de vida útil. A afinidade das células MG-63 para amostras selecionadas de ferrite foram testadas, assim como a influência em relação à adesão e proliferação celular ao ser removido um campo magnético permanente. Tanto as ferrites $Ni_{0.27}Cu_{0.14}Zn_{0.6}$ como Sr-Ca testadas, mostraram fortes evidências de serem citocompatíveis. O potencial de não toxicidade do material, permitiu o desenvolvimento de um modelo de demonstração onde o princípio de um atuador ferromagnético acoplado ao dispositivo de fixação e controlado através de um campo magnético foi facilmente perceptível. O modelo de demonstração mostrou que a nova solução desenvolvida para melhorar a recuperação da fratura ossea foi capaz de refletir as

necessidades do clínico e, ao mesmo tempo, respeitar o processo biológico do organismo humano. Desta forma, o objetivo delineado nesta tese foi alcançado com sucesso.

Contents

| | |
|--|-------|
| Acknowledgments | v |
| Publications | ix |
| Abstract | xiii |
| Resumo | xv |
| List of Figures | xix |
| List of Tables | xxvii |
| Nomenclature | xxix |
| | |
| CHAPTER 1 | 1 |
| 1. Introduction | 1 |
| 1.1. Motivation | 1 |
| 1.2. Thesis objectives | 12 |
| 1.3. Document structure | 13 |
| 1.4. References | 15 |
| | |
| CHAPTER 2 | 21 |
| 2. Literature review | 21 |
| 2.1. Tibia mechanical functional structure and hierarchical organization | 21 |
| 2.2. From mechanical stimulus to bone formation | 40 |
| 2.3. Fracture and healing | 65 |
| 2.4. Intramedullary nailing biomechanical concept evolution: Understand the past to predict the future | 74 |
| | |
| CHAPTER 3 | 123 |
| 3. Bone-intramedullary nail system stability | 123 |
| 3.1. Material and methods | 130 |
| 3.2. Results | 150 |
| 3.3. Discussion | 158 |
| 3.4. Conclusion | 167 |
| 3.5. References | 168 |

| | |
|--|----------------|
| CHAPTER 4 | 175 |
| 4. Actuator selection | 175 |
| 4.1. Piezoelectric stacks | 176 |
| 4.2. Electromagnetic vibration actuator | 199 |
| 4.3. References..... | 204 |
| CHAPTER 5 | 209 |
| 5. Cytocompatibility evaluation | 209 |
| 5.1. Materials and methods | 211 |
| 5.2. Results | 222 |
| 5.3. Discussion..... | 238 |
| 5.4. Conclusions | 244 |
| 5.5. References..... | 244 |
| CHAPTER 6 | 249 |
| 6. Bone healing enhancement device: Concept demonstration model | 249 |
| 6.1. Materials and methods | 251 |
| 6.2. Results and discussion..... | 253 |
| 6.3. Conclusion | 255 |
| 6.4. References..... | 256 |
| CHAPTER 7 | 259 |
| 7. General conclusion and future work | 259 |
| CHAPTER 8 | 261 |
| 8. Appendix | 261 |

List of Figures

| | |
|--|----|
| Figure 1.1 - Few worldwide epidemiological studies on the incidence of tibia fractures. TF -Tibia fractures, TSF -Tibia shaft fractures. World map image obtained from [24] and incidence calculated based on total country or city population data from [25, 26].... | 2 |
| Figure 1.2 - Accidental and intentional percentage tibia fractures according to the age groups and gender which occurred between the XIX and XX century, based on medical records from Coimbra and Lisbon. Data entirely obtained from [28]. The age groups were defined according to the criteria used by Buikstra and Ubelake [32]..... | 3 |
| Figure 1.3 - Overall thesis structure and how its chapters and sections are linked together | 15 |
| Figure 2.1 - Representation of the tibia positioning in the lower leg (d), with localization of the main anatomical landmarks from the posterior (b) and anterior view (c) and cross-section images (a) along the tibia showing its shape variation as well as cortical and trabecular bone portions. | 24 |
| Figure 2.2 - Diagram showing tibia diaphysis bone microscopic hierarchical organization and its main cellular population. Adapted from [66-71] | 27 |
| Figure 2.3 - Schematic representation of mechanical loading that causes interstitial fluid flow through bone's lacuna-canalicular network (adapted from Duncan et al. [9]). The tension/compression stresses associated with bending cause a pressure gradient that promotes fluid flow along the osteocyte | 43 |
| Figure 2.4 - Mechanical usage window defined by Frost's "mechanostat" theory of bone adaptation to strain (adapted from Duncan et al. [9] and Frost [95]). The horizontal arrow at the bottom shows the typical minimum effective strain (MES) levels and the set point values for the bone's thresholds and ultimate strength – microstrain ($\mu\epsilon$), stress (MPa) and unit-load (kg/mm^2) | 48 |
| Figure 2.5 - Schematic chronological representation of the turning points in the evolution of the intramedullary fixation, from the 16th century and up to the 20th century. Information is arranged according to: (a) Timeline, (b) Application sites, (c) Materials used, (d) Biomechanical concept | 75 |
| Figure 2.6 - Diagram showing Küntscher femoral nail (from two different views) with the clover-leaf cross-section (a) and the longitudinal slot (b) | 79 |
| Figure 2.7 - Image exemplifying the overall structure of a flexible reamer (a) with the distal drill bit, a Rush nail (b) with a proximal hook end that prevents rotation and stabilizes the fracture and an Ender's nail (c)..... | 81 |

| | |
|---|-----|
| Figure 3.1 - Diagram showing the physiological orientation of the tibia. Where the orientation planes - coronal (a) and sagittal (b) - and the tibia reference axes: the vertical axis (dark dotted line), the mechanical axis (dark gray continuum line or (c)) and the anatomical axis (light gray continuum line), are represented. A - Medial spine (or medial intercondylar eminence), B - Center of the tibia, C - Knee center, D - Ankle center, E - Lateral spine (or lateral intercondylar eminence) | 131 |
| Figure 3.2 - SawBones manufacture information [21] and physiological values from literature [22, 54-56] on cortical bone thickness distribution along the tibia | 132 |
| Figure 3.3 - Illustration of the segmentation adopted, the theoretical cortical wall-thickness considered based on literature and the average wall-thickness obtained after appropriate SolidWorks canal-formation tools were applied..... | 134 |
| Figure 3.4 - A 4-point bending jig at different process stages: (A) 3D SolidWorks version, (B) 3D printed ABS replicate version and (C) Aluminium alloy AA6082-T6 machined final version..... | 136 |
| Figure 3.5 - Image of the torsional test top jig with the 3D printed personalized bone contact zone | 137 |
| Figure 3.6 - Testing configuration, grips designs and the measurement devices used in the axial compression assay on the intact composite tibia model: (A) Illustration of the test set-up with detailed information of the jigs from a sagittal section and (B) Image of the test set up | 138 |
| Figure 3.7 - Testing configuration, grips design and the measurement devices used for the 4-point bending assay on the intact composite tibia model: (A) Illustration of the test set-up with the tibia on coronal orientation and with a exemplification of the switching mechanism used between the coronal and sagittal loading mode and (B) Image of the test set up for 4-point bending with the tibia sagittal orientation..... | 139 |
| Figure 3.8 - Testing configuration used for the shear assay on the intact composite tibia model with the bone on sagittal orientation: (A) Illustration of the test set-up and (B) Image of the test set-up..... | 139 |
| Figure 3.9 - Custom testing configuration and the measurement devices used for the torsional assay on the intact composite tibia model where: (A) Simplified illustration of the torsional test set-up and (B) Image of the test set-up. The measuring apparatus used to record the system rotation - (a) weight and their support structure fall and (b) laser projected and motion registration – and the (c) thrust ball bearing and (d) graph paper, are also represented..... | 140 |

| | |
|--|-----|
| Figure 3.10 - Schematic representation of the electronic spackle pattern interferometry (ESPI) experimental arrangement system. Image constructed based in information from [69, 70, 74, 75] and the image of the computer was obtained from [76] | 143 |
| Figure 3.11 - Schematic representation of the digital image correlation (DIC) technique using virtual extensometers experimental arrangement system where: (A) Light source, (B) CCD digital camera, (C) Speckled composite tibia under 4-point bending loading and (D) speckled surface under analysis. Image constructed based in information from [87] and the image of the computer was obtained from [76] | 146 |
| Figure 3.12 - Schematic representation of the strategy used for the calculation of the horizontal and vertical gauges displacements variations during torsional assays..... | 147 |
| Figure 3.13 - ESPI analysis on the tibia midsection site displacement from the whole bone structure axial compression at (A) 20 and (B) 80 N. The results are presented as a (a) three-dimensional displacement map, (b) two-dimensional displacement map and the (c) displacement along the x-axis at position $y = 24.6 \mu\text{m}$ | 152 |
| Figure 3.14 - Cross-section of the tibia-intramedullary nail finite element model displacement distribution in yy direction (mm) during 4-point bending load in the sagittal plane and in response to 20 Nm bending moment..... | 153 |
| Figure 3.15 - Comparison of the bone fragments (upper and lower portion) and intramedullary nail deformation from finite element simulation (FE) at the (A) axial and (B) anteroposterior direction and in response to 150 N axial compression loading of the osteotomized composite tibia fixed with the intramedullary nail system..... | 155 |
| Figure 3.16 - Bone fragments (upper and lower portion) and intramedullary nail rotation registers from finite element simulation (grey) and mechanical experimentation DIC-measurements (diagonal stripes) in response to 5 Nm torsional loading of the osteotomized composite tibia fixed with the whole intramedullary nail system. FE - Finite element simulation, ME - Mechanical experimentation DIC measurements | 155 |
| Figure 3.17 - Bone fragments (upper and lower portion) and intramedullary nail deflection registers from finite element simulation (grey) and mechanical experimentation DIC-measurements (diagonal stripes) as a response to 20 Nm N 4-point bending loading in the (A) sagittal and (B) coronal plane of the whole osteotomized composite tibia fixed with the intramedullary nail system. FE - Finite element simulation, ME - Mechanical experimentation DIC measurements..... | 156 |
| Figure 3.18 - Bone fragments (upper and lower portion) and intramedullary nail deflection registers from finite element simulation (FE) and mechanical experimentation DIC-measurements (ME) as a response to 100 N shear loading in the (A) sagittal and (B) | |

| | |
|---|-----|
| coronal plane of the whole osteotomized composite tibia fixed with the intramedullary nail system | 157 |
| Figure 4.1 - Schematic cross-sectional representation of a multilayer PZT piezo-stack with longitudinal expansion, built up from individually contacted piezoceramic discs. Based on [9, 16, 18, 24]. | 181 |
| Figure 4.2 - Schematic representation from the anterior and lateral perspective of the set-up system based on a piezo stack (C) which was placed on a solid base and was mounted into a mechanical press (D) with known load (E), moving the attached mechanics (D) by electrical voltage stimulation. The strain of the stack is measured with the use of a laser Doppler vibrometer optical sensor head (A) which laser beam direction is controlled by mirror system (B) | 189 |
| Figure 4.3 - Actuator finite element model simulation during intramedullary nail hammering where (A) is the normal stress distribution at the piezo-stack surface in direction X (direction of the piezoelectric effect), (B) in the normal strain distribution in direction X and (C) is the normal shear strain distribution in the YZ plane..... | 191 |
| Figure 4.4 - Actuator finite element model simulation during intramedullary nail removal where (A) is the normal stress distribution at the piezo-stack surface in direction X (direction of the piezoelectric effect), (B) in the normal strain distribution in direction X and (C) is the normal shear strain distribution in the YZ plane | 192 |
| Figure 4.5 - Schematic voltage/stroke diagram for the model Pst 150/2x3/5 stack actuator under different loads..... | 193 |
| Figure 4.6 - Schematic voltage/stroke diagram for the model Pst 150/2x3/7 stack actuator under different loads..... | 193 |
| Figure 4.7 - Finite element analysis concept used for the understanding of the relation between the actuator force application and the generated interfragmentary site motion. The 150 N actuator force case was used for exemplification..... | 195 |
| Figure 4.8 - Examples of different ferrite sizes and shapes | 204 |
| Figure 5.1 - Chart showing the overall structural organization of the experiments and the associated evaluation methods | 211 |
| Figure 5.2 - The test materials considered in the study: (A) Zn irregular shaped ferrite sample and (B) Sr-Ca ferrite sample showed from different views | 212 |
| Figure 5.3 - Resazurin assay: non reduced blue resazurin compound is present in the wells with the ferrite samples and the fluorescent pink product in the positive control wells. | 215 |

| | |
|--|-----|
| Figure 5.4 - Day 4 CAM assay protocol overview were: (A) albumin removal, (B) CAM dissociation from the egg shell membrane, (C) isotonic solution injection and (D) the square window creation for blood vessels development monitoring, are represented | 219 |
| Figure 5.5 - MTT measurements of MG-63 cells cultured on Zn irregular ferrite samples after 1 and 3 days. The values are the mean \pm SD and expressed as percentage of positive controls (cell seeding density of 5×10^4 cell/ml)..... | 223 |
| Figure 5.6 - Ferrite surface topographies after 3-day culture with MG-63 cells obtained from optical microscopy: (A and C) Cell adhesion and proliferation on ferrite samples and (B and D) Negative control samples which were not exposed to cells. Images magnification of 0.7X and 2X was used in the top and bottom images, respectively. Note the purple precipitates present on the seeded samples (A and C), compared to the non-seeded samples (B and D) (cell seeding density of 5×10^4 cell/ml)..... | 224 |
| Figure 5.7 - SEM image of Zn ferrite non-fractured surface. Images were obtained from secondary electrons. Image magnification of 2500X..... | 224 |
| Figure 5.8 - X-ray spectrum of the Zn ferrite. The horizontal axis is the energy scale and the vertical axis is the number of photons per energy interval. The x-ray identification, element, is indicated in the vicinity of the peaks..... | 225 |
| Figure 5.9 - Average measurement of static contact angle on Zn ferrite surface. The image represents a 103.5° contact angle | 226 |
| Figure 5.10 - Photographs of CAM (A) through in ovo analysis immediately after ferrite sample deposition and (B) after 11 days of incubation through ex ovo analysis. The arrow indicates the presence of new blood vessels sprouting towards the ferrite sample | 227 |
| Figure 5.11 - Average number of CAM total blood vessels of type I (grey with diagonal stripes), II (diagonal stripes) and III (dark grey with diagonal stripes) and convergence blood vessels of type I (grey), II (white) and III (dark grey) on CAM images at day 0 and 3 from Zn ferrite sample deposition | 227 |
| Figure 5.12 - Average blood vessels diameter of type I (dark grey), II (diagonal stripes) and III (grey) calculated from CAM images recorded at 0 and 72 hours after Zn ferrite sample deposition | 228 |
| Figure 5.13 - MTT counts on MG-63 cells cultured on Zn (in grey) and Sr-Ca (diagonal stripes) ferrite samples, 1 and 3 days. The MTT counts are presented as the mean \pm standard deviation and expressed as percentage of positive controls (cell seeding density of 5×10^4 cell/ml)..... | 229 |
| Figure 5.14 - Resazurin measurements at 1, 3, 7 and 11 days of MG-63 cells cultured on Sr-Ca ferrite at a demagnetized state through different methods: Curie temperature under | |

an oxygen environment (dark grey - Tc+O₂), Curie temperature under nitrogen environment (diagonal stripes - Tc+N₂) and strong external magnetic field with opposite polarity (light grey - E). The resazurin counts are presented as the mean \pm standard deviation and expressed as percentage of control (cell seeding density of 2×10^4 MG-63 cell/ml). The results obtained from resazurin measurements on permanent magnetic samples were used as control. (* - Significantly different from control; ** - Significantly different from Tc+N₂) 230

Figure 5.15 - Resazurin counts at 1, 3, 7 and 11 days of MG-63 cells cultured on Curie temperature and under nitrogen environment demagnetized Sr-Ca ferrite samples with additional mechanical cleaning (denoted as "MC") and without the mechanical cleaning (denoted as "No MC"). The resazurin counts are presented as the mean \pm standard deviation and expressed as percentage of controls (cell seeding density of 2×10^4 MG-63 cell/ml). The results obtained from resazurin measurements on permanent magnetic samples were used as control. (* - Significantly different from "No MC") 231

Figure 5.16 - X-ray spectrum of the Sr-Ca ferrite. The horizontal axis is the energy scale and the vertical axis is the number of photons per energy interval. The x-ray identification, element, is indicated in the vicinity of the peaks 232

Figure 5.17 - Average measurement of static contact angle on Sr-Ca ferrite surface. The image is a representation of a 68.4° contact angle 233

Figure 5.18 - SEM photographs from 1 day incubation of MG-63 cells cultured on Sr-Ca ferrite demagnetized surface through (A,B) strong external magnetic field of opposite polarity and (C,D) Curie temperature and under an oxygen atmosphere. Images were obtained from secondary electrons. Two magnifications are shown: 2500X (A,C) and 5000X (B,D) 234

Figure 5.19 - SEM photographs from 1 day incubation of MG-63 cells cultured on Sr-Ca ferrite demagnetized surface through Curie temperature and under a nitrogen atmosphere and subjected to abrasive mechanical cleaning. Images were obtained from secondary electrons. Two magnifications are showed: 2500X (A) and 5000X (B)... 235

Figure 5.20 -Profilometry 3D images of the Sr-Ca ferrite surfaces as determined from microscope-based white light interferometry and where the influence of the de-magnetization process and the absence of it, was evaluated: (A) magnetic, (B) de-magnetized through the application of a strong electric field, (C) de-magnetized with Curie temperature in an oxygen atmosphere, and (D) ferrite de-magnetized with Curie

| | |
|---|-----|
| temperature in a nitrogen atmosphere. Images magnification of 0.25X was used for (A) and 0.5X was used for (B), (C) and (D) samples | 235 |
| Figure 5.21 - Surface topographies of the Sr-Ca ferrite surfaces as determined from microscope-based white light interferometry and where the influence of the abrasion mechanical cleaning was evaluated: (A) demagnetized Sr-Ca ferrite through Curie temperature in a nitrogen atmosphere and not subjected to hard mechanically cleaned surface and (B) the same material however subjected to abrasive mechanical cleaning. Images magnification of 0.5X was used..... | 237 |
| Figure 6.1 - Schematic representation of the proposed magnet actuator device linked to an intramedullary nail for bone healing enhancement. The implanted actuator is externally activated and controlled by a handheld emitting device which electrical current is obtained from a frequency generator amplified signal. Tibia with fibula and intramedullary nail image obtained from [9] and fracture image obtained from [10] | 250 |
| Figure 6.2 - Block diagram of the general constative components in the concept demonstration models..... | 251 |
| Figure 6.3 - Schematic representation of the (C) concept model developed for 'proof of concept' demonstration purpose and the set-up system used for the frequency measurements based in the model 2. The system electronical apparatus comprises: (A) laser Doppler vibrometer optical sensor head, (B) oscilloscope, (D) amplifier, (E) laser Doppler vibrometer controller and (F) laser Doppler vibrometer signal analyser unit | 252 |
| Figure 8.1 - Photographic registers from the intramedullary nail implantation process..... | 261 |
| Figure 8.2 - X-ray from the tibia composite with the intramedullary nail implanted from the (A) frontal and (B) medial view | 262 |

List of Tables

| | |
|--|------------|
| <i>Table 2.1 - Peak tibiofemoral joint compressive forces during several daily activities and expressed as times the body weight.....</i> | <i>25</i> |
| <i>Table 2.2 - In vivo humans bone strain values measured during different types of physical activities, reported in the literature.....</i> | <i>49</i> |
| <i>Table 2.3 - AO classification of diaphyseal long bones fractures. The fracture type could be A: Simple fractures without a third fragment; A1: spiral, A2: oblique ($\geq 30^\circ$), A3: transverse ($< 30^\circ$); B: Wedge fractures with a third or more fragments, but with contact between the fragments; B1: spiral wedge, B2: bending wedge, B3: fragment wedge; C: Complex fractures; C1: spiral, C2: segment, C3: irregular. The fracture group could be 1: Fractures in torsion; 2: Fracture in bending or 3: Fracture due to other mechanisms. Adapted from [3, 14, 16].....</i> | <i>67</i> |
| <i>Table 2.4 - Schematic representation of the three-stage model for secondary bone healing. The information is arranged according to: (a) visual representation, (b) general description of the main events that characterize each stage, (c) duration of each stage and (d) stiffness alteration with the increase in the Young's modulus. Adapted from: [20, 31-33].....</i> | <i>71</i> |
| <i>Table 2.5 - Selected mechanical properties of different types of intramedullary nailing materials in comparison with the cortical bone. UTS – Ultimate tensile strength, TYS – Tensile yield strength.....</i> | <i>95</i> |
| <i>Table 3.1 - Review on in vitro mechanical experimentation (ME) and/or finite element analysis (FE) of tibia bone with or without an intramedullary nail implanted. M – Medium size, L - Large size, S – Sagittal plane, C - Coronal plane, IR - Internal rotation, ER - External rotation, AT - Anterior surface in tension, PT - Posterior surface in tension, LT - Lateral surface in tension, NIA – No information available.....</i> | <i>126</i> |
| <i>Table 3.2 - Comparison between the 4th generation composite intact tibia mechanical experimentation (ME) and finite element simulation (FE) with published experimental data from the study developed by Anneliese Heiner [20] where the same tibia model was considered. NIA – No information available.....</i> | <i>151</i> |
| <i>Table 3.3 - Stiffness (mean value \pm SD) of the composite tibia-intramedullary nail based on mechanical experimentation with data from the machine system and DIC measurement method and from the finite element (FE) simulation and their comparison to published data from the study developed by Penzkofer et al. [11]. SS - stainless steel, TA - titanium alloy, UNCOMP - uncompressed bone-intramedullary nail</i> | |

| | |
|---|-----|
| <i>construct system and COMP - compressed bone-intramedullary nail construct system</i> | 153 |
| <i>Table 4.1 - Average interfragmentary displacement (μm) for each actuator force applied (N)</i> | 194 |
| <i>Table 4.2 - Permanent magnets types and typical properties. Data obtained from: [3, 66, 72-76]</i> | 201 |
| <i>Table 5.1 - Scoring scheme for irritation testing with hen's egg chorioallantoic membrane ...</i> | 226 |
| <i>Table 5.2 - Surface roughness parameters measured in two directions (x and y) of the rougher magnetic and demagnetized ferrite samples through different methods (strong electric field (E), Curie temperature in an oxygen atmosphere ($T_c + O_2$) and Curie temperature in a nitrogen atmosphere ($T_c + N_2$). Data is shown as arithmetic means \pm standard deviation ($\pm SD$) and expressed in μm. Ra: average surface roughness, Rq: root mean square roughness, Rz: mean peak-to-valley roughness</i> | 236 |
| <i>Table 5.3 - Surface roughness parameters measured in two directions (x and y) of the demagnetized Sr-Ca ferrite through Curie temperature in a nitrogen atmosphere ($T_c + N_2$) and the ferrite material in the same conditions however subjected to additional mechanical cleaning (+ MC) surface treatment. Data is shown as arithmetic means \pm standard deviation ($\pm SD$) and expressed in μm. Ra: average surface roughness, Rq: root mean square roughness, Rz: mean peak-to-valley roughness</i> | 237 |
| <i>Table 8.1 - Properties of some different types of actuators. The two test samples are highlighted in dark grey</i> | 263 |
| <i>Table 8.2 - Few parameters adopted in the studies where sheep was used for the evaluation of intramedullary nail fixation device. OD – outer diameter, L- length</i> | 267 |

Nomenclature

Abbreviations/acronyms

| | |
|--------|---|
| 3D | Three-dimension |
| ABS | Acrylonitrile butadiene styrene |
| AC | Alternating current |
| AISI | American Iron and Steel Institute |
| AO | <i>Arbeitsge-meinschaft für Osteosynthesefragen</i> (meaning Association for Osteosynthesis) |
| ASIF | Association for the Study of Internal Fixation |
| ASLS | Angular stable locking system |
| ASTM | American Society for Testing and Materials |
| AT | Anterior surface in tension |
| ATP | Adenosine triphosphate |
| BMU | Basic multicellular units |
| BSE | Back-scattered electrons |
| BW | Body weight |
| CAD | Computer-aided design |
| CAGR | Compound annual growth rate |
| CAM | Chorioallantoic membrane |
| CCD | Charged coupled device |
| CENFIM | <i>Centro de Formação Profissional da Indústria Metalúrgica e Metalomecânica</i> (meaning Vocational Training Centre of the Metal Industry) |
| DIC | Digital image correlation |
| CNC | Computer numerically controlled |
| COMP | Compressed bone-intramedullary nail construct system |
| CT | Computed tomography |
| DGAV | <i>Direcção-Geral de Alimentação e Veterinária</i> (meaning Portuguese National Authority for Animal Health) |
| DMSO | Dimethyl sulphoxide |
| E | Electrical field |
| EDS | Energy-dispersive X-ray spectroscopy |
| EDTA | Ethylenediaminetetraacetic acid |

| | |
|---------|--|
| ENaC | Epithelial sodium channels |
| ER | External rotation |
| ESIN | Elastic stable intramedullary nailing |
| ESPI | Electronic speckle pattern interferometry |
| FAST | Flexible axial stimulation |
| FBS | Foetal bovine serum |
| FCT | Foundation for Science and Technology |
| FDM | Fused deposition modelling |
| FE | Finite element |
| FEPA | Federation of European Producers of Abrasives |
| FIN | Flexible intramedullary nailing |
| GmbH | <i>Gesellschaft mit beschränkter Haftung</i> (meaning company with limited liability) |
| HET | Hen's egg test |
| HET-CAM | Hen's egg test - Chorioallantoic membrane |
| ICCVAM | Interagency Coordinating Committee on the Validation of Alternative Methods |
| IPC/I3N | Institute of Nanostructures, Nanomodelling and Nanofabrication |
| INEGI | <i>Instituto de Ciência e Inovação em Engenharia Mecânica e Engenharia Industrial</i> (meaning Institute of Science and Innovation in Mechanical and Industrial Engineering) |
| IR | Internal rotation |
| IS | Irritation score |
| ISO | International Organization for Standardization |
| LAETA | Associated Laboratory for Energy, Transports and Aeronautics |
| LC | Lacuno-canalicular |
| LEPABE | Laboratory for Process Engineering, Environment, Biotechnology and Energy |
| LET | <i>Laboratório de Ensaios Tecnológicos</i> (meaning Technological Testing Laboratory) |
| LOME | <i>Laboratório de Óptica e Mecânica Experimental</i> (meaning Laboratory of Optics and Experimental Mechanics) |
| LT | Lateral surface in tension |
| LVM | Low carbon Vacuum melt Molybdenum |
| MC | Mechanical cleaning |

| | |
|--------|---|
| ME | Mechanical experimentation |
| MEM | Minimum essential medium |
| MES | Minimal effective strain |
| MMPA | Magnetic Materials Producers Association |
| MRI | Magnetic resonance imaging |
| MTT | 3-(4,5-dimethylthiazol-2-yl)-2,5-diphenyltetrazolium bromide |
| NADP | Nicotinamide adenine dinucleotide phosphate |
| NIA | No information available |
| NO | Nitric oxide |
| NSAID | Nonsteroidal anti-inflammatory drugs |
| OD | Outer diameter |
| OPG | Osteoprotegerin |
| PBS | Phosphate buffer saline |
| PGE2 | Prostaglandin E2 |
| PLLA | Poly(L-lactide) acid |
| PMMA | Poly(methyl methacrylate) |
| PT | Posterior surface in tension |
| PVDF | Polyvinylidene fluoride |
| PZT | Lead zirconate titanate |
| RANKL | Receptor activator of nuclear factor-kappaB ligand |
| RIA | Reamer/Irrigator/Aspirator |
| SAW | Surface acoustic wave |
| SD | Standard deviation |
| SEM | Scanning electron microscopy |
| SIGN | Surgical Implant Generation network |
| SS | Stainless steel |
| TA | Titanium alloy |
| TF | Tibia fractures |
| TSF | Tibia shaft fractures |
| TYS | Tensile yield strength |
| UK | United Kingdom |
| UNCOMP | Uncompressed bone-intramedullary nail construct system |
| UPTEC | <i>Parque de Ciência e Tecnologia da Universidade do Porto</i> (meaning Science and Technology Park of University of Porto) |
| USA | United States of America |

| | |
|------|------------------------------|
| UTS | Ultimate tensile strength |
| WCIF | Wright cell imaging facility |

Chemical nomenclature

| | |
|--|----------------------|
| <i>Al</i> | Aluminum |
| <i>Al₂O₃</i> | Aluminum oxide |
| <i>Au</i> | Gold |
| <i>Ba</i> | Barium |
| <i>BaTiO₃</i> | Barium titanate |
| <i>C</i> | Carbon |
| <i>Ca</i> | Calcium |
| <i>CaCO₃</i> | Calcium carbonate |
| <i>Ca₁₀(PO₄)₆(OH)₂</i> | Hydroxyapatite |
| <i>Co</i> | Cobalt |
| <i>CO₂</i> | Carbon dioxide |
| <i>Cr</i> | Chromium |
| <i>Cu</i> | Copper |
| <i>Fe</i> | Iron |
| <i>Fe₂O₃</i> | Ferric oxide |
| <i>Fe₃O₄</i> | Magnetite |
| <i>MgAl₂O₄</i> | Magnesium aluminate |
| <i>Mn</i> | Manganese |
| <i>Mn₃Al₂Si₃O₁₂</i> | Spessartine |
| <i>Mo</i> | Molybdenum |
| <i>NaCl</i> | Sodium chloride |
| <i>NaOH</i> | Sodium hydroxide |
| <i>Nb</i> | Niobium |
| <i>Nd₂Fe₁₄B</i> | Neodymium-iron-boron |
| <i>Ni</i> | Nickel |
| <i>NiTi</i> | Nitinol |
| <i>O</i> | Oxygen |
| <i>O₂</i> | Oxygen gas |
| <i>P</i> | Phosphorus |
| <i>Pb</i> | Lead |

| | |
|-----------------------|--|
| $Pb(Zr_{1-x}Ti_x)O_3$ | Lead zirconate titanate (or PZT) general molecular formula |
| Pd | Palladium |
| S | Sulfur |
| Si | Silicon |
| Sr | Strontium |
| $SrFe_{12}O_{19}$ | Strontium hexaferrite |
| $SrCO_3$ | Strontium carbonate |
| Ti | Titanium |
| TiO_2 | Titanium dioxide |
| V | Vanadium |
| Zn | Zinc |

Symbols

| | |
|---------------|---|
| ΔL | Change in length |
| Δx | Horizontal displacement |
| Δy | Vertical displacement |
| λ | Wavelength |
| β | Rotation angle |
| BH_{max} | Maximum value of energy product |
| B_r | Flux density |
| B_s | Saturation flux density |
| C | Distance between the inner and outer support or Capacitance |
| d_{ij} | Piezoelectric coefficient |
| E | Electrical field strength or Young Modulus |
| ε | Strain |
| F | Force |
| f | Frequency |
| H | Magnetic field |
| H_c | Coercive field |
| I | Momento of inertia or electrical current |
| L | Original length |
| Q | Electrical charge |

| | |
|------------|--|
| r | Intramedullary nail mean radius with respect to the closed structure |
| R_a | Average surface roughness |
| R_q | Root mean square roughness |
| R_z | Mean peak-to-valley roughness |
| δ | Data given by the DIC method |
| S | Slope of the tangent of the initial straight portions of the load-deflection curve |
| $secC$ | Coagulation reaction starting time |
| $secH$ | Hemorrhage reaction starting time |
| $secL$ | Vascular lyses reaction starting time |
| S_{ij} | Actuator strain |
| s_{33}^E | Compliance |
| t | Intramedullary nailwall thickness or Time |
| T_c | Curie temperature |
| t_i | Initial position |
| t_f | Final position |
| u_i | Initial permeability |
| u_{max} | Maximum permeability |
| V | Voltage |
| V_{p-p} | Peak-to-peak voltage |

1. Introduction

This PhD thesis was funded by the Foundation for Science and Technology (FCT) through the research grand SFRH/BD/87089/2012. The thesis was developed in the framework of the Doctoral Program in Mechanical Engineering in association with the Associated Laboratory for Energy, Transports and Aeronautics (LAETA), Laboratory for Process Engineering, Environment, Biotechnology and Energy (LEPABE) and the Institute of Nanostructures, Nanomodelling and Nanofabrication (IPC/I3N) as part of the development of an actuator for bone healing enhancement. The experimental research was conducted at the Faculty of Engineering of the University of Porto, with the collaboration of the Laboratory for Bone Metabolism and Regeneration at the Faculty of Dental Medicine of the University of Porto and *Artur Salgado S.A.* All the biocompatibility experiments were developed at the Laboratory for Bone Metabolism and Regeneration. The intramedullary nail used during the research study and all the implantation devices required were provided by *Artur Salgado S.A.*

1.1. Motivation

1.1.1. Tibia shaft fractures: An underestimated problem

Tibial shaft fractures are the most common long bone injuries [1-3]. Most fractures occur between the mid-shaft region and the distal third of the tibia, where the smallest cross-section and moment of inertia are present [3-6]. The tibia shaft fractures are also considered a very painful injury, as demonstrated in a study developed by Kane *et al.* [7] where this type of fractures attained the highest pain rankings.

The epidemiology of the tibial diaphysis fractures was evaluated in a few studies [8-18]. The incidence was reported based on its variation over the years and between different countries and cities, as presented in Figure 1.1. Although, as stated by Larsen *et al.* [9], most epidemiological studies are conducted without a geographically well-defined and complete population and the data obtained cannot be extrapolated to a nationwide scale, few representative insights on this fractures type were still considered.

A common characteristic reported in most studies is the tibial shaft fractures incidence with respect to age and gender. There are two main tibial shaft fractures peaks distributions: the first in young males and the second in older women. In men, the pattern is generally characterized by a high peak at younger age - between 10 to 34 years - which gradually falls until about 60 years, when it then rises again. The female incidence rate, however, reached its lowest values at younger ages, between 20 to 39 years, then increases after menopause, which occurs around 45 years. The rate obtained in older men is normally lower than older female peak. However, in general, the number of fractures affecting men are considered to be at least twice than that affecting women. High tibial fractures registered in men are normally associated as being caused by sport injuries (*e.g.* soccer and skiing) or traffic accidents. In older women, the low bone mass and high prevalence osteoporosis, which characteristically increases with aging, may greatly influence the tibial peak fracture incidence. In elderly, tibia shaft fractures lead to acute inpatient stay, post-acute patient stay and home healthcare as well as outpatient visits and physical and occupational therapy. Also such fractures in this age group are starting to be associated with high mortality rates, which values have demonstrated to be as high as the ones obtained in hip fractures [12, 16, 19-23].

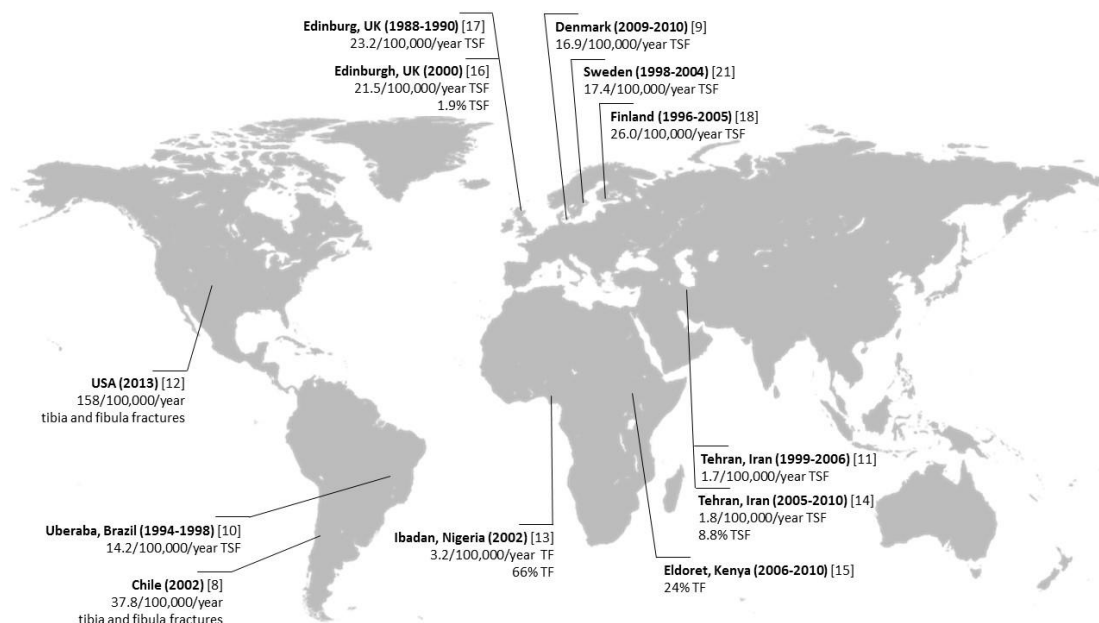


Figure 1.1 - Few worldwide epidemiological studies on the incidence of tibia fractures. TF -Tibia fractures, TSF -Tibial shaft fractures. World map image obtained from [24] and incidence calculated based on total country or city population data from [25, 26]

In Portugal, there is a lack on nationwide level published data concerning tibia diaphyseal fractures epidemiology characterization, where validated fracture classification, trauma mechanism, length of hospital stay and treatment adopted, are reported. This limitation may be due to the difficulty in obtaining complete statistical detailed country information [19]. Such

knowledge would help to understand the current state of the nation and its evolutionary behavior in the last decades. This would allow for the development of prevention and treatment strategies [10, 14]. However, based on few unpublished references [27] and available literature [28-31], some generalizations were made. Similarly to what is verified worldwide, and as stated during a Portuguese AoTrauma Course [27], in Portugal tibia fractures are also considered as the most common among long bones and are associated with a high rate of open injuries which are considered the more severe cases. The results obtained in a study developed by Mário Peneda [28], “blamed” falls and also road-traffic accidents as the two main causes for lower limb injuries. Based on this study, it was also possible to present a preliminary insight on the country’s gender and age group related tibial fractures incidence (see Figure 1.2). There seem to be a general high predominance (minimum 3-fold) of tibia fractures among men when compared to women. The higher male values are among young and middle-aged adults. The causal factors of such gap are unknown. In women, there is a trend in increase tibial fractures beginning in middle age. According to data from the Portuguese National Health Service [30, 31], the stabilization of this injuries with intramedullary nail fixation method through open fracture reduction, is the sixth most frequent muscular-skeletal chirurgical procedure developed at operating rooms across the country. The number of intramedullary nailing implantations records showed an increase in 324 more cases in 2013 from the 4031 registered in 2009.

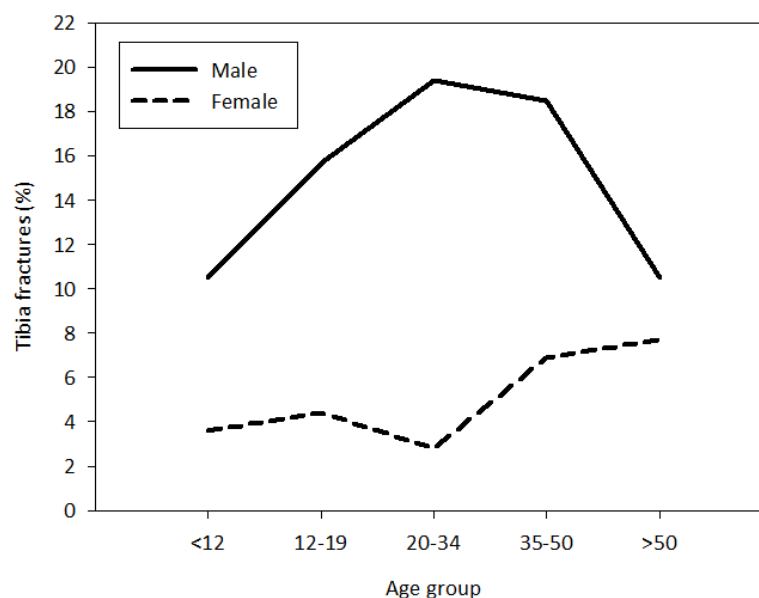


Figure 1.2 - Accidental and intentional percentage tibia fractures according to the age groups and gender which occurred between the XIX and XX century, based on medical records from Coimbra and Lisbon. Data entirely obtained from [28]. The age groups were defined according to the criteria used by Buikstra and Ubelake [32]

In comparison with other long bones, tibia fractures are the ones in which healing is most problematic not only due to the demanding mechanical requirements placed upon this bone

during normal daily activities, but most importantly as a result of the tibiae's reduced amount of soft tissue [3-6, 33]. Tibia shaft fractures are also more commonly associated with severe trauma due to traffic accident. Such type of impact normally leads to high-energy injuries such as open fractures. The high rate of severe trauma cases may be a consequence of tibial shaft soft tissue reduced protection where its asymmetric positioning leaves the anteromedial surface more vulnerable. In most studies, males are associated with a greater frequency of high-energy trauma which peak incidence is among individuals between 10 to 40 years old. In general, the high-energy trauma frequency among women is low throughout life. Tibia open shaft fractures are particularly difficult to manage and are associated with complications such as wound infection [34] and problems with bone healing. Infections associated with fracture-fixation devices in tibia are generally lower in closed fractures, between 0.9 to 4.45% [35]. However, it may rise up to 33% [36] in open fracture cases. The more common problems with bone healing are delayed unions (defined as fractures that have not achieved union at 4.9 months post-fracture) or in more severe cases non-unions (defined as fractures that have not achieved union within 6 to 9 months post-fracture). These undesirable results extend the patient disability and lead to substantial pain. Nevertheless, such disproportionate healing period can occur in any fracture site with higher probabilities in open fractures. Delayed unions and non-union cases, where high-energy trauma is not present, are normally associated to excessive interfragmentary movement, avascularity of fragments, infection or a combination of all those variables. Hence, the type of stabilization method adopted influences the healing rate. Although a profound understanding of the factor contributing for healing failure is lacking, variables like age, gender, hormonal effects, bone necrosis and percent pre-reduction displacement may have a significant impact [1, 3-6, 9, 12, 17, 21, 37-41].

1.1.2. Intramedullary nail: A good stabilization method with space for improvement¹

i) Range of application and biomechanical principle

For the vast majority of tibial shaft fractures in adults, interlocking reamed intramedullary nails has become the standard care procedure [42, 43]. The current widespread indication for the use of interlocking intramedullary nailing includes: (a) the management of closed fractures with the exception of proximal and distal fractures of the tibia that are contraindicated due to special positions [44], (b) acute closed fractures [45], (c) open fractures [46, 47] and (d) serious and

¹ The presentation of the concept behind the thesis motivation: Rosa, N., Simoes, R., Magalhães, F. D., Marques, A. T. Enhanced bone healing through mechanical stimulation by implanted piezoelectric actuators, in *International joint Conference on Biomedical Engineering Systems and Technology (BIOSTEC)*, 2014. Angers, France. These conference presentation received the "Best PhD Project Award".

complicated fractures. The latter indication cases includes: segmental fractures, polytraumatized patients and additional ipsilateral fractures, morbid obesity [48], failed non-operative treatment of tibial shaft fractures, late management of open tibial fractures, when the definitive care is implemented after the damage control orthopedics concept in polytraumatized patient (*i.e.* conversion of an external fixator or internal fixator to an intramedullary nailing) [44, 46] and also in pathological fractures (*e.g.* fracture caused by bone metastatic) [44]. From a biological and mechanical perspective, intramedullary nailing offers several advantage when compared to other stabilization procedures (*e.g.* cast, external fixator and internal fixator). This procedure is considered to require a minimal surgical approach for its implantation. Also, indirect fracture reduction with reduce disturbance to the fracture site is sometimes possible. This fixation method preserves the periosteal blood supply and even when the reaming technique is adopted (removal of circumferential layers from the bone endosteal surface resulting in the elimination of bone irregularities and enlargement of the medullary canal diameter) the endosteal vasculature is re-established. The central positioning of the intramedullary nail allows it to function as a load-sharing device. During the early healing stage when the fracture site is instable, the nail supports most of the weight applied on the limb. The stress will gradually be transferred to the interfragmentary site with the progressive stiffening of the local tissues (from granulation tissue to cartilage-like and finally calcified callus) [39]. Another interesting characteristic of this stabilization method is that the surgical procedure duration for intramedullary nail implantation is lower than the amount of time required for internal fixation application [27, 49], with average procedure period of 1.9 hours [35]. According to the marked research report [50], internal fixators already form the largest segment of the orthopedic trauma fixation devices market and they are also associated with a trend in future demand increase, where a 6.8% compound annual growth rate (CAGR, calculated as geometric average of annual growth rates [51]) from 2014-2020, is predicted.

ii) Slow healing time

The intramedullary nail fixation technique is considered an effective stabilization method and its good reputation is due to its high rate of successful healing cases. However, tibia shaft fractures stabilized with intramedullary nail may still be associated with a prolonged healing time [12]. As showed in the study developed by Ouyang *et al.* [44], where an extended evaluation (follow-up period around 26.2 months) on the patients' average healing time based on a wide range of interlocking intramedullary nails designs in isolated long bone fractures (*e.g.* tibia, femur and humeral) was taken in consideration, the mean time for tibia fracture union was 5.2 months. Besides the prolonged recovery time, patients that undergo a surgical procedure -

such as intramedullary nail implantation - require a longer hospital stay as demonstrated in the study developed by Weiss *et al.* [21], where tibia shaft fractures average hospitalization healing period was 4 (\pm 9) days. Larsen *et al.* [9], reported the inpatient duration with average values of 9.4 (\pm 9.7) days. A higher average hospital stay for the management of tibial diaphyseal fractures with intramedullary nail was stated by Downing *et al.* [35] as 12.1 days. The management of tibial diaphyseal fractures has always held a particular interest for orthopedic surgeons due to the challenge they represent and the healing process duration is an important parameter with significant burden to the health system and direct implications on the patient's physical and emotional wellbeing.

The reduce nationwide understanding of the epidemiology and costs to society and healthcare system associated with tibial shaft fractures treated with intramedullary nail, limits the conclusions drawn on the subject. However, it is of general belief that the tibia shaft fractures slow healing process presents a substantial burden to society and patients. The management and recovery process of tibia shaft fractures is often complex and challenging in financial terms not only to the healthcare system, but also in human aspects and facility requirements, since such procedure requires experienced orthopedic surgeons, qualified support staff, expensive equipment and a good rehabilitation strategy (*e.g.* physiotherapy, medication and follow-up physicians visits) [15]. There is also the social economic burden associated with tibia shaft fractures due to the labor hours lost since the younger generation are the prime victims of this type of injury [23, 52]. The weeks off work comprises the incident occurrence and management time and also the recovery time required until patients can return to their normal routine. According to Downing *et al.* [35] the recovery process may require an average of 15 weeks off work which may also include around 6.1 outpatients appointments. According to a recent study developed by Antonova *et al.* [12], in the United States around 500 000 tibia and fibula fractures occur each year which result in 77 000 hospitalizations and account for 569 000 hospital days. Although, it may not be up-to-date, a study presented by Downing *et al.* [35], gives an insight on tibia shaft fractures cost in the UK and Heckman and Sarasohn-Kahn [41] estimate the cost in the USA. The first study pointed-out a mean hospital cost when intramedullary nailing stabilization method is used of £2226 (around 3183.2€ in 1997 [53]) per patient, with a total cost to society of £6592 (around 9426.6€ in 1997 [53]) per patient when the patient mean time off work is also considered. In the second study, the costs considered were only for tibial shaft fracture management with general operative treatment and no specific stabilization procedure considered. The costs for both surgery and recovery phase were estimated as \$20575 (around 17756.2€ in 1997 [53]) per patient and the outpatient rehabilitation process solely would be

\$4317 (around 3725.6€ in 1997 [53]) per case. It is important to highlight that although more closely associated with high-energy open fractures, delay and non-unions cases further worsen the burden of tibia shaft fractures. Tibia shaft fracture also affect patient's psychological and physical quality of life [12, 54]. The high amount of medication (*e.g.* strong opioids, NSAID's, benzodiazepines and injectable corticoids) used by tibia shaft fractures patients during the healing process is a pertinent detail highlighted by Antonova *et al.* [12]. Besides the burden this may represent for patients, according to Heckman and Sarasohn-Kahn [41] the medication taken during fracture management and the follow-up period could average around \$2000 (around 1726€ in 1997 [53]) per case. Hence, tibia shaft fracture healing time represent a considerable economic burden to worldwide society but also to patient's well-being [12, 21, 37]. Although, no decision should be made solely from an economic basis, more than ever there is an awareness of expenditure in the health service, the concern in cost reduction [35]. The burden associated with tibia shaft fractures is expected to increase with the tendency in world population augmentation, which consequently will lead to a higher number of tibia injuries and also with the expected increase in the number of aging-related injuries [33, 55].

iii) Mechanical stimulus effect on the healing time

Human life preservation, bone healing, soft tissue treatment and limb angular and rotational motion recovery are the orthopedic surgeon's main concern when treating tibia shaft fractures [27, 42]. However, the duration of the healing process is also an important variable for the physician and healthcare system but most importantly for the patient. It is well-accepted that the mechanical environment at the fracture site can profoundly influence the rate and quality of the bone fracture repair [39]. The stiffness of the intramedullary nail-bone structure and the limb weight bearing or load applied to the fracture site regulate the local mechanical stimulus, *i.e.* determine the amount of motion between the bone fragments and consequently the strain suffered by the healing tissue [56, 57].

The most critical period of bone healing is the first few weeks after fracture [58-60]. Although one of the main advantage of intramedullary nailing is that it allows patients premature mobilization [49, 61, 62], during the early healing phase the fracture-site mechanical stimulus mainly results from partial weight-bearing from patient reduced mobility. According to Joseph Borrelli [46], the standard post-operative care, when intramedullary nailing stabilization technique is used in lower extremity bones, includes partial weight-bearing during the first 6 weeks accompanied with quadriceps strengthening and motion of the ankle and knee exercises. However, patient recovery procedure may vary between countries and even between hospitals

in the same nation. Despite studies, such as the one developed by Gaebler *et al.* [63], state that small diameter tibial nails (between 7 and 8 mm) in non-segmental fractures presents a strength capable of supporting full weight-bearing in the post-fracture phase; normally full weight-bearing is only allowed after radiographic evidence of callus formation and pain-free weight bearing is evident. This again usually occurs 6 weeks after nail implantation. Quadriceps strengthening exercises as well as a range of motion exercises of the ankle and knee start as soon as possible. After union is verified, patients are discharged and a follow-up procedure is adopted [5, 46]. Gardnera *et al.* [59] also states that at 4 weeks there is already a callus formation which calcifies in the following weeks. By the 8th week, the callus is already able to support compressive loads. From then and until the end of the bone recovery, callus shape and material properties suffer transformation to re-establish its original characteristic. As demonstrated in the study developed by Joslin *et al.* [64], inpatients with a healthy healing progress, weight-bearing increases steadily with time and its return to normal values generally indicates that clinical union of the fracture has occurred. This process appears to be accompanied by the increase load withstand by the healing tissue. This low frequency mechanical stimulus experienced by the limb during the early healing stage may represent a limitation and an opportunity to intervene positively to improve healing process [64]. Hence, as stated by some authors [43, 58-60], interfragmentary stimulus have a higher influence when applied soon after injury, *i.e.* first few weeks after stabilization device implantation. However, for the bone fracture recovery to be optimized, the one-week post-surgery delay in the beginning of stimulus application should be respected. Such procedure will allow the initiation of the body healing response to occur, by permitting soft tissue healing and by not disturbing the early vascular response (which precede and determines the organization of the osteogenesis) which is very sensitive to the initial mechanical environment [65, 66].

Currently in use and in research stage, bone healing stimulation methods include the supply of osteoprogenitor and mesenchymal stem cells to the fracture site and local application of growth factors, which sometimes are complemented by therapies such as low-intensity pulse ultrasound, electrical stimulation and extracorporeal shock waves. The currently use of cell culture techniques present some limitations such as the high number of required cells, associated risks in infectious diseases transference, and also the fact it involves an invasive surgery. Growth factors are natural potent inducers of endochondral ossification (*e.g.* bone morphogenetic proteins, transforming growth factor β and insulin-like growth factor). However, there are several issues about their use, including safety where supraphysiological concentrations of growth factors are needed to obtain the desired osteoinductive effects, the

high cost of treatment, and more importantly, the potential for ectopic bone formation. In relation to the externally applied signals - such as ultrasound, electrical and shock waves - these interventions are in most of the cases prescribed and may be expected to be more effective, in fracture delay and non-union cases. In addition to the variety of research studies where the use of this external interventions is associated with a positive skeletal response, several other controversial reports about their efficacy did not detect treatment effects in animal or clinical studies. In those studies, some drawbacks and limitations are identified associated to their use and availability and even its cost-effectiveness [55, 60, 65, 67-73]. Therefore, we may conclude that the current strategies for bone regeneration exhibit relatively satisfactory results. There is still a need for a practical cost-effective a new approach with well-defined specifications and regimes for individual patients at determined point in the healing process that is capable of accelerating the fracture healing process in such a way that the need for intramedullary nail fixation is reduce to a minimum necessary time-period.

Currently the concept that mechanical stimulus at the fracture site are essential for bone repair is well accepted. However, one of the greatest drawback in the bone-healing mechanical stimulation field is that there is an insufficient knowledge on the mechanical environment that promotes healing and the available theories for fracture enhancement are sometimes contradictory. Despite the great effort made in literature, a quantifiable relationship between the rate of healing and mechanical stimulus at the fracture site has never been established. The knowledge gap on the ideal mechanical environment has prevented wider-scale harnessing of bone's mechanosensitivity to enhance healing [27, 33, 39, 56, 57, 74]. In the attempt to determine the relevant window of bone-repair mechanical stimulation, *in vivo* internal loads acting on long bones during daily activities were considered of special interest in fracture healing research. Few recent studies [75-80] are starting to show evidences on the importance of daily low-amplitude high-frequency strain stimulus in bone remodeling process and in the reduction of osteoporosis. Such small strain stimulus with values less than $5\ \mu\epsilon$ that occurs at a higher frequency, between 10 to 100 Hz, are believed to be as effective or even more in maintaining bone mass. Since fracture healing is a regenerative process of osseous tissue, *in vivo* load application systems, such as individual limb compressive and whole-body vibration, were tested to demonstrate the impact of low-magnitude high-frequency strain stimulus in inducing callus formation and mineralization, hence accelerating fracture healing. Several studies [80-86] started considering the possible advantages of applying low-magnitude high-frequency interfragmentary strain stimulus to accelerate bone-healing process. In the primordial studies such as the one developed by Kenwright *et al.* [86], the which at the time were considered as

micro-motions, were evaluated in respect to with healing enhancement. In this clinical study, the early application of cyclic of up to 1 mm micro-movement at the tibia fracture site showed a significant increase in the rate of healing. In another clinical study developed by Noordeen *et al.* [85], an interesting conclusion was taken. It was demonstrated that a maximum of 2 mm axial cyclic movement during weight-bearing with a unilateral external fixator retarded the fracture healing in three weeks. On the contrary, the delay on the application of this stimulus between four to six weeks did not induce any backlog in the healing process. Although it may have not been evident in this study, the results obtained may have been pointing out to the importance of lower amplitude stimulus applied in earlier stage of healing. Hence, in the latter case, during the patients early healing phase the fixator was locked. However, locked fixator already encourages some amount of low-amplitude motion at the fracture site because of pin bending and movement at the bone-pin interface. Hence, the present of micro-motion in healing enhancement may already have been present. The importance of controlled fracture site micro-motion (around 0.6 mm) imposed after unilateral external fixator frame and at a very early phase (first few days after fracture) when mechanical stimulation may be most effective and when the active loading by the patient is minimum, was highlighted in the clinical study developed by Kershaw *et al.* [87]. Although, the earlier studies focus on interfragmentary stimulus magnitude by measuring and comparing the effect of bone fragment displacement, several studies [84, 88, 89] highlighted the importance that the amount of interfragmentary motion should depend more on the relation of displacement to the width of the fracture gap (also known as strain). Although, Comiskey *et al.* [74], claimed benefits on the application of cyclic displacements less than 7% of the width of the fracture gap, the positive effect of even lower strain values were presented in some studies. There is evidence that uniaxial strains between 0.3% and 2.8% are capable of stimulating *in vitro* osteoblast proliferation and synthesis [60]. Goodship *et al.* [83] reinforce the idea that mechanical stimulus do not need to be large to positively influence the fracture-healing process. In their study, they applied a short duration (17 minutes), low-magnitude (25 $\mu\epsilon$) high-frequency (30 Hz) interfragmentary axial displacement on a 3 mm mid-diaphyseal osteotomized sheep tibia. This study demonstrated that physiological loading with additional short period of low-amplitude – which were less than 1% of the fracture gap width and less than 6% of the 0.45 mm displacement measured at the site during ambulation - high-frequency strain will positively influence the rate of healing. In the study developed by González-Torres *et al.* [82], the importance of the frequency value in the mechanical stimulus for the regulation of bone healing was evaluated. In this study, a finite element model of a sheep tibia metatarsus fracture allowed the conclusion that the change in the frequency of the external mechanical stimulus directly affects the interstitial fluid flow

velocity in the fracture callus. It was also suggested that, to obtain a more significant effect, higher frequencies (between 50 to 100 Hz) with lower amplitude (displacements that are less than 0.6% of the width of the fracture gap) than the ones used in previous works are needed. Other studies [23, 65, 69, 70, 81, 90] have also demonstrated the potent effect of low-amplitude high-frequency oscillatory accelerations (or vibrations), rather than deformations. Based on the demonstrated potent osteogenic effect of this stimulus, its potential was recently evaluated in bone fracture treatment. A beneficial effect of low-magnitude high-frequency vibration was reported by Leung *et al.* [23]. In their study, osteotomized rat tibiae with intramedullary Kirschner wires were stimulated by a vibration platform with 35Hz and which generates a 0.3g (with g referring to earth's gravitational acceleration, 9.8 m/s^2), actuating 20 minutes a day, for 5 days a week during a total study period of 9 weeks. This type of stimulus showed a positive osteogenic effect through the formation of a larger amount of callus, accelerated callus remodeling and fracture site healing, comparatively to the non-stimulated ones. In a study developed by Hwang *et al.* [65], the impact of short duration very small amplitude oscillatory motions, 45 Hz at 0.4 g for 20 minutes per day during 3 weeks, applied locally (oppositely to whole body vibrations) in enhancing healing process in scaffolded and non-scaffolded calvarial defects in rats, were evaluated. This stimulus enhanced the healing process in defect without scaffolds by increasing the formed bone volume and thickness in 84% and 33% higher, respectively. However, this effect was more evident in the presence of existing collagen scaffold. This study also demonstrated that the beneficial effect of the stimulus applied during the 3-week experimental period continued even during the following 4-week rest period. In a more recent study, based on the concept that bone cells loss sensitivity to mechanical stimuli under continued stimulation [91], Gao *et al.* [92] evaluated the influence low-magnitude high-frequency vibration with different rest period regimes on rat transverse fracture models with Kirschner wire fixation. This study confirmed the importance of different rest period regimes which significant improved the macro- and nano-level bone mechanical properties, the tissue mineral density and nano-level bone special arrangement. The most significant effect was 35 Hz at 0.25 g vibrational loading per day in which three bouts of 5 min of vibration were separated by 4 h. The low-intensity high-frequency vibration stimulus, perception capability are not only limited to bone cells. As demonstrated in an *in vitro* study developed by Pongkitwitoon *et al.* [90], there was an increase in macrophage proliferation and pro-healing phenotype promotion in response to high-frequency oscillations, 100 Hz, when applied at low intensities of 0.15 g, during only 3 days of simulation. Macrophages play a critical role in the bone healing process and the high sensitivity for this stimulus could lead to a reduction in the inflammation response.

During the last decade, evidence on the potentiality of the low-amplitude high-frequency mechanical stimulus in enhancing bone-healing process, has been accumulated. Although the different experimental conditions adopted by the studies cited (*e.g.* study model, stabilization device used, duration of the experiment, etc.) limit robust and detailed conclusion taken on the precise most effective values of the stimulus, literature showing promising results created high expectation about this concept. This is increased by the attractive feature of such stimulus being considered physiological and not compromising the natural healing process [27, 39, 56, 57].

In the present study, it is hypothesized that there is a positive correlation between the additional application of low-magnitude high-frequency interfragmentary mechanical stimulus at early healing stage and the rate of healing. Hence, it will be assumed that by upgrading the “gold standard” stabilization procedure where high rate of successful healing cases are already obtained, with short period of low-amplitude high-frequency mechanicals stimulus locally at the fracture site, enhancement fracture repair progress could be achieved. Such physiological mechanical stimulus were selected for this study not only based on the inspiring potential of these stimulus, but also due to the fact that they are considered safe, do not interfere negatively in the biological process of bone healing, and do not represent any risk for the stabilization device (*e.g.* mechanical failure). Hence, if a well-aimed and well-timed intervention could accelerate the physiological process of fracture healing and improve the quality of bone regeneration, this would decrease the patient healing time, facilitate an earlier rehabilitation, reduce the length of hospitalization stay and the patient discomfort associated with tibia fractures. In addition, by hypothesizing that the time required for fracture healing costs more money than the early intervention actuator to shorten the time of fracture healing, the total cost for society associated with tibia diaphysis fracture stabilized with intramedullary nail could be reduced.

1.2. Thesis objectives

The main goal of this PhD thesis is to innovate and upgrade the already successful existing intramedullary nail stabilization method by developing an actuator device linked to (or capable to be used simultaneously with) the fixation method which, through physiological mechanical stimulation, is capable of accelerating the bone fracture-healing process. As a guiding principle and based on values considered in literature, the actuator should be capable to induce interfragmentary stimulus of at least $5\ \mu\epsilon$ at physiological frequencies between 10 to 100 Hz. Other variables defining the loading protocol include the number of loading sessions, 5 days per week at a duration of 17 minutes per day. It is also intended that the stimulus would start to be

applied as soon as 5 to 7 days after intramedullary nail implantation. The clinical need of the idea was determined and the actuator features requirements were established to suit patient needs and orthopedic surgeons demand's. Hence, it would be desirable that the actuator could present the following characteristics:

- 1) The actuator should add an additional stimulus to the already interfragmentary motion obtained from patient early weight-bearing in the conventional intramedullary nail-bone system stability configuration.
- 2) The actuator should induce a physiological mechanical stimulus and avoid the disruption of the physiological fracture-healing process.
- 3) The actuator should be conceived to stimulate patients during post-surgery phase when they normally have low physical activity levels.
- 4) The actuator should not cause any additional pain or discomfort to the patient.
- 5) Changes in the principles, implantation procedure (*e.g.* reaming diameter), surgical instrumentation used for implantation and in the implant should, with the existence of the actuator should be avoided.

The presence of the actuator should not alter the duration of the intramedullary nail implantation procedure.

- 6) It is desirable that the device allows the physician to constantly adjust the stimulus ("therapy") generated by the actuator.
- 7) The energy/power for the actuator performance should come from a source outside the human body and should not expose the interior of the organism to the external hazards.
- 8) The energy/power for the actuator should be rechargeable and be used in more than one patients which would decrease the costs associated to the device application.
- 9) The actuator developed should have a feasible and attractive cost/benefit ratio.

The long-term goal for the actuator is that it could enhance the patient mental and physical well-being and minimize the economic burden associated with tibia fractures treated with intramedullary nail.

1.3. Document structure

This thesis is organized in a seven-chapter structure, as can be seen in Figure 1.3. In the **Chapter 2: Literature Review**, the fundamental concepts and important considerations required to understand the complex and multidisciplinary subject addressed in this thesis, are explained. In a focused review, all the essential background that will be most useful as input for a greater understanding of bone-implant systems, will be described. This chapter is also divided in four

sub-chapters were the following sequential topics are discussed: bone mechanics dependence on its hierarchical arrangement, bone self-adaptive capability, clinical fractures and bone healing and regeneration based on intramedullary nail fixation stability. The first presents bone as a living composite with a complex mechanical behavior that result from its multi-levelled hierarchical structure and arrangement. Another important bone characteristic is the ability to adapt its mass, microstructure and properties to the dynamic mechanical environment. Hence, in the second sub-chapter this is highlighted and essential topics related to the origin of mechanical stimulus in bone, the biomechanisms associated with mechanotransduction, the nature of physiological bone stimuli and the test systems most commonly used to study the mechanical stimulation of bone, are clarified. In the next sub-chapter, the general insights on the concept of tibial shaft fractures are presented and are accompanied with a comprehensive description on the physiological fracture healing process. The final sub-chapter concludes the chapter with the analysis of the intramedullary nail fracture stabilization method biomechanical concepts, its important historical evolution turning points, comments on some peripheral events that affected its development and presents the recent innovations, which will stablish the adequate knowledge framework for intramedullary nail improvement.

The experimental research developed is presented in four chapters and the information is described according to the methodology used, the results obtained and its discussion. The analysis was developed in a two-phase study. It starts, in **Chapter 3**, with an experimental understanding of the intramedullary nail fixation method stability concept. In this chapter, by pointing towards a clear understanding of tibia-intramedullary nail construct stability and the amount of interfragmentary motion expected during patients partial-weight bearing early healing phase a simple methodology was development. This methodology comprehends a set of testing conditions for mechanical experimentation and finite element model validation and analysis. In the second phase of the study and as part of the bone fracture-healing enhancement actuator device development in **Chapter 4**, few potential candidates were considered and the best material was selected. However, before they can be considered suitable to be used *in vivo*, in **Chapter 5**, the selected material actuator cytotoxicity was evaluated and the risk for *in vivo* implantation was assessed. In **Chapter 6**, the actuator efficiency was evaluated through the analysis of its performance when placed in a concept validation system. Finally, in **Chapter7**, conclusions on the developed study are drawn, showing the prevailed future work direction in hope for the proposal improvement.

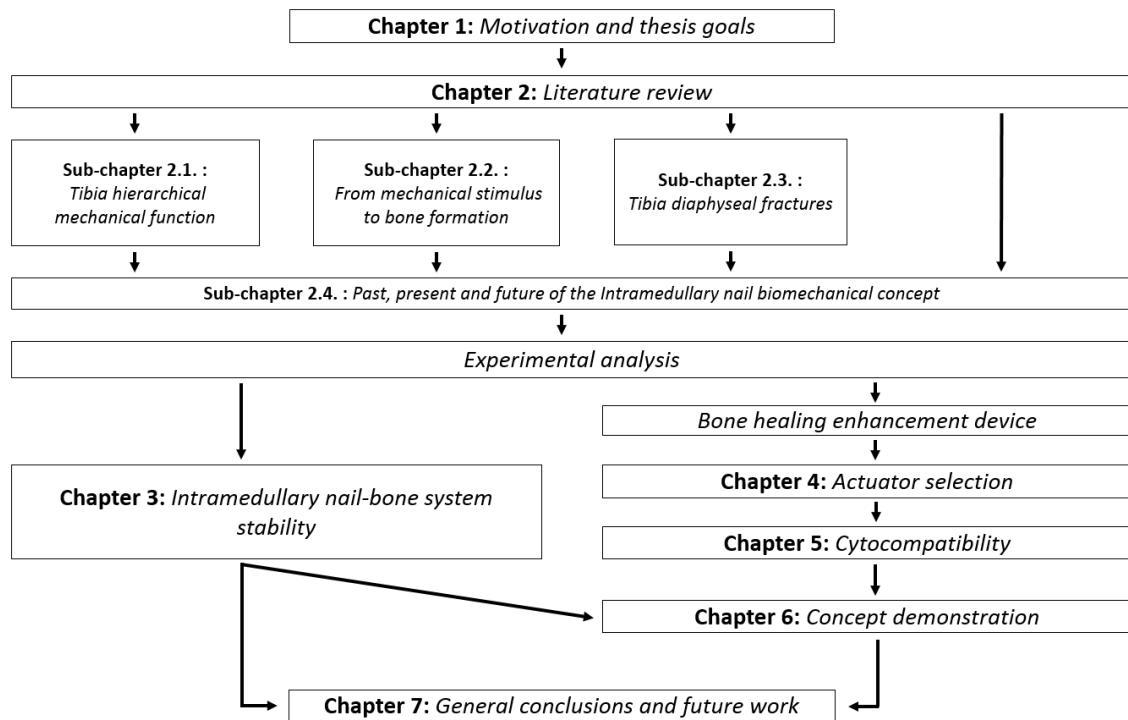


Figure 1.3 - Overall thesis structure and how its chapters and sections are linked together

1.4. References

1. LeClere, L.E. and R.M. Lucas, *Tibial shaft fractures*, in *Orthopaedic rehabilitation of the athlete: Getting back in the game*, B. Reider, G. Davies, and M.T. Provencher, Editors. 2014, Elsevier Health Sciences: Philadelphia, USA. p. 1360-1384.
2. Egol, K., K.J. Koval, and J.D. Zuckerman, *Handbook of fractures*. 4th ed, ed. K. Egol, K.J. Koval, and J.D. Zuckerman 2012, Philadelphia, USA: Lippincott Williams & Wilkins.
3. Trafton, P.G., *Tibial shaft fractures*, in *Skeletal trauma: Basic science, management, and reconstruction*, B.D. Browner, et al., Editors. 2003, Elsevier Science: Pennsylvania, USA. p. 2131-2255.
4. Schmitt, K.-U., et al., *Trauma biomechanics: An introduction to injury biomechanics*. 4th ed 2014, London, UK: Springer.
5. Lacroix, D. and P.J. Prendergast, *Three-dimensional simulation of fracture repair in the human tibia*. *Computer Methods in Biomechanics and Biomedical Engineering*, 2002. **5**(5): p. 369-376.
6. Court-Brown, C.M., *Fractures of the tibia and fibula*, in *Rockwood & Green's Fractures in Adults*, R.W. Bucholz, J.D. Heckman, and C.M. Court-Brown, Editors. 2006, Lippincott Williams & Wilkins. p. 2080-2148.
7. Kane, R.L., et al., *Visual Analog Scale pain reporting was standardized*. *Journal of Clinical Epidemiology*, 2005. **58**(6): p. 618-623.
8. Medina, E. and A.M. Kaempffer, *Consideraciones epidemiológicas sobre los traumatismos en Chile*. *Revista Chilena de Cirugía*, 2007. **59**(3): p. 175-184.
9. Larsen, P., et al., *Incidence and epidemiology of tibial shaft fractures*. *Injury*, 2015. **46**(4): p. 746-750.
10. Grecco, M.A.S., et al., *Epidemiology of tibial shaft fractures*. *Acta Ortopédica Brasileira*, 2002. **10**(4): p. 10-17.
11. Madadi, F., et al., *Epidemiology of adult tibial shaft fractures: A 7-year study in a major referral orthopedic center in Iran*. *Medical Science Monitor*, 2010. **16**(5): p. 217-221.

12. Antonova, E., et al., *Tibia shaft fractures: costly burden of nonunions*. BMC Musculoskeletal Disorders, 2013. **14**(42): p. 1-10.
13. Ifesanya, O.A., et al., *Changing Trends In The Pattern Of Tibial Fractures In Nigeria: A Review Of 70 Cases*. Journal of Orthopaedics, 2008. **5**(2): p. 1-16.
14. Mehrpour, S.R., et al., *Descriptive epidemiology of traumatic injuries in 18890 adults: A 5-year-study in a tertiary trauma center in Iran*. Asian Journal of Sports Medicine, 2015. **6**(1): p. 23129-23135.
15. Ayumba, B.R., et al., *Management of Patients with Post-Traumatic Exposed Bones at Moi Teaching and Referral Hospital, Eldoret, Kenya*. East African Orthopaedic Journal, 2015. **9**(1): p. 21-26.
16. Court-Brown, C.M. and B. Caesar, *Epidemiology of adult fractures: A review*. Injury, 2006. **37**(8): p. 691-697.
17. Court-Brown, C.M. and J. McBirnie, *The epidemiology of tibial fractures*. Journal of Bone and Joint Surgery, British Volume, 1995. **77-B**(3): p. 417-421.
18. Väistö, O., *Intramedullary Nailing of Tibial Shaft Fracture: with special attention given to anterior knee pain*, in *Department of Surgery in the Orthopaedic and Traumatology Unit 2011*, University of Tampere: Tampere, Finland.
19. Singer, B.R., et al., *Epidemiology of fractures in 15 000 adults*. Bone and Joint Journal, 1998. **80**(2): p. 243-248.
20. Grütter, R., et al., *The epidemiology of diaphyseal fractures of the tibia*. Injury, 2000. **31**(3): p. 64-94.
21. Weiss, R.J., et al., *Decreasing incidence of tibial shaft fractures between 1998 and 2004: information based on 10,627 Swedish inpatients*. Acta Orthopaedica, 2008. **79**(4): p. 526-533.
22. Clement, N.D., et al., *The outcome of tibial diaphyseal fractures in the elderly*. Bone and Joint Journal, 2013. **95**(9): p. 1255-1262.
23. Leung, K.S., et al., *Low-magnitude high-frequency vibration accelerates callus formation, mineralization, and fracture healing in rats*. Journal of Orthopaedic Research, 2009. **27**(4): p. 458-65.
24. *World map blank without borders*, 2009: The free media repository at Wikimedia Commons.
25. The World Bank Group. *Total population*. 2016; World Bank Open Data: free and open access to data about development in countries around the globe.]. Available from: <http://www.worldbank.org/>.
26. United Nations Statistics Division. *Total population, both sexes combined (thousands)*. 2016; Available from: <http://data.un.org/Default.aspx>.
27. Felicíssimo, P., et al., *Aotrauma course - Basic principles of fracture management*, 2014, AOTrauma Europe: Tomar, Portugal.
28. Peneda, M.P.R.C., *Fraturas acidentais e intencionais violentas: Impressões médicas de arquivo de Coimbra e Lisboa entre os séculos XIX-XX*, in *Department of Life Sciences 2014*, Faculdade de Ciências e Tecnologia da Universidade de Coimbra: Coimbra, Portugal.
29. Matias, F.A.L., *Relatório de Estágio em Ortopedia*, in *Department of Orthopaedic 2013*, University of Porto: Instituto de Ciências Biomédicas Abel Salazar.
30. Portuguese National Health Service, *Morbilidade Hospitalar – Serviço Nacional de Saúde 2009*, 2009, General Directorate of Health: Lisbon, Portugal. p. 155.
31. Portuguese National Health Service, *Morbilidade Hospitalar – Serviço Nacional de Saúde 2013*, 2014, General Directorate of Health: Lisbon, Portugal. p. 377.
32. Buikstra, J.E. and D.H. Ubelaker, *Standards for data collection from human skeletal remains: proceedings of a seminar at the Field Museum of Natural History*, ed. J. Haas, et al. 1994, Fayetteville, Arkansas: Arkansas Archeological Survey.

33. Morgan, E.F. and J. Lei, *Toward Clinical Application and Molecular Understanding of the Mechanobiology of Bone Healing*. Clinical Reviews in Bone and Mineral Metabolism, 2015. **13**(4): p. 256-265.
34. Trampuz, A. and W. Zimmerli, *Diagnosis and treatment of infections associated with fracture-fixation devices*. Injury, 2006. **37**(2): p. S59-S66.
35. Downing, N.D., D.R. Griffin, and T.R. Davis, *A comparison of the relative costs of cast treatment and intramedullary nailing for tibial diaphyseal fractures in the UK*. Injury, 1997. **28**(5-6): p. 373-375.
36. Badhulkar, S. and H.K.T. Raza, *Open fractures*. Indian journal of Orthopaedics, 2008. **42**(4): p. 365-367.
37. Patel, M., J. Herzenberg, and J.J. McCarthy. *Tibial nonunions: Background, epidemiology, etiology*. [WebMD Health Professional Network] 2014; Available from: <http://emedicine.medscape.com/article/1252306-overview>.
38. Dutta, S.K. and D. Datta, *Biomechanics of fractures*, in *Applied Orthopaedic Biomechanics*, S.K. Dutta and D. Datta, Editors. 2008, BI Publications Pvt Ltd: New Delhi, India. p. 50-58.
39. Harwood, P.J., J.B. Newman, and A.L.R. Michael, *Mini-symposium: Basic science of trauma (ii) An update on fracture healing and non-union*. Orthopaedics and Trauma, 2010. **24**(1): p. 9-23.
40. Court-Brown, C.M., et al., *The epidemiology of open long bone fractures*. Injury, 1998. **29**(7): p. 529-534.
41. Heckman, J.D. and J. Sarasohn-Kahn, *The economics of treating tibia Fractures the cost of delayed unions*. Bulletin Hospital for Joint Diseases, 1997. **56**(1): p. 63-72.
42. Favela, J. and C.A. Collinge, *Tibia shaft distal third: Treatment with an intramedullary nail*, in *Fractures of the Tibia: A Clinical Casebook*, N.C. Tejwani, Editor 2016, Springer: London, UK. p. 131-139.
43. Hernández-Vaquero, D., et al., *Dynamisation and early weight-bearing in tibial reamed intramedullary nailing: its safety and effect on fracture union*. Injury, 2012. **43**(S2): p. S63-S67.
44. Ouyang, X., et al., *Interlocking Intramedullary Nails in Fracture Treatment*. Cell biochemistry and biophysics, 2015. **73**(1): p. 261-265.
45. Al-Omari, A., P. Kendrick, and C.S. Roberts, *Antegrade intramedullary nailing of the humerus*, in *Practical procedures in orthopaedic trauma surgery*, P.V. Giannoudis and P. Hans-Christoph, Editors. 2014, Cambridge University Press: New York, United States of America. p. 48-52.
46. Borrelli, J., *Intramedullary nailing of the tibia*, in *Practical procedures in orthopaedic trauma surgery*, P.V. Giannoudis and P. Hans-Christoph, Editors. 2014, Cambridge University Press: New York, United States of America. p. 346-354.
47. Wehner, T., et al., *Improvement of the shear fixation stability of intramedullary nailing*. Clinical Biomechanics, 2011. **26**(2): p. 147-151.
48. Lichte, P. and P. Hans-Cristoph, *Tibia shaft fractures*, in *Bone and joint injuries: Trauma surgery III*, H.-J. Oestern, O. Trentz, and S. Uranues, Editors. 2014, Springer - Verlag: London, United Kingdom. p. 341-346.
49. Horn, J., *Intramedullary nailing of long bone fractures. Experimental in-vivo and in-vitro studies.*, in *Faculty of Medicine 2011*, Oslo Universitetssykehus: Oslo, Norway.
50. Transparency Market Research, *Orthopedic Trauma Fixation Devices Market - Global Forecast, Share, Size, Growth and Industry Analysis 2014 - 2020*, 2014: New York, USA.
51. Moutinho, L. and G.D. Hutcheson, *The SAGE dictionary of quantitative management research 2011*, London, UK: SAGE.
52. Xavier, C.A.M. and J.R. Carvalheiro, *Incidencia de fraturas, exceto de crânio, no município de Ribeirão Preto, SP (Brasil) nos anos de 1969-1970*. Revista de Saúde Pública, 1978. **12**: p. 432-442.

53. OANDA Europe Limited. *Historical Exchange Rates*. 2016; Commercial website providing current and historical world currencies exchange rate data]. Available from: <https://www.oanda.com/>.
54. Mackenzie, E.J., et al., *Return to work following injury: The role of economic, social, and job-related factors*. American Journal of Public Health, 1998. **88**(11): p. 1630-1637.
55. Mavčič, B. and V. Antolič, *Optimal mechanical environment of the healing bone fracture/osteotomy*. International Orthopaedics, 2012. **36**(4): p. 689-695.
56. Giannotti, S., et al., *Current medical treatment strategies concerning fracture healing*. Clinical Cases in Mineral and Bone Metabolism, 2013. **10**(2): p. 116-120.
57. Claes, L., S. Recknagel, and A. Ignatius, *Fracture healing under healthy and inflammatory conditions*. Nature Reviews Rheumatology, 2012. **8**(3): p. 133-143.
58. Kalfas, I.H., *Principles of bone healing*. Neurosurgical Focus, 2001. **10**(4): p. 1-4.
59. Gardner, T.N., et al., *The influence of mechanical stimulus on the pattern of tissue differentiation in a long bone fracture—an FEM study*. Journal of Biomechanics, 2000. **33**(4): p. 415-425.
60. Bailón-Plaza, A. and M.C.H. van der Meulen, *Beneficial effects of moderate, early loading and adverse effects of delayed or excessive loading on bone healing*. Journal of Biomechanics, 2003. **36**(8): p. 1069-1077.
61. Eveleigh, R.J., *A review of biomechanical studies of intramedullary nails*. Medical Engineering and Physics, 1995. **17**(5): p. 323-331.
62. Synthes, *PFNA. Proximal Femoral Nail Antirotation - Technique Guide*, 2014: Oberdorf, Switzerland. p. 5.
63. Gaebler, C., et al., *The fatigue strength of small diameter tibial nails*. Injury, 2001. **32**(5): p. 401-405.
64. Joslin, C.C., et al., *Weight bearing after tibial fracture as a guide to healing*. Clinical Biomechanics, 2008. **23**(3): p. 329-333.
65. Hwang, S.J., et al., *Extremely small-magnitude accelerations enhance bone regeneration: a preliminary study*. Clinical Orthopaedics and Related Research, 2009. **467**(4): p. 1083-1091.
66. Wallace, A.L., et al., *The vascular response to fracture micromovement*. Clinical Orthopaedics and Related Research, 1994. **301**: p. 281-290.
67. Dimitriou, R., et al., *Bone regeneration: current concepts and future directions*. BMC Medicine, 2011. **9**(66): p. 1-10.
68. Victoria, G., et al., *Bone stimulation for fracture healing: What's all the fuss?* Indian Journal of Orthopaedics, 2009. **43**(2): p. 117-120.
69. Judex, S., T.J. Koh, and L. Xie, *Modulation of bone's sensitivity to low-intensity vibrations by acceleration magnitude, vibration duration, and number of bouts*. Osteoporosis International, 2015. **26**(4): p. 1417-1428.
70. Qing, F., et al., *Administration duration influences the effects of low-magnitude, high-frequency vibration on ovariectomized rat bone*, 2015, Wiley Periodicals, Inc.: Journal of Orthopaedic Research. p. 1-11.
71. Goldstein, C., S. Sprague, and B.A. Petrisor, *Electrical stimulation for fracture healing: Current evidence*. Journal of Orthopaedic Trauma, 2010. **24**(3): p. 62-65.
72. Kumagai, K., et al., *Low-intensity pulsed ultrasound accelerates fracture healing by stimulation of recruitment of both local and circulating osteogenic progenitors*. Journal of Orthopaedic Research, 2012. **30**(9): p. 1516-1521.
73. Verdonk, R., et al., *Biological methods to enhance bone healing and fracture repair*. Arthroscopy: The Journal of Arthroscopic and Related Surgery, 2015. **31**(4): p. 715-718.
74. Comiskey, D.P., et al., *The role of interfragmentary strain on the rate of bone healing—A new interpretation and mathematical model*. Journal of Biomechanics, 2010. **43**(14): p. 2830-2834.

75. Fritton, S., P., K. McLeod, J., and C. Rubin, T., *Quantifying the strain history of bone: spatial uniformity and self-similarity of low-magnitude strains*. Journal of Biomechanics, 2000. **33**(3): p. 317-325.
76. Rubin, C.T., et al., *Inhibition of osteopenia by low magnitude, high-frequency mechanical stimuli*. Drug Discovery Today, 2001. **6**(16): p. 848-858.
77. Huang, R.P., C.T. Rubin, and K.J. McLeod, *Changes in postural muscle dynamics as a function of age*. The Journals of Gerontology Series A: Biological Sciences and Medical Sciences, 1999. **54**(8): p. B352-B357.
78. Sehmisch, S., et al., *Effects of low-magnitude, high-frequency mechanical stimulation in the rat osteopenia model*. Osteoporosis International, 2009. **20**(12): p. 1999-2008.
79. Rubin, C., et al., *Mechanical strain, induced noninvasively in the high-frequency domain, is anabolic to cancellous bone, but not cortical bone*. Bone, 2002. **30**(3): p. 445-452.
80. Wolf, S., et al., *The effects of external mechanical stimulation on the healing of diaphyseal osteotomies fked by flexible external fixation* Clinical Biomechanics, 1998. **13**(4-5): p. 359-364.
81. Wolf, S., et al., *Effects of high-frequency, low-magnitude mechanical stimulus on bone healing*. Clinical Orthopaedics and Related Research, 2001. **385**(192-198).
82. González-Torres, L.A., et al., *Influence of the frequency of the external mechanical stimulus on bone healing: A computational study*. Medical Engineering and Physics, 2010. **32**(4): p. 363-371.
83. Goodship, A.E., T.J. Lawes, and C.T. Rubin, *Low-magnitude high-frequency mechanical signals accelerate and augment endochondral bone repair: Preliminary evidence of efficacy*. Journal of Orthopaedic Research, 2009. **27**(7): p. 922-930.
84. Yamaji, T., et al., *The effect of micromovement on callus formation*. Journal of Orthopaedic Science, 2001. **6**: p. 571-575.
85. Noordeen, M.H., et al., *Cyclical micromovement and fracture healing*. Journal of Bone and Joint Surgery, British Volume, 1995. **77**(4): p. 645-648.
86. Kenwright, J., et al., *Axial movement and tibial fractures. A controlled randomised trial of treatment*. Journal of Bone and Joint Surgery, British Volume, 1991. **73**(4): p. 654-659.
87. Kershaw, C.J., J.L. Cunningham, and J. Kenwright, *Tibial external fixation, weight bearing, and fracture movement*. Clinical Orthopaedics and Related Research, 1993. **293**: p. 28-36.
88. Perren, S.M., *Evolution of the internal fixation of long bone fractures. The scientific basis of biological internal fixation: choosing a new balance between stability and biology*. Bone and Joint Journal, 2002. **84**: p. 1093-1110.
89. Hak, D.J., et al., *The influence of fracture fixation biomechanics on fracture healing*. Orthopedics, 2010. **33**: p. 752-755.
90. Pongkitwitoon, S., et al., *Low-intensity vibrations accelerate proliferation and alter macrophage phenotype in vitro*. Journal of Biomechanics, 2016. **49**(5): p. 793-796.
91. Robling, A.G., D.B. Burr, and C.H. Turner, *Recovery periods restore mechanosensitivity to dynamically loaded bone*. Journal of Experimental Biology, 2001. **204**: p. 3389-3399.
92. Gao, J., et al., *Multi-level assessment of fracture calluses in rats subjected to low-magnitude high-frequency vibration with different rest periods*. Annals of Biomedical Engineering, 2016: p. 1-16.

“The healing of a fracture is one of the most remarkable of all repair processes in the body”

B. McKibbin

2. Literature review

2.1. Tibia mechanical functional structure and hierarchical organization

Introduction

Bone, the main component of the skeleton system, is a crucial constituent of the complex and coordinated multipart “machine” that is the human body [1, 2]. Besides its biological role as mineral reservoir (*e.g.* for calcium, phosphate and magnesium), calcemia regulation and its role as host site for the hematopoietic tissue (*e.g.* bone marrow), bone fulfils a range of demanding mechanical functions. It is responsible for internal organs (*e.g.* the brain) and tissue (*e.g.* bone marrow) protection and also body support and motion through muscles attachment to its surface [3-5]. When standing, balance is maintained by delicate anterior-posterior and medial-lateral movements while during gait controlled motion is secured by an elaborated mechanism of load transfer, ground impact and propulsion [6, 7]. The mechanical behavior of bone is determined by its composition and structural organization at the different length-scales which it established, to a certain extent, by its mechanical environment [8, 9]. There has been an increasing interest in understanding the principles that determine the multi-level hierarchical properties of biological composites. These living materials present a combination of mechanical properties which have not yet been attained by synthetic composites with similar configurations [10, 11]. Hence, the structure-property relationship in bone combined with its adaptive ability makes it an exceptional composite with high interest in engineering and material design. This sub-chapter focuses on the human tibia, aiming to describe the hierarchical organization of bone on progressively smaller scales and hopefully contribute for a better understanding on how the arrangement-based mechanical properties in each level influences the bone whole-structure biomechanical behavior.

It is important to highlight that during this thesis the orientation terms used will always refer to the human body in standard anatomical position. The three basic reference planes, **sagittal** (divides the body into symmetrical right and left halves) **coronal** (passes through bregma, divides the body into anterior and posterior halves and is placed at right angle to the sagittal plane) and

transverse (which slices through the body at any height but always passes perpendicular to the sagittal and coronal plane) will be considered. The orientation terms such as **proximal** (nearest the axial skeleton), **distal** (farthest from the axial skeleton), **medial** (towards the midline), **lateral** (away from the midline), **anterior** (towards the front of the body) and **posterior** (towards the back of the body), will also be used [12].

2.1.1. Macrostructure

The tibia is a long bone from the appendicular skeleton, which alongside with the fibula constitute the two bones of the lower leg. The tibia is the larger, thicker bone on the medial side and articulates proximally at the knee joint and distally at the ankle (see Figure 2.1.d) [7, 13, 14]. Similarly to other long bones, the tibia, can be divided into epiphysis, metaphysis, and diaphysis (see Figure 2.1.c). The central portion of the bone is characterized by the lowest width dimension and it is called the shaft (or **diaphyseal region**) [7, 15, 16]. This region - characterized by an approximately triangular cross-section shape with an anteriorly directed apex as exemplified in the Figure 2.1.a – is located between the wider proximal and distal extremities that form the articular ends [15-17]. The tibia diaphysis is divided into three surfaces (**medial, lateral, and posterior surfaces**) by three borders (**anterior, interosseous and medial borders**) [7]. The **epiphyseal region** is located at each bone extremity and connects to the diaphysis through the **metaphyseal region**. The hollow region in the diaphysis is called the medullary cavity, which is filled with vessels, nerves and the bone marrow. During skeleton growth, the epiphysis and metaphysis are separated by the epiphyseal cartilage which becomes ossified in adult bone [5, 18]. According to Ales Hrdlicka [19], one of the most interesting peculiarities of the human tibiae is its inter- and intra-individual variability. Although, the diaphysis shape variations are significant - phenomena best appreciated in transverse cross-sections - the anatomical specificity in shape and size in the extremities of the bone are relatively less. In terms of length and medullary canal diameter, the adult tibia may range from less than 300 mm to more than 470 mm and the minimal diameter of the medullary canal may also vary from less than 8 mm to more than 15 mm [17].

The **periosteum**, a connective tissue composed externally by a fibrous layer and internally by a cellular layer known as cambium, covers the entire length of the tibia with the exception of the articulating surface and at ligament and tendon insertion points [5, 15, 18, 20, 21]. Bones have both an external blood supply from the overlying periosteum and an endosteal blood supply through a nutrient artery [22]. The tibia also has the **nutrient foramen**, a hole at the proximal one-third to one-half of the posterior surface of the tibia through which vessels and nerves enter

and exit. The **medullary cavity** surface also has a membranous lining, the endosteum, where bone formation, repair and remodeling occurs [16, 18, 23].

Proximally, the tibia articulates at the tibiofemoral joint through the **tibial plateau** which is divided into two articular sections the tibial **medial** and **lateral condyle** (one for each femoral condyle). The articular facets are separated by a fibrocartilaginous ring called menisci, which increases the congruence between the articular surfaces, distributes weight-bearing forces, acts as shock absorber and reduces the friction between the structures. The tibial condyles are separated by two superior projections of non-articular bone, the **intercondylar eminences** also known as the tibial spines. Inferior to the condyles on the anterior surface of the proximal tibia is a rough protuberance, called the **tibial tuberosity**, and it is where the *patellar ligament* of the *quadriceps femoris muscle* (major lower leg extensor at the knee) is inserted [6, 12, 14, 24, 25]. The **soleal** (or popliteal) line crosses the proximal one-third to one-half of the posterior tibial surface from superolateral to inferiorlateral and defines the inferior boundary of the *popliteus muscle* insertion (flexural and medial rotator of the tibia) and gives rise to the *popliteus fascia* and *soleus muscle* (plantarflexor of the foot and the ankle). Distally the tibia inferior surface, **tibial platform**, is shaped like a rectangular box with a bony prominence on the medial side, called the **medial malleolus** [14]. The lateral surface of the distal end of the tibia is occupied by a deep triangular notch, known as the **fibular notch**, to which the distal head of the fibula is anchored by a thickened part of the interosseous membrane [7]. The ankle forms a saddle joint that allows two degrees of freedom. The tibia - through its tibial platform and the medial malleolus - and the fibula, press against the medial and lateral end of the saddle-shaped *talus* - a tarsal bone - to form the ankle joint. Because the upper surface (or trochlear surface) of the talus rest entirely against the tibia and the upper end of the fibula does not contact the femur, body weight is carried downward to the talus through the tibia alone, hence the fibula bears no weight [7, 24, 26]. Each of the tibial anatomical landmarks mentioned above are represented in Figure 2.1.b and 1.c.

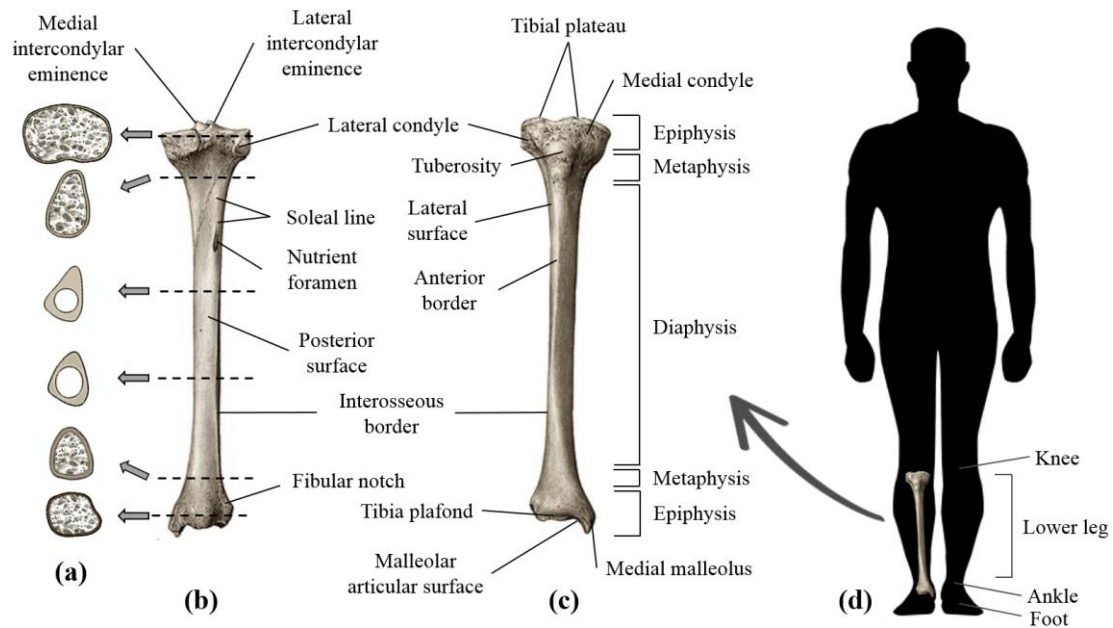


Figure 2.1 - Representation of the tibia positioning in the lower leg (d), with localization of the main anatomical landmarks from the posterior (b) and anterior view (c) and cross-section images (a) along the tibia showing its shape variation as well as cortical and trabecular bone portions.

At the highest hierarchical level, the tibia is constituted by the cortical bone also known as compact bone and trabecular bone (also known as cancellous or spongy bone). Although, they have similar composition, the different structure arrangement and porosity level grants each structure unique mechanical properties and function [27]. The cortical bone is a solid, dense structure with a porosity of less than about 30%. For example, adult human femoral cortical bone porosity can vary from as low as 5% at age of 20 and up to 30% above the age of 80 [12, 28, 29]. The trabecular bone has a spongier, lightweight and honeycomb structure with porosity values of approximately 70% with higher values in cases such as the elderly spine where 95% porosity are reached [12, 30-34].

The tibia is a complex support structure in the body system [35] and during daily activities, such as normal level walking, the tibiofemoral joint experiences high compressive loads around 3 times the body weight (normally expressed as $\times BW$), *i.e.* 2058 N if a 70 Kg adult was considered. However, more strenuous activities such as squats can rise the load for values up to 7.3 times the body weight, *i.e.* 5008 N if the same body weight was considered (see table 2.1). According to Taylor *et al.* [36], average shear anterior to posterior forces of 0.5 and 1.3 BW during walking and stair climbing, respectively, have been measured in the human knee. However, the loads presented within the joints are higher than the ones along the long bones as the result of the action of the musculature crossing the joints.

Table 2.1 - Peak tibiofemoral joint compressive forces during several daily activities and expressed as times the body weight

| Activity | | Knee contact force (×BW) | | | Study ¹ | References |
|-------------------|------------|--------------------------|----------------------|------------|--------------------|------------|
| | | Medial | | Lateral | | |
| | | 1 st peak | 2 nd peak | | | |
| Level walking | | 3.2 | | | <i>In vivo</i> | [37] |
| | | 2.8 | | | Simulation | [38] |
| | | < 2.4 | 2.4 | 1 | <i>In vivo</i> | [39] |
| | | 2.2 - 2.5 | 2.37 - 2.51 | Similar | <i>In vivo</i> | [40] |
| | | 2.8 | | | <i>In vivo</i> | [41] |
| | | 3.3 | | | Simulation | [42] |
| | | 3.1 | | | Simulation | [43] |
| | | 4.0 | | | <i>In vivo</i> | [44] |
| | | 2.8 | | | <i>In vivo</i> | [45] |
| | | 2 | | 1.5 | <i>In vivo</i> | [46] |
| | | 1.3 - 1.5 | 1.3 - 1.5 | 0.8 - 1.15 | <i>In vivo</i> | [47] |
| | | 2.8 | | | Simulation | [38] |
| | | 3.3 | | | Simulation | [42] |
| | | 2.9 | | | <i>In vivo</i> | [48] |
| Stair | Ascending | 2.28 - 2.5 | 2.28 | - | <i>In vivo</i> | [40] |
| | | 2.8 | | | <i>In vivo</i> | [41] |
| | | 5.3 | | | <i>In vivo</i> | [44] |
| | | 2.9 | | | <i>In vivo</i> | [45] |
| | | 5.4 | | | Simulation | [43] |
| | | 2.63 - 2.81 | 2.8 | - | <i>In vivo</i> | [40] |
| | Descending | 3.1 | | | <i>In vivo</i> | [41] |
| | | 3.3 | | | <i>In vivo</i> | [45] |
| Rising from chair | | 2.09 | - | - | <i>In vivo</i> | [40] |
| | | 2.6 | | | <i>In vivo</i> | [45] |
| | | 3.38 – 7.89 | | | <i>In vivo</i> | [49] |
| Jogging | | 3.6 | | | <i>In vivo</i> | [41] |
| Squats | | 7.3 | | | <i>In vivo</i> | [44] |
| | | 6.3 | | | <i>In vivo</i> | [50] |
| | | 4.7 - 5.6 | | | <i>In vivo</i> | [51] |

¹ The correct determination of the load applied to the tibia bone would be through the measurement the forces in *in vivo*, which is clearly limited and not feasible in healthy subjects or in patients with pathology not requiring a total knee replacement. Therefore, in most studies were physiological data was acquired, “kinesiological techniques” such as high speed time camera, force platform and electromyographic recorder, were used and the results obtained were considered in this thesis as being *in vivo* or as close as possible to *in vivo* data.

The diaphysis, which is responsible for the transmission of load between the two extremities (epiphysis and methaphysis both ends), has stiff cortical bone walls [18, 22]. The tibia epiphysis are characterized by a bulk of trabecular bone (containing vessels, nerves and bone marrow), which is coated with a thin layer of cortical tissue [16, 23]. Cortical bone carries a considerable share of the total skeleton load. As demonstrated in a study developed by Papini *et al.* [52] there was a negligible variation in axial and torsional stiffness values prediction by the finite element model if only cortical bone was considered in the simulation. This was justified by the considerable difference between the Young’s modulus of cortical (10-40 GPa) [53-58] and the

trabecular bone (0.05-0.5 GPa) [53]. This demonstrated that it is the cortical rather than the spongy bone which is responsible for most of the weight support. In the epiphyseal and metaphyseal region, where cortical bone thickness is reduced, weight-bearing is achieved by stress reduction with the increase in surface area and load diversion. Stress varies inversely with the loaded cross-sectional area which indicates that stress on the joint will be reduced with the increase in the surface area. The spongy nature of the tibia segment ends confers weight-bearing distribution in local trabeculae, hence it dissipates loads and absorbs energy. As the weight-bearing is transfer from the metaphysis to the diaphysis, it becomes more dependent on the cortical layer, which, in turn, becomes thicker and more resistant [8, 59]. It is important to highlight that the expansion of the bone ends are limited by the reduction of the joint friction to a minimum value (*e.g.* reduce weight of the bone ends will reduce the normal reaction force and reduce length of the radius of curvature will reduce the magnitude of moment of friction). In the tibiofemoral joint, the body weight-bearing load on the tibia plateau is assumed to be divided into a central concentric and a medial and lateral eccentric knee contact force (split around 60 and 40% on the medial and lateral condyles, respectively). The higher loads on the medial side relatively to the lateral side (see Table 2.1) is consistent with the fact that the medial side of the tibia has a larger condyle and bone also is denser and stronger than that of the lateral side. Hence, there is a balance in the bending stress generated between the condyles. Although, only a few important features on the weight-bearing mechanism of the proximal tibia were here presented, the contact mechanism between the femoral and tibial articular surfaces are complex and consist of many unique feature and its biomechanics is not still fully understood [16, 39, 57, 60]. In the case of the ankle, it is expanded to a lesser extent when compared to the upper joint. This occurs since the load of body weight that is transmitted through the lower leg divide itself into two components, which resolve into vertical and horizontal forces, when it reaches the talus trochlea. The horizontal force will stretch the plantar ligaments and muscles and the vertical load will be lesser than the actual load transmitted along the long bone [16].

2.1.2. Microstructure

There are two type of bone tissues: the primary or **woven bone**, present in newly developed immature bone at fracture site callus, and the **lamellar bone**, which is the more mature form of bone, found in the adult human skeleton. In cortical bone, lamellar bone can be found as extended parallel arrays called **circumferential lamellae** and also as smaller lamellae cylindrical structures arrangement called **osteon** (or Haversian system). Each osteon consists of about 10 to 30 lamellae arranged in concentric cylinders built up around the neurovascular channel called the **Haversian canal** (with around 50 μm in diameter). They lie very roughly along the long axes

of a bone and are considered the structural and remodeling unit for cortical bone (see Figure 2.2). An additional source of blood and nerve supply to the compact bones come from the **Volkman's canals** also known as perforating canal. These transverse or oblique canals carry blood vessels from the periosteal and endosteal surfaces to the osteons. The outer surface of the osteon constituted by a thin layer of calcified mucopolysaccharides, the **cement line**, function as a barrier that affects crack propagation. The cancellous bone consists primarily of lamellae, arranged in a less organized lattice-like network of matrix spikes, called **trabeculae**, to form a network of rods and plates which on average have thickness in the range of 100-200 μm . The trabeculae are interspersed with large bone spaces (in the order of 500 to 1500 μm) filled with bone marrow. This trabecular architecture varies across anatomic site and age [5, 12, 18, 28, 30-34, 61-65].

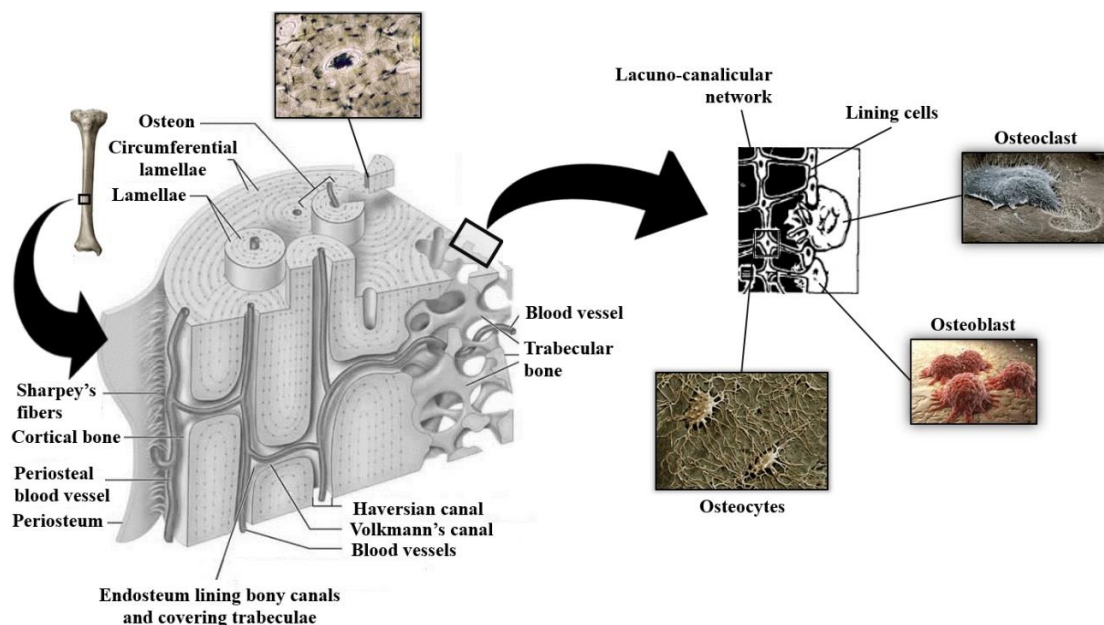


Figure 2.2 - Diagram showing tibia diaphysis bone microscopic hierarchical organization and its main cellular population. Adapted from [66-71]

Bone, as a highly vascular mineralized connective tissue, consists of various types of cells, a complex extracellular matrix and extracellular fluid. Although, the cells of the neurovascular supply and those of the periosteum, endosteum and marrow, also constitute the cellular component of bone, the specialized mature bone cells involved in the formation, modeling, and remodeling of bone are: osteoblasts, osteoclasts and osteocytes (see Figure 2.2) [62, 66, 67].

Undifferentiated mesenchymal stem cells form the **osteoprogenitor cells**, which are spindle-shaped cells with migratory behavior that are present in the periosteum, endosteum, and Haversian canals. These cells are on standby, waiting for a stimulus to proliferate and

differentiate into osteoblasts. The main factors responsible for inducing osteoprogenitor cells differentiation into osteoblasts include: bone morphogenetic proteins, transforming growth factor- β , fibroblast growth factor, insulin-derived growth factor, platelet-derived growth factor, and interleukins. **Osteoblasts** are mononuclear cells, around 15 to 30 μm in size, with eccentrically placed spherical nucleus and high cytoplasm composition comprising rough endoplasmic reticulum, golgi apparatus, and mitochondria. Osteoblasts contain active cytoskeletal proteins to maintain their structural integrity as well as to facilitate mobility and attachment to surfaces. Their contact interactions with neighboring osteoblasts and osteocytes at intercellular gap junctions are achieved by the extensions created by their plasma membranes. Osteoblasts are secretory cells, responsible for the formation of the pre-mineralized bone matrix, called **osteoid**, predominantly comprising bony matrix proteins such as type I collagen and trace quantities of collagen type V, and also other non-collagenous proteins such as osteopontin, osteocalcin, osteonectin, osteoprotegerin, bone morphogenetic proteins, and glycoproteins. The mineralization process of the osteoid involves supersaturation of extra cellular fluids at local zones and increased osteoblastic alkaline phosphatase activity, which raises local calcium and phosphate concentrations. Osteoblasts produce osteocalcin protein, which binds calcium and further concentrates local calcium levels [20, 62, 65, 72, 73].

The osteoblast produced can become osteocyte, **lining cell**, or can die by programmed cell death, also known as apoptosis [72, 73]. Mature **osteocytes** are stellate or dendritic shaped cell (as can be seen in Figure 2.2), and are entrapped within the **lacuno-canalicular network** of bone. The osteocytes are entrapped inside ellipsoidal spaces called **lacunae** (found at the border of adjacent lamellae), from which radiate minute canals called **canaliculi**. Each lacuna hosts one osteocyte which is surrounded by a thin layer of extracellular fluid. Osteocytes develop as many as eighty long and slender dendritic cytoplasmic processes, within little channels - canaliculi - which radiate out about 15 μm in all directions (but with a highest density perpendicular to the bone surface) and connects them together, hence forming a stellar network within bone volume. The canaliculi connect the Haversian canal to all the lacunae in the osteon, thereby, bringing the nourishment from the canal to all osteocytes via canalicular network. In bone, gap junctions are present between the tips of the cell processes of connecting osteocytes and osteoblast. These gap junctions are transmembranar channels bidirectionally connecting the cytoplasm of two adjacent cells and regulating the passage of molecules less than 1 kDa. The more mature osteocytes are connected by these cell processes to neighboring osteocytes and the most recently incorporated osteocytes are connected to neighboring osteocytes and to the cell lining the bone surface. Some of the osteocytes processes oriented to the bone surface

appear not to connect with the lining cells, but to pass through this cell layer, thereby establishing a direct contact between the osteocyte syncytium and the extra-osseous space. This complex network is believed to formulate a nervous-like system that coordinates bone metabolism and production [33, 61-63, 72, 74, 75]. As mentioned above, osteocytes derive from osteoblasts. During the process of bone formation some osteoblast, involved in the production of bone matrix, become embedded in that matrix. The fundamental question how osteoblasts are “buried” remains largely unanswered. The matrix around the newly incorporated cell is not yet calcified (osteoid) but gradually calcifies as the formation front moves away because of continuing osteoblastic activity. The osteoid osteocytes still possess many features of the original osteoblast and their major functions are to simultaneously: regulate mineralization because they are not as active as osteoblasts in the generation of mineralized matrix, reduce the number of organelles and cytoplasmic volume and gain the long connective slender cell processes [72, 76, 77].

Osteoclasts are multinucleated (ten or more nuclei), polymorphic, irregularly shaped giant cells (15 to 20 μm or more) that originate from monocytes and macrophages (two types of white blood cells). They are specialized in local removal of bone during growth and during remodeling of osteons and bone surfaces. These cells are found in depressions called Howship's lacunae or resorption bay. For bone resorption to occur, osteoclast has an interface known as the "ruffled brush" border, formed by highly enfolded plasma membrane, which increases the surface area. The "ruffled brush" border is surrounded by a clear zone as well as a well-defined zone of actin filaments responsible for bone resorption. Osteoclast bind to bone surfaces via anchoring proteins such as integrin's, create a seal, and lower the pH by releasing protons (*e.g.* hydrogen ions via carbonic anhydrase) and by expressing acid hydrolases (*e.g.* tartrate-resistant acid phosphate). This environment is suited to increase the solubility of hydroxyapatite crystals as well as destroy organic matrix with lysosomal (cathepsin K) and non-lysosomal (collagenase) enzymes. The osteoclastic bone resorption is inhibited by calcitonin and interleukin-10 and stimulated by osteoblast-derived signals, cytokines from cells, including macrophages and lymphocytes (*e.g.* interleukin-1), and blood-circulating factors (*e.g.* parathyroid hormone). Bisphosphonates indirectly inhibit osteoclastic function by preventing the formation of the “ruffled brush” border [62, 72].

Osteoblasts, osteoclasts, and osteoprogenitor cells highly populate periosteum and endosteum. Less differentiated, less active osteoblasts reside in 'resting zones', entrapped within the active-lining cell layers, and, in relatively quiescent bone, osteoblasts reside more commonly on

endosteal than on periosteal surfaces. The entrapped osteoblasts are activated by disruption of the active-lining cell layer itself. More differentiated, more active osteoblasts line are present at the bone-forming surfaces of growing or remodeling bone, as a bone-forming monolayer. The bone cells are present in different proportions and have different lifespans. Osteocytes are by far the most abundant cellular component of mammalian bones, making up 95% of all bone cells (20,000 to 80,000 cells per mm³ bone tissue). There are approximately ten times more osteocytes than osteoblasts in an individual bone. The number of osteoclast is only a fraction of the number of osteoblast. In terms of lifetime, osteoclasts live only for a few days or weeks (between 1 to 25 days) and osteoblasts - while they are making bone - live between a few months for up to 200 days. The lifespan of lining cells would approximate the time interval between successive remodeling cycles at the same location, which is usually between 1 and 10 years. Osteocytes, permanently confined within the lacuna-canalicular system, can live between 1 to 50 years. In many regions of the skeleton, osteocytes persist until the bone in which they lie is reabsorbed, so that their lifespan is the same as of the bone. However, in regions where turnover is very low, osteocytes can die by programmed death also known by apoptosis, leaving the lacuna empty. Due to the difficulty in attributing a fixed lifespan to osteocytes, it is possible to consider that they die at a fractional rate of approximately 2.5 % per year [72, 74, 76-78]. Although our current knowledge on osteocytes lags behind what we know of the properties and functions of both osteoblast and osteoclast, recent evolution on osteocytes isolation techniques, in situ hybridization procedures and molecular biological techniques will greatly contribute for further knowledge about this least understood bone cell type [74, 75]

2.1.3. Nanostructure

Bone is composed on a weight basis, of approximately 60% inorganic component, 30% organic, and 10% water, whereas on a volume basis, these proportions are around 40%, 35%, and 25%, respectively [28, 79]. The organic phase of the bone composite consists primarily of **type I collagen** (90% by weight), some other minor collagen types (III and VI), and a variety of non-collagenous proteins such as laminin, fibronectin, vitronectin, osteocalcin, osteonectin, osteopontin, and bone sialoprotein. Type I collagen, as well as other connective tissues, is a large fibrous protein with a highly repetitive amino acid sequence [Gly(glycine)-X-Y]_n (often X is proline and Y is hydroxyproline). The type I collagen is a very rigid linear molecule with 300 nm in length. In its structure there are three polypeptid chains (two identical and one unique) rearranged in a triple helix and cross linked by hydrogen bonding between hydroxylproline and other charged residues [12, 21, 28, 32, 80]. The inorganic phase of bone is a ceramic crystalline-type mineral, as an impure form of naturally occurring calcium phosphate, most often referred

to as **hydroxyapatite** - $Ca_{10}(PO_4)_6(OH)_2$. Bone hydroxyapatite is not pure hydroxyapatite, because the tiny apatite crystals contain impurities such as potassium, magnesium, strontium, sodium (in place of the calcium ions), carbonate (4 to 6% of the phosphate groups are replaced by carbonate groups), and chloride or fluoride (in place of the hydroxyl ions). These impurities reduce the crystallinity of the apatite and consequently alter some properties, such as solubility, which is crucial for mineral homeostasis and bone adaptation. There is a long ongoing debate about the nature of the mineral particle shape - needles versus platelets. The majority of the studies describe the mineral particles as plate-like shape with a wide range of geometrical dimensions. The thickness of the platelets ranges from 2 to 7 nm, the length from 15 to 200 nm and the width from 10 to 80 nm [21, 28, 81].

The mechanical properties of bone tissue depend both on the inorganic, the organic and the water constituent. These components have extremely different mechanical properties [32]. The mineral phase in bone guarantees its stiffness behavior. Therefore, when the organic collagen in bone is removed – by heat or leach - mature bone becomes brittle. The increase in the mineral content can also transforms bone in a brittle material with reduce fracture energy [12, 32, 79]. The intermolecular cross-linking packing structure of type I collagen matrix confers robustness to the structure in bone and this material characteristic allows bone to have mechanical properties such as tensile strength and viscoelasticity. The viscoelasticity is a result of the hydrated characteristic of type I collagen. Therefore, when the mineral phase is removed, bone behaves as a malleable material [12, 32, 65, 81]. The bone water content is an essential component since it confers much of bone unique strength and resilience by stress reduction during dynamic loading. Hence, dry bone is stiffer and much more brittle than its hydrated version [72, 82]. Thus, collagen-mineral composite presents exceptional properties by achieving the optimal combination of stiffness and simultaneously fracture toughness behavior.

Collagen-mineral composite system consists of collagen fibrils with tiny mineral particles. The collagen fibril are formed by parallel disposition of collagen molecules in a quarter-staggered array. Within these structures, between molecules ends, there are gaps of approximately 40 nm in size, known as “holes zones”. The arrangement of the **collagen fibril** in bundles form the **collagen fiber**. The un-mineralized collagenous osteoid is the framework upon which hydroxyapatite crystals are deposited. The hydroxyapatite deposition starts in “holes zones”, in the form of flat plates, parallel to each other and to the axis of collagen fibrils. The glycoproteins, proteoglycans and osteocalcin (the most abundant non-collagenous protein of bone) due to

their highly ion-binding ability have an important role in calcification and adhesion of the hydroxyapatite to the collagen [5, 18, 21, 65, 81, 83].

The collagen-mineral system is arranged in parallel arrays within thin sheets called **lamellae**. As stated previously the organization of the lamellae differ between cortical and trabecular bone. As stated by Fratzl *et al.* [32] in cortical bone the lamellae are assembled in a “rotated plywood-like fashion”. In cancellous bone and according to Chen *et al.* [79], these structures are strongly fused together, forming a sheet-like structure. It is important to highlight that mature bone should not be analyzed as an isolated mineral crystallite-reinforced collagen matrix composite. Indeed, it should be evaluated as an interpenetrating composite of several the collagen-mineral structures which nanoscale arrangement and material properties will determine the mechanical behavior of bone at any other hierarchical level. The orientation of collagen and carbonated hydroxyapatite needles, the local degree of mineralization, the structural connection between mineral crystallites and the mineral-collagen interface are fundamental nano-structural variables which greatly influence the mechanical behavior at the micro- and macro-structural level [29, 79].

2.1.4. Mechanical structure

The ordered lamellar structure confers bone tissue an **anisotropic** behavior with direction-dependent material properties. Cortical bone **strength** defined as the **ultimate stress** (or ultimate strength the maximum value of stress that a specimen can bear and that is required to fracture), **yield stress** (the stress above which the tissue no longer behaves elastically) and **Young’s modulus** (or elastic modulus describes the material stiffness and corresponds to the elastic region slope in the stress-strain curve) have higher values along the longitudinal direction, *i.e.* the direction aligned with the diaphyseal axis, than transversely. Although the microstructural mechanism that causes the differences in yield and post-yield behavior is still not completely understood it is of general accepted that when cortical bone is loaded past the yield point it accumulates permanent damage within the bone tissue. Such phenomena may also occur even when cortical bone is unloaded near the yield point. After the yield point is exceeded the reloading modulus presents a lower value. This is associated to cortical bone degradation characteristic. The tissue microstructure deterioration appears as “microdamage” accumulation as a result of sustain or cyclic loading. Both case over time induce fatigue fracture. Reduction in the mechanical properties due to sustained or cyclic loading over time induces fatigue fracture – bone fracture and its recovery by intramedullary nail stabilization technique will be discussed in more detailed in Chapter 2.3 and 2.4, respectively. In such case, cortical bone has a greater

resistance in compression than in tension. Unlike the ultimate stresses, which are higher in compression, **ultimate strains** (defined as the strain that occurs at fracture) are higher in tension for longitudinal loading. Although only moderately, another important characteristic of cortical bone is its **viscoelasticity**. This means that the stress developed within the bone and consequently its stiffness and strength are dependent on the rate at which bone is strained. Such behavior is a result of internal energy losses due to friction in the structure (intrinsic viscoelasticity) or fluid flow (fluid-dependent viscoelasticity) during deformation. A six order of magnitude increase in **strain rate** will only change the Young's modulus by a factor of two and strength by a factor of three. The positive effect of this property is accentuated during impact loading (*e.g.* high energy impact), where strength can increase by a factor of three [18, 28, 84-86].

In trabecular bone, the porosity where the shape (*e.g.* aspect ratio), amount, and orientation distribution of pores, is an important variable. Besides its impact in the micro- and macro-architectural trabeculae arrangement, it greatly influences the structure mechanical properties. Similarly, to cortical bone, in trabecular bone the strength is highest in compression then in tension and lowest in shear. Oppositely to the fairly linear behavior verified at low values of stress in the cortical bone stress-strain curve, in trabecular bone, such performance is absent and there is no clear linear region. The nonlinearity is even present at low stress levels. An interesting property of the trabecular bone is that it can absorb substantial energy on mechanical failure. Although it yields in compression at strains between 0.7 to 1%, it can sustain compressive strains of up to 50% while maintaining its load-bearing capacity. Thus, when compressed beyond yield, the apparent modulus will reduce as a result of microcracks formation instead of individual trabeculae fracture. Upon repeated compressive loads events, trabecular bone tendentially will loss stiffness and accumulate residual strain. Regarding trabecular tissue failure behavior, its ultimate yield strains are higher in compression than in tension and fatigue strength is lower than that of cortical bone. Similarly to cortical bone, also trabecular bone is slightly viscoelastic [18, 21, 28, 54, 64, 65, 87-90].

Independently of being haversian or trabecular, the bone's internal architecture and structure arrangement, and consequently its mechanical properties, are determined to a certain degree by adaptive mechanisms sensitive to their mechanical environment. This occurs through osteoclasts continuous removal of old bone - process known as bone resorption - and its replacement with newly synthesized osteoid and its mineralization by osteoblast - process called ossification or bone formation - to form new bone. Bone remodeling is also present in the

recovery process during injuries (*e.g.* fractures) in preventing future fracture by recovering daily activity-based microdamage in the bone tissue. The Bone mechanotransduction behavior will be discussed in Chapter 2.2. Hence, cortical and trabecular bone mechanical properties will vary with the anatomic site (different bones from the same donor have demonstrated different mechanical properties), spatial positioning within the bones (*e.g.* between the epiphysis and diaphysis), disease (such as osteoarthritis) and age (balance between bone loss and gain is disrupted) which alter bone microstructure, loading direction and loading mode [9, 18, 21, 81, 91-93].

2.1.5. Conclusion

Synthetic composites have been developed intensively over the last decades and have demonstrated an ascending application in a wide range of industries from civil infrastructures, transportations, aerospace and even in the medical field. The high expectation placed on these materials created a need to innovate and to push the thinking beyond the conventional. The structure-function relation experienced in bone could serve as a model for the improvement of synthetic composites. This highly effective natural composite presents an exceptional combination of properties optimized by an evolutionary adaptive process to succeed in the surrounding environment. As highlighted in this chapter, the bone has unique combination of features includes its toughness, strength and stiffness, excellent bonding between different materials (such as between organic and inorganic compounds), the structural design of interface sites that allow good load distribution, its viscoelastic behavior, its energy absorption capacity, good fatigue resistance, and also its self-adaptive and self-regenerative abilities. The perception of bone as living organ and how its hierarchical organization at different levels influences its properties is essential to understand the structure-function relationship. Such knowledge will also help mimicking desirable features in synthetic composites and introduce novelty innovation in their structure, morphology and mechanical properties. Although, the contemporary understanding and consensus on the concepts behind the structure-function relationship have advanced enormously, the bone structure hierarchical complexity, the extremely small scale involved in the lower hierarchical level and the fact that unlike the cases with engineering composites, isolating the different phases of bone tissue often involves process that alter the properties being measured, increases the challenge associated with the study of bone at the different length scales [21, 28]. The successful translation of the principles in innovative composite technology will depend on future progress in research tools and technical approaches, such as new high-resolution imaging methods and compositional measurement techniques (*e.g.* quantitative three-dimensional microcomputed tomography, Raman

microspectroscopy, backscattered electron imaging and infrared spectroscopy), finite element modeling, nanotechnology (e.g. nanoindentation), acoustic microscopy, and histological and morphometric analysis. These techniques will hopefully bring additional insights on this intricate composite and greatly contribute for synthetic composites progress to satisfy the current and future demands of engineering industry [21, 28, 94, 95].

2.1.6. References

1. Pitanguy, I., *II Aesthetic Plastic Surgery of Head and Neck*, in *Aesthetic Plastic Surgery of Head and Body*, I. Pitanguy, Editor 2012, Springer Science & Business Media: Heidelberg, Germany.
2. Adams, M.A., *Functional anatomy of the musculoskeletal system*, in *Gray's Anatomy: The Anatomical Basis of Clinical Practice*, S. Standring, Editor 2015, Elsevier Health Sciences: London, UK. p. 81-122.
3. Bonucci, E., *Basic composition and structure of bone*, in *Mechanical testing of bone and the bone-implant interface*, Y.H. An and R.A. Draughn, Editors. 2000, CRC Press: Florida, USA. p. 3-22.
4. Whiting, W.C. and R.F. Zernicke, *Biomechanics of musculoskeletal injury*. 2nd edition ed2008, Stanningley, United Kingdom: Human Kinetics.
5. Péoc'h, M., *Normal histological architecture of tissue*, in *Biomechanics and Biomaterials in Orthopedics*, D.G. Poitout, Editor 2004, Springer-Verlag: London, UK. p. 189-191.
6. Ledoux, W.R. and M.E. Hahn, *Lower limb structure, function, and locomotion biomechanics*, in *Orthopaedic Biomechanics*, B.A. Winkelstein, Editor 2013, CRC Press: Florida, USA. p. 265-300.
7. Drake, R.L., W. Vogl, and A.W.M. Mitchell, *Gray's Basic Anatomy* 2012: Elsevier Health Sciences. 265-340.
8. Keller, T.S. and M.A. Liebschner, *Tensile and Compression Testing of Bone*, in *Mechanical Testing of Bone and the Bone-Implant Interface*, Y.H. An and R.A. Draughn, Editors. 2000, CRC Press: London, UK. p. 175-206.
9. Rosa, N., et al., *From mechanical stimulus to bone formation: A review*. Medical Engineering and Physics, 2015. **37**: p. 719-728.
10. Bouchbinder, E. and E.A. Brener, *Viscoelastic fracture of biological composites*. Journal of the Mechanics and Physics of Solids, 2011. **59**(11): p. 2279-2293.
11. Libonati, F. and L. Vergani, *Understanding the structure–property relationship in cortical bone to design a biomimetic composite*. Composite Structures, 2016. **139**: p. 188-198.
12. White, T.D., M.T. Black, and P.A. Folkens, *Human osteology* 2012, Oxford, UK: Academic press.
13. Krishnakanth, P., *Mechanical considerations in fracture fixation*, in *Faculty of Built Environment and Engineering* 2012, Queensland University of Technology: Brisbane, Australia.
14. Long, B.W., E.D. Frank, and R.A. Ehrlich, *Radiography Essentials for Limited Practice*. 4th edition ed2014, Missouri, United States of America: Elsevier Health Sciences.
15. Bertocci, G., *Long bone fractures biomechanics*, in *Child Abuse and Neglect: Diagnosis, Treatment, and Evidence*, C. Jenny, Editor 2010, Elsevier Health Sciences: Missouri, USA. p. 317-325.
16. Dutta, S.K. and D. Datta, *Long bone shape its mechanical significance*, in *Applied Orthopaedic Biomechanics*, S.K. Dutta and D. Datta, Editors. 2008, BI Publications Pvt Ltd: New Delhi, India. p. 41-49.

17. Trafton, P.G., *Tibial shaft fractures*, in *Skeletal Trauma: Basic Science, Management, and Reconstruction*, B.D. Browner, et al., Editors. 2003, Elsevier Science: Pennsylvania, USA. p. 2187-2293.
18. Shore, S.W., et al., *Bone biomechanics*, in *Orthopaedic Biomechanics*, B.A. Winkelstein, Editor 2013, CRC Press: Florida, USA. p. 3-47.
19. Hrdlicka, A., *Study of the normal tibia*. American Anthropologist, 1898. **11**(10): p. 307-312.
20. Mckibbin, B., *The biology of fracture healing in long bones*. Journal of Bone and Joint Surgery [Br], 1978. **60-B**(2): p. 150162.
21. Morgan, E.F., G.L. Barnes, and T.A. Einhorn, *The bone organ system: Form and function*, in *Osteoporosis*, D. Feldman, et al., Editors. 2008, Academic Press: London, UK. p. 3-25.
22. Porteous, M. and S. Bäuerle, *Techniques and Principles for the Operating Room* 2010, Stuttgart, Germany: Georg Thieme Verlag.
23. Taddei, F., et al., *Subject-specific finite element models of long bones: An in vitro evaluation of the overall accuracy*. Journal of Biomechanics, 2006. **39**(13): p. 2457-2467.
24. Cartmill, M., W.L. Hylander, and J. Shafland, *Human Structure* 1987, London, England: Harvard University Press.
25. O'Connor, A. and K. McCreesh, *Function and dysfunction of joint*, in *Principles of Neuromusculoskeletal Treatment and Management: A Handbook for Therapists*, N.J. Petty, Editor 2011, Elsevier Health Sciences: London, UK. p. 3-56.
26. Herman, I.P., *Physics of the human body*. 2nd ed. Biological and Medical Physics, Biomedical Engineering, ed. I.P. Herman 2016, New York, USA: Springer.
27. Rho, J.-Y., L. Kuhn-Spearing, and P. Zioupos, *Mechanical properties and the hierarchical structure of bone*. Medical Engineering and Physics, 1998. **20**(2): p. 92-102.
28. Keaveny, T.M., E.F. Morgan, and O.C. Yeh, *Bone mechanics*, in *Standard Handbook of Biomedical Engineering & Design*, M. Kutz, Editor 2003, McGraw-Hill: New York, USA. p. 200-222.
29. Ascenzi, M.-G., et al., *Individual-specific multi-scale finite element simulation of cortical bone of human proximal femur*. Journal of Computational Physics, 2013. **244**: p. 298-311.
30. Morgan, E.F. and T.M. Keaveny, *Dependence of yield strain of human trabecular bone on anatomic site*. Journal of Biomechanics, 2001. **34**(5): p. 569-577.
31. McCalden, R.W., J.A. McGeough, and M.B. Barker, *Age-related changes in the tensile properties of cortical bone. The relative importance of changes in porosity, mineralization, and microstructure*. The Journal of Bone and Joint Surgery, 1993. **75**(8): p. 1193-1205.
32. Fratzl, P., et al., *Structure and mechanical quality of the collagen–mineral nanocomposite in bone*. Journal of Materials Chemistry, 2004. **14**(14): p. 2115-2123.
33. Cowin, S.C., *Bone poroelasticity*. Journal of Biomechanics, 1999. **32**(3): p. 217-238.
34. Weinbaum, S., S.C. Cowin, and Y. Zeng, *A model for the excitation of osteocytes by mechanical loading-induced bone fluid shear stresses*. Journal of Biomechanics, 1994. **27**(3): p. 339-360.
35. Minns, R.J., G.R. Bremble, and J. Campbell, *The geometrical properties of the human tibia*. Journal of Biomechanics, 1975. **8**(3): p. 253-255.
36. Taylor, W.R., et al., *Tibio-femoral joint contact forces in sheep*. Journal of Biomechanics, 2006. **39**(5): p. 791-798.
37. Lu, T.-W., et al., *Validation of a lower limb model with in vivo femoral forces telemetered from two subjects*. Journal of Biomechanics, 1997. **31**(1): p. 63-69.
38. Lu, T.-W., et al., *Comparison of telemetered femoral forces with model calculations*. Journal of Biomechanics, 1998. **31**(1): p. 47.
39. Hurwitz, D.E., et al., *Dynamic knee loads during gait predict proximal tibial bone distribution*. Journal of Biomechanics, 1998. **31**(5): p. 423-430.

40. Taylor, S.J.G., et al., *The forces in the distal femur and the knee during walking and other activities measured by telemetry*. The Journal of Arthroplasty, 1998. **13**(4): p. 428-437.
41. Taylor, S.J.G. and P.S. Walker, *Forces and moments telemetered from two distal femoral replacements during various activities*. Journal of Biomechanics, 2001. **34**(7): p. 839-848.
42. Wehner, T., L. Claes, and U. Simon, *Internal loads in the human tibia during gait*. Clinical Biomechanics, 2009. **24**(3): p. 299-302.
43. Taylor, W.R., et al., *Tibio-femoral loading during human gait and stair climbing*. Journal of Orthopaedic Research, 2004. **22**(3): p. 625-632.
44. Nagura, T., et al., *Tibiofemoral joint contact force in deep knee flexion and its consideration in knee osteoarthritis and joint replacement*. Journal of Applied Biomechanics, 2006. **22**: p. 305-313.
45. D'Lima, D.D., et al., *An implantable telemetry device to measure intra-articular tibial forces*. Journal of Biomechanics, 2005. **38**(2): p. 299-304.
46. Zhao, D., et al., *In vivo medial and lateral tibial loads during dynamic and high flexion activities*. Journal of Orthopaedic Research, 2007. **25**(5): p. 593-602.
47. Kim, H.J., et al., *Evaluation of predicted knee-joint muscle forces during gait using an instrumented knee implant*. Journal of Orthopaedic Research, 2009. **27**(10): p. 1326-1331.
48. D'Angeli, V., et al., *Load along the tibial shaft during activities of daily living*. Journal of Biomechanics, 2014. **47**(5): p. 1198-1205.
49. Ellis, M.I., B.B. Seedhom, and V. Wright, *Forces in the knee joint whilst rising from a seated position*. Journal of Biomedical Engineering, 1984. **6**(2): p. 113-120.
50. Wilk, K.E., et al., *A comparison of tibiofemoral joint forces and electromyographic activity during open and closed kinetic chain exercises*. American Journal of Sports Medicine, 1996. **24**: p. 518-527.
51. Dahlkvist, N.J., P. Mayo, and B.B. Seedhom, *Forces during squatting and rising from a deep squat*. Engineering in Medicine, 1982. **11**(2): p. 69-76.
52. Papini, M., et al., *The biomechanics of human femurs in axial and torsional loading: Comparison of finite element analysis, human cadaveric femurs, and synthetic femurs*. Journal of Biomechanical Engineering, 2007. **129**(1): p. 12-19.
53. Hench, L.L. and J. Wilson, *Introduction*, in *An Introduction to Bioceramics*, L.L. Hench and J. Wilson, Editors. 1993, World Scientific: London, UK. p. 1-24.
54. Currey, J., *Cortical bone*, in *Handbook of Biomaterial Properties*, J. Black and G. Hastings, Editors. 1998, Springer Science & Business Media: London, UK. p. 3-13.
55. Morawska-Chochół, A., et al., *Influence of the intramedullary nail preparation method on nail's mechanical properties and degradation rate*. Materials Science and Engineering: C, 2015. **51**: p. 99-106.
56. Ramakrishna, S., et al., *Biomedical applications of polymer-composite materials: A review*. Composites Science and Technology, 2001. **61**(9): p. 1189-1224.
57. Byrne, D.P., D. Lacroix, and P.J. Prendergast, *Simulation of fracture healing in the tibia: Mechanoregulation of cell activity using a lattice modeling approach*. Journal of Orthopaedic Research, 2011. **29**(10): p. 1496-1503.
58. Wang, X., et al., *Fundamental biomechanics in bone tissue engineering*, ed. K.A. Athanasiou. 2010, California, United States of America: Morgan & Claypool.
59. Neto, R.B., J.D.M.B.A. Rossi, and T.P. Leivas, *Experimental determination of bone cortex holding power of orthopedic screw*. Revista do Hospital das Clínicas da Faculdade de Medicina da Universidade de São Paulo, 1999. **54**(6): p. 181-186.
60. Hashemi, J., et al., *The geometry of the tibial plateau and its influence on the biomechanics of the tibiofemoral joint*. The Journal of Bone and Joint Surgery, 2008. **90**(12): p. 2724-2734.

61. Jayakumar, P. and L. Silvio, *Osteoblasts in bone tissue engineering*. Proceedings of the Institution of Mechanical Engineers, Part H: Journal of Engineering in Medicine, 2010. **224**(12): p. 1415-1440.
62. Lemaire, T., et al., *A multiscale theoretical investigation of electric measurements in living bone*. Bulletin of Mathematical Biology, 2011. **73**(11): p. 2649-2677.
63. Kulkarni, N.V., *Clinical anatomy for students: Problem solving approach* 2007: Jaypee Brothers Publishers.
64. Keaveny, T.M., *Cancellous bone*, in *Handbook of Biomaterial Properties*, J. Black and G. Hastings, Editors. 1998, Springer Science & Business Media: London, UK. p. 15-23.
65. Dutta, S.K. and D. Datta, *Composition of musculoskeletal structures*, in *Applied Orthopaedic Biomechanics*, S.K. Dutta and D. Datta, Editors. 2008, BI Publications Pvt Ltd: New Delhi, India. p. 29-37.
66. Rubin, C.T., K.J. McLeod, and S.D. Bain, *Functional strains and cortical bone adaptation: epigenetic assurance of skeletal integrity*. Journal of Biomechanics, 1990. **23**: p. 43-54.
67. Marieb, E.N. and K. Hoehn, *Human Anatomy & Physiology*, ed. S. Beauparlant 2004: Pearson Benjamin Cummings.
68. pixshark.com, *Labeled Compact Bone Slide*.
69. Mackenzie, K., *Osteocytes in bone*, in *by-nc-nd 4.0*, B0008430, Editor 2011, Welcome Images: University of Aberdeen.
70. Larsen, H.A., *Osteocalcin - et hormon fra knoglerne gemmer måske på helbredets livsnøgle*, 2011, Holistica-Medica A/S: Hornsyld, Denmark.
71. Arnett, T., *Scanning electron micrograph showing osteoclast resorbing bone*, in *Eastface Technology* 2015, Bone Research Society.
72. Ahn, A.C. and A.J. Grodzinsky, *Relevance of collagen piezoelectricity to "Wolff's Law": A critical review*. Medical Engineering and Physics, 2009. **31**(7): p. 733-741.
73. Bonewald, L.F., *The amazing osteocyte*. Journal of Bone and Mineral Research, 2011. **26**(2): p. 229-238.
74. Franz-Odenaal, T.A., B.K. Hall, and P.E. Witten, *Buried alive: how osteoblasts become osteocytes*. Developmental Dynamics, 2006. **235**(1): p. 176-190.
75. Compston, J.E., *Principles of bone biology*. Clinical Endocrinology, 1997. **46**(6): p. 781-781.
76. Cartmell, S., A. Rupani, and R. Balint, *Osteoblasts and their applications in bone tissue engineering*. Cell Health and Cytoskeleton, 2012. **49**: p. 49-61.
77. Aarden, E.M., P.J. Nijweide, and E.H. Burger, *Function of osteocytes in bone*. Journal of Cellular Biochemistry, 1994. **55**(3): p. 287-299.
78. Manolagas, S.C. and A.M. Parfitt, *What old means to bone*. Trends in Endocrinology and Metabolism, 2010. **21**(6): p. 369-374.
79. Chen, P.-Y., et al., *Minerals form a continuum phase in mature cancellous bone*. Calcified Tissue International, 2011. **88**(5): p. 351-361.
80. Zhang, L. and T.J. Webster, *Nanotechnology and nanomaterials: promises for improved tissue regeneration*. Nano Today, 2009. **4**(1): p. 66-80.
81. Fonseca, J.E., *Bone: a story of breakthroughs, a promising future*. Medicographia, 2012. **34**(2): p. 142-148.
82. Jilka, R.L., B. Noble, and R.S. Weinstein, *Osteocyte apoptosis*. Bone, 2013. **54**(2): p. 264-271.
83. Metzler, D.E. and C.M. Metzler, *Biochemistry: The chemical reactions of living cells*. 2nd ed, ed. D.E. Metzler. Vol. 1. 2001, London, UK: Academic Press.
84. An, Y.H., W.R. Barfield, and R.A. Draughn, *Basic concepts of mechanical property measurement and bone biomechanics*, in *Mechanical Testing of Bone and the Bone-Implant Interface*, Y.H. An and R.A. Draughn, Editors. 2000, CRC Press: Florida, USA. p. 23-40.

-
85. Arnold, P.A., *Validation of mechanical response tissue analysis by three-point mechanical bending of artificial human ulnas*, in *Department of Biological Sciences* 2013, Ohio University: Ohio, USA.
 86. Carnelli, D., *Orientation and length-scale dependent mechanical properties in lamellar bone at the micro and nanostructural hierarchical levels*, 2010, Politecnico di Milano: Milan, Italy.
 87. Fan, Z., et al., *Anisotropic properties of human tibial cortical bone as measured by nanoindentation*. *Journal of Orthopaedic Research*, 2002. **20**(4): p. 806-810.
 88. Morgan, E.F., G.L. Barnes, and T.A. Einhorn, *The bone organ system: Form and function*, in *Osteoporosis*, R. Marcus, et al., Editors. 2008, Elsevier: London, UK. p. 3-25.
 89. Parkinson, H. and N.L. Fazzalari, *Characterisation of trabecular bone structure*, in *Skeletal Aging and Osteoporosis*, M.J. Silva, Editor 2013, Springer: London, UK. p. 31-51.
 90. Rahmoun, J., et al., *Micromechanical modeling of the anisotropy of elastic biological composites*. *Multiscale Modeling and Simulation*, 2009. **8**(1): p. 326-336.
 91. Kini, U. and B.N. Nandeesh, *Physiology of bone formation, remodeling, and metabolism in Radionuclide and Hybrid Bone Imaging*, I. Fogelman, G. Gnanasegaran, and H. van der Wall, Editors. 2012, Springer-Verlag: Heidelberg, Germany. p. 29-57.
 92. Clarke, B., *Normal bone anatomy and physiology*. *Clinical journal of the American Society of Nephrology*, 2008. **3**(3): p. 131-139.
 93. Bueno, E.M. and J. Glowacki, *Biologic Foundations for Skeletal Tissue Engineering*. *Synthesis lectures on Tissue Engineering*, ed. K.A. Athanasiou and J.K. Leach 2011, USA: Morgan and Claypool.
 94. Gosman, J.H., et al., *Development of cortical bone geometry in the human femoral and tibial diaphysis*. *The Anatomical Record*, 2013. **296**(5): p. 774-787.
 95. Kourtis, L.C., et al., *A new software tool (VA-BATTS) to calculate bending, axial, torsional and transverse shear stresses within bone cross sections having inhomogeneous material properties*. *Computer Methods in Biomechanics and Biomedical Engineering*, 2008. **11**(5): p. 463-476.

2.2. From mechanical stimulus to bone formation²

Understanding the influence of mechanical stimuli on the structure of bone has long been a topic of scientific interest. To the best of our knowledge, Galilei [1], noticed a relationship between body weight and bone size and shape. However, mechanical forces were not identified as responsible for shaping the architecture of the skeleton until the 19th century, in studies developed by Meyer [2], Culmann [3] and Roux [4].

The German anatomist von Meyer identified arched trabecular patterns in a sagittally sectioned human first metatarsal and calcaneus, and Culmann, a pioneer of graphical methods in engineering, suggested that the patterns appeared to be aligned along principal stress directions produced by functional loading [5]. In 1881, Roux proposed that the apposition and absorption of bone is a biological stress-controlled process [6, 7].

However, Julius Wolff [8], - influenced by von Meyer-Culmann interactions in 1867 - became associated to the concept of bone adaptation. He claimed that the shape of bone is related to mechanical stress by *Wolff's law of bone transformation*. Although this law is an overly simplified mathematical approach, the concept has been accepted by the scientific community. Recent interpretations of "Wolff's Law" have proposed that bone mass and architecture are to some extent governed by adaptive mechanisms that are sensitive to their mechanical environment [9-11].

Over the years, remarkable work has been done to elucidate bone mechanotransduction and its response to mechanical stimulation. The first contact with this subject can be overwhelming due to the complexity and multidisciplinary mechanisms involved. This review aims to establish the state of the art of this area while simultaneously clarifying some basic yet important questions on which light has been shed during recent years, such as

- What is the origin of the mechanical stimulus? How is it triggered?
- How does bones mechanotransduction work?
- What are the normal physiological bone stimuli?
- What test systems are commonly used to study bone's mechanical stimulation?

² Adapted from: Rosa, N., Simoes, R., Magalhães F. D. and Marques, A. T., *From mechanical stimulus to bone formation: A review*. Medical Engineering & Physics, 2015. **37**(8): 719-28.

2.2.1. Mechanical stimulus

Bone mass is maintained by and adapted to mechanical strain, primarily as the result of muscular contraction [12, 13]. Some key aspects are currently accepted by the scientific community at large and should be mentioned.

First, long bones deformation is obtained by an orchestrated muscle activity as demonstrated by Duda *et al.* [14]. Using a finite element strain distributions model, these authors concluded that simplified load regimes produced differences in strain as high as 26% compared with regiments that included all thigh muscles. Although this study focused only on the proximal femur situation, this concept can be generalized to other bones in the human body.

Second, the forces experienced by bone arise from muscle action rather than from mere gravitational forces [15]. Hence, muscle mass/strength correlates with bone strength [12]. This concept was demonstrated in a study by Sievänen *et al.* [16]. The patella bone mineral apparent density and average strain magnitude were measured in a chained event experiment that included one-year unilateral strength training interventions, an accidental knee ligament rupture and a two-year rehabilitation period. The patella was selected as the target bone because it is a non-weight-bearing bone that receives mechanical stimuli from only the quadriceps activity. Sievänen *et al.* showed that a decline in muscle mass precedes a decline in bone strength under conditions of disuse and that the recovery of muscle mass increases before bone mass. In another study, Schönau *et al.* [17] compared the muscle development with age as well as muscle development and bone strength.

Disuse can be asserted to cause muscle wasting and bone loss, whereas physical activity increases muscle strength and bone mass. However, according to Rittweger *et al.* [15], this relationship only holds to a certain extent. The authors claim that muscular exercise can only enhance bone strength up to 1-2% because tendon stiffness may limit the musculoskeletal peak forces.

In several studies [9, 12, 16, 18], a time lag of up to 5 days was registered between a single period of mechanical loading *in vivo* and the onset of collagen and mineral apposition increases on the bone surface. This phenomenon is justified by the delay between the initial formation of new bone and the establishment of fully mineralized and mature bone.

The third key aspect was stated in one of the earliest far-reaching interpretations of bone loading made by Pauwels [19], who suggested that bending moments are transmitted along

limbs by a combination of tensile forces in the muscle and compressive forces on bone. Hence, gravitational forces tend to lower and collapse our body segments in any upright posture. However, bending moments are accentuated rather than reduced due to the physiological curvature of long bones. In response to these external loads, muscles not only provide the necessary moment equilibrium in joints, but they counteract the passive bending moments along bones in an energetically efficient manner, as stated by Munih *et al.* [20]. While reducing the bending stress, muscles increase the axial compressive load irrespective of the posture to ensure minimal bone stress and minimal bone weight [21]. From all registered loading modes in long bone, bending is the most significant for bone adaptation [22-24].

Fourth and last, in addition to mechanical stimuli, bone remodelling may also be regulated by hormones, such as estrogen and parathyroid hormone [25, 26], and induced by nervous system [18, 27] and inflammatory reactions [28].

2.2.2. Mechanotransduction system

Over the last several years, osteocytes have become generally accepted as the mechanosensory cells within the bone. Osteocytes coordinate the remodelling process by converting external mechanical forces into biochemical responses – a process known as mechanotransduction. However, the mechanism by which these cells sense the mechanical loads and facilitate adaptive alterations in bone mass and architecture is not yet completely understood [10, 18, 29, 30].

i) Stimuli perceived by osteocytes

Osteocytes are generally assumed to react to bone deformation or to one of the consequences of bone deformation, such as shear stress due to load-induced fluid flow, electric fields caused by stress-generated streaming potentials, and hydrostatic pressure [22, 31, 32].

Cell deformation

The immediate consequence of mechanical loading is strain, which is a small deformation throughout the calcified matrix. These stimuli will stretch the osteocytes to the same extent as the surrounding bone tissue. When stretched in one direction, bone tends to slightly contract in the perpendicular direction. Hence, direct biaxial osteocyte strain is common [9, 33]. Several authors [33-35] suggest that the strains experienced by an osteocyte are much higher than those measured on the bone surface, with registered amplification factors that are up to 9 times larger than the applied global strain. This difference may be due to a magnification effect caused by the cell's complex surrounding pericellular and extracellular matrix. In a recent study, Wang *et*

al. [36] proposed that the strain amplification factor positively correlates with the loading frequency and loading strain.

Shear induced by fluid-flow

Loading the bone first pressurizes the interstitial fluid around the osteocytes before flow is initiated [32]. A study developed by Gardinier *et al.* [37] predicted that *in vivo* osteocytes could experience hydrostatic pressures of up to 5 MPa. The interstitial fluid within the lacuno-canalicular (LC) is then driven to flow through the thin layer of non-mineralized pericellular matrix surrounding the osteocytes and towards the Haversian or Volkmann's channels [22, 32]. In this sense, bone can be compared to a water-soaked sponge. A compressive force on the sponge will squeeze water out of it. Similarly, mechanical loading will result in a flow of interstitial fluid through the LC network of bone (see Figure 2.3) [38]. The flow of interstitial fluid through the LC network places shear stress on the cell membranes. This stress is thought to initiate a biochemical response from the cells [39].

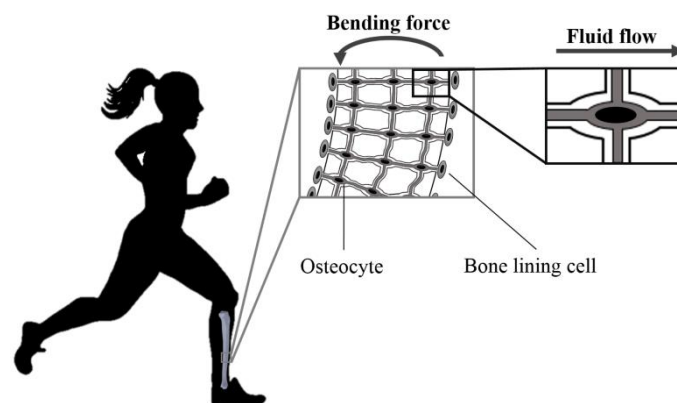


Figure 2.3 - Schematic representation of mechanical loading that causes interstitial fluid flow through bone's lacuno-canalicular network (adapted from Duncan *et al.* [9]). The tension/compression stresses associated with bending cause a pressure gradient that promotes fluid flow along the osteocyte

Piekarski [40] was the first researcher to propose that mechanical loading induces fluid-flow in bone. He stated that this flow enabled nutrition and waste removal.

The effect of the three-dimensional LC network complex geometry of bone on the fluid flow shear stress stimuli mechanism and its role in osteocyte mechanobiology are not yet fully understood. However, a recent study developed by Verbruggen *et al.* [41] showed that individual osteocytes may be subjected to a maximum shear stress stimulus of approximately 11 Pa and an average fluid velocity of 60.5 $\mu\text{m/s}$ in response to vigorous activity. Mechanosensing bone cells also seem to be able to sense low fluid-flow stress values, as demonstrated by Morris *et al.* [42], Delaine-Smith *et al.* [43], Young *et al.* [44].

Several studies have also evaluated the responsiveness of bone cells to different flow profiles. Of these studies, we would like to highlight the important work developed by Jacobs' group [45-47], in which they studied oscillating, pulsatile and steady fluid flow. These studies showed that pre-osteoblast cell lines recognized both steady unidirectional and oscillating fluid flow as an osteogenic stimulus, but the latter was considered to be more realistic in physiologic terms than steady or pulsatile flow. This condition occurs because induced flow through the LC network is reversed when the bone is unloaded [46, 47]. Case *et al.* [46] also claimed that the flow duration and inclusion of rest periods may influence flow effects.

Streaming potentials

In the mid-1960s, researchers observed that mechanical strains generated electrical potential differences along the lateral and longitudinal axes of compact bone. These differences may exert direct effects on bone cells because the *in vivo* application of an electromagnetic field to bone is known to inhibit bone resorption and stimulate bone formation. Of all of the mechanisms proposed to explain the strain-generated potentials, two were selected for analysis: streaming potentials and piezoelectricity [9, 10, 48].

Streaming potentials are electric fields caused by stress-generated fluid-flow. Initially, streaming potentials were thought to be generated by electrokinetic effects that are associated with the collagen-apatite porosity system of connected micropores. Currently, pores are considered to be the canaliculi in mineralized bone. The bone surface is negatively charged; thus, the interstitial fluid cations that are being forced through channels are attracted to the surface, producing a surplus of ions in the fluid. The voltage that results from this imbalance of ions is positive in the direction of flow. The streaming potential produced by interstitial fluid-flow in bone is believed to be able to produce a number of responses in osteocytes, including the activation of voltage-operated channels in the cellular membrane. Thus, this streaming potential serves to trigger the mechanotransduction process [32, 49-51].

Piezoelectricity

Yasuda [52] was the first researcher to observe piezoelectric behaviour in bone tissue. Subsequently, Fukada *et al.* [53] systematically investigated and measured the direct and converse piezoelectric effect in dry specimens cut from human and ox femurs. The centrosymmetric crystal structure of hydroxyapatite excludes the possibility of observing these piezoelectric properties, as demonstrated in de-collagenated bone [54]. Minary-Jolandan *et al.*

[55] found that isolated collagen fibrils have unipolar axial polarizations and behave mainly as shear piezoelectric materials with a shear piezoelectric constant of $d_{15} \approx 1 \text{ pm V}^{-1}$ (or pC N^{-1}).

In a recent study, Ahn *et al.* [10] explored the possible influence of bone piezoelectricity on streaming potentials. The piezoelectricity of collagen may influence the magnitude of the zeta potential and thus the streaming potential. Therefore, it may indirectly modify the stiffness and fluid dynamics of bone. The load may also create a local fixed charge density that may modify the steady state fluid content of the bone and consequently the amount available for transfer from the collagen-hydroxyapatite microporosity to the LC system. This influence in turn affects the fluid-flow around the osteocytes. In a complementary multiscale approach study developed by Lemaire *et al.* [56] utilized a coupled poro-elastic model of cortical tissue to determine that *in vivo* electric measurements at the organ scale are due to streaming currents.

Although the precise stimuli bone cells experience *in vivo* are not yet fully understood, a number of theoretical and experimental studies over the past decade have uncovered strong evidence favouring direct cell strain and interstitial fluid-flow as the most likely stimuli for mechanosensation, instead of streaming potentials or hydrostatic pressure. These studies further support that shear stress induced by fluid-flow is the predominant stimuli recognized by osteocytes, as opposed to direct mechanical strain by substrate stretching [32, 33, 37, 39, 57, 58].

ii) Mechanism of stimuli perception

Osteocytes may sense loads via several mechanisms. Both cell body and dendritic processes have been proven to perceive mechanical forces. Several *in vitro* studies [33, 59-61] have attempted to decipher the part of the cell – body or dendritic process – that is more sensitive to mechanical forces. Although it remains a controversial subject, the prevalent, widely accepted, hypothesis proposes that the osteocyte cell process is responsible for mechanosensation [62].

Several excellent papers on the mechanisms for the initial detection and conversion of a mechanical force into a biochemical signal, such as [21, 32, 63] and references within these papers, have been written, and the reader is referred to these studies for many of the details. Integrins, cation non-selective channels and the bone cell primary cilium are proposed to be involved in the osteocyte perception process of the mechanical signal.

One critical transduction pathway consists of strengthening ligand-integrin-cytoskeleton linkages in response to a force. Integrins are a superfamily of cell adhesion receptors that bind to extracellular matrix ligands, cell-surface ligands, and soluble ligands. The transfer of forces

across cell adhesions allows focused stresses applied on the surface membrane to affect distant sites, such as the mitochondria and nucleus [22, 56, 64, 65].

Ion channels, which are located in bone cell membranes, form strain-sensitive systems that respond to several stimuli, such as ligand binding, voltage changes, stretching and fluid shearing, via cellular ion fluxes. Several of these channels have been detected in osteocyte cultures: a Gd^{3+} sensitive non-selective cation channel; the volume sensitive epithelial-like Na^+ channel ENaC; secondary driven Ca^{2+} channels, such as the voltage-dependent L-type channels or Na^+/Ca^{2+} exchange channels; and Cl^- and K^+ channels. Integrins and stretch-activated channels also seem to be linked. Hence, cell stretching may lead to an increase in lateral membrane tension, which activates mechanically gated ion channels, *i.e.*, stretch-activated channels. Stretch-activated cation channels are also thought to be responsible for mechanotransduction in osteoblasts [64, 66-68].

Primary cilia are structures that project from the cell surface and deflect under fluid-flow. Currently, research points to the following flow-induced cilia response: increase in *cox-2* gene expression, prostaglandin E2 release (which is an important chemical mediator in the mechanotransduction process, as outlined in the following section) and an increase in the OPG/RANKL (nuclear factor-kappaB ligand/osteoprotegerin) ratio. The cilia-based osteocyte response is independent of intracellular calcium. Many interesting aspects of the role of primary cilia in bone mechanotransduction remain to be studied [30, 69, 70].

Although osteocyte sensing mechanisms have been individually presented, researchers strongly believe that these mechanisms are highly associated; therefore, there is no single transduction pathway [9].

iii) Osteocytes biochemical stimuli-induced responses

The *in vivo* and *in vitro* osteocyte responses to load include the production of several biochemically relevant messengers [57, 71, 72] such as Ca^{2+} , nitric oxide and prostaglandin E2.

One of earliest osteocyte responses to mechanical stimulation is calcium (Ca^{2+}) exchange between the extracellular and intracellular medium. This response propagates to the neighbouring cells, suggesting that the cellular network communicates and synchronizes via this mechanism. This response initiates a number of essential downstream signalling pathways, *e.g.* ATP, nitric oxide and prostaglandin E2 (PGE2) release [9, 60, 73, 74].

Nitric oxide (NO) and PGE2 are considered potent anabolic regulators of bone growth. Studies have shown [75, 76] that the inhibition of only one of the two rapidly released small molecules at the time of mechanical stimulation suppresses the osteogenic response to mechanical stimulation.

NO is responsible for stimulating bone formation by inhibiting osteoclast formation and inducing osteoblasts differentiation. This anabolic regulator is also responsible for maintaining the viability of osteocytes and enhancing PGE2 [77]. Klein-Nulend *et al.* [78] examined the effect of pulsating fluid flow (0.5 ± 0.02 Pa, 5 Hz and 0.4 Pa/sec) stimulation on chicken calvarial osteocytes. NO showed a maximum effect after 5 minutes, decreasing afterwards. PGE2 effect was significant after 10 minutes, which was maintained throughout 60 minutes.

PGE2 is an important signalling molecule because it not only stimulates osteogenic function in existing osteoblasts but also increases the production of osteoblasts by recruiting and promoting the differentiation of precursor cells. Another molecule that has similar effects to PGE2 on the signalling of the osteogenic process is the insulin-like growth factor I [9, 32, 78-82].

During bone remodelling, a cutting cone of osteoclasts, followed by a reversal or transition zone of osteoblast precursors and a closing cone of osteoblasts, constitute the basic multicellular units (BMU), which move in tandem. In modelling, bone resorption driven by osteoclasts and osteoblast-mediated bone formation actuate independently on different surfaces of the skeleton as bone is reshaping to adapt to different loading conditions [29, 71, 83-85].

2.2.3. Bone strain *in vivo*

The quantification of human normal bone strain is an important step in understanding the response of bone to mechanical stimuli [86]. One of the first contributions to this subject was made by Hert *et al.* [87], Hert *et al.* [88]. By applying loads to rabbit tibiae diaphysis using transcutaneous pins and Bowden cables, they showed that dynamic, but not static strains, increase bone formation. Today, the response of bone cells to mechanical stimuli is well accepted to be modulated by the parameters of the applied strain, namely, the magnitude, rate and duration of the applied load [9, 55, 89].

Although Hert *et al.* [88] could determine the magnitude of the applied load in their experiment, they could not determine either the physiological strains in that region or the strains that the loading engendered [86]. The *in vivo* measurement of strain in bone tissue surface was not possible until the development of strain gauges, the gold-standard for measuring bone strain

[90-92]. The use of strain gauges on the bone surface was reportedly introduced as early as the mid-twentieth century [86, 93].

Following Roux's footprints, Frost [94] developed an important concept: the "mechanostat" for bone adaptation to strain. This theory proposes a mechanical usage window and introduces the concept of minimal effective strain (MES). Frost compiled his various works that concern mechanical stimuli for bone regeneration in a 2003 paper [95], which describes the "mechanostat" as follows (see Figure 2.4): he claimed a threshold for disuse-mode remodelling (MESr), 50-100 $\mu\epsilon$, below which bone is removed and weakened. He defined the modelling region (MESm) between 1000 and 1500 $\mu\epsilon$, where mechanically controlled modelling begins and could increase if strains exceed this upper limit. Frost believed that strain stimuli between MESr and MESm could define the region of naturally acceptable whole-bone strength relative to the typical peak voluntary mechanical load on a loadbearing bone during typical physical activities and the span of a normal "bone-strength/bone-load" ratio. According to this theory, the microdamage threshold (MESp) is approximately 3000 $\mu\epsilon$ and loads that can fracture a healthy young adult bone cause strains centred near 25000 $\mu\epsilon$ (Fx).

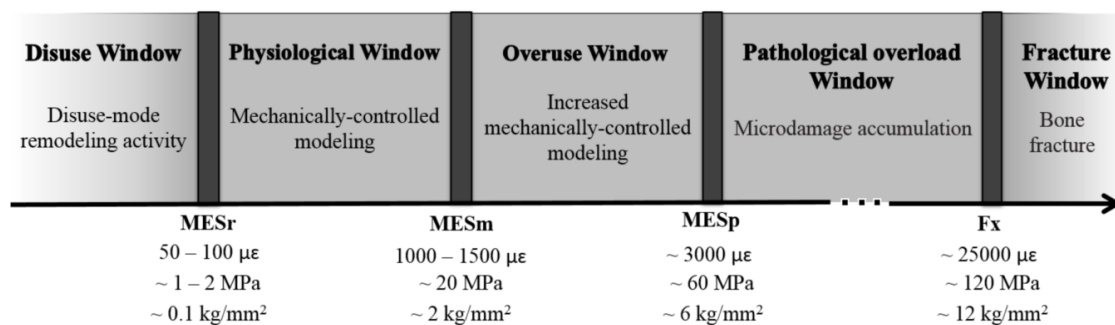


Figure 2.4 - Mechanical usage window defined by Frost's "mechanostat" theory of bone adaptation to strain (adapted from Duncan et al. [9] and Frost [95]). The horizontal arrow at the bottom shows the typical minimum effective strain (MES) levels and the set point values for the bone's thresholds and ultimate strength – microstrain ($\mu\epsilon$), stress (MPa) and unit-load (kg/mm²)

Even though several researchers [23, 96-98] support Frost's MESm concept of an increase in bone mass and remodelling when a mechanical load surpasses a threshold, criticism has also been raised. Some researchers [7, 86] claim that Frost's theory is a qualitative theoretical construction of several hypotheses and that the precise threshold limits that control bone remodelling remain unknown.

A dataset based on several studies was created to evaluate the ability of various types of vigorous physical activities to "stimulate bone formation" according to the MES concept (see Table 2.2). In all selected studies, the test subjects were healthy, young adult or middle-aged

humans of both genders, and the peak strains were obtained by directly attaching strain gauges to the tibia bone surface.

An analysis of Table 2.2 indicates that of the vigorous activities considered, bicycle riding at 60 cycles/s produced the lower peak strain values both in compression and tension sites, with magnitudes on the order of 291 and 271 $\mu\epsilon$, respectively. Normal walking activity, depending on the type of floor or grade (levelled, uphill or downhill gait), can lead to compression bone strain values ranging from 308 to 950 $\mu\epsilon$. Table 2.2 also shows that, when considering the same type of physical activity and muscular contraction, different sites on the tibia present different local deformations.

Table 2.2 - In vivo humans bone strain values measured during different types of physical activities, reported in the literature

| Activity | Type | Strain ($\mu\epsilon$) | | Strain rate ($\mu\epsilon/\text{sec}$) | | Region ^a | Test ^b | Reference |
|----------------------------|------------------------|--------------------------|---------|--|---------|---------------------|-------------------|-----------|
| | | Compressive | Tensile | Compressive | Tensile | | | |
| Walking | Level | 308 | - | 2300 | - | (A) | (a) | [92] |
| | | 544 | 437 | 7183 | 11006 | - | | [96] |
| | | 334 | - | - | - | (B) | (b) | [97] |
| | | 950 | - | - | - | (C) | (c) | [106] |
| | Uphill | 454 | 840 | 3306 | 3955 | (D) | | |
| Walking (≥ 20 kg) | Downhill | 630 | 440 | 8176 | 7113 | - | | |
| | Level | 414 | 531 | 10846 | 9566 | - | | [96] |
| | Uphill | 557 | 381 | 6437 | 11434 | - | | |
| Walking (21-45 kg) | Downhill | 680 | 509 | 10645 | 8989 | - | | |
| | Level | 751 | 601 | 17892 | 9839 | - | | |
| Walking (≤ 46 kg) | Level | 393 | - | 2500-2700 | - | | (a) | |
| Running | Level | 412 | - | - | 4200 | (A) | | [92] |
| | Jogging | 879 | 625 | 27376 | 13913 | - | | |
| | Sprint (13.88 km/h) | 1321 | 646 | 34457 | 20237 | - | | [96] |
| | Sprint (17 km/h) | 2104 | 1415 | 14543 | 7780 | (D) | (c) | [98] |
| | Uphill | 954 | 633 | 23834 | 17475 | - | | |
| Zigzag running | Downhill | 517 | 707 | 26337 | 16710 | - | (a) | [96] |
| | Uphill | 1226 | 743 | 20930 | 13638 | - | | |
| Bicycle | Downhill | 1147 | 707 | 30039 | 15653 | - | | |
| | 60 cycles/s | 291 | 271 | 1510 | 1286 | (D) | - | [106] |
| Forward jump | 30 cm | 1600 | - | - | - | (B) | (b) | [97] |
| | | 3450 | - | - | - | (C) | | |
| | Height of 26 cm | 1905 | 896 | 13178 | 7621 | | | |
| Vertical drop | Height of 39 cm | 1990 | 921 | 11342 | 5021 | (D) | (c) | [98] |
| | Height of 45 cm | 2128 | - | - | - | (B) | (b) | [97] |
| | Height of 45 cm | 436 | - | - | - | (C) | | |
| | Height of 52 cm | 2098 | 1007 | 8663 | 4796 | (D) | (c) | [98] |

^a The anatomical regions considered in these articles were: (A) Anteromedial aspect of the tibial midshaft, (B) Anterior middiaphysis of the distal tibia, (C) Posteromedial part of the distal tibia and (D) Medial aspect of the mid-diaphysis of the tibia.

^b The subjects used in the studies were all active healthy adult: (a) male. (b) female and (c) males and female group tests.

Running can lead to compressive bone strains from 879 $\mu\epsilon$ during jogging to 2104 $\mu\epsilon$ during 17 km/h sprints. The highest strain was registered during a forward jump and vertical drop, which led to compressive deformations of up to 3450 $\mu\epsilon$. In addition to the maximum strain values mentioned, *in vivo* measurements of human tibiae strains do not seem to exceed 2000 $\mu\epsilon$, even during vigorous running activity.

The data presented in Table 2.2 suggest that the peak strain compressive values tend to be higher than the tension values, with the exception of walking and running downhill.

Both the strain magnitude and strain rate are considered essential parameters in the stimuli process. In Table 2.2, the strain rates were again lower during bicycle riding at 60 Hz, with both compressive and tensile values of approximately 5 Hz. Higher strain rates were registered during sprint running, with values of up to 26 and 31 Hz in compression and tension, respectively. These data are in the physiological strain rate range claimed in other studies [9, 55, 89, 99, 100], between 1 and 60 Hz.

The data in Table 2.2 should be considered an approximation of real values because the effect of muscle fatigue on the bone strains and strain rates, as has often been identified *in vivo*, cannot be excluded in all studies. However, physical activities, such as sprinting or running in a zigzag, forward jumping and vertical dropping, may increase bone formation if we consider these data to be physiological values and 1000 $\mu\epsilon$ at 1 Hz cyclic mechanical loading is assumed as the MESm [101-103]. Importantly, only tibiae shaft measurements were considered, and conclusions based on these data should not be extrapolated to the spine and may or may not be valid for other bones in the body [98, 104-106]

Normally a large portion of human daily routine includes events that are associated with far smaller strain magnitudes than vigorous physical activities, such as standing and sitting. According to Huag *et al.* [107], very low strains, those significantly smaller than 5 $\mu\epsilon$, at high frequency strains are constantly bombarding the human skeleton. This finding was confirmed by Fritton *et al.* [90], who counted the daily (12 to 24 h) strain events and showed that large strains (exceeding 1000 $\mu\epsilon$) seldom occur throughout the day and that very small strains (less than 10 $\mu\epsilon$) occur thousands of needs to be assessed.

Rubin *et al.* [108] asserted that the strain magnitude and strain rate of bone are related. In this study, they noticed that cortical bone mass could be maintained via the application of a 800 $\mu\epsilon$

peak-induced load at a frequency of 3 Hz for 600 seconds per day. Furthermore, only 200 $\mu\epsilon$ was necessary to maintain cortical bone mass for the same loading regimen if the strain was applied at 30 Hz. In a study by Weinbaum *et al.* [99], 250 $\mu\epsilon$ at 15 Hz produced a fluid shear stress that was 3.75 times that of a 1000 $\mu\epsilon$ at 1 Hz stimulus and exceeded the threshold for excitation. Moreover, Rubin *et al.* [108] showed that the combination of an even lower strain amplitude than the ones tested by [99], *i.e.*, less than 10 $\mu\epsilon$, with a high-frequency physiological strain rate between 10 and 100 Hz could stimulate bone growth by doubling its formation rate. These findings led to the development of several studies based on the potential use of such stimuli [109-111].

These findings indicate that low-amplitude high-frequency postural strains due to muscular contractions could be as or even more effective in maintaining bone mass than high-amplitude low-frequency strains due to locomotion. This behaviour may explain why astronauts lose bone mass in a microgravity environment, where the need to maintain posture is absent, despite rigorous exercise, or why 3 h/day of quiet standing has been shown to prevent bone loss in bed rest patients [90, 112, 113].

2.2.4. Test system for mechanic stimulation study

Selecting the most suitable test model for a stimulation study of bone mechanical behaviour is very important. Several test systems are available and are grouped in four categories: *in vivo*, *in vitro*, *ex vivo* and *in silico*.

i) In vivo

For *in vivo* testing, although no species fulfils the requirements of an ideal animal model, the dog is perhaps described as having the most similar bone structure to humans. However, using companion animals for medical research is associated with ethical implications. Other species, such as sheep and pigs, have also been suggested. Some researchers have also shown a preference for using rats and mice as experimental animal models [114-118]. According to the literature, rabbits may be the least similar to humans in terms of bone structure and properties. When possible, other bone study test models should be used prior to *in vivo* experimentation because the latter is expensive, leads to animal sacrifice, presents a large degree of systemic complexity and often is not considered satisfactory for the investigation of the mechanism that underlies cellular processes in bone [119-122].

ii) *In vitro* and *ex vivo*

In vitro bone research includes three main branches: cell culture, for which cells are mechanically or enzymatically harvested from tissue and proliferate in a suspension or attached to a surface or monolayer; tissue culture, for which tissue fragments are maintained without not necessarily preserving architecture; and organ culture, for which organs (in whole or in part) or tissues are maintained or grown *in vitro* [123]. Several methodologies to provide mechanical stimuli for experimental study are reviewed by Ehrlich *et al.* [86], Brown [124], Brown [125].

Since Gluckmann [126] first used *in vitro* bone cell cultures to study the effects of mechanical stimuli in bone formation, this system has been considered to be an acceptable and common approach. This test system was also adapted to meet the purposes of more specific research, such as the study of cell responsiveness to fluid flow, first via the development of the parallel plate flow chamber by [127], as well as in a number of other studies [47, 128] that developed similar experimental devices. The advantage of using cell culture systems is that the local environment can be tightly controlled, such as ensuring the absence of growth hormones. A great number of molecular and biochemical tools are also available to ensure that experimental replicates are almost identical, which simplifies statistical analysis and quantification [119, 123, 129].

The most common bone cell cultures used for *in vitro* mechanical stimulation experiments are osteoblastic (*e.g.*, MC3T3-E1), osteocytic (*e.g.*, MLO-Y4) and less often, osteoclastic-like cell cultures. Due to their availability and ease of use, osteoblast cell lines are used in many studies to infer osteocytes behaviour. While osteocytes are the descendants of osteoblasts and similarities would be expected for cells of the same lineage, these cells have distinct differences, particularly in their responses to mechanical loading [9, 32, 33, 130].

For studies of the osteocyte physiological response to mechanical loading, two-dimensional cell culture conditions are arguably far too simple and hardly representative of the complex bone environment. This approach overlooks many parameters known to be essential for accurately reproducing the mechanotransduction process. Three-dimensional cell-growth environments have been developed in an attempt to overcome some cell culture disadvantages, mimic the physiological complexity of real tissue, and avoid the use of bone organ cultures [121]. Several materials have been tested as scaffolds, such as collagen glycosaminoglycan [131, 132] and porous chitosan [133]. Under static culture conditions, cell proliferation in scaffolds is limited by diffusion, due to increases in the cell mass and decreases in the effective porosity resulting from matrix deposition. Fluid transport and cell distribution, as well as cell stimulation and

differentiation may be improved via the use of bioreactors for three-dimensional scaffold systems [134, 135]. Flow perfusion bioreactors are more commonly used than any other bioreactor for three-dimensional bone stimulation studies. These bioreactor systems pump culture medium through the scaffold's interconnected pores, which are held in place across the continuously circulating flow. These devices enable the close monitoring and precise control of several environmental conditions, such as the temperature, pH, oxygen and nutrient supply inside the scaffold and removal of waste products and metabolites. They also provide a high degree of reproducibility and automation, which favours the development and maturation of bone cells in scaffolds [134, 136, 137].

An understanding of the behaviour and responses of cells cultured on scaffolds should guide the scaffold optimization process. The pore size, pore interconnectivity and total porosity are essential parameters for scaffold development. The pore size affects cell migration into the scaffold and influences the amount of fluid that reaches the cells. It also determines the mechanical load to which the cells are exposed, *i.e.*, the wall shear stress and the hydrostatic wall pressure that acts on the cells [138-143].

In vivo, osteocytes are attached to their mineralized matrix either via tethering filaments or perhaps via integrin-based focal adhesions. When these cells are seeded on a stiff two-dimensional surface, they are not surrounded by a pericellular matrix. Thus, they will spread out and form only integrin-based attachments with the substrate. In three-dimensional cultures, the pores dimensions of the scaffold will influence the initial cell attachment levels and the morphology of attachment, such as a flat morphology (akin to a two-dimensional monolayer culture), which occurs for large pores, and a bridging morphology. The pore size affects the cell's ability to span the void space [32, 144, 145].

Cell attachment can influence the dynamics of surface-cell-flow relationships and thus impact the magnitude of cytoskeletal deformations. According to Klein-Nulend *et al.* [32], round non-adherent osteocytes are more sensitive to mechanical stimuli than adherent ones. In a study by Jungreuthmayer *et al.* [143], three-dimensional culture conditions required lower fluid flow rates to obtain bone formation than two-dimensional culture conditions, *i.e.*, the increased cell deformability leads to increased cellular shear stress sensitivity. One advantage of two-dimensional systems over three-dimensional cell-scaffolds systems is that cellular loss due to fluid shear stress investigations is not a major concern in two-dimensional systems. In these systems, the levels of shear stress required to induce cellular detachment are orders of magnitude greater than those expected to cause osteogenesis *in vivo*. In three-dimensional cell-

scaffolds systems, if a cell adapts a bridging morphology type, it will experience greater levels of cytoskeletal deformation than a flat cell when subjected to the same flow conditions [146]. Furthermore, according to Klein-Nulend *et al.* [32], the flow-induced stimulus for two-dimensional cell cultures is the same on the cell process and cell body in nearly all experiments.

Although tremendous advances have been made in the development of three-dimensional scaffold-based systems for bone cells studies that could reproduce both the formation of an organized bone-like matrix and cell-mediated substrate degradation, this methodology is also associated with limitations depending on the aim of a study [121, 136].

To study bone's physiological strain profile *in vitro*, the bone's natural microenvironment must be mimicked. The osteocyte mechanosensation response depends on the type of material to which they are attached. Hence, scaffolds that mimic the properties of native bone should be used. However, the osteocyte mechanical conditions *in vivo* are not clearly understood, which precludes the reliable recreation of these conditions in an *in vitro* experiment. Variables such as the complex lacuna-canalicular geometry and the distribution of the cell's focal adhesions play an important role in the osteocyte mechanotransduction process [60, 147, 148].

The critical requirement for *in vitro* models that represent the physiological diversity and complexity of the bone formation process have led to the development of different test systems, such as bone organ cultures or *ex vivo* bone culture systems.

Organ culture has been used for more than 50 years in an attempt to bridge the gap between cell culture and *in vivo* models [123, 149, 150]. The pioneering work of Fell *et al.* [151] in this field is known worldwide.

Organ culture provides a model that is, in certain aspects, more similar to the *in vivo* situation. This testing system respects the bone's natural three-dimensional structure and retains the extracellular matrix, which allows normal cell-matrix attachment sites to be maintained. The conservation of the tissue architectural organization will most likely simulate the physiological distinct mechanical consequence of loading, such as strain, fluid shear stress, and streaming potentials. Another great advantage of using organ culture technology is that they are not as complex as the whole animal and local effects, such as mediators and mechanical stress, can be isolated from systemic ones, such as steroids, other hormones and toxins [89, 120, 149, 152].

The main disadvantages of using organ cultures are 1) the loss of a vascular system, which limits the organ sample size that can be harvested; 2) explants cannot be used for experiments longer

than 24 h; and 3) the artificial environment created requires that the investigator exercises caution in the interpretation of the results and their extrapolation to an *in vivo* situation [86, 89, 120, 123, 149, 150].

In recent years, the evolution of bioreactor devices for the application of specific mechanical stimuli and controlled medium recirculation has favoured cell viability and prolonged culture time of bone explants [121]. A system that shows a successful applicability of these strategy was developed by Davies *et al.* [153]. In this *ex vivo* system, a mechanical loading and measurement system are combined with a cancellous bone diffusion culture-loading chamber named ZetOS™. This bioreactor maintains bone biopsy cultures for extended periods of time whilst preserving the natural three-dimensional architecture and inter-cellular interactions of several cell types.

iii) In silico

The use of conceptual and mathematical models has already proven valuable in bone research [154]. Advances in scientific knowledge, mathematical modelling, and computer technology has facilitated the integration of numerical equations into finite element models [155]. A variety of computational approaches [156-161] have been developed in an attempt to understand the mechanotransduction process and response to mechanical stimulus in bone, such as interstitial fluid flow [41, 162] and direct cell strain [36].

A good example of the integration of *in silico* analysis with *in vivo* and *in vitro* studies is the work developed by Yang *et al.* [163]. The authors studied the strain field in mice tibiae using micro CT-based finite element analysis together with diaphyseal strain gauge measurements during *in vivo* dynamic compression loading. Furthermore, as suggested by Webster *et al.* [164], future computational approaches should focus on merging models from different scales into a fully integrated multiscale modelling approach, which would enhance both the predictive and descriptive ability of computationally models and consequently facilitate the generation of new hypotheses and new experimental studies.

2.2.5. Conclusion

The scientific community has long recognized the importance of mechanical loading conditions in defining the mass and structure of bone. Bending moment stimuli are experienced by and transmitted along long bones via a combination of its physiological curvature, gravitational load (body weight) and the load applied by balanced muscle activities. Hence, muscle and bone are coupled as a functional unit. During mechanotransduction, osteocytes play the role of sensory cells within the bone, and their response is most likely mediated by strain-derived fluid flow

shear stress through the lacuno-canalicular network. Osteocytes will respond to these mechanical stimuli by opening stretch-activated ion channels and increasing the levels of intracellular Ca^{2+} and protein Kinase C, which consequently stimulate the release of potent anabolic regulators of bone growth, such as NO and PGE2.

The mechanical stimulus strain magnitude and rate are important parameters. Low frequency, high magnitude strains occur during vigorous activities, such as running and jumping, and exert a recognized positive effect on bone formation/remodelling. Conversely, the relevance of high frequency, low magnitude strains associated with events such as standing or sitting as bone mechanical stimuli is now starting to be taken into consideration.

Isolated cell lines in mechanical stimulation studies are important to investigate the behaviour of individual bone cell populations during mechanotransduction. For studies of the bone mechanical and biological environments *in vivo*, two-dimensional osteoblast- or osteocyte-like cell cultures and the use of cells scaffolds do not fully mimic the real bone environment, which is an organ system with complex and distinct cell interactions. Thus, defining the type of study and the variables that need be included in the system is important to select the proper test model.

With this review an attempt was made to clarify important notions related to the adaptation behaviour of bone to external load stimuli. Although mechanical forces clearly affect the bone's behaviour, this relationship remains poorly understood. Continued studies of both the mechanical (*e.g.*, bone muscle interactions) and biological fields (*e.g.*, mechanisms and pathways underlying bone remodelling and mechanotransduction) are necessary. Moreover, biomechanical cross-talk should not be neglected. New research tools, such as advanced algorithms and techniques to assess the mechanical environment of bone *in vivo*, should allow integrated approaches to capture the complex dynamics of bone biomechanical behaviour. A better understanding of bone's response process to mechanical stimuli should provide new insights into diseases, such as osteoporosis, hyperparathyroidism, hyperthyroidism, Paget's disease and osteopetrosis.

2.2.6. References

1. Galilei, G., *Discorsi e dimostrazioni matematiche intorno a due nuove scienze attenenti alla meccanica ed ai movimenti locali*. 1st ed 1638, Leida: Società Editrice Fiorentina.
2. von Meyer, G.H., *Die architektur der spongiosa*. Archiv für Anatomie, Physiologie und Wissenschaftliche Medizin, 1867. **34**: p. 615-628.
3. Culmann, K., *Die graphische statik* 1866, Zürich: Meyer & Zeller.

4. Roux, W., *Die entwicklungsmechanik; ein neuer Zweig der biologischen Wissenschaft*. Roux, *Vorträge und Aufsätze, part I*1905, Leipzig: Engelmann.
5. Skedros, J.G. and R.A. Brand, *Biographical sketch: Georg Hermann von Meyer (1815–1892)*. *Clinical Orthopaedics and Related Research*, 2011. **469**(11): p. 3072-3076.
6. Carter, D.R., *Mechanical loading histories and cortical bone remodeling*. *Calcified Tissue International*, 1984. **36**(1): p. S19-S24.
7. Huiskes, R., *If bone is the answer, then what is the question?* *Journal of Anatomy*, 2000. **197**(2): p. 145-156.
8. Wolff, J., *Das gesetz der transformation der knochen*1892, Berlin: Verlag von August Hirschwald.
9. Duncan, R.L. and C.H. Turner, *Mechanotransduction and the functional response of bone to mechanical strain*. *Calcified Tissue International*, 1995. **57**(5): p. 344-358.
10. Ahn, A.C. and A.J. Grodzinsky, *Relevance of collagen piezoelectricity to "Wolff's Law": A critical review*. *Medical Engineering & physics*, 2009. **31**(7): p. 733-741.
11. Skerry, T.M., *One mechanostat or many? Modifications of the site-specific response of bone to mechanical loading by nature and nurture*. *Journal of Musculoskeletal and Neuronal Interactions*, 2006. **6**(2): p. 122-7.
12. Burr, D.B., *Muscle strength, bone mass, and age-related bone loss*. *Journal of Bone and Mineral Research*, 1997. **12**(10): p. 1547-1551.
13. Bakker, A.D., et al., *The production of nitric oxide and prostaglandin E2 by primary bone cells is shear stress dependent*. *Journal of Biomechanics*, 2001. **34**(5): p. 671-677.
14. Duda, G.N., et al., *Influence of muscle forces on femoral strain distribution*. *Journal of Biomechanics*, 1998. **31**(9): p. 841-846.
15. Rittweger, J., et al., *Persisting side-to-side differences in bone mineral content, but not in muscle strength and tendon stiffness after anterior cruciate ligament reconstruction*. *Clinical Physiology and Functional Imaging*, 2011. **31**(1): p. 73-79.
16. Sievänen, H., A. Heinonen, and P. Kannus, *Adaptation of bone to altered loading environment: a biomechanical approach using X-ray absorptiometric data from the patella of a young woman*. *Bone*, 1996. **19**(1): p. 55-59.
17. Schönau, E., et al., *Influence of muscle strength on bone strength during childhood and adolescence*. *Hormone Research*, 1996. **45**(Suppl. 1): p. 63-66.
18. Klein-Nulend, J., R.G. Bacabac, and M.G. Mullender, *Mechanobiology of bone tissue*. *Pathologie Biologie*, 2005. **53**(10): p. 576-580.
19. Pauwels, F., *Biomechanics of the Locomotor Apparatus*1980, Berlin: Springer Berlin Heidelberg.
20. Muni, M., A. Kralj, and T. Bajd, *Bending moments in lower extremity bones for two standing postures*. *Journal of Biomedical Engineering*, 1992. **14**(4): p. 293-302.
21. Lanyon, L.E., *Using functional loading to influence bone mass and architecture: objectives, mechanisms, and relationship with estrogen of the mechanically adaptive process in bone*. *Bone*, 1996. **18**(1): p. S37-S43.
22. Aarden, E.M., P.J. Nijweide, and E.H. Burger, *Function of osteocytes in bone*. *Journal of Cellular Biochemistry*, 1994. **55**(3): p. 287-299.
23. Rubin, C.T., K.J. McLeod, and S.D. Bain, *Functional strains and cortical bone adaptation: epigenetic assurance of skeletal integrity*. *Journal of Biomechanics*, 1990. **23**(1): p. 43-54.
24. Turner, C.H. and F.M. Pavalko, *Mechanotransduction and functional response of the skeleton to physical stress: the mechanisms and mechanics of bone adaptation*. *Journal of Orthopaedic Science*, 1998. **3**(6): p. 346-355.
25. Waung, J.A., J.H.D. Bassett, and G.R. Williams, *Thyroid hormone metabolism in skeletal development and adult bone maintenance*. *Trends in Endocrinology and Metabolism*, 2012. **23**(4): p. 155-62.

26. Cauley, J.A., *Estrogen and bone health in men and women*. Steroids, 2015. **Article in press**.
27. Elefteriou, F., P. Campbell, and Y. Ma, *Control of bone remodeling by the peripheral sympathetic nervous system*. Calcified Tissue International, 2014. **94**(1): p. 140-151.
28. Redlich, K. and J.S. Smolen, *Inflammatory bone loss: pathogenesis and therapeutic intervention*. Nature reviews Drug discovery, 2012. **11**(3): p. 234-50.
29. Manolagas, S.C. and A.M. Parfitt, *What old means to bone*. Trends in Endocrinology and Metabolism, 2010. **21**(6): p. 369-374.
30. Temiyasathit, S. and C.R. Jacobs, *Osteocyte primary cilium and its role in bone mechanotransduction*. Annals of the New York Academy of Sciences, 2010. **1192**(1): p. 422-428.
31. Isaacson, B.M. and R.D. Bloebaum, *Bone bioelectricity: What have we learned in the past 160 years?* Journal of Biomedical Materials Research, 2010. **95**(4): p. 1270-1279.
32. Klein-Nulend, J., et al., *Mechanosensation and transduction in osteocytes*. Bone, 2013. **54**(2): p. 182-190.
33. Bonivitch, R.A., L.F. Bonewald, and D.P. Nicolella, *Tissue strain amplification at the osteocyte lacuna: a microstructural finite element analysis*. Journal of Biomechanics, 2007. **40**(10): p. 2199-2206.
34. Vaughan, T.J., S.W. Verbruggen, and L.M. McNamara, *Are all osteocytes equal? Multiscale modelling of cortical bone to characterise the mechanical stimulation of osteocytes*. International journal for numerical methods in biomedical engineering, 2013. **29**(12): p. 1361-72.
35. McGarry, J.G., et al., *A comparison of strain and fluid shear stress in stimulating bone cell responses—a computational and experimental study*. The FASEB Journal, 2005. **19**(3): p. 482-4.
36. Wang, L., J. Dong, and C.J. Xian, *Strain amplification analysis of an osteocyte under static and cyclic loading: A finite element study*. BioMed Research International, 2015. **2015**.
37. Gardinier, J.D., et al., *In situ permeability measurement of the mammalian lacunar–canalicular system*. Bone, 2010. **46**(4): p. 1075-1081.
38. Ajubi, N.E., et al., *Pulsating fluid flow increases prostaglandin production by cultured chicken osteocytes—a cytoskeleton-dependent process*. Biochemical and Biophysical Research Communications, 1996. **225**(1): p. 62-68.
39. Bacabac, R.G., et al., *Nitric oxide production by bone cells is fluid shear stress rate dependent*. Biochemical and Biophysical Research Communications, 2004. **315**(4): p. 823-829.
40. Piekarski, K., *Transport mechanism operating between blood supply and osteocytes in long bones*. Nature, 1977. **269**(5623): p. 80-82.
41. Verbruggen, S.W., T.J. Vaughan, and L.M. McNamara, *Fluid flow in the osteocyte mechanical environment: A fluid–structure interaction approach*. Biomechanics and Modeling in Mechanobiology, 2014. **13**(1): p. 85-97.
42. Morris, H.L., et al., *Mechanisms of fluid-flow-induced matrix production in bone tissue engineering*. Proceedings of the Institution of Mechanical Engineers, Part H: Journal of Engineering in Medicine, 2010. **224**(12): p. 1509-21.
43. Delaine-Smith, R.M., S. MacNeil, and G.C. Reilly, *Matrix production and collagen structure are enhanced in two types of osteogenic progenitor cells by a simple fluid shear stress stimulus*. European Cells and Materials, 2012. **24**: p. 162-74.
44. Young, Y.-N., et al., *Multiscale modeling of primary cilia*, in *Multiscale Modeling in Biomechanics and Mechanobiology*, S. De, W. Hwang, and E. Kuhl, Editors. 2015, Springer. p. 87-110.
45. Donahue, T.L.H., et al., *Mechanosensitivity of bone cells to oscillating fluid flow induced shear stress may be modulated by chemotransport*. Journal of Biomechanics, 2003. **36**(9): p. 1363-71.

46. Case, N., et al., *Steady and oscillatory fluid flows produce a similar osteogenic phenotype*. *Calcified Tissue International*, 2011. **88**(3): p. 189-97.
47. Jacobs, C.R., et al., *Differential effect of steady versus oscillating flow on bone cells*. *Journal of Biomechanics*, 1998. **31**(11): p. 969-76.
48. Hastings, G. and F. Mahmud, *Electrical effects in bone*. *Journal of Biomedical Engineering*, 1988. **10**(6): p. 515-521.
49. Starkebaum, W., S.R. Pollack, and E. Korostoff, *Microelectrode studies of stress-generated potentials in four-point bending of bone*. *Journal of Biomedical Materials Research*, 1979. **13**(5): p. 729-751.
50. Salzstein, R.A. and S.R. Pollack, *Electromechanical potentials in cortical bone—II. Experimental analysis*. *Journal of Biomechanics*, 1987. **20**(3): p. 271-280.
51. Salzstein, R.A., et al., *Electromechanical potentials in cortical bone—I. A continuum approach*. *Journal of Biomechanics*, 1987. **20**(3): p. 261-270.
52. Yasuda, I., *The classic: fundamental aspects of fracture treatment, reprinted from J Kyoto Med Soc, 4:395-406, 1953*. *Clinical Orthopaedics and Related Research*, 1977. **124**: p. 5-8.
53. Fukada, E. and I. Yasuda, *On the piezoelectric effect of bone*. *Journal of the Physical Society of Japan*, 1957. **12**(10): p. 1158-1162.
54. Marino, A.A., R.O. Becker, and S.C. Soderholm, *Origin of the piezoelectric effect in bone*. *Calcified Tissue Research*, 1971. **8**(1): p. 177-80.
55. Minary-Jolandan, M. and M.-F. Yu, *Nanoscale characterization of isolated individual type I collagen fibrils: polarization and piezoelectricity*. *Nanotechnology*, 2009. **20**(8): p. 085706.
56. Lemaire, T., et al., *A multiscale theoretical investigation of electric measurements in living bone*. *Bulletin of Mathematical Biology*, 2011. **73**(11): p. 2649-2677.
57. Schaffler, M.B., et al., *Osteocytes: master orchestrators of bone*. *Calcified Tissue International*, 2013. **94**(1): p. 1-20.
58. Iolascon, G., G. Resmini, and U. Tarantino, *Mechanobiology of bone*. *Aging clinical and experimental research*, 2013. **25**(1): p. 3-7.
59. Han, Y., et al., *Mechanotransduction and strain amplification in osteocyte cell processes*. *Proceedings of the National Academy of Sciences of the United States of America*, 2004. **101**(47): p. 16689-16694.
60. Adachi, T., et al., *Calcium response in single osteocytes to locally applied mechanical stimulus: differences in cell process and cell body*. *Journal of Biomechanics*, 2009. **42**(12): p. 1989-1995.
61. Thi, M.M., et al., *Mechanosensory responses of osteocytes to physiological forces occur along processes and not cell body and require $\alpha V\beta 3$ integrin*. *Proceedings of the National Academy of Sciences of the United States of America*, 2013. **110**(52): p. 21012-21017.
62. Thi, M.M., et al., *Mechanosensory responses of osteocytes to physiological forces occur along processes and not cell body and require $\alpha V\beta 3$ integrin*. *Proceedings of the National Academy of Sciences*, 2013. **110**(52): p. 21012-17.
63. Robling, A.G. and C.H. Turner, *Mechanical signaling for bone modeling and remodeling*. *Critical reviews in eukaryotic gene expression*, 2009. **19**(4): p. 319-38.
64. Ross, T.D., et al., *Integrins in mechanotransduction*. *Current Opinion in Cell Biology*, 2013. **25**(5): p. 613-8.
65. Ozcivici, E., et al., *Mechanical signals as anabolic agents in bone*. *Nature Reviews Rheumatology*, 2010. **6**(1): p. 50-9.
66. Mikuni-Takagaki, Y., et al., *The role of calcium channels in osteocyte function*. *Journal of Musculoskeletal and Neuronal Interactions*, 2002. **2**(3): p. 252-255.
67. Liedert, A., et al., *Signal transduction pathways involved in mechanotransduction in bone cells*. *Biochemical and Biophysical Research Communications*, 2006. **349**(1): p. 1-5.

68. Rawlinson, S.C.F., A.A. Pitsillides, and L.E. Lanyon, *Involvement of different ion channels in osteoblasts' and osteocytes' early responses to mechanical strain*. Bone, 1996. **19**(6): p. 609-614.
69. Malone, A.M.D., et al., *Primary cilia mediate mechanosensing in bone cells by a calcium-independent mechanism*. Proceedings of the National Academy of Sciences of the United States of America, 2007. **104**(33): p. 13325-13330.
70. Delaine-Smith, R.M., A. Sittichokechaiwut, and G.C. Reilly, *Primary cilia respond to fluid shear stress and mediate flow-induced calcium deposition in osteoblasts*. The FASEB journal, 2014. **28**(1): p. 430-9.
71. Pajevic, P.D., *Recent Progress in Osteocyte Research*. Endocrinology and Metabolism, 2013. **28**(4): p. 255-261.
72. Hum, J.M., et al., *Mechanical Loading in Osteocytes Induces Formation of a Src/Pyk2/MBD2 Complex That Suppresses Anabolic Gene Expression*. PLoS One, 2014. **9**(5): p. e97942.
73. Lu, X.L., et al., *Calcium response in osteocytic networks under steady and oscillatory fluid flow*. Bone, 2012. **51**(3): p. 466-473.
74. Lemaire, T. and S. Naili, *Possible role of calcium permselectivity in bone adaptation*. Medical Hypotheses, 2012. **78**(3): p. 367-369.
75. Fox, S.W., T.J. Chambers, and J.W. Chow, *Nitric oxide is an early mediator of the increase in bone formation by mechanical stimulation*. American Journal of Physiology. Endocrinology and Metabolism, 1996. **270**(6): p. E955-E960.
76. Chow, J.W.M., et al., *Role of nitric oxide and prostaglandins in mechanically induced bone formation*. Journal of Bone and Mineral Research, 1998. **13**(6): p. 1039-1044.
77. Klein-Nulend, J., et al., *Nitric oxide signaling in mechanical adaptation of bone*. Osteoporosis International, 2014. **25**(5): p. 1427-37.
78. Klein-Nulend, J., et al., *Pulsating fluid flow increases nitric oxide (NO) synthesis by osteocytes but not periosteal fibroblasts-correlation with prostaglandin upregulation*. Biochemical and Biophysical Research Communications, 1995. **217**(2): p. 640-648.
79. Vatsa, A., et al., *Bio imaging of intracellular NO production in single bone cells after mechanical stimulation*. Journal of Bone and Mineral Research, 2006. **21**(11): p. 1722-1728.
80. Tan, S.D., et al., *Osteocytes subjected to fluid flow inhibit osteoclast formation and bone resorption*. Bone, 2007. **41**(5): p. 745-751.
81. Vezeridis, P.S., et al., *Osteocytes subjected to pulsating fluid flow regulate osteoblast proliferation and differentiation*. Biochemical and Biophysical Research Communications, 2006. **348**(3): p. 1082-1088.
82. Dirckx, N., M. Hul, and C. Maes, *Osteoblast recruitment to sites of bone formation in skeletal development, homeostasis, and regeneration*. Birth Defects Research Part C: Embryo Today: Reviews, 2013. **99**(3): p. 170-91.
83. Hambli, R. and R. Rieger, *Physiologically based mathematical model of transduction of mechanobiological signals by osteocytes*. Biomechanics and Modeling in Mechanobiology, 2012. **11**(1-2): p. 83-93.
84. Robling, A.G., A.B. Castillo, and C.H. Turner, *Biomechanical and molecular regulation of bone remodeling*. Annual Review of Biomedical Engineering, 2006. **8**: p. 455-498.
85. Sims, N.A. and C. Vrahnas, *Regulation of cortical and trabecular bone mass by communication between osteoblasts, osteocytes and osteoclasts*. Archives of biochemistry and biophysics, 2014. **561**: p. 22-8.
86. Ehrlich, P.J. and L.E. Lanyon, *Mechanical strain and bone cell function: a review*. Osteoporosis International, 2002. **13**(9): p. 688-700.
87. Hert, J., M. Liskova, and B. Landrgot, *Influence of the long-term, continuous bending on the bone. An experimental study on the tibia of the rabbit*. Folia Morphologica, 1969. **17**(4): p. 389.

88. Hert, J., M. Liskova, and J. Landa, *Reaction of bone to mechanical stimuli. 1. Continuous and intermittent loading of tibia in rabbit*. Folia Morphologica, 1971. **19**(3): p. 290-300.
89. Kunnel, J.G., J.L. Gilbert, and P.H. Stern, *In vitro mechanical and cellular responses of neonatal mouse bones to loading using a novel micromechanical-testing device*. Calcified Tissue International, 2002. **71**(6): p. 499-507.
90. Fritton, S.P., K. J McLeod, and C.T. Rubin, *Quantifying the strain history of bone: spatial uniformity and self-similarity of low-magnitude strains*. Journal of Biomechanics, 2000. **33**(3): p. 317-325.
91. Hoshaw, S.J., et al., *A method suitable for in vivo measurement of bone strain in humans*. Journal of Biomechanics, 1997. **30**(5): p. 521-524.
92. Lanyon, L.E., et al., *Bone deformation recorded in vivo from strain gauges attached to the human tibial shaft*. Acta Orthopaedica Scandinavica, 1975. **46**(2): p. 256-68.
93. Mikić, B. and D.R. Carter, *Bone strain gage data and theoretical models of functional adaptation*. Journal of Biomechanics, 1995. **28**(4): p. 465-469.
94. Frost, H.M., *Bone "mass" and the "mechanostat": a proposal*. Anatomical Record, 1987. **219**(1): p. 1-9.
95. Frost, H.M., *Bone's mechanostat: a 2003 update*. Anatomical Record, 2003. **275**(2): p. 1081-1101.
96. Burr, D.B., et al., *In vivo measurement of human tibial strains during vigorous activity*. Bone, 1996. **18**(5): p. 405-410.
97. Ekenman, I., et al., *Local bone deformation at two predominant sites for stress fractures of the tibia: an in vivo study*. Foot and Ankle International, 1998. **19**(7): p. 479-484.
98. Milgrom, C., et al., *Do high impact exercises produce higher tibial strains than running?* British Journal of Sports Medicine, 2000. **34**(3): p. 195-199.
99. Weinbaum, S., S.C. Cowin, and Y. Zeng, *A model for the excitation of osteocytes by mechanical loading-induced bone fluid shear stresses*. Journal of Biomechanics, 1994. **27**(3): p. 339-360.
100. Henstock, J.R., et al., *Cyclic hydrostatic pressure stimulates enhanced bone development in the foetal chick femur in vitro*. Bone, 2013. **53**(2): p. 468-77.
101. Poliachik, S.L., et al., *32 wk old C3H/HeJ mice actively respond to mechanical loading*. Bone, 2008. **42**(4): p. 653-659.
102. Rubin, C.T. and L.E. Lanyon, *Regulation of bone mass by mechanical strain magnitude*. Calcified Tissue International, 1985. **37**(4): p. 411-417.
103. Turner, C.H., et al., *Mechanical loading thresholds for lamellar and woven bone formation*. Journal of Bone and Mineral Research, 1994. **9**(1): p. 87-97.
104. Al Nazer, R., et al., *Flexible multibody simulation approach in the analysis of tibial strain during walking*. Journal of Biomechanics, 2008. **41**(5): p. 1036-1043.
105. Milgrom, C., et al., *The effect of muscle fatigue on in vivo tibial strains*. Journal of Biomechanics, 2007. **40**(4): p. 845-850.
106. Milgrom, C., et al., *In vivo strain measurements to evaluate the strengthening potential of exercises on the tibial bone*. Journal of Bone and Joint Surgery. British Volume, 2000. **82**(4): p. 591-594.
107. Huang, R.P., C.T. Rubin, and K.J. McLeod, *Changes in postural muscle dynamics as a function of age*. The Journals of Gerontology Series A: Biological Sciences and Medical Sciences, 1999. **54**(8): p. B352-B357.
108. Rubin, C.T., et al., *Inhibition of osteopenia by low magnitude, high-frequency mechanical stimuli*. Drug Discovery Today, 2001. **6**(16): p. 848-858.
109. Judex, S. and C.T. Rubin, *Is bone formation induced by high-frequency mechanical signals modulated by muscle activity?* Journal of Musculoskeletal and Neuronal Interactions, 2010. **10**(1): p. 3-11.

110. Afzal, S.Y., et al., *The effect of low magnitude mechanical stimulation (LMMS) on bone density in patients with Rett syndrome: A pilot and feasibility study*. Journal of pediatric rehabilitation medicine, 2014. **7**(2): p. 167-78.
111. Padilla, F., et al., *Stimulation of bone repair with ultrasound: A review of the possible mechanic effects*. Ultrasonics, 2014. **54**(5): p. 1125-45.
112. Dionyssiotis, Y., et al., *Impact on bone and muscle area after spinal cord injury*. BoneKEY Reports, 2015. **4**.
113. Lloyd, S.A., et al., *Interdependence of muscle atrophy and bone loss induced by mechanical unloading*. Journal of Bone and Mineral Research, 2014. **29**(5): p. 1118-30.
114. Hsieh, Y.-F., et al., *Mechanical loading of diaphyseal bone in vivo: the strain threshold for an osteogenic response varies with location*. Journal of Bone and Mineral Research, 2001. **16**(12): p. 2291-7.
115. Noble, B.S., et al., *Mechanical loading: Biphasic osteocyte survival and targeting of osteoclasts for bone destruction in rat cortical bone*. American Journal of Physiology-Cell Physiology, 2003. **284**(4): p. C934-43.
116. Robling, A.G., et al., *Mechanical stimulation of bone in vivo reduces osteocyte expression of Sost/sclerostin*. Journal of Biological Chemistry, 2008. **283**(9): p. 5866-75.
117. Raab-Cullen, D.M., et al., *Periosteal bone formation stimulated by externally induced bending strains*. Journal of Bone and Mineral Research, 1994. **9**(8): p. 1143-52.
118. Moustafa, A., et al., *The mouse fibula as a suitable bone for the study of functional adaptation to mechanical loading*. Bone, 2009. **44**(5): p. 930-5.
119. Pearce, A., et al., *Animal models for implant biomaterial research in bone: a review*. European Cells and Materials, 2007. **13**: p. 1-10.
120. Jones, D.B., et al., *Development of a mechanical testing and loading system for trabecular bone studies for long term culture*. European Cells and Materials, 2003. **5**: p. 48-59.
121. Papadimitropoulos, A., et al., *A 3D in vitro bone organ model using human progenitor cells*. European Cells and Materials, 2011. **21**: p. 445-58.
122. Meakin, L.B., J.S. Price, and L.E. Lanyon, *The contribution of experimental in vivo models to understanding the mechanisms of adaptation to mechanical loading in bone*. Frontiers in Endocrinology, 2014. **5**(154): p. 1-13.
123. Davies, C.M., et al., *Mechanically loaded ex vivo bone culture system 'Zetos': systems and culture preparation*. European Cells and Materials, 2006. **11**: p. 57-75.
124. Brown, T.D., *Techniques for mechanical stimulation of cells in vitro: a review*. Journal of Biomechanics, 2000. **33**(1): p. 3-14.
125. Brown, T.D., *Devices and techniques for in vitro mechanical stimulation of bone cells*, in *Bone mechanics handbook*, S.C. Cowin, Editor 2001, CRC Press: Florida. p. 27-1-27-22.
126. Glucksmann, A., *The role of mechanical stresses in bone formation in vitro*. Journal of Anatomy, 1942. **76**(Pt 3): p. 231-9.
127. Frangos, J.A., L.V. McIntire, and S.G. Eskin, *Shear stress induced stimulation of mammalian cell metabolism*. Biotechnology and Bioengineering, 1988. **32**(8): p. 1053-60.
128. Nauman, E.A., et al., *Quantitative assessment of steady and pulsatile flow fields in a parallel plate flow chamber*. Annals of biomedical engineering, 1999. **27**(2): p. 194-9.
129. Huesa, C., M.H. Helfrich, and R.M. Aspden, *Parallel-plate fluid flow systems for bone cell stimulation*. Journal of Biomechanics, 2010. **43**(6): p. 1182-9.
130. Kadow-Romacker, A., et al., *Effect of mechanical stimulation on osteoblast-and osteoclast-like cells in vitro*. Cells Tissues Organs, 2008. **190**(2): p. 61-8.
131. Chang, Y.-H., et al. *A 3D environment influences osteocyte function*. in *BMC Proceedings*. 2015. Dublin, Ireland: BioMed Central Ltd.

132. Keogh, M.B., F.J. O'Brien, and J.S. Daly, *A novel collagen scaffold supports human osteogenesis—applications for bone tissue engineering*. Cell and tissue research, 2010. **340**(1): p. 169-77.
133. Su, W.-T., Y.-T. Wang, and C. C-M, *Optimal fluid flow enhanced mineralization of MG-63 cells in porous chitosan scaffold*. Journal of the Taiwan Institute of Chemical Engineers, 2014. **45**(4): p. 1111-1118.
134. Plunkett, N. and F.J. O'Brien, *Bioreactors in tissue engineering*. Technology and Health Care, 2011. **19**(1): p. 55-69.
135. Porter, B.D., et al., *Noninvasive image analysis of 3D construct mineralization in a perfusion bioreactor*. Biomaterials, 2007. **28**(15): p. 2525-33.
136. Haycock, J.W., *3D cell culture: a review of current approaches and techniques*, in *3D Cell Culture*, J.W. Haycock, Editor 2011, Springer. p. 1-15.
137. Vetsch, J.R., R. Müller, and S. Hofmann, *The evolution of simulation techniques for dynamic bone tissue engineering in bioreactors*. Journal of tissue engineering and regenerative medicine, 2013.
138. Murphy, C.M., M.G. Haugh, and F.J. O'Brien, *The effect of mean pore size on cell attachment, proliferation and migration in collagen–glycosaminoglycan scaffolds for bone tissue engineering*. Biomaterials, 2010. **31**(3): p. 461-6.
139. O'Brien, F.J., et al., *The effect of pore size on permeability and cell attachment in collagen scaffolds for tissue engineering*. Technology and Health Care, 2007. **15**(1): p. 3-17.
140. Murphy, C.M., et al., *Cell-scaffold interactions in the bone tissue engineering triad*. European Cells and Materials, 2013. **26**: p. 120-32.
141. Cartmell, S.H., et al., *Effects of medium perfusion rate on cell-seeded three-dimensional bone constructs in vitro*. Tissue Engineering, 2003. **9**(6): p. 1197-1203.
142. McCoy, R.J., C. Jungreuthmayer, and F.J. O'Brien, *Influence of flow rate and scaffold pore size on cell behavior during mechanical stimulation in a flow perfusion bioreactor*. Biotechnology and Bioengineering, 2012. **109**(6): p. 1583-94.
143. Jungreuthmayer, C., et al., *Deformation simulation of cells seeded on a collagen-GAG scaffold in a flow perfusion bioreactor using a sequential 3D CFD-elastostatics model*. Medical Engineering & Physics, 2009. **31**(4): p. 420-7.
144. McCoy, R.J. and F.J. O'Brien, *Visualizing feasible operating ranges within tissue engineering systems using a “windows of operation” approach: A perfusion-scaffold bioreactor case study*. Biotechnology and Bioengineering, 2012. **109**(12): p. 3161-71.
145. O'Brien, F.J., et al., *The effect of pore size on cell adhesion in collagen-GAG scaffolds*. Biomaterials, 2005. **26**(4): p. 433-41.
146. McCoy, R.J. and F.J. O'Brien, *Influence of shear stress in perfusion bioreactor cultures for the development of three-dimensional bone tissue constructs: a review*. Tissue Engineering Part B: Reviews, 2010. **16**(6): p. 587-601.
147. Bonewald, L.F., *The amazing osteocyte*. Journal of Bone and Mineral Research, 2011. **26**(2): p. 229-238.
148. Mauney, J.R., et al., *Mechanical stimulation promotes osteogenic differentiation of human bone marrow stromal cells on 3-D partially demineralized bone scaffolds in vitro*. Calcified Tissue International, 2004. **74**(5): p. 458-468.
149. Meghji, S., P.A. Hill, and M. Harris, *Bone organ cultures*, in *Methods in bone biology*, T.R. Arnett and B. Henderson, Editors. 1998, Springer: London. p. 106-126.
150. David, V., et al., *Ex vivo bone formation in bovine trabecular bone cultured in a dynamic 3D bioreactor is enhanced by compressive mechanical strain*. Tissue Engineering, 2008. **14**(1): p. 117-126.
151. Fell, H.B. and E. Mellanby, *The effect of hypervitaminosis A on embryonic limb-bones cultivated in vitro*. Journal of Physiology, 1952. **116**(3): p. 320-349.

152. Pitsillides, A.A. and S.C.F. Rawlinson, *Using cell and organ culture models to analyze responses of bone cells to mechanical stimulation*, in *Bone research protocols*, M.H. Helfrich and S.H. Ralston, Editors. 2012, Springer: New York. p. 593-619.
153. Davies, C.M., et al., *Ex-vivo trabecular bone percolation system: development for evaluation of implant surfaces*. European Cells and Materials, 2001. **2**(Suppl 1): p. 63.
154. Defranoux, N.A., et al., *In silico modeling and simulation of bone biology: A proposal*. Journal of Bone and Mineral Research, 2005. **20**(7): p. 1079-84.
155. Colloca, M., et al., *A multiscale analytical approach for bone remodeling simulations: Linking scales from collagen to trabeculae*. Bone, 2014. **64**: p. 303-313.
156. Idhammad, A., A. Abdali, and N. Alaa, *Computational simulation of the bone remodeling using the finite element method: An elastic-damage theory for small displacements*. Theoretical Biology and Medical Modelling, 2013. **10**(1): p. 1-11.
157. Schulte, F.A., et al., *Local mechanical stimuli regulate bone formation and resorption in mice at the tissue level*. PloS one, 2013. **8**(4): p. e62172.
158. Geris, L., J. Vander Sloten, and H. Van Oosterwyck, *In silico biology of bone modelling and remodelling: Regeneration*. Philosophical Transactions of the Royal Society A: Mathematical, Physical and Engineering Sciences, 2009. **367**(1895): p. 2031-53.
159. Levchuk, A., et al., *The Clinical Biomechanics Award 2012—Presented by the European Society of Biomechanics: Large scale simulations of trabecular bone adaptation to loading and treatment*. Clinical Biomechanics, 2014. **29**(4): p. 355-62.
160. Birkhold, A.I., et al., *Mineralizing surface is the main target of mechanical stimulation independent of age: 3D dynamic in vivo morphometry*. Bone, 2014. **66**: p. 15-25.
161. Hambli, R., *Connecting mechanics and bone cell activities in the bone remodeling process: an integrated finite element modeling*. Frontiers in bioengineering and biotechnology, 2014. **2**(6): p. 1-12.
162. Kameo, Y. and T. Adachi, *Interstitial fluid flow in canaliculi as a mechanical stimulus for cancellous bone remodeling: in silico validation*. Biomechanics and Modeling in Mechanobiology, 2014. **13**(4): p. 851-60.
163. Yang, H., et al., *Characterization of cancellous and cortical bone strain in the in vivo mouse tibial loading model using microCT-based finite element analysis*. Bone, 2014. **66**: p. 131-9.
164. Webster, D. and R. Müller, *In silico models of bone remodeling from macro to nano—from organ to cell*. Wiley Interdisciplinary Reviews: Systems Biology and Medicine, 2011. **3**(2): p. 241-51.

2.3. Fracture and healing

This review is primarily concerned with general insights on the concept of tibial shaft fractures, and with a comprehensive description on the physiological fracture healing process. It is intended to attain a better understanding of the intramedullary nail stabilization method, namely in terms of its biomechanical benefits for improving fracture healing.

2.3.1. Tibia diaphyseal fractures








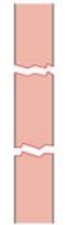

During daily activities, the tibial bone diaphysis withstands a complex pattern of stress and strain, which may be magnified during more extreme activities. During non-habitual scenarios such as trauma, the load imposed on the bone may exceed its inherent mechanical properties. When this load is above the yield point, deformation is no longer reversible and permanent damage is registered. When load passes the ultimate strength, structural discontinuity takes place with or without loss of alignment, *i.e.*, **bone fracture** occurs [1-4]. The bone fracture also relates to the speed at which the loads are applied, which can be expressed in terms of energy at failure [5] or, as suggested by another author [3], the work of fracture, which is the amount of work that has to be performed on a material to break. This behavior is a result of bone viscoelastic properties. The bone energy storing capacity is directly proportional to the speed of loading. Hence, when bone contacts with a high velocity object it will absorb a very high magnitude of energy before failure. At the point of failure, the stored energy will be release and cause osseous disruption and sometimes also surrounding tissues damage [4]. Hence, the severity of soft tissue and osseous injury are dependent on the energy absorbed by the limb at the time of the impact. However, most of the times the soft tissue in the body (such as the skin, fat, fascia, tendons, ligaments, joint capsules and muscles tissues) will reduce the impact suffered by the bones, by absorbing energy and propagation of stress waves in the body [3, 6].

Bone fractures can be generated by direct or indirect trauma. **Direct injuries** are caused by the generation of a fracture at the site of the impact. This may occur through tapping when a small force is acting over a small area (*e.g.* blow by a walking stick), crushing when a large force is applied over a large area (*e.g.* a car accident), or penetration when a large force will act on a small area (*e.g.* gunshot). When a low energy contact is involved, normally a transverse fracture with little or no comminution is generated. Direct high energy contact will lead to a greater amount of energy being transmitted to the bone, most probably resulting in a more severe fracture, also known as high energy fracture. Direct high energy contact will most probably result in comminuted fractures with additional soft tissue injury. **Indirect injuries** occur when a causative force is transmitted to one or more joints leading to a fracture at some distance from

the site of impact (*e.g.* slipping on a wet floor, downhill skiing or gymnastics). The biomechanical anisotropic behavior of long bones allows for different diaphyseal fracture patterns, as a result of load mode and orientation [1, 5, 7, 8]. Considering this, indirect fractures caused by traction generate a transverse fracture perpendicular to the force applied, bending results in transverse fracture with butterfly fragments, torsion may cause a spiral fracture, and simultaneous bending and torsion result in an oblique fracture [1, 4, 7]. Some examples of the average energy transmitted in different injury mechanism are: 136 Joules for fall from curb, between 407 and 678 Joules for skiing injury, 2712 J for high-velocity gunshot wound from a single missile, and 135582 J for a 32 Km/h bumper injury (assuming bumper strikes fixed target). There are also other types of fractures, such as the **fatigue fractures** as a result of repetitive stress from cyclic loading over a period of time (*e.g.* running), and **pathological fractures**, which occur at loads lower than the expected tolerance limit as a consequence of the normal integrity and strength of bone being compromised due to invasive disease or destructive process (*e.g.* neoplasm, necrosis, metabolic disease, osteoporosis and infection) [1, 4, 9-11].

It is of no interest for this thesis to discuss the different fracture classifications. So, throughout the thesis the AO classification for fractures categorization was adopted, since it is considered to be useful in delineating fracture morphology and it can also be used to evaluate its severity. The AO classification (the AO letters stand for Arbeitsgemeinschaft für Osteosynthesefragen meaning Association for the Study of Internal Fixation) for fractures of the tibial diaphysis is based on the classes presented in Table 2.3. The severity of the fracture increases from type A to C and from group 1 to 3. Regardless of the treatment and fixation system adopted, high-energy impact tibia fractures, which result in complex open fractures (*i.e.* osseous disruption in which a break in the skin and underlying soft tissue communicates directly with the fracture) with severe tissue damage, are the ones associated with higher complication rates and prolonged union times [1, 3, 6, 9, 12-15].

Table 2.3 - AO classification of diaphyseal long bones fractures. The fracture type could be A: Simple fractures without a third fragment; A1: spiral, A2: oblique ($\geq 30^\circ$), A3: transverse ($< 30^\circ$); B: Wedge fractures with a third or more fragments, but with contact between the fragments; B1: spiral wedge, B2: bending wedge, B3: fragment wedge; C: Complex fractures; C1: spiral, C2: segment, C3: irregular. The fracture group could be 1: Fractures in torsion; 2: Fracture in bending or 3: Fracture due to other mechanisms. Adapted from [3, 14, 16]

| Type | Group | | |
|---------------------|---|--|---|
| | 1 | 2 | 3 |
| A Simple |  Spiral |  Oblique |  Transverse |
| B Wedge |  Spiral |  Bending |  Multifragmentary |
| C Complex |  Spiral |  Segmental |  Irregular |

2.3.2. Stability of fixation and type of healing of the fracture

There are two basic histological types of bone healing which are greatly influenced by the mechanical stability at the fracture site: primary and secondary healing. The **direct** or **primary bone healing** is more uncommon. For this to occur, the fixation method has to guarantee **absolute stability** by securing bone fragments contact, hence guaranteeing none or very reduced interfragmentary movement, and subjecting the cells within the fracture to no strain. Through this healing path, the close proximity of the bone fragments surface will guarantee bridging by osteonal cutting cones formation and Haversian system (or osteon), similarly to the normal bone remodeling process. Hence, the BMU, will tunnel across the boundary between fragments and then bridge bone fragments with new bone tissue. The absence of mechanical stimulus at the fracture site will inhibit callus formation. Fractures treated with open reduction,

in which interfragmentary compression is achieved, such as with a lag crew or with a plate placed in compression mode, will heal by primary fracture healing. **Indirect or secondary bone healing** occurs in the vast majority of bone injuries. This healing type occurs as a consequence of **relative stability** provided by the fracture fixation technique, which confers some degree of interfragmentary motion at the fracture site. Fractures treated with more flexible stabilization methods such as plaster of Paris, braces, or through an operative treatment with external fixator, bridging plate or intramedullary nails, allow movement. The interfragmentary motion generated will stimulate callus formation and led to bone recovery through secondary fracture healing [17-21].

Bone possesses the intrinsic capacity for self-regeneration in response to injury [22]. Another unusual characteristic is its ability to restore its mechanical competence and structural morphology, contrarily to other tissues that heal through the formation of a poor quality connective tissue scar, such as the skin and muscle [10, 17]. However, bone healing is a complex event, characterized by a sequential series of overlapping phases, as a consequence of a coordinated interaction of multiple processes [17, 23, 24]. The current understating on bone's healing behavior followed a lengthy and controversial path that dates back to 1930, when Arthur Ham [25] first published a description of the early phases of healing based on histological analysis of fractured rabbit fibulae and ribs. Although there is no clear delineation of events during the course of secondary bone healing, for simplification purposes, a three-stage model of the conventionally healing process, as suggested by Claes *et al.* [20], was considered. This three phase process is initiated with the inflammation response and a hematoma formation, followed by the repair phase, which is characterized by the callus formation, the endochondral and intramembranous ossification and woven bone formation, which is subsequently remodeled to restore the lamellar bone structure at the final remodeling phase [24]. A schematic representation of the phase model is present in Table 2.4.

i) Hematoma/Inflammation phase

A fracture is typically associated with distortion of the marrow architecture and disruption of the local soft tissue integrity and normal vasculature, which leads to decrease perfusion of blood flood to the fracture site (also known as hypoperfusion). This, consequently, deprives the osteocytes from nutrition and causes local bone necrosis. The exposure of vascular endothelium and intravascular cells triggers the coagulation cascade, leading to hematoma formation within the fracture site during the first few hours and days. Polymorphonuclear neutrophils are activated and begin resorption of dead cells and bone debris at the fracture site.

Shortly after injury a local inflammatory response is initiated in response to the release of inflammatory mediators from the fracture hematoma. This response is characterized by an increase in blood flow, increase vascular permeability, macrophages and other inflammatory cells (*e.g.* granulocytes, lymphocytes, and monocytes) migration, combat infection, release a series of cytokines (*e.g.* IL-1 and IL-6) and growth factors (*e.g.* bone morphogenetic protein-2, -4, -5 and -6), and advance clotting into a fibrinous thrombus. Finally, the hematoma is invaded by fibroblast, which start laying down fibrin meshwork and these begins transforming the hematoma into granulation tissue. Overtime, granulation tissue is invaded by new capillaries network, which supply the fractured zone with cells and mediators. What occurs subsequently at the fracture site is largely dictated by the mechanical environment [19, 21, 23, 24, 26, 27].

ii) Repair phase

The repair phase, which partially overlaps with the inflammatory phase, is characterized by the formation of soft and hard callus as a reaction to interfragmentary movement, through the process of endochondral and intramembranous ossification. It has been increasingly recognized that both callus are formed simultaneously. Intramembranous bone formation starts at a region where the periosteum and vascularization are not disturbed by the trauma and where interfragmentary movements cause minimal tissue strain. In such cases, there is no cartilaginous tissue generation and mineralized bone matrix is formed directly through periosteal osteoblasts collagen synthetization. Hence, hard callus is formed in the absence of cartilaginous template through intramembranous bone formation. In tandem with this, there will also occur bone formation in the medullary region through endochondral ossification with soft callus, followed by hard callus formation. Higher tissue strain closer to the fracture line and insufficient blood supply reduces the amount of new vessel formation which lead to low oxygen tension. This will impair osteoblastic activity and allow chondrocyte differentiation and proliferation, triggering the formation of cartilaginous tissue. Further growth of periphery callus is driven by chondrocytes, with cartilaginous tissue formation. Soft callus size and cartilaginous tissue content increases up to its maximal volume with increasing interfragmentary movement. Upon bridging of the fracture by the cartilaginous callus wedges, the interfragmentary movement and tissue strain during fracture loading is markedly reduced, allowing for blood vessels to invade the calcified cartilage (process known as **angiogenesis**) and resulting in tissue hypervascularization. Hence, it is the gradual increase in callus volume, along with progressive tissue calcification during endochondral ossification that with time increases fractures stiffness and stability. Concomitantly with the formation of new blood vessels, chondrocytes become hypertrophic, release calcium and undergo apoptosis. The dead chondrocytes in the calcified

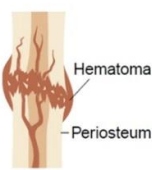
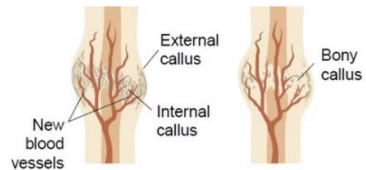

matrix, become invaded by new blood vessels which allow the recruitment of mesenchymal stem cells and monocytes. The latter differentiate into osteoclast-like cells, which absorb the calcified cartilage. The mesenchymal stem cells differentiate into osteoblasts which fill the resorption lacunae with immature or woven bone. This process of cartilaginous mass replacement into woven bone is known as endochondral ossification and continues until fracture fragments bridging occurs. Woven bone is laid down relatively fast - around 4 μm per day – and, depending on the type of fracture, the fixation method and the age of the patient, bony bridging may be achieved in around 16 weeks [17, 19-21, 23, 24, 27-29].

iii) Remodeling phase

Once union has occurred the immature bone has evolved into a fully-loadable structure. Woven bone resembles a spongy bone but with collagen fibers arranged in meshwork or felt-like pattern. In contrast to normal lamellar bone, the collagen fibers and apatite crystals in the matrix within the woven bone are haphazardly orientated. The apatite crystals are averagely smaller in size in woven bone and this tissue also presents a greater percentage of non-collagenous elements in the matrix than mature bone. The fibrils random orientation profoundly affects the mechanical properties of the immature bone since it has a more isotropic behavior, *i.e.*, its mechanical properties do not depend on the direction along which the forces are applied, and its strength and stiffness have lower values than the ones presented by the lamellar bone. Therefore, this newly formed bone is less able to withstand forces than the mature bone. Woven bone is also characterized by a higher osteocytes density. These are randomly and unevenly distributed within large spherical to plump spindle-shaped lacunae. The fracture remodeling process slowly replaces woven with lamellar bone over periods of months, by osteon formation, recovering its highly ordered micro-architecture and with this the normal mechanical characteristics. This final healing phase will also be characterized by reshaping of the diaphyseal bone through the resorption of the periosteal and medullar callus by the osteoclastic activity. Most inflammatory cytokine levels are reduced and the vascularization is restored to pre-fracture levels during the repair phase. The remodeling stage is completed when the bone recovers its original shape, structure and mechanical properties [2, 19-21, 27, 28, 30]. The precise amount of time required for this to occur at the level of the collagen-mineral architecture is not yet fully clarified, but it is assumed to take several years. In a study developed by Bacon *et al.* [10] the crystallographic texture of the hydroxyapatite in fractured sheep tibia was measured in detail throughout the healing process, using neutron diffraction. The results showed that the healing bone re-arrangement characterized by the transition from the

structurally randomly organized woven bone to the collagen fibers and external stress-oriented hexagonal hydroxyapatite crystals, is still not achieved even after 22 months of healing.

Table 2.4 - Schematic representation of the three-stage model for secondary bone healing. The information is arranged according to: (a) visual representation, (b) general description of the main events that characterize each stage, (c) duration of each stage and (d) stiffness alteration with the increase in the Young's modulus. Adapted from: [20, 31-33]

| | Hematoma/inflammation | Repair | Remodeling |
|-----|--|--|---|
| (a) |  |  |  |
| (b) | <ul style="list-style-type: none"> Local bone necrosis Hematoma formation Local inflammatory response Granulation tissue formation Capillaries network invasion | <ul style="list-style-type: none"> Endochondral ossification: cartilaginous tissue, soft callus, angiogenesis, hard callus Intramembranous ossification: mineralized bone matrix | <ul style="list-style-type: none"> Woven bone replaced by lamellar bone Periosteal and medullary callus absorption Inflammatory cytokines levels and vascularization reduced |
| (c) | Injury to 3 days | 4 days to months (around 16 weeks) | Months to years |
| (d) | 3 MPa | 10 – 5 000 MPa | ~ 20 000 MPa |

An optimization of the bone fracture repair process was proposed by Giannoudis *et al.* [17] through what he denominated the 'diamond concept' for the treatment of fractures. This model suggests the spatial and temporal coordinated interaction between four essential elements: the potent osteogenic cell populations, the cellular matrix that provides the natural scaffold for the cellular events and interactions, the signaling molecules (*e.g.* interleukins and fibroblast growing factor) that might induce a cascade of cellular events that initiate and control the healing process and the mechanical stability. These factors can be influenced by a variety of systemic and local aspects, such as trauma severity, type and location of the fracture, quality of fracture realignment, presence of comorbid diseases (*e.g.* rheumatoid arthritis, diabetes mellitus, obstructive pulmonary disease and systemic lupus erythematosus) or infections, drug therapies (*e.g.* anticoagulants, corticosteroids and antibiotics), patient age and gender, patient pre-injury mobility, patient psychological state, smoking and alcohol consumption. Any alteration of the healing cycle will affect the physiological sequence of fracture healing and will origin complications [17, 19, 20, 24, 34]. If all the other elements are prevailing in a favoring environment for physiological fracture healing to occur, the mechanical environment at the fracture site will be profoundly responsible for influencing the behavior of the recovery tissues and will determine the duration of the healing process. The fracture stabilization method adopted will greatly determine the mechanical environment at the fracture site. This will be

discussed in more detailed in sub-chapter 2.4., through the clarification the role of the intramedullary nail in the mechanical stimulus generation.

2.3.3. References

1. Johner, R., et al., *The point of view of the clinician: A prospective study of the mechanism of accidents and the morphology of tibial and fibular shaft fractures*. Injury, 2000. **31**(3): p. 45-93.
2. Morgan, E.F., G.L. Barnes, and T.A. Einhorn, *The bone organ system: Form and function*, in *Osteoporosis*, R. Marcus, et al., Editors. 2008, Elsevier: London, UK. p. 3-25.
3. Herman, I.P., *Physics of the human body*. 1st ed. Biological and medical physics, biomedical engineering, ed. E. Greenbaum 2007, Heidelberg, Germany: Springer.
4. Dutta, S.K. and D. Datta, *Biomechanics of fractures*, in *Applied Orthopaedic Biomechanics*, S.K. Dutta and D. Datta, Editors. 2008, BI Publications Pvt Ltd: New Delhi, India. p. 50-58.
5. Autefage, A., *The point of view of the veterinary surgeon: Bone and fracture*. Injury, 2000. **31**(3): p. 50-55.
6. French, B. and P. Tornetta, *High-energy tibial shaft fractures*. Orthopedic Clinics of North America, 2002. **33**(1): p. 211-230.
7. Schmitt, K.-U., et al., *Trauma biomechanics: An introduction to injury biomechanics*. 4th ed 2014, London, UK: Springer.
8. LeClere, L.E. and R.M. Lucas, *Tibial shaft fractures*, in *Orthopaedic rehabilitation of the athlete: Getting back in the game*, B. Reider, G. Davies, and M.T. Provencher, Editors. 2014, Elsevier Health Sciences: Philadelphia, USA. p. 1360-1384.
9. Egol, K., K.J. Koval, and J.D. Zuckerman, *Handbook of fractures*. 4th ed, ed. K. Egol, K.J. Koval, and J.D. Zuckerman 2012, Philadelphia, USA: Lippincott Williams & Wilkins.
10. Bacon, G.E. and A.E. Goodship, *The healing process for fractured tibia bones of sheep studied by neutron diffraction*. Journal of Applied Crystallography, 2007. **40**(2): p. 349-353.
11. Shore, S.W., et al., *Bone biomechanics*, in *Orthopaedic Biomechanics*, B.A. Winkelstein, Editor 2013, CRC Press: Florida, USA. p. 3-47.
12. Bauer, G.C., P. Edwards, and P.H. Widmark, *Shaft fractures of the tibia. Etiology of poor results in a consecutive series of 173 fractures*. Acta Chirurgica Scandinavica, 1962. **124**: p. 386-395.
13. Court-Brown, C.M. and J. McBirnie, *The epidemiology of tibial fractures*. Journal of Bone and Joint Surgery, British Volume, 1995. **77-B**(3): p. 417-421.
14. Grütter, R., et al., *The epidemiology of diaphyseal fractures of the tibia*. Injury, 2000. **31**(3): p. 64-94.
15. Claes, L., et al., *Monitoring and healing analysis of 100 tibial shaft fractures*. Langenbeck's Archives of Surgery, 2002. **387**(3): p. 146-152.
16. AO Foundation, *Müller AO classification of fractures - Long bones*, AOTrauma, Editor 2010, AO Foundation: Switzerland. p. 9.
17. Giannoudis, P.V., T.A. Einhorn, and D. Marsh, *Fracture healing: The diamond concept*. Injury, 2007. **38**(4): p. S3-S6.
18. Hak, D.J., et al., *The influence of fracture fixation biomechanics on fracture healing*. Orthopedics, 2010. **33**(10): p. 752-755.
19. Harwood, P.J., J.B. Newman, and A.L.R. Michael, *Mini-symposium: Basic science of trauma (ii) An update on fracture healing and non-union*. Orthopaedics and Trauma, 2010. **24**(1): p. 9-23.
20. Claes, L., S. Recknagel, and A. Ignatius, *Fracture healing under healthy and inflammatory conditions*. Nature Reviews Rheumatology, 2012. **8**(3): p. 133-143.

21. Morgan, E.F. and J. Lei, *Toward Clinical Application and Molecular Understanding of the Mechanobiology of Bone Healing*. Clinical Reviews in Bone and Mineral Metabolism, 2015. **13**(4): p. 256-265.
22. Dimitriou, R., et al., *Bone regeneration: current concepts and future directions*. BMC Medicine, 2011. **9**(66): p. 1-10.
23. Mckibbin, B., *The biology of fracture healing in long bones*. Journal of Bone and Joint Surgery [Br], 1978. **60-B**(2): p. 150162.
24. Schindeler, A., et al., *Bone remodeling during fracture repair: The cellular picture*. Seminars in Cell & Developmental Biology, 2008. **19**(5): p. 459-466.
25. Ham, A.W., *A histological study of the early phases of bone repair*. Journal of bone and joint surgery, American volume, 1930. **12**(4): p. 827-844.
26. *hypoperfusion*, in *Dorland's Illustrated Medical Dictionary* 2011, Elsevier Saunders: Philadelphia, USA. p. 904.
27. Kalfas, I.H., *Principles of bone healing*. Neurosurgical Focus, 2001. **10**(4): p. 1-4.
28. Péoc'h, M., *Normal histological architecture of tissue*, in *Biomechanics and Biomaterials in Orthopedics*, D.G. Poitout, Editor 2004, Springer-Verlag: London, UK. p. 189-191.
29. Dutta, S.K. and D. Datta, *Biomechanics of fracture healing*, in *Applied Orthopaedic Biomechanics*, S.K. Dutta and D. Datta, Editors. 2008, BI Publications Pvt Ltd: New Delhi, India. p. 59-69.
30. Dutta, S.K. and D. Datta, *Composition of musculoskeletal structures*, in *Applied Orthopaedic Biomechanics*, S.K. Dutta and D. Datta, Editors. 2008, BI Publications Pvt Ltd: New Delhi, India. p. 29-37.
31. Baroth, S., *Developement of injectable calcium phosphate ceramics for bone repair*, in *School of biology and health* 2009, Nantes University: Nantes, France. p. 8.
32. Mavčič, B. and V. Antolič, *Optimal mechanical environment of the healing bone fracture/osteotomy*. International Orthopaedics, 2012. **36**(4): p. 689-695.
33. Bailón-Plaza, A. and M.C.H. van der Meulen, *Beneficial effects of moderate, early loading and adverse effects of delayed or excessive loading on bone healing*. Journal of Biomechanics, 2003. **36**(8): p. 1069-1077.
34. Felicíssimo, P., et al., *Aotrauma course - Basic principles of fracture management*, 2014, AOTrauma Europe: Tomar, Portugal.

2.4. Intramedullary nailing biomechanical concept evolution:

Understand the past to predict the future

Bone is a remarkable composite tissue with outstanding self-repair capability, recovering its form without permanent scar [1]. From all the long bone stabilization techniques invented, intramedullary nailing has evolved in such a successful manner that it has become one of the most recommended procedures among physicians. In this sub-chapter a biomechanical perspective through a brief review on the evolution of the intramedullary nailing concept by highlighting the important turning points in its history, is provided (see Figure 2.5). Through the understanding of the evolution taken by this stabilization methodology, and considering the latest biomechanical developments, it will be possible to infer on the required research paths for further biological and mechanical implant optimization. Although intramedullary nailing is generally associated with good clinical outcomes, there is still room to enhance fracture healing quality and recovery time, where the adequate knowledge framework for subsequent research efforts in this field will be established in this sub-chapter.

2.4.1. Stabilization based on intuition

The earliest records of human attempts to deal with fracture problems come from ancient prehistoric men [2, 3]. But, it was not until the 16th century that the anthropologist Bernardino de Sahagun reported, for the first time, the use of intramedullary fixation methods by the Aztec population [4, 5]. For fractures and dislocations, the Aztecs physicians used traction, counter-traction, manipulation and immobilization techniques. In non-union cases, they scraped the bone and implanted a resinous wood stick in the medullary canal to stabilize it [6]. According to Sven Young [7] the resinous wood could have functioned as an anti-infectious after the peg was inserted.

Although the foundations for injury treatment were already established by Hippocrates and other Greek physicians, and the marrow canal was considered as a logic place for the implantation of a bone stabilizer, only decades later was this technique applied with considerable success. Yet, there was still a great need for a more profound understanding of the underlying mechanical principles of the complex bone healing process [2, 3, 8].

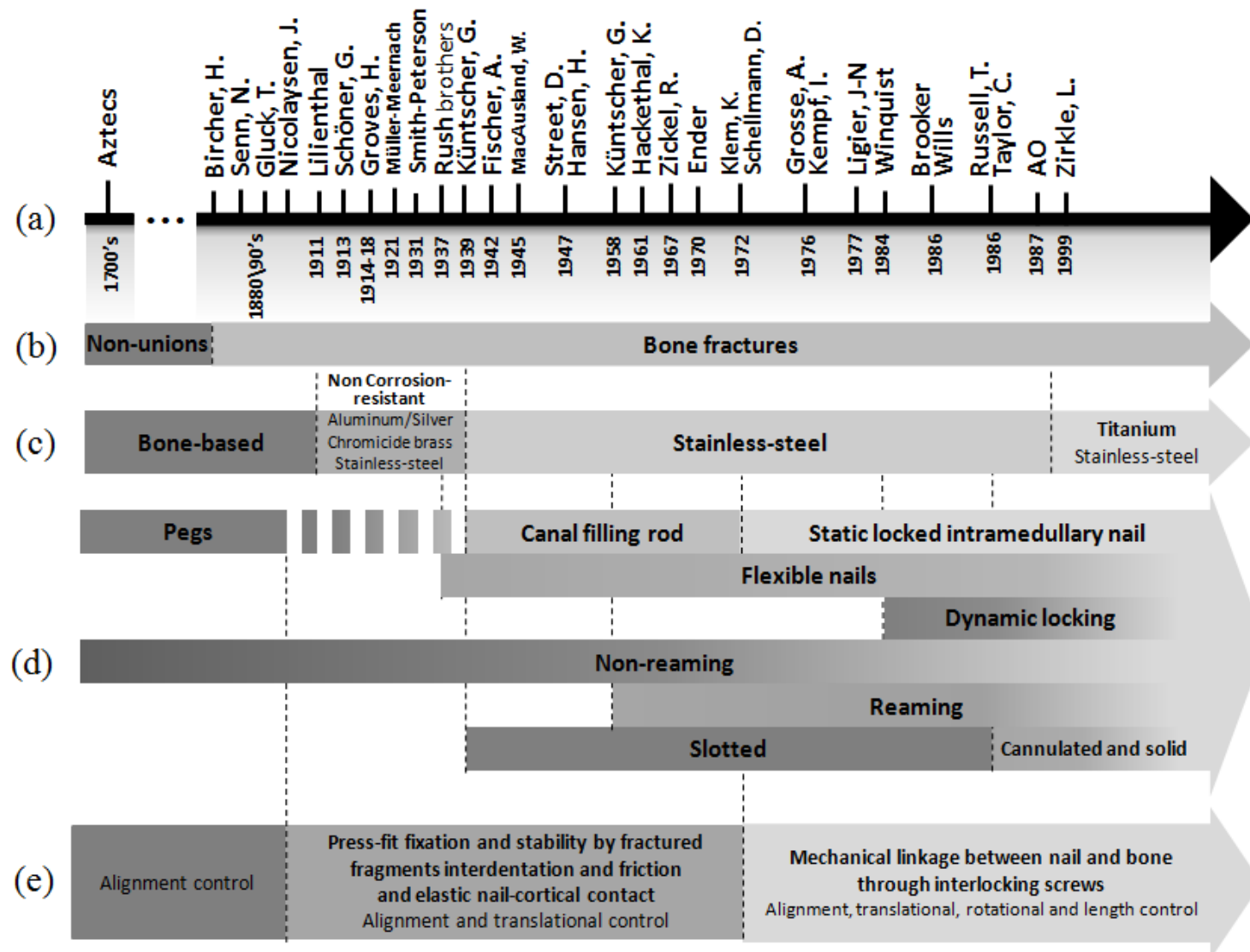


Figure 2.5 - Schematic chronological representation of the turning points in the evolution of the intramedullary fixation, from the 16th century and up to the 20th century. Information is arranged according to: (a) Timeline, (b) Application sites, (c) Materials used, (d) Biomechanical concept

2.4.2. The first pioneers in intramedullary nailing

During the 19th century there was an increased interest in the potentialities of intramedullary fixation for fracture treatment. At that time, most of the work with intramedullary nailing appeared to revolve around the use of ivory pegs developed towards patients with non-unions and not bone fractures. Oppositely to extraneous bodies made of metal, such as bullets, which became encapsulated with fibrous tissue, early implants made of ivory and human bone were resorbed over time [5, 9, 10]. Although in Europe there was preference for ivory material, studies in United States Høglund [11] reported experiments with autologous bone [4]. The controversy behind autologous intramedullary splints was based on the danger that the creation of a new wound represented for patients [12].

The 19th century witnessed the introduction of the foundations of modern medicine with the invention of general anesthesia (ether and chloroform), administrated for the first time by William Morton in 1846, the development of aseptic conditions marked by the pioneer work of Joseph Lister with carbolic acid spray around 1865, and also the discovery of X-ray imaging by Wilhelm Röntgen in 1895. The latter, allowed fracture diagnosis, monitoring fracture healing, and detection of any complications. These landmarks created the conditions for operative treatment of fractures [4, 5, 13, 14].

Soon after, ivory pins were used for the stabilization of fresh fractures. It was Bircher, in 1886 [15], who for the first time recommended this application when reduction could not be held by traction or plaster [5, 7]. An interesting but at the same time not always referenced work was developed in the 1890's by a German surgeon pioneer in joint replacement, Themistocles Gluck. He developed intramedullary ivory cylinders that were placed in patients with long bone fractures. This technique allowed bone alignment and fixed the fracture in place while it healed. It was also claimed that Gluck ivory cylinders could have been forerunners of Küntscher nail [13, 16]. During the same decade, Nicholas Senn [17] also experimented with intramedullary fixation technique by placing cow bone perforated cylinders in the medullary canal.

Nicolaysen of Norway is considered in literature [4, 5] as being responsible for introducing the "intramedullary nail" concept. He was the first to describe the biomechanical principles of this technique in the treatment of proximal femur fracture [18]. He also highlighted the need to increase the nail's length for a greater biomechanical advantage and to provide protection to almost the entire bone. Intramedullary nails were more frequently used to stabilize pertrochanteric fracture (fractures involving the proximal femur where the fracture line passes through both the lesser and greater trochanters) [14, 19].

The subsequent logical idea was to provide additional stability with static locking through nail/bone interlocking in the proximal region of the bone and in the distal opposite end. The first experiments with interlocking intramedullary nail were developed by Gluck in 1881 [20]. This device was designed to be applied in patients with pseudarthroses. After tissue resection a hollow ivory nail was inserted in the intramedullary canal and locked by transversely passing ivory interlocking pins in the nail extremity holes [4, 5]. Although some researchers tested this approach the interlocking intramedullary nail only became a current medical procedure years later with Küntscher nail designs.

The fast body absorption of ivory-based materials and, in some cases, the inability of the implant to achieve the appropriate length, made these fixators incapable of providing the stability required for fractures healing [21]. Hence, during the beginning of the 20th century there seemed to begin a search for finding suitable materials with different mechanical properties. Records show that in 1911, Dr. Lilienthal from New York, implanted an aluminum intramedullary splint in a femur shaft fracture. A couple of years later, in 1913, Schöner used ductile silver pins in lower arm fractures [22]. In 1921 Oskar Müller-Meernach, from Germany, tested stainless steel and chromic acid brass with a X-shaped cross-section intramedullary nails [3, 5, 7, 23]. A referenced work in this field was developed by Hey Groves of England, during World War I. According to literature he was the first to advocate the use of metallic medullary nailing. His work-focus was on the application of steel intramedullary nails for the treatment of gunshot wounds. Since the nail was implanted through retrograde procedure with fracture exposure, the risk of infection greatly increased. The high infection risk of the open technique implantation, the fact that steel cause tissue reaction and consequently implant loosening and the general belief that this method could not provide sufficiently rigidity without additional external splintage led to the unacceptance of these intramedullary nails. Hey Groves also tested several nail designs and claimed that the solid nails were able to give the maximum strength [4, 7, 24-26]. Another attempt to use metal as a standard intramedullary nail material was present in the work developed by Smith-Petersen, in 1931 [27] where stainless steel nails were used for the treatment of femoral neck fractures. The Smith-Petersen nail was a three flutes design with a star-shaped cross section to obtain rotational stability in the bone-implant construct. Despite the innovative nail design concept, the steel used by Smith-Petersen showed corrosion problems and bone inflammatory reactions. Corrosion tends to occurs due to gradual degradation of metallic implants by electrochemical reaction which arises in the human body's electrolytic environment. Corrosion will change the surface of the metal, weaken the implant, and lead to the release of ions into the body fluids. The stabilizer developed by Smith-Petersen was also

available in vitallium, a cobalt-based alloy. At the time vitallium seem to cause the least body reaction than any other metal used than. However, it showed lower strength than stainless steel, the amount presented was capable of immobilizing bone fragments, if there was additional proper external support. The use of stainless steel as an implantable material, only started with the introduction of 18-8 stainless steel which had far-superior corrosion resistance to any other metal type at that time [3-5, 28-33]. The application of the intramedullary nail concept to other bone fractures such as the fibula and the calcaneus was also evaluated [34].

All the fracture fixation designs and materials evaluated until the beginning of the 20th century were not capable of transforming the intramedullary nailing technique in a recognized medical procedure. The reduced knowledge in the complex biomechanics of bone healing, and the lack of precise data concerning the loading of bone and implants during fracture treatment, lead to the development of models that presented failures [35]. This limited their wide acceptance in the orthopedic market. In return, the learning process provided the foundations for the revolutionary discoveries that emerged in the following decades.

2.4.3. From concept to clinical widespread acceptance

Although there is a considerable controversy in awarding a particular researcher's role along the history of intramedullary nailing evolution, it is of general agreement that Gerhard Küntscher - a German physician known as the "founder of modern intramedullary nail" – had a significant impact on the designs and surgical techniques associated with intramedullary nailing [36].

During the World War II, Küntscher presented his pioneer concept which he named "marrow nailing" through a V-shaped (triangular in cross-section) corrosion-resistant V2A stainless steel intramedullary nail [37, 38]. At the end of the 40's decade, in collaboration with Pohl, an instrument maker and metallurgist, Küntscher developed a dorsal slotted clover-leaf cross-sectional intramedullary nail design (see Figure 2.6) [3, 4, 38, 39]. Both nails were developed for the treatment of femoral fractures and were inserted through an antegrade method at a fracture-site distant location which guaranteed no disturbance to the injured region. The nail implantation was possible with the use a head worn fluoroscopy technique. Both nails also had a hole near the end for ease of removal [40, 41].

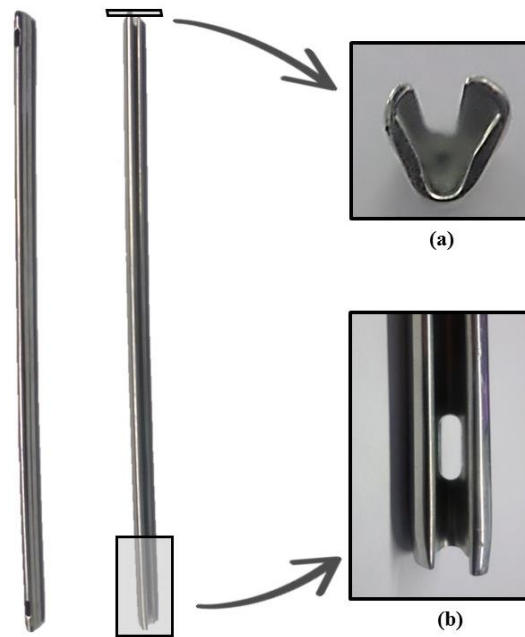


Figure 2.6 - Diagram showing Küntscher femoral nail (from two different views) with the clover-leaf cross-section (a) and the longitudinal slot (b)

Küntschner's intramedullary nails presented a slotted configuration, meaning they had a longitudinal cut along the entire length of the shaft. The radial compression of driving the large diameter nail into the tight medullary canal led to the reduction of the nail outer diameter and the squeeze of the slot slightly closed, *i.e.* nails were inserted press-fitted into the medullary canal. This concept of a nail elastically compressed to fit the medullary canal avoids any undesirable mechanical stress on the bone during nail implantation. This is relevant because bone is a hard and brittle material, meaning that rupture occurs for low deformations [42]. The recoil of the nail to its original shape created nail-bone contact, where friction and an elastic union between the implant and the inner medullary cavity were responsible for limiting bone motion in relation to the nail. The resistance to rotation and axial motion at the fracture site was guaranteed by interdigitating of the fracture fragments and endosteal contact with the nail above and below the fracture site. Küntscher compared the intramedullary nail-in-bone mechanical stability concept with the elastic and frictional forces that piece of wood would exert in a carpenter's nail when it is driven into it [7, 43-45]. The nail cross section geometry plays a crucial role in the nail-bone contact mechanics. Nails with a sharp corner, such as the V-shaped design, or fluted edges, as in the clover-leaf design, resist torsional forces to a greater degree than smooth-walled intramedullary nails. With the V-shaped design the nail-bone contact area was limited to the lines along the three edges of the implant which would register the highest values of mechanical stress and strain (deformation per unit length) [28, 42]. Also as claimed by Stedtfeld [45] the high cyclic strain produced on that region would have led to bone resorption

and consequently nails loosening overtime. The Küntscher V-shaped nail was easy to construct but the clover-leaf nail design provided greater strength and achieved fixation in the isthmus [38]. The latest design guaranteed a resistance to shortening or rotation of the bone around the nail whilst bearing weight. Such nail placement facilitated load and stress transfer through both the fractured bone and the nail itself and the elastic deformation of the nail occurs in firm contact with the hard bone of the surrounding cortex. Also the V-shaped nail only allowed for compression in one plane and the clover-leaf nail design could be compressed from all sides [7, 41, 45]. The removal of Küntscher nail was also not an easy task. The infra-isthmal bone ingrowth of callus into the slot prevented the passage of the distal part of the nail through the narrow isthmal zone [45].

The alternative to the Küntscher first nail design, was developed by the Rush brothers, in 1937. These were long and thin stainless steel elastic nails, pre-bent to the appropriate configuration before insertion, which provided a three-point fixation to counteract the tendency of axial displacement at the fracture site. The performance of the nail was limited by the elastic mechanical behavior of stainless steel. Rotational stability was poor and too high nail loads led to secondary bending, nail back-out at the entrance site, nail penetration on the cancellous bone, nail intra-articular perfusion and fracture mal-union [3, 4, 7, 45, 46]. Improvement on this nail design was registered in the following years, for example through the “bundle nailing” developed by Hackethal [47] and the Ender nails [39, 48, 49] (see Figure 2.7b and 2.7c). Despite its lower performance when compared to Küntscher nail designs, the Rush brothers intramedullary nailing concept was an important landmark in the history of intramedullary fixation, since it greatly influenced the biomechanical principles behind the flexible intramedullary nailing (also known as elastic stable intramedullary nailing), introduced by Jean-Noël Ligier, Jean-Paul Métaizeau and their colleagues in 1977 and used now-a-days for pediatric fractures [50, 51].



Figure 2.7 - Image exemplifying the overall structure of a flexible reamer (a) with the distal drill bit, a Rush nail (b) with a proximal hook end that prevents rotation and stabilizes the fracture and an Ender's nail (c)

Despite its limitations, the slotted clover-leaf nail design and implantation technique had a good acceptance in Europe. The advantages of this method were: relative simplicity, no need for external fixation, the joints were kept mobile, allowed early ambulation (patients were out of bed in a matter of days rather than months) and the overall good results obtained when compared to the frequent intervention of traction (or “extension” as it was often called) followed by casting [7, 48, 52, 53]. In the United States, there was initial skepticism around Küntscher innovative intramedullary nailing technique - American POWs with these surgical implants were thought to be subject to some sort of German torture device. But public opinion ended up improving, triggered by the description of this technique in a Time Magazine article entitled “Amazing Thighbone” in March 12, 1945 [54]. The fabrication and implantation of the first American Küntscher nailing, made of tantalum, was done by Williams MacAusland [3, 48]. By 1947, Dana Street and Harvey Hansen [52] had developed the solid diamond shaped Hansen-Street nails and the cloverleaf pins. The solid diamond-shaped nail was inserted via retrograde method. With this method the nail was introduced into the proximal fragment from the fracture site and brought out at one end of the bone. After reduction, the nail is driven across the fracture site and into the distal fragment. During this decade, many clinicians adopted an open nailing

technique to avoid the side effects caused by early radiological techniques, such as head worn fluoroscopy. Albeit there is no control on the point of exit of the nail in the retrograde method and there is a higher incidence of infection and non-union cases, the compressed fit solid diamond shaped Hansen-Street nails provide a good resistance to fracture rotation and also great bending resistance if it was inserted with the widest diameter (or major axis) resisting the load [3, 4, 28]. The development of the X-ray image intensifier in 1955, created conditions to develop interlocking nail designs and allowed re-adoption of less invasive and closed nailing techniques without excessive radiation exposure, eliminating exposure of the fracture site, minimizing soft tissue trauma and maintaining periosteal vascular supply and reduced risk of infection. In the closed method, the medullary cavity is entered through a small opening, distant from the fracture site at the end of the bone [4, 5, 7, 28, 43, 48].

i) Reaming or non-reaming

The 50's were also marked by the introduction of intramedullary reamers. There are reports of experiments with the intramedullary canal reaming technique by Fischer in 1942 [55], but it was Küntscher [56], with the development of guided flexible reamers that allowed for this clinical procedure to have widespread acceptance within the orthopedic community. The reaming procedure consisted in removing circumferential layers from the long bones endosteal surface which results in the removal of bone irregularities and enlargement of the canal diameter. After medullary reaming, nails wide enough to occupy the entire cross section of the medullary canal were inserted and spanned the entire length of the long bone. Reaming was an important procedure because it enlarged the medullary canal to an adequate working length. In addition, this technique allowed increasing the size of the medullary canal and inserting a nail with a larger diameter. This provided greater stability and replaced the function of the bone during its initial recovery phase. According to Küntscher "callus is extremely sensitive to mechanical stresses and can only develop when complete mechanical rest prevails" [56]. After the reaming technique was established, Küntscher clover-leaf femoral nails enlarged their diameter to values between 16 and 18 mm. Stability and length were achieved by the contact between the major proximal and distal bone fragments. Hence, the mechanical superiority of larger nails after reaming by increasing the contact area between the nail and the medullary wall; according to Smith *et al.* [57] 1 mm reaming can increase the contact area by 38% - increase the nail rigidity in bending and torsion and enhance the overall bone-implant system stability. This fixation technique was excellent for transverse, short and oblique mid-shaft fractures but it required a proper bone reduction during the reaming procedure since eccentric reaming causes mal-reduction of the fracture [28, 29, 38, 56, 58, 59]. Although Küntscher original reamers' design has suffered a

considerable upgrade along the years (*e.g.* reamer head design), the fundamental concept has been maintained until now (see Figure 2.7) [39].

Now-a-days there is still a controversy on the benefits of the reaming technique. One of the most polemic characteristics of this technique is the damage to the endosteal blood supply caused by the reaming process. In these circumstances the blood supply to the bone becomes centripetal, where the bone vascularizes rapidly from the periosteal surface to the marrow cavity [60]. According to Dagrenat and Kempf [51] the endosteal vascularization may take around 3 weeks to be restored when the nail is implanted without reaming, and approximately 6 weeks when reaming is adopted. In a fractured sheep tibia model study developed by Schennitsch *et al.* [61] it was demonstrated that blood flow within fracture callus of callus and early strength and stiffness of union are similar following intramedullary nailing with or without reaming. But this may not hold true if cortical vascularity has been significantly disturbed by the initial injury. In these cases, non-reamed intramedullary nailing lowers the risk of an insufficient blood supply for secondary bone healing which may be of particular relevance for severe open fractures where it is already significantly compromised. An advantage of the non-reamed intramedullary nailing procedure is it's reduce surgical time when compared to the reaming intramedullary nailing. The non-reamed intramedullary nailing is also associated with less blood loss and reduced heat production. Consequently, thermal bone necrosis is reduced by up to 70%, since above 56 °C bony enzymes such as alkaline phosphatase begins to denature, which causes local necrosis and jeopardizes the healing process. The use of reamed intramedullary nailing for the treatment of open fractures is associated with a potential risk of deep infection caused by the spread of bacteria from the contaminated wound along the medullary canal. Favoring the use of reaming with interlocked nails is the superior biomechanical stability provided by this technique under load-bearing conditions which reduces the amount of undesirable high stresses at the fracture site. Recent clinical studies have shown that non-reamed intramedullary nailing tends to prolong the healing time comparatively to reamed nailing. This may be associated with the flexible fixation behavior of the bone-implant complex under shear loads, caused by the movement of the intramedullary nailing within the medullary canal [3, 28, 43, 44, 57, 62-64]. According to the study developed by Forster *et al.* [65], the reaming procedure reduces the time of union by around 7 weeks and is associated with a lower rate of non-union (from 1 to 7%). Nail sliding during the implantation is affected by the long bones medullary wall irregularities which can be smoothed through reaming procedure, hence reducing the minimal force required to insert the nail [3, 28]. Another positive effect of reaming is the deposition of medullary contents and osteo-inductive factors at the fracture site which acts like an autologous bone

graft. A study developed by Hoegel *et al.* [66] have demonstrated that viable bone cells can be obtained from intramedullary reaming [38, 57].

It is important to notice that the nailing event by itself already affects the endosteal vasculature as a consequence of the forcible introduction of a foreign body [67]. In the same way, the reaming process will lead to an increase of the intramedullary canal compartmental pressure which forces debris into the venous circulation [38]. This intra-medullary canal pressure may lead to systemic embolization of the medullary cavity contents, particularly fat, into the venous system which may cause the obstruction of nutritive arteries and transcortical blood vessels and in more severe cases could be lethal [67-69]. This nailing limitation had already been recognized by Küntscher, who at the time advised delay and caution during surgery [56]. Predecessor experiments in reducing this nail-adverse effect by the removal of the medullary content through the combination of suction and irrigation were developed by Danckwardt-Lillieström *et al.* [70]. But it took several years until this strategy was enhanced it with the invention of the Reamer/Irrigator/Aspirator (RIA) [71] by James Green [72, 73] and assigned by Synthes Inc. (West Chester, Pennsylvania, USA) in 2001 [67]. The RIA system has other uses than merely removal of bone marrow and reaming debris from the medullary cavity such as: clearance of the medullary canal from infected bone tissue, effectively sizing the medullary canal for intramedullary nail implantation and harvest finely morselized autogenous bone and bone marrow for posterior used as an intraoperative source of autologous, osteogenic material [71, 74-76].

Although experienced orthopedic surgeons should be knowledgeable of both the reamed and un-reamed nailing techniques, the decision of which technique to apply is entirely of the surgeon responsibility. During the last ten years, developed countries have shown an increased preference for the use of reamed nailing, saving the un-reamed procedure for open fractures or cases where there is a specific contraindication. There is a trend with reamed nailing involving limited reaming or “ream to fit” techniques where the reamer size is a millimeter or two larger than the size of the selected nail and reamer increments of 0.5 mm are applied until the desired diameter is achieved. This “limited reaming” strategy seems to balance the benefits and detriments of reaming by reducing the amount of bone removal (*i.e.* avoiding the decrease in cortical wall width in the detriment of bone strength) and endosteal blood supply damage to the point that it allows for the use of a nail diameter that is large enough for a proper healing process to occurs and for the integrity and well-function of the nail (*e.g.* no nail breaking) to maintain until the bone as healed [3, 4, 28, 35, 39, 59, 77].

ii) Locked intramedullary nails

Although intramedullary nailing through direct nail-bone contact stabilization along the reamed medullary canal was considered a very successful long bone fracture fixation method, it was not suitable for injuries involving greater obliquity, comminution or bone loss and fractures in the proximal and distal region [38, 43]. In those cases, the bone resistance to axial load was lost and limb shortening and implant protrusion were observed [43]. This limitation required a development of a more stable fixation through the invention of interlocking screws. Although registers showed that this strategy was introduced in 1953 by Modny and Bambara [78], the nail interlocking concept only was spread during the 70's. This invention, accompanied by decreased enthusiasm in compression plating, was a new breakthrough for intramedullary nailing indications. Following the steps of Gerhard Küntscher, that had already been working on the idea of interlocking nails, in 1968, and which he called 'detention' nailing, Klaus Klem and Dieter Schellmann, devised implants based on conventional slotted clover-leaf Küntscher nail with proximal and distal double medio-lateral holes for bone screws and called their method 'interlocking nailing'. Klem and Schellmann published their paper on interlocking nailing after Küntscher's death, in 1972 [3, 5, 16].

Interlocked intramedullary nails marked the beginning of the second generation nailing and changed concepts of fracture stabilization from press-fit contact with the medullary wall and interdentation of bone fragments to mechanical linkage between nail and bone through interlocking screws [29, 45]. Static locking of intramedullary nail by employing screws both proximally and distally to the fracture sites is able to prevent relative rotation or sliding movements between the two bone extremities. This approach is also capable to maintain length, physiological alignment of the system, and bone reduction position which provides good stability for soft tissue and bone healing. The distance between the nearest locking screw from the top and the bottom position where the nail engages the bone determines the intramedullary nail working length and reflects the length of nail carrying the majority of the load across the fracture site. The resistance to bending and torsion is a function of the nail working length. Here the bending stiffness of a nail is inversely proportional to the square of its working length, while the torsional stiffness is inversely proportional to its working length. Hence, shorter working length guarantees a stronger fixation and for a longer working length it is expected that a greater amount of movement occurs at the fracture site when limb load is applied [28, 59]. Another advantage is the fact that the locking screws do not interfere with the vascularization of the fracture region and will allow patients to have a more reasonable post-operative recovery by helping to create the adequate environment to treat the fracture and to permit full function,

mainly earlier patient mobilization in order to allow accelerating the patient's return to previous mobility [46, 47, 79]. The introduction of intramedullary nailing static locking, created a renewed interest in this fixation method, allowed to a wide spectrum of indications for nailing, and triggered the development of a variety of new designs and implantation procedures besides the already mentioned Klemm-Schellmann nail. We highlight the partially slotted Grosse-Kempf nail developed in 1976 by Arsene Grosse and Ivan Kempf in France, which has a non-slotted a configuration in a proximal zone to prevent nail opening problems and for proximal locking, and an image mounted device for distal targeting and interlocking. In 1986, the slotted Brooker-Wills interlocking nail with proximal oblique screw and expanding distal condylar blades; a year later the slotted AO proximal keystone configuration nail; and a few years later, in 1992, Toney Russell and Charlie Taylor developed the slotted Russell-Taylor nail. All these nail designs are obliquely fixed with screws, with the exception of the AO nail which uses two transverse screws proximally [3, 4, 29, 43, 48, 50, 53, 80].

iii) Nail bending design

Another controversial subject is the nail bending design. Intramedullary nails started by having straight designs, as in the case of the original clover-leaf slotted nail. Küntscher devised the implantation of the non-curved nail straight into the upper part of the bone to avoid posterior cortex puncture [81]. Seifeldin and Khedr [82] also state that the amount of curvature could be adjusted by the surgeon himself before definitely counter-sinking the nail into the cavity. However, when implanted Küntscher intramedullary nails were examined; longitudinal 3- or 4-point jamming was encountered in the sagittal plane due to the difference in curvature between the nail and the femur [51]. The implantation of the intramedullary nail differs between long bones. The tibial nail, differently from the femoral one, should not be driven into the bone from the proximal side along the prolongation of the axis of the medullary canal since this approach demands a penetration in the tibial intercondylar area. Hence, there is risk to damage the medial meniscus, the lateral tibial plateau and the ligamentum transversum [35, 81]. Also, during the following years there was a need to correlate the nail design in a manner that it respected the natural anatomical structure of the bone and also facilitated the implantation procedure [35, 82]. Herzog [83] modified the nail by adding an angle formed near the proximal end of the nail to allow a lower insertion point above the tibial tubercle in the bone anterior site. This proximal bending shape characterized the second generation Küntscher tibial nail shape and it was named "Herzog bending". However, the nail in this position irritated the patellar tendon if a protruding nail was left [35, 81, 82]. In the late 80's the AO modified the nail bending shape where there was a distalization of the bending point to lengthen the cortical contact of the nail along the

upper anterior cortex of the tibia and also to facilitate the nail insertion into the cavity. This alteration was named the “AO bending”. Also, in some rigid tibial nails a minor distal anterior bending was added to facilitate the sliding of the implant into the cavity [82].

iv) From slotted to non-slotted nails

Since the 1980's and up to the beginning of the 21st century, there was a replacement of the slotted nail designs by non-slotted ones [4, 82]. A study based on slotted Grosse-Kempf nail developed by Gimeno [49] demonstrated that the transition zone between the non-slotted and slotted part - characterized by an alteration of the material thickness – results in stress concentration. The authors also reported breakage to occur due to high load bearing on the stress concentration zone of the nail [79]. Gimeno and his co-workers concluded that the slotted Grosse-Kempf nail was most affected by torsional forces and that compression and flexion were well tolerated by the nail. In addition, according to Stedtfeld [45] reduced bending resistance of thinner walls slotted intramedullary nails may lead to their deformation during implantation in the presence of stronger bending loads caused by curvature difference between the nail and the medullary cavity. Gimeno *et al.* [49] full weight bearing until fracture consolidation since torsional forces tend to increase on walking and are maximal when the unaffected leg is off the ground. For a better understanding of the impact of the slot in the torsional behavior of intramedullary nails, if a cylindrical intramedullary nail is considered, the slot will lead to a reduction on the torsional load carrying capacity by a factor of $\frac{t}{3r}$, where t is the wall thickness and r the mean radius with respect to the closed structure [44]. Also, although the first Küntscher nail designs were claimed to have a good resistance to bending in any direction [59], by reducing the wall-width in the slotted intramedullary nail the resistance to bending in the frontal or sagittal plane -depending on the position where the slot was present – would also decrease [45]. Considering all these limitations, a design improvement required the use of a uniform thickness and elimination of the slotted part to increase the nail overall stability and particularly to increase the resistance to torsional forces. Also, according to Dagrenat and Kempf [51], - albeit intramedullary nail suffered a reduction in thickness from 1.7 mm to 1.35 mm, with the transition from the slotted to the non-slotted intramedullary nails the bending stiffness still suffered an increase of 25%, in the transition. An advantage favoring the used of non-slotted cannulated nails was the possibility to a guide wire, inserted along the longitudinal cannulated nail and simplify the insertion and centering operations of the nail inside the medullary canal [48, 84]. The slotted nail model also allowed the use of antero-posterior locking screw at tibial nail [45]. Besides all the advantages on the non-slotted configuration, at the time, there seemed to be a certain skepticism based on previous undesirable bone fragmentation cases from hoop

stresses during nail insertion. In 1986, Russel and Taylor were the first to present a non-slotted (or closed section) large diameter femoral nail. The introduction of this nail was only possible due to use of the gun-drilling computerized machining technique which allowed for the construction of a nail with a lower bending stiffness than the intact femur and with a good rotational stability. The Russel-Taylor nail required no reaming procedure prior to its implantation and was used for virtually the same indications as reamed locking nails. Following the Russel-Taylor nail satisfactory results, the locked intramedullary nails design concept evolved from the non-slotted configuration to cannulated and solid nail design. In the following years, a few new nail designs based on this latest concept emerged, such as the Derby nail. The Derby nail is fixed proximally using four distally facing pins which lock into the great trochanter of the femur. These pins are attached to the collar that can be threaded over the outside of the intramedullary nail head [29, 39, 80].

2.4.4. Current nails concepts in developed countries

When fractures are treated with interlocked intramedullary nails, the fixation system provides relative stability, meaning that there is interfragmentary motion stimulus which induces callus formation. This process is also known as secondary or indirect fracture healing. The use of larger diameter nails, as a consequence of reaming, led to the appearance of a high stress shielding phenomenon which caused non-union and delayed union cases. The intramedullary nail stability system is based on the stress shielding effect of the implant. When two or more components with different Young's modulus constitute a mechanical system, the phenomena of loads, stresses, and strains redistributions will occur. The body with the higher elastic modulus will bear more loads and the component with a lower Young's modulus will bear less load which consequently will be translated in lower stress and strain [85]. Larger diameter nails are stiffer than smaller diameter ones with the same cross-sectional shape, which represents an increase in stress shielding, greatly influencing bone healing stress stimulation. If a solid circular nail is considered, the bending rigidity is proportional to the third power, and the torsional rigidity is proportional to the fourth power of the nail diameter. Considering now the use of the larger diameter nails with high rigid properties and which would be firmly attached to the bone fragments through the interlocking screws, such situation would cause the implants to carry the majority of the load, shielding the bone from the stress and strains. Hence, the use of a rigid fixation method with higher elastic modulus than the surrounding structures will impose a certain stress-shielding effect on the bone and on the interfragmentary healing tissues. The appearance of the high stress-shielding effects had led static locking to be perceived as a potential problem and to cause non-unions. Hence, static interlocking nail has started to be

considered as a load-bearing device instead of a load-sharing device [38, 41, 86]. In an attempt to reduce the stress-shielding effect and promote healing, Grosse and Kempf emphasized nail 'dynamization'. Conversion to dynamic locking involves the removal or the absence of a set of screws, performed only at one extremity of the bone, - proximal or distal depending on the location of the fracture and always on the long fragment. The fixed end will be responsible for ensuring the rotational stability of the fracture while the opposite extreme is free to slightly slide inside the bone. In 1984, Winquist and his co-workers validated this concept after extensive experimental evaluation [3, 38, 45, 80, 84]. 'Dynamization' nails started to be recommended regularly as the only stabilization mode or as a secondary procedure after static locked intramedullary nail had demonstrated undesirable results. These locking mode was able to increase the loading of the fracture site and was believed to avoid non-unions and delayed union cases [38, 80].

Recent discovery of the detrimental effects of medullary canal over-reaming and the advent of the "limited reaming" technique lead to the adoption of anatomically respectful smaller diameter nails in statically locked mode, which became standard. The use of smaller diameter intramedullary nails (*e.g.* recent Russel-Taylor nails design for femur fractures stabilization reduced nail diameter for values between 10 and 12 mm for men as well as women) progressively reduced the reservations against the static locked nailing concept. Coupled with the recognition that this locking mode does not always cause nonunion and delayed union cases, have led to the discontinued use of the 'dynamization' process as a routine procedure. As a load-sharing device, the intramedullary nailing will initially bear most of the load. The use of lower diameter intramedullary nails will reduce the rigidity of the fixation system; therefore, the static locking mode will provide a large enough transmission of load to the fracture site and stimulation of micro movements capable of inducing the callus development. As the interfragmentary tissue starts to heal and its Young's modulus increases, the load is then gradually transferred to the bone for complete fracture consolidation [3, 29, 38, 48, 57, 62, 79, 80]. Presently, surgeons only perform secondary 'dynamization' in cases where there is evidence of delayed union or non-union. Although the secondary 'dynamization' procedure is considered a simple outpatient procedure, the surgery for the removal of the locking screws represents more pain to the patient and also an additional economic burden for the health care services [45, 48, 87].

In the 1990s titanium was introduced as a new material, through the Alta nail system, in the form of closed section nails with proximal and distal transverse locking. Before that, AISI 136

LVM ASTM F138 stainless steel, generally known as the medical grade stainless steel, was the most commonly used material in the manufacturing of intramedullary nails [4, 30, 41, 48]. According to Thomas DeCoster [48], when titanium was first introduced in the market, it was considered to be more suitable for construction of small diameter tibial intramedullary nails, since it presented sufficient strength without too much stiffness, hence avoiding nail breakage and non-union cases. Nowadays both materials are widely accepted; but a growing preferential tendency for titanium alloy in detriment of stainless steel materials has been registered [7, 30, 45, 88]. Titanium alloys are primarily type Ti-6Al-4V, although the more recent Ti-6Al-7Nb also presents interesting properties. The popularity of titanium alloy nails can be justified by their mechanical properties. When compared to medical grade stainless steel, titanium has a Young's modulus closer to the intact diaphyseal cortical bone, and higher fatigue strength and yield strength than medical grade stainless steel (see Table 2.5). Also, titanium is lighter with a density value around 4.5 g/cm^3 comparatively with the 8 g/cm^3 (approximately) of stainless steel. [45, 77, 89]. From a biological perspective both materials are considered biocompatible, *i.e.* are able to function *in vivo* without eliciting an intolerable response of the body, either locally or systemically. The type 136 LVM alloy - where "V" denotes to vacuum-melt stainless steel - presents a good corrosion resistance to chloride solution through the formation of a ceramic-like oxidation coating and due to recent addition of molybdenum ("M" denomination) and decrease percentage of carbon, from 0.08 to less than 0.03 wt% ("L" meaning Low carbon) [30, 89]. Titanium is no exception and surface alteration was required to avoid the release of aluminum, vanadium or niobium toxic ions to the surrounding tissues. Hence, a California Company, ACE, introduced a surface treatment technique called 'tiodizing' which allowed the use of titanium alloys for implant fabrication allowing the development of a protective film of titanium oxide (TiO_2). This technique consists of an electrolytic process that enhances anti-galling and mechanical resistance without any dimensional change [7, 30, 45, 89]. Another characteristic favoring titanium intramedullary nails is that this material shows less magnetic resonance imaging interference than that observed for stainless steel implants [77].

Locked intramedullary nails that are used today worked by the principles on fracture management determined by the AO foundation in 1958 which are applied not only to intramedullary nailing but to all internal fixation in general. Hence, this stabilization technique permits maintaining the anatomic reduction obtained by the orthopedic surgeon, guarantees bone alignment, stabilizes fracture fragments and also allows load transfer across the fracture site and the occurrence of micromovements at the fracture site that are capable of promoting healing. By respecting these principles, early patient's mobilization and reduced recovery time

can be achieved [80, 90]. Although patient recovery procedure may vary between countries and even between hospitals in the same nation, according to Joseph Borrelli [91], the standard postoperative care and rehabilitation procedures when intramedullary nailing stabilization technique is used in lower extremity bones, includes mobilization, partial weight-bearing during the first 6 weeks accompanied with quadriceps strengthening and motion of the ankle and knee exercises. For the upper extremity, when patient is awake, Codman, elbow and wrist range of motion exercises are applied, but shoulder motion and weight-bearing on the arm are restricted initially [92, 93]. Despite de fact that studies such as [94] have proved that the fatigue strength of several small diameter tibial nails (between 7 and 8 mm) in non-segmental fractures are high enough to support full weight-bearing, this is normally delayed until radiographic evidence of callus formation is seen on the bone and pain-free weight bearing is evident, which again usually occurs 6 weeks after nail implantation. Quadriceps strengthening exercises as well as a range of motion exercises of the ankle and knee are started as soon as possible. After union is verified, patients are discharged and are sent to physiotherapy [91, 95]. For the upper extremity fractures, during rehabilitation, a sling is usually continued until good fracture healing is demonstrated and physical therapy is normally avoided immediately after surgery [92]. Results obtained in the study developed by Ouyang *et al.* [96] where a prolonged evaluation (follow-up period around 26.2 months) on the patients' average healing time based on a wide range of interlocking intramedullary nails designs in isolated long bone fractures (*e.g.* tibia, femur and humeral) was taken in consideration, the mean time to fracture union was 5.2 months

There is currently a widespread indication for the use of interlocking intramedullary nailing which includes: (a) the management of closed fractures with the exception of proximal and distal fractures of the tibia that are contraindicated due to special positions [96], (b) acute closed fractures [92], (c) open fractures (type I, II, IIIa and IIIb according to Gustilo classification) [63, 91] and (d) serious and complicated fractures. The latter indication cases include segmental fractures, polytraumatized patients and additional ipsilateral fractures, morbid obesity [97], failed non-operative treatment of tibial shaft fractures, late management of open tibial fractures or when the definitive care is implemented after the damage control orthopedics concept in a polytraumatized patient (*i.e.* conversion of an external fixator or internal fixator to an intramedullary nailing) [91, 96] and also in pathological fractures (*e.g.* fracture caused by bone metastatic) [96].

2.4.5. Current nails concepts in developing countries

While in developed countries, intramedullary nailing is considered the gold standard of care for long bones fractures, in low-income countries the reduced access to implants and instrumentation limits orthopedic surgeons to fracture management through traction. As an alternative and since its introduction in 1999, the Surgical Implant Generation network (SIGN) intramedullary nail has been a well-accepted stabilization method by developing countries and is currently associated with a low complication rate. SIGN intramedullary nail was developed and is freely distributed by the non-profit organization SIGN Fracture Care International, founded by Dr. Lewis G. Zirkle. The fixation system was designed so that surgeons can rely on their tactile senses through the use of the “slot finder” in conjunction with targeting device so the interlocking screws can be correctly placed. The system can be used in conditions where orthopedic traction table, real-time x-ray intra-operatively such as the C-arm image intensifier and power equipment are absent. The SIGN intramedullary nail is a solid stainless steel structure in order to increase the stiffness and facilitate the correct position of the distal slots in the nail, to reduce the surface area of the implant and dead space in the intramedullary canal and reduce the risk of bacterial infection. This intramedullary nail also has a proximal bend which allows it to be used for tibia fractures as well as in antegrade and retrograde femoral nailing and humerus nailing [7, 98]. Before the development of the SIGN intramedullary nails, and when intramedullary nail fracture management were required and available, Rush or ender nails and more commonly open reduction with unreamed Küntscher nails for treatment of tibial and femoral fractures were the preferable fixation methods used. Küntscher nails were so commonly used due to their low cost, reduced surgery duration, acceptable intraoperative bleeding in acute fractures and reasonable outcomes notwithstanding the infection and mechanical complications which this technique is associated [99, 100].

2.4.6. Current nail biomechanical improvements and upgrades

When the blood supply at the fracture site is adequate, the healing outcome of a long bone fracture is strongly determined by the mechanical environment. The mechanical conditions at a fracture site, such as the gap size and configuration, and most importantly the interfragmentary movement which is determined by the fixation system stability and functional loading, greatly influence the rate and quality of the callus formation during the healing process. Therefore, callus formation requires controlled amount of stress occurring at both ends of the fracture, and interfragmentary movements under functional loading [63, 101, 102]. There is insufficient knowledge on the physiological mechanical environment that promotes fracture healing and how to adapt the intramedullary nail rigidity to mimic such environment. Hence, it remains

unclear which is the “ideal” mechanical environment at the fracture site, evidencing the urgent need for an exhaustive study on this matter, and that will also greatly impact future improvement of intramedullary nailing systems [41, 103].

The relevant mechanical stimulus window which is both safe and capable of enhancing bone-repair determines the strain range between the minimum required for the induction of callus and the maximum which allows bony bridging. It has been registered that high implant stiffness may shield the callus from mechanical stimulus, suppressing the osteogenic response and lead to delayed or atrophic nonunion [104, 105]. However, very recent studies [105-107] are starting to demonstrate a positive correlation that underestimated high-frequency low-magnitude interfragmentary micro motions have on the rate and quality of bone fracture healing. According to Gómez-Benito *et al.* [108] these stimuli may be associated with the promotion of endochondral ossification and an increase in the rate of cell proliferation and tissue synthesis. Although several studies support this concept, it is not yet fully clarified. On the other hand, overloading the callus with too flexible fixation implants, causes large amount of interfragmentary movements, which may induce repetitive micro-ruptures in the callus formation, derail the healing process and lead to subsequent complications, such as malunion or delayed and hypertrophic non-unions cases [41, 103, 104]. Although earlier studies focus on interfragmentary stimulus magnitude by measuring and comparing the effect of bone fragment displacement, several studies [109-114] claim that the amount of interfragmentary motion should depend less on the displacement of the fragments alone but more on the relation of displacement to the width of the fracture gap. Comminuted fractures are more tolerant to motion than simple fractures since in this type of injuries the overall displacement is shared between each fragment [110]. The importance of frequency value in the mechanical stimulus was also considered. In a study developed by González-Torres *et al.* [108], a finite element model of a sheep tibia metatarsus fracture allowed concluding that the change in the frequency of the external mechanical stimulus directly affects the interstitial fluid flow velocity in the fracture callus. Goodship *et al.* [105] reinforce the idea that mechanical stimulus does not need to be large to positively influence the fracture-healing process. In their study, they applied a short duration (17 minutes), low-magnitude (25 $\mu\epsilon$), high-frequency (30 Hz) interfragmentary axial displacement on a 3 mm mid-diaphyseal osteotomized sheep tibia. This study demonstrated that physiological loading with additional short period of low-amplitude (which were less than 1% of the fracture gap width and less than 6% of the 0.45 mm displacement measured at the site during ambulation) high-frequency strain could positively influence the rate of healing. There is also evidence that uniaxial strains between 0.3% and 0.8% are capable of stimulating *in*

vitro osteoblast proliferation and synthesis [104]. Research is also starting to point out the importance and sensitivity of the healing tissue to biomechanical environment during the initial phase of bone-healing [103]. This concept is supported by Comiskey *et al.* [115], who claim there is a positive correlation between the initially applied interfragmentary strain and the rate of healing. A study developed by Bailón-Plaza and van der Meulen [104] highlights the adverse effects of delaying mechanical stimulation.

Several factors have been suggested to determine the mechanical environment at the fracture site; those that result from the stiffness of the implant, such as the rigidity of the nail and the screws, and those that result from movements between the different components that constitute the bone-implant structure construct [116]. Strategies have been developed to try to guarantee an “optimum” implant stability and interfragmentary mechanical environment [117-120]. Among these, some authors have focused on experimenting with different biomaterials to evaluate the positive impact that they may have on the mechanical behavior of the bone-implant system and consequently on the healing process. Other authors seem to be more concerned with increasing the structure stability. This is achieved by reducing the amount of movements that result from the clearance of the nail within the medullary cavity and from the compliance of the bone-implant connection

i) New intramedullary nail materials

Although medical grade stainless steel and titanium alloys intramedullary nails are able to satisfactorily stabilize most long bone fractures, several authors [38, 41, 88] claim that their Young's Moduli are too high in relation to intact diaphyseal cortical bone, when titanium alloy implants are considered, therefore shielding the bone from the stress it would naturally experience. Hence, recent research has been developed to find biocompatible materials capable of reducing the disproportion between the living tissue and the implant. Table 2.5. compares a few considered intramedullary nailing materials mechanical properties with those of the cortical bone. Recent research studies have been developed towards three types of biomaterials that seem to hold promise: resorbable reinforced composites, magnesium and shape memory alloys [4, 89].

Table 2.5 - Selected mechanical properties of different types of intramedullary nailing materials in comparison with the cortical bone. UTS – Ultimate tensile strength, TYS – Tensile yield strength

| Material | Young modulus (GPa) | Shear modulus (GPa) | Density (g/cm ³) | TYS at 2% (MPa) | UTS (MPa) | Reference |
|--|--|---|------------------------------|--|---|-----------------------------------|
| AISI 136 LVM type (ASTM F138) ^a | 193-200 | 74-77 | 7.94-8 | 170-205 | 500-700 | [30, 88, 111, 121-124] |
| Ti-6Al-4V (ELI) ^b | 100-118 | 41.2-44.5 | 4.43 | 747-795 | 860-950 | [30, 88, 124-128] |
| Ti-6Al-7Nb ^c | 100-114 | 36-41 | 4.52 | 800-1024 | 869-1086 | [111, 124, 127] |
| Poly(L-lactide) acid (PLLA) | 10-50 | 1.2-3 | 1.21-1.28 | 48-60 | 48-60 | [88, 111, 129, 130] |
| Flax/epoxy | 12.98-35 | 1.87 | 1.3 | NIA | 100-300 | [41, 111, 131, 132] |
| Carbon fiber/epoxy | 10-300 | 3.8-6.3 | 1.55-1.58 | 1700-2170 | 1700-2170 | [41, 111, 131, 133] |
| Carbon fiber/flax/epoxy | 5.09-121 | 4.7-5 | 1.3-1.6 | n/a | 172.4-400 | [41, 131] |
| Polymethyl methacrylate (PMMA) | 2.2-55 | 0.6-1.12 | 1.12-1.2 | 60-85 | 95-100 | [130, 133-137] |
| Mn-based | 41-45 | 15-18 | 1.74-1.84 | 120-130 | 195-230 | [111, 138, 139] |
| Ni-Ti alloys | Austenitic 53.5-110 Martensitic 21-69 | Austenitic 16.9-31 Martensitic 6.8-18.75 | 6.45 | Austenitic 100-800 Martensitic 50-300 | Austenitic 800-1500 Martensitic 103-1100 | [140-143] |
| Cortical bone | 10-40 | 3.3-6.2 | 1.8-2.1 | 114-130 | 120-160 | [88, 111, 125, 131, 138, 144-147] |

Main alloy compositions (wt%):

^a ≤0.03 in carbon (C), ≤1 in silicon (Si), ≤2 in manganese (Mn), ≤0.045 phosphorus (P), ≤0.015 sulfur (S), 17-19 in chromium (Cr), 2.5-3 in molybdenum (Mo) and 12.5-15 in nickel (Ni) [121]

^b Balanced amount of titanium (Ti) around 90, 5.5-6.75 in aluminum (Al); 3.5-4.5 in vanadium (V), 0.08 in carbon (C) and 0.2 in oxygen (O) [88]

^c Balanced amount of titanium (Ti), 5.50-6.50 in aluminum (Al); 6.50-7.50 in Niobium (Nb), 0.08 in carbon (C) and 0.20 in oxygen (O) [127]

An economic alternative to expensive titanium alloys for use as intramedullary nail material are polymers such as the poly(methyl methacrylate), or PMMA. This is an acrylic plastic commonly used in orthopedics as bone cement. In comparison to the metallic alloys, the mechanical properties of PMMA are more similar to those of human cortical bone [89]. A preliminary study developed by Lewis *et al.* [134] focused on the application of such materials in developing countries. It was possible to conclude that although PMMA intramedullary nails present relative stability in bending and torsion with mean shear modulus and flexural stiffness of 0.17 GPa and 358 N/mm, respectively, larger PMMA nails are required to reach the same stiffness as a small metal nail. An advantage of PMMA is that this material allows the introduction of antibiotic without substantially affecting the material mechanical properties. Even though there appear to be advantages in using PMMA for intramedullary nails, its potential clinical applications still need further investigation. An example of a commercially-available nailing system is the CarboFix “Piccolo” intramedullary nails made of carbon-fiber-reinforced polyetheretherketone (PEEK) polymer where the fibers can be oriented in different directions. This material gives the fixation device an elastic modulus close to that of cortical bone and its radiolucent property permits improved, artifact-free radiographic imaging [148-150].

Another group of promising biomaterials are magnesium alloys. These have attracted great attention in recent years. These materials present superior mechanical properties when compared to pure polymers, since they have a higher strength and Young’s modulus similar to cortical bone [88]. In terms of their biological properties, as shown in the study presented by Pichler *et al.* [151], magnesium alloys are well tolerated in both osteoblasts and growth plate chondrocytes and are considered a biocompatible material. Another interesting characteristic is their biodegradation ability, which renders implant removal unnecessary, hence avoiding a secondary unnecessary surgery. Although this is a very useful characteristic, earlier experiments with these materials showed that they present fast degradation in aqueous solutions that consequently leads to production of high amounts of hydrogen gas. This gas is not directly harmful for the bone tissue, but nevertheless it accelerates the degradation of magnesium alloys and jeopardizes the healing process [151]. This limitation has already been overcome in the study developed by Rössig *et al.* [152]. For the first time, the biocompatibility and degradation behavior of the magnesium-based LAE442 intramedullary interlocked nailing system was evaluated on an *in vivo* sheep model and compared to standard stainless steel nails. During the 24 weeks study the LAE442 intramedullary nail showed slight decreased in implant volume and the local biocompatibility was considered to be suitable. Another example of such an attempt to overcome the limitations showed by pure polymers is present in the work developed by

Morawska-Chochół *et al.* [88] where reabsorbable polylactide reinforced with magnesium alloy fibers were tailored to approximate bone properties. According to this author, the strength properties demonstrated by intramedullary nails composed by this material should be sufficient to ensure long bone fracture stabilization. The use of reinforced composites allows adapting their mechanical properties based on the requirements by changing the fiber orientation and their arrangement or volume fraction [41].

Other new interesting intramedullary nails materials are shape memory alloys. These materials gained popularity due to their extraordinary mechanical properties, namely the superelasticity and the shape memory effect. The latter allows the material to return to its original shape when subjected to some appropriate thermal procedure, even after plastic deformation takes place. The family of Ni-Ti alloys (nitinol alloys) is the most commonly tested material because of its good biocompatibility, substantial resistance to corrosion and fatigue, and the fact that its elastic modulus is quite close to that of human bone, which makes it suitable for orthopedic surgery [30, 153-156]. In a research study developed by Da *et al.* [157, 158], the Ti-Ni shape memory alloy interlocked intramedullary nail, produced by Lanzhou Seemine Shape Memory Alloy Co. Ltd, was considered a strong and reliable fixation implant, with lower stress shielding effect and good biocompatibility. These nails could easily be deformed at a temperature between 0 to 5 °C and returned to their original shape at body temperature. This led to the development of high axial pressure as a consequence of the alloy recovery force to its original shape allowing early load bearing and knee joint motion. Ni-Ti shape memory alloys may have a potential as intramedullary fixation applications but there is still much work ahead.

Stress shielding effect for the consolidation of a fracture would thus be reduced by the use of an intramedullary nail of a material with lower Young's modulus and therefore guarantee a lower stiffness. However, this must be balanced by the need for a greater stability while the bone is healing. Although research has been conducted to achieve such equilibrium, intramedullary nails made of metals such as stainless steel and titanium are still the preferable choice due to their validated high biocompatibility, toughness and durability [30, 159].

ii) Reduce screw-to-nail compliance

In the absence of cortical contact and with the use of locking screws, the stiffness of the bone-implant construction is almost exclusively defined by the load transfer through the interlocking screws. This assembly is subjected to a complex physiological loading which may be analyzed as combination of three main types of load: pure shear and torsion which create a non-uniform shear loading within the tissue, axial compression and bending forces which result in

compression in one side and tension in the other [1, 38, 57, 103]. As previously mentioned, the screws engaging the bone cortices aim to counteract rotational, axial and bending forces and stabilize the bone-implant construct. Few attempts have been made to increase the stability of the intramedullary nail-bone construct by modifying the locking option [160, 161]. However good results have been achieved by removing the play between nail-screw interface. In traditional interlocking nails there is always a certain amount of compliance between the screw and the nail. The toggling is a consequence of the intentionally undersized screw relative to the nail hole - size disparity averaging 0.13 mm - which supports targeting and insertion of the screws without bending. This screw-to-nail toggle leads to interfragmentary motion that is particularly noticeable in torsion and which according to Augat *et al.* [116], could reach values as high as 10 mm. These interfragmentary movements are believed to increase the likelihood of a non-union or delayed-union, especially in osteoporotic bones weakened by age [162-164]. The advantage of removing the compliance at the nail-screw interface to provide enhanced bone-implant construct stiffness is demonstrated in a study developed by Kaspar *et al.* [103]. In their experimental study using an angular stable tibial intramedullary nail obtained by modifying the nail holes' threads so the bolts fit exactly into the holes, they found that the higher stiffness construction led to significantly smaller interfragmentary movements in all directions and that this caused histological, radiographic, and biomechanical superior bone healing during the nine weeks' experimentation. Also the higher angular stable tibial nails allowed early functional weight-bearing without the disadvantages of excessive interfragmentary movements.

In 2009, a new strategy known as angular stable locking system (ASLS), was designed by Alberto Dell'Oca [165] so that all the holes in the nail can be locked at a stable angle fractures. The ASLS consist in a dowel (or sleeve) assembled on a screw with three different outer diameters. When the sleeve-screw combination is inserted into the nail, the sleeve expands in the nail hole resulting in a tight fit that prevents toggling between nail and screw. Also the angular stable locking nail has a more even load distribution over the nail, therefore decreasing individual stress raisers, reducing loosening of locking screws [162, 166]. When introduced, the ASLS used PEEK. This was gradually replaced by a more biodegradable material: 70:30 poly(L-lactide-co-D,L-lactide) dowels [166, 167]. The latter has resorbable properties which may lead to an intrinsic dynamization. According to Höntzsch [162] the reabsorption process never starts before 12 weeks. In an *in vitro* porcine model study developed by Wähnert *et al.* [167], the ASLS with the latest sleeve material showed a 70% higher torsional stiffness, 8 times higher neutral zone and 0.5 times smaller range of motion than the conventional locking system in the treatment of unstable distal tibial fractures. From the axial loading biomechanical perspective,

the author concluded that ASLS lead to a 10% higher stiffness and 12% lower range of motion. Hence, this system provides a significantly higher axial and torsional stiffness, and significantly less fracture gap movement; therefore, it allows an overall higher stability when compared to a conventional locking mode [120]. Another advantage of the ASLS is that it was designed to enable it to be used in all existing intramedullary nails so that there is no need to invest in new nails or in nail adaptation procedure. An alternative design was proposed by Garlock *et al.* [164] to allow the bone and nail hole to be misaligned yet still creating an angle-stable construct. However, as suggested by Höntzsch *et al.* [168], there is still lack of compelling clinical trial data on the ASLS system for distal tibial fractures. Note that although the Synthes ASLS case was described here in some detail as an example, other commercially available angle-stable designs feature an interface that reduces the screw-nail hole clearance when compared to traditional ones, such as the Smith and Nephew Trigen Meta-nail [169-171], that reaches a locked compression with angular stability through threaded screw holes with polyethylene brushing, and the Zimmer Natural Nail System with the Stabilize Technology [172], the interface of which links the nail to the interlocking screws [163].

In addition to tailoring the bone-implant construct stiffness to allow a controlled magnitude interfragmentary motion for promoting fracture healing, the direction of interfragmentary movements also play a determinant role in the bone healing final outcome [101, 173]. It is of general agreement that axial interfragmentary compression movement promotes callus formation, but the influence of shear displacement on bone healing is still the subject of controversy [103, 174]. According to Steiner *et al.* [101] interfragmentary axial compression stimulus are more beneficial than fracture shear movement. Also translational shear (or pure shear) is more impeding than torsional shear for a majority of different combinations of loading magnitudes. As reported by Penzkofer *et al.* [161] shear movements at the fracture site may tend to damage the inner cortex and may also produce increased play between the nail and the surrounding bone. Concerning bending loading, it has been shown that it may result in asymmetric callus formation, where healing may be considerably inhibited on the tensile side of the callus and promoted in the compressive side [1]. In the screw-to-bone toggling reduction methods previously described, the increase in the overall fixation system stiffness, constructively reduced unfavorable (*e.g.* shear and torsion) interfragmentary movements which are detrimental to fracture healing; however, they also reduced the beneficial compression movements at the fracture site.

The primary goal of fracture treatment is to provide an optimum mechano-biological environment for each stage of fracture healing [41]. Hence, the best way to promote callus development is to allow movements that stimulate and favors healing and hinders those that may disrupt it [174]. By limiting the dimensional play between the screw and the nail with the ASLS, the torsional stability is enhanced and the axial stiffness of the bone-implant construction is also increased, leading to a reduction in the amount of axial interfragmentary movement, which is required for optimal secondary fracture healing [173]. Ideally, the fixation implant should adequately counter bending, torsion, and shear stress, while only fractionally countering compressive stress. This may be translated as “selective stress shielding” [41, 85]. This evidence has prompted the development of a new nail design [173], called the Flexible Axial Stimulation (FAST) which can simultaneously provide controlled axial interfragmentary motion with reduced torsional shear. In this nail, the dynamic slot of the standard nail was widened and a press-fit bushing inserted. Although this new nail design may potentially enhance healing, additional studies are required to validate the possibility of this approach enabling the ideal mechanical environment at the fracture site.

2.4.7. Other fields improved

Besides the improvements at a biomechanical level, intramedullary nails have also been subject to upgrades in different fields as described in subsequent sections.

i) Radiation exposure reduction

The use of locked intramedullary nails demands precise localization of the nail holes for the correct placement of the locking screws. The proximal locking process, which is similar in the humerus, femur and tibia bone, is quite simple since the insertion handle serves as the aiming device for the placement of the screws [35, 175]. On the other hand, the localization of the distal nail holes is not so simple. It can be done using the ‘nail-mounted target device’ method, which fell in disuse due to the high number of cases of nail misguide caused by torsion and bend over the length of the nail upon its insertion in the bone. It can also be done using the ‘image-mounted device’ and the ‘free hand technique’ methods, which beside the use of fluoroscopic image guidance, are considered to cause nicks to the hole edge during drilling which weakens the strength of the nail hole. Finally, there is also the ‘AO radiolucent drill’ method. Fluoroscopic guidance-based intramedullary nailing procedure requires very long operating times and consequently a long exposure to ionizing radiation by the patient and also the surgeon and the medical staff. However, when any inadvertent misplacement of the distal locking screw occurs, corrective procedure takes place and the surgical time and radiation exposure will increase [79,

84, 176, 177]. The exposure to ionizing radiation is not limited to the distal locking procedure; it is present during what are considered as the most challenging steps in intramedullary nailing: entry point selection and fracture reduction. During these steps the attempt to obtain three-dimensional alignment is achieved with the use of two-dimensional fluoroscopic images [178, 179]. Even though occupational ionizing radiation exposures are subjected to strict international regulation, with upper limit values set between 20 and 50 mSv [180, 181] for the whole body and 500 mSv for extremities (*i.e.* hands and feet)[180], body regions such as the surgeon's hands (considered to receive the highest doses) are often exposed directly to the X-ray beam. This constant ionizing radiation exposure is in many cases associated with cell death, mutagenesis and carcinogenesis radiobiological effects [182, 183]. There have been several studies concerning the radiation exposure for patient, surgeon and medical staff during intramedullary nailing procedure. Madan and Blakeway [180] evaluated the radiation exposure to patients' gonads and surgeons' hands in a comparative study between Russell–Taylor and Marchetti–Vincenzi intramedullary nailing. The mean radiation time by consultants was lower than that of middle-grade surgeons both during tibial nailing (0.56 and 1.28 min) and femoral nailing (0.52 and 1.61 min), respectively. The study also showed the impact of distal locking procedure on the amount of radiation exposure by demonstrating that Marchetti–Vincenzi nailing – where locking is determined by the use of the proximal locking screws since distal locking is automatically obtained by firm grip of the pre-bent wires in the distal bone spongiosa [184] - presented significantly less amount than Russell–Taylor nailing. The author also advises protective measures against exposure at fluoroscopy (*e.g.* thyroid shields and lead-lined gloves) which according to this study is capable of decreasing the radiation dosage exposure from 0.330 to 0.021 mSv in tibial nailing and from 1.272 to 0.080 mSv in femoral nailing. In a similar study developed by Müller *et al.* [183] where the radiation of 41 intramedullary nailing of femur and the tibia was monitored by ring dosimeters, mean ionizing radiation dose for one intervention was 1.27 mSv for the dominant hand of the primary surgeon and 1.29 mSv to the first assistant. The average fluoroscopy time per procedure was 4.6 min. Although Müller and his co-workers observed higher radiation time and consequently higher surgeon radiation dosage exposure and in both studies the overall radiation to patient, surgeon and operating room staff were within acceptable limits, there is undoubtedly a need for the development of a strategy to reduce the amount of radiation and exposure time.

Novel and inventive approaches have been developed to replace or facilitate distal screw locking and/or reduction of radiation exposure [46, 185]. The concern in reducing the exposure time to radiation may date back as early as 1986 with the development of the Brooker-Wills nails which

achieves distal fixation through deployed fins that attach into bone distal cortices after nail insertion is completed. There are several records of late perforation of the knee joint demanding premature removal of the implant caused by deployed fins strategy which end up limiting this technique. Also, distally screw-locked implant presents higher rotation stability when compared to the deployed fins fixation method [80, 177]. A more recent attempt to develop self-locking intramedullary nails is present in the work developed by Liu *et al.* [186] where a rounded solid nail can be directly screwed into the medullary cavity with the side-locking tag to achieve anti-rotation and anti-contraction. Although this technique exhibits a significantly shorter operation time, lower operative blood loss and higher healing rate, some postoperative complications occurred including radial nerve injury and incision infection in the case of humeral intramedullary nailing.

A different inventive approach that tried to avoid dependence on radiation-based image guidance for nail distal locking were developed by Durham and Crickenberger [177]. This author uses a magnetic targeting system for the detection of the distal nail holes through neodymium-iron-boron magnets that are placed at the level of the distal screw holes to be targeted. The author claims that this x-ray radiation free method increases the speed and reproducibility of such a complicated step. Although the work developed by Durham was in its research stage, there is already a commercially available digital targeting system developed by Smith and Nephew, the Trigen Sureshot. This targeting system is based on magnetic field generation, a guide wire which passes through the nail and spreads the magnetic field and virtual imaging to facilitate distal locking without X-ray radiation. In a study developed by Dursun *et al.* [187], when compared with the freehand locking technique, the commercially available magnetic locking technique reduced the operation times to 1/3 (average of 5 min) and radiation exposure to less than a quarter (around 8 s). The major limitation of this approach is its high cost and the need for customized intramedullary nails and tools such as a drill that does not disrupt the magnetic field [187, 188]. We do believe that there is still space for further investigation on robust strategies to make distal locking easier, and reduce the amount of radiation, and exposure time.

ii) Measurement of fracture healing

Fracture healing follow-up has traditionally been assessed by manual examination to evaluate the stiffness of the fracture combined with radiographic clinical evaluation to monitor the evolution of the bridging callus [91, 95, 189, 190]. As suggested by Joslin *et al.* [191] weight-bearing can also be considered as a valuable guide for fracture healing since increases in weight bearing achieved post-fracture appeared to reasonably correlate with increases in fracture

stiffness, and the return to weight bearing generally indicates that the union of the fracture has occurred. Although there is no consensus in the definition of an endpoint for fracture healing, it may be defined as successful when there is a presence of bridging callus, the fracture line is absent and the fracture stiffness is higher than 15 Nm/deg [191-193]. These traditional evaluation methods are largely a matter of clinical judgement, may vary between different clinician's assessment, and in many cases can be considered unreliable [189, 194]. As healing progresses through several stages - hematoma formation, cellular proliferation, gradual calcification - there is a steady increase in the mechanical properties of the tissue at the fracture site and the healing bone eventually approximate approaches the performance of intact bone. However, the changes in the mechanical properties of the callus are non-linear. The fracture callus is a viscoelastic structure, in which the viscous component with only minor mechanical recovery capability decreases, while the elastic part increases during the course of bone repair, from around 0.2 MPa Young's modulus in the granulation tissue to 1 GPa in the immature bone and 6 GPa for mature (also known as woven) bone [144, 192, 195]. Hence, there is a need for an accurate quantitative evaluation of the state of the fracture healing at any given time [189, 194]. This information could be used to indicate the rate of healing progress for a single patient, improve patient's outcomes by enabling a common endpoint of fracture healing to be defined. Hence, treatment could be discontinued, and improve the recovery procedure by evaluating the effect of different fracture treatment regimens on callus formation and compare results among a groups of patients. The existence of quantifiable information that is able to sequentially monitor and assess the process on the healing progress would help the surgeon to develop more secure decisions for possible early intervention, reducing the risks of delayed repair and non-union, and reducing additional cost for patients and health care services [189, 191, 194].

Several techniques have been introduced to objectively assess the mechanical properties of healing fractures along time from which we would highlight the fracture stiffness measurements, vibration analysis and the ultrasonic technique. These methods will be described briefly in this section.

The callus stiffness will increase with the decrease in the amount of connective tissue and cartilage and with the increase in fraction of mineralized bone [196]. Strength is defined by fracture failure, which obviously hinders the direct measurement of this parameter. On the other hand, measurements of stiffness imply determination of deflection generated by an applied load. Hence, the measured parameter is stiffness of the healing fracture, which also correlates with the bone strength during callus formation. This characterizes the resistance to

deformation and has the potential to provide both a measure of the rate of healing and an objective definition of union [192, 193, 197-199]. Fracture stiffness is an appropriate measure of fracture healing and can be obtained by either direct evaluation of callus stiffness or vibrational analysis [197, 200].

For a direct measurement of callus stiffness, the most accurate method to measure local deflection (or angulation) at the fracture site, with direct access to the healing fracture mechanical integrity as a function of external loading, is through the temporary removal of all fixation devices. In principle, this is only possible for patients who are treated by external fixators or by cast and potentially induces discomfort. In the case of internal fixation with plates or intramedullary nails, direct measurement of the mechanical integrity of the healing fracture is challenging and requires a more sophisticated method such as instrumented implants. This technique employs biocompatible strain gauges directly attached to the osteosynthesis device [115, 192, 193, 199]. An interesting example of this method is present in the prototype developed by Greve *et al.* [201], where an instrumented intramedullary nail with a wireless SAW (Surface Acoustic Wave) strain-sensor aims to follow the progress of bone healing by measuring strain. The study showed that sensor sensitivity was adequate for the intended application but this model still requires further upgrading to make it compatible for all nail designs and still requires improvements in the antenna design.

Instrumented implants are promising strategies, but; they still require clinical validation. Also, it is expected that further progress on micro-technology will eventually increase their widespread applications and clinical acceptance [192, 199].

An alternative technique for direct assessment of the mechanical properties of a healing fracture is vibration analysis. This is based on the propagation of mechanical waves through the tissue and the attenuation in either velocity or amplitude across the healing site. Primary techniques include resonant frequency analysis and ultrasound [202].

Resonant frequency analysis is based on the tendency of a material (bone) to oscillate at maximum amplitude with a certain frequency. As bone heals, the change in elasticity alters the resonant frequency [199, 200, 202]. The natural frequencies at which long bones resonate are at the lower end of the audible spectrum (100–500 Hz) [192]. Accordingly to [195] as the development of the callus goes beyond the original bone, the natural frequency becomes higher than that of the intact bone until the callus disappears and the original dimension and natural frequency of bone is restored. In resonant frequency, the conduction of a vibration analysis for

assessing fracture healing demands a mechanical signal as to be introduced into the bone and then transmitted across the fracture site so the frequency response can be determined. Changes in resonant frequency have been shown to depend on the length, density and structural stiffness of the bone [192]. A substantial amount of research [203-205] has been carried out in resonant frequency analysis of fracture healing, and some promising results have been obtained.

Although resonant frequency analysis has been shown to highly correlate with flexural rigidity, it is less reliable when applied to fractures with overlying soft tissue and rigidly stabilized fractures. The technique however appears to be unable to monitor the healing of hairline fractures as the shift in natural frequency is too small for detection [192, 193, 200].

Experiments with healing assessment in fractured bone by percussing proximally and auscultating distally where sound alteration constitutes the evaluation criterion were published as early as 1932 [206]. However, it was not until 1958 that the propagation velocity in fractured human bones was measured *in vivo* for the first time by Anast *et al.* [207]. Since then several studies [208-210] have evaluated the potential of this non-invasive technique for the assessment of bone fracture healing. Quantitative ultrasound is a low-cost, safe and easy to operate procedure. It is associated with a lack of ionizing radiation and can be applied to practically all types of fractures in long bones, promising noninvasive technology [196, 202]. These waves will travel in a material with velocities that are characteristic of its mechanical and structural properties. Hence, they are primarily affected by the Young's modulus and density. The attenuation is largely influenced by porosity and anisotropy [192, 209, 211].

Although there is already some research on the potential of ultrasonic devices (*e.g.* SoundScan 2000 [212]) that tries to overcome some limitations on this method (such as associated measurement errors and problems with soft tissue), this technique is only now starting to gradually become a standard part of clinical practice and there is still a need for the validation of the diagnostic ability of ultrasound for bone fracture healing monitoring. Even though vibrational techniques in general are relatively easy to perform, they have not been widely accepted the subject is and it still remains under research [192, 193, 196, 198, 213].

Currently, there is no "Gold Standard" non-invasive diagnosis tool which can replace the physical examination and conventional radiography to assess the progress of fracture healing [190]. The different methods researched do not correlate very well because they all assess different features of fracture healing [192]. There is still a need for accurate and precise instruments that capture the multiple factors that constitute biological and clinical fracture-healing.

Technological advances such as terahertz pulsed imaging and spectroscopy – radiation with very low photon energy and which does not pose any ionization hazard for biological tissues – may represent a promising diagnostic method for bone fracture monitoring [214, 215]. Until reliable technologies become available and their use is supported by evidence, researchers will have to choose from the available methods and report outcomes with awareness of the limitations of the employed method [199].

iii) Implant failure and nail removal

There may be an assumption that after bone formation and patient full recovery is achieved, metal implants must be removed from inside the organism. However, in current days, this is not considered as a standard procedure. Intramedullary nails are proper load-sharing devices and the implant non removal after fracture healing would not result in regional osteopenia. Nail removal implies a secondary surgical intervention which bring patients additional psychological and physical discomfort, represents high costs for the health care services, and is associated with surgical procedure risks (*e.g.* nail incarceration and equipment breakage) and also post-operative complications (*e.g.* hematoma formation, re-fracture, delayed wound healing, incidence of infection, pain syndromes and even death). Although in the end of the 20th century nail removal after bone recovery was performed for almost all the intramedullary nailing cases, nowadays it is only indicated for specific situations such as infection in healed fracture, consistent pain or discomfort (*i.e.* anterior knee pain) and as suggested by Cheung *et al.* [159] in patients engaging in high risk activities such as competitive athletics. When nail removal is necessary, it should only occur 12 to 24 months after its implantation in order to ease the procedure and avoid high rate of complications due to bony remodeling and incorporation. Pediatric elastic nails are an exception since they are almost always removed. There is a preference for removing the nail 6 to 7 months after insertion. This is considered a safe intervention with minor complications occurring on only about 7% of the patients [48, 57, 88, 91, 216, 217]. However, there may be a need for implant replacement surgery when nail or screw breakage occurs before healing is completed, or when bending or loosening of the locking screws occurs [79, 159]. These kinds of implant failure are not infrequent and they represent a difficult problem for the orthopedic surgeon, especially when the fracture site is united [218]. There is a relative race between bone healing and screw and/or implant failure. The stress in the material immediately surrounding the “defect”, *i.e.* in the screw hole, is higher than that predicted for the bulk. The holes’ effect on the strength of the material is referred to as a “stress concentration effect”. According to Cheung *et al.* [159], stress concentration is most probably responsible for the reported refractures nucleating from screw hole and may also lead to screw

loosening. Also, load transfer between bone and screws leads to considerably large stress concentrations in the screw. Locked nails or screw breakage, particularly at the distal interlocks, are more challenging to be removed and are also the most common occurrence, since this is considered the weak part of intramedullary nail. Reducing the number of screws will cause an increase in stress, since load transfer occurs over a smaller number of screws. A similar effect may also be caused by premature full weight-bearing in the early post-operative stage, or in delayed or non-union situations and in recurrent trauma [29, 44, 57, 159, 218, 219]. According to Lewis *et al.* [134], eccentric screw placement of the locking screws halves the failure strength in four-point bending and misplaced screw location results in early failure at the screw site rather than the osteotomy, presumably due to crack initiation in the nail. Nail failure may also be reduced, by using a larger nail diameter and increasing wall thickness of the nail in the vicinity of the hole, which will increase its strength. Also, in order to reduce the amount of failure cases in the small diameter statically locked intramedullary nails currently used, larger interlocking bolts (5.0 mm diameter) were adopted [28, 77]. New manufacturing techniques for titanium intramedullary nails, such as the “cold working expansion” [220], can minimize nail-screw breakage. This is achieved by plastic deformation of the implant around the periphery of the hole in a uniform manner that generates a zone of residual compressive stresses and improves the fatigue resistance and increase the strength of the implant in the interlocking holes’ region. This is especially important in nails with small diameters. New nail designs that present higher biomechanical stability, such as the small caliber Retrograde Tibial Nail, for the treatment of distal tibia fractures, combine a minimally invasive local intramedullary osteosynthesis with the ability to securely fix the fracture by multiple ASLS. The procedure spares the knee joint and the patella tendon and also leaves most of the medullary canal uninvolved. It is always unadvised to hammer the screw into position, since this may cause micro-fractures on the bone leading to early loosening, being safer to screw it into position [28, 134, 166]. For biomechanical stability to be achieved, the patient’s post-operative weight-bearing directives should be respected, appropriate nail diameter and sufficient nail length should be selected, there should be a skillful insertion of the distal screw, and the critical role of stable proximal interlocking screws in reducing stress should be taken into consideration [79, 159].

Several methods using different instruments for removal of broken intramedullary nails have been proposed. A few examples are: hook [221], guide wires [222, 223], Steinmann pin [224], laparoscopic forceps [225], Arthroscopic Flipcutter [219], and more recently the Nancy nail [226]. However, these methods have limitations such as limited availability and inability of some techniques to address broken solid intramedullary nails (*i.e.* Arthroscopic Flipcutter). An

alternative procedure was developed by Yadav *et al.* [218], where through a solid K-nail reamer, distal broken cannulated femoral nail fragment can be removed by an antegrade approach. This is a considerably simple method that does not require creating an additional incision or exposing patient and surgeon to ionizing radiation.

2.4.8. Conclusion

The recent developments in the intramedullary nailing field were key to the current success and good reputation of this excellent stabilization method. However, there is plenty of space to enhance fracture healing quality and recovery time. The greatest limitations in the improvement of bone-implant system biomechanical behavior and consequently the healing process include the limited knowledge on the ideal fracture site mechanical environment throughout the healing process and the contradictory available theories on the subject; however, a major issue is also the difficulty in translating the biomechanical principals supported by *in vivo* animal experiments into clinical-relevance functional designs. The continued progress on bone healing biology research, the increasing understanding on the relationship between the mechanical environment and the healing process, and the recent trend of using engineering tools for the study of biological processes and for obtaining a more accurate prediction of the biomechanical behavior of implants *in vivo*, will guarantee that intramedullary nailing will continue to improve.

Even though the concept that bone apposition and removal is a biological stress-controlled process was already in place in the 19th century [227], our modern understanding of the bone's complex healing behavior had a long and conflicting theoretical path, where even now there are still many questions to be answered until all the process is fully understood [1]. We believe that the future will bring a better understanding of the relationship between fracture healing biology and mechanics. This will most likely translate into a tendency to combine the intramedullary nail's great mechanical stability with strategies to modulate the surrounding biological environment such as through surface engineering and bioactive coatings and consequently achieve a more appropriate bone healing environment. This trend will – in the future – evolve to multiple functionalities surface coating of the implants towards satisfying the current clinical need. Coating strategies will ideally combine the ability for prevention and treatment of fracture- and implant-related infections through local delivery of antibiotics such as aminoglycosides (*e.g.* gentamicin) or antimicrobial peptides (as alternative to the rise in antibiotic resistant bacteria's) and control release of osteoinductive growth factors (*e.g.* bone morphogenic protein-2 and -7) for enhancement of bone healing [228-231]. Recent studies are already starting to show this tendency [232-235]. A promising product already in the market is

the Expert Tibia Nail PROtect option, which offers protection from bacterial colonization through local antibiotic prophylaxis coating while maintaining the same technique and instrumentation as the uncoated nails. However, bioactive coatings are still associated with challenges such as penetration and diffusion barriers for antibiotic dissemination (*e.g.* tissue change due to inflammation or necrosis), the fact that even high doses of active substances may not always ensure adequate levels of effect, the high cost of growth factors, and also the potential for ectopic bone formation caused by growth factors (not to mention the challenging regulatory pathway associated) [234, 236].

The ongoing evolution on sensor technology, in terms of size and invasiveness of sensors reduction as well as in data acquisition duration and accuracy, allows assuming that improvements will be focused on *in vivo* monitoring of the nail biomechanical behavior and the clinical evolution of bone's healing status. Favoring the real-time data acquisition is the innovative progress in fully implantable wireless technology, such as telemetry, with advantages in patient safety (*e.g.* complete isolation from the electrical network) and longer-term data monitoring (*e.g.* less likely to be damaged as a result of broken interconnections). The acquired feedback data will not only guarantee a safer patient recovery process (*e.g.* personalized rehabilitation strategies and identification of implant failure), but will also contribute for continuous intramedullary nail design improvement. The information obtained will also be used to improve the reliability clinically-representative finite element models with increased efficiency and performance assessment of current and upcoming intramedullary nail designs. [237-240].

Knowledge on biomechanics has greatly contributed to the evolution of intramedullary nailing. Studies of the bone load response and its influence on tissues growth and regeneration made important contributions to the biomechanics of fractures. By knowing how micromovements and mechanical stresses stimulate bone cells and by incorporating these findings in new nail designs, it is possible to improve devices so they can immobilize the fracture without precluding optimal healing conditions. A more ambitious approach would allow for an acceleration of the already reduced healing time and also recovery of early non-union or delayed union cases, without the need for surgical intervention. This will be the challenge of the coming developments of these devices. So we should expect the evolution of intramedullary nailing to continue and novel implants to be developed.

2.4.9. References

1. Betts, D.C. and R. Müller, *Mechanical regulation of bone regeneration: theories, models, and experiments*. Frontiers in Endocrinology, 2014. **5**(211): p. 1-14.
2. Kempf, I. and K.-S. Leung, *Introduction*, in *Practice of intramedullary locked nails: scientific basis and standard techniques recommended by AIOD*, I. Kempf, et al., Editors. 2002, Springer - Verlag: Heidelberg, Berlin
3. Seligson, D., *History of intramedullary nailing*, in *Intramedullary nailing: A comprehensive guide*, P.M. Rommens and M.H. Hessmann, Editors. 2015, Springer: London, United Kingdom. p. 3-12.
4. Bong, M.R., K.J. Koval, and K.A. Egol, *The history of intramedullary nailing*. Bulletin of the NYU Hospital for Joint Diseases, 2006. **64**(3-4): p. 94-97.
5. Knothe, U., M.L.K. Tate, and S.M. Perren, *300 years of intramedullary fixation—from Aztec practice to standard treatment modality*. European Journal of Trauma, 2000. **26**(5): p. 217-225.
6. Farril, J., *Orthopaedics in Mexico*. The Journal of Bone and Joint Surgery. American Volume, 1952. **34**(3): p. 506-512.
7. Young, S., *Orthopaedic trauma surgery in low-income countries: follow-up, infections and HIV*. Acta Orthopaedica Scandinavica. Supplementum, 2014. **85**(356): p. 1-35.
8. Whiting, W.C. and R.F. Zernicke, *Biomechanics of musculoskeletal injury*. 2nd ed, ed. L.D. Robertson, E.H. Mustain, and M.J. Zavala 2008, Stanningley, UK: Human Kinetics.
9. Hopkins, W. and C.B. Penrose, *On the organization and absorption of sterilized dead bone dowels*. Journal of the American Medical Association, 1890. **XIV**(14): p. 505-508.
10. Savory, W.S., *On the absorption of dead bone*. Medico-Chirurgical Transactions, 1864. **47**: p. 103–112.
11. Høglund, E.J., *New method of applying autogenous intramedullary bone transplants and of making autogenous bone-screws*. Surgery, Gynecology and Obstetrics, 1917. **24**: p. 243-246.
12. Warbasse, J.P., *Glück on osteoplasty*. Annals of Surgery, 1896. **23**(3): p. 312–316.
13. Eynon-Lewis, N.J., D. Ferry, and M.F. Pearce, *Themistocles Glück: an unrecognised genius*. British Medical Journal, 1992. **305**(6868): p. 1534-1536.
14. Bartoníček, J., *Early history of operative treatment of fractures*. Archives of Orthopaedic and Trauma Surgery, 2010. **130**(11): p. 1385-1396.
15. Bircher, H., *Eine neue methode unmittelbarer retention bei fracturen der röhrenknochen*. Archiv für klinische Chirurgie, 1886. **34**: p. 410-422.
16. An, Y.H., *Internal fixation in osteoporotic bone* 2011, New York, USA: Thieme.
17. Senn, N., *A new method of direct fixation of the fragments in compound and ununited fractures*. Annals of Surgery, 1893. **18**(2): p. 125–151.
18. Nicolaysen, J., *Lidt on diagnosen og behandlungen av. fr. colli femoris*. Nordiskt Medicinskt Arkiv, 1897. **8**(1).
19. Nelson, F.R.T. and C.T. Blauvelt, *A manual of orthopaedic terminology*. 8th ed 2015, Philadelphia, USA: Elsevier Health Sciences.
20. Glück, T., *Autoplastische transplantation*. Berlin klinische Wochenschrift, 1881. **19**.
21. Watson-Jones, R., et al., *Medullary nailing of fractures after fifty years*. Journal of Bone and Joint Surgery. British Volume, 1950. **32 B**(4): p. 694-729.
22. Schöne, G., *Zur behandlung von vorderarmfrakturen mit bolzung*. Münchener Medizinische Wochenschrift, 1913. **60**: p. 2327-2328.
23. Müller-Meernach, O., *Die Bolzung der Brüche der langen Röhrenknochen*. Zentralblatt für Chirurgie, 1933. **29**: p. 1718-1723.
24. King, R., *Küntscher nailing of the tibia—a new tibial jig*. Injury, 1980. **11**(3): p. 256-257.

25. Groves, E.W.H., *On the application of the principle of extension to comminuted fractures of the long bone, with special reference to gunshot injuries*. British Journal of Surgery, 1914. **2**(7): p. 429-443.
26. Groves, E.W.H., *Ununited fractures, with special reference to gunshot injuries and the use of bone grafting*. British Journal of Surgery, 1918. **6**(22): p. 203-247.
27. Smith-Petersen, M.N., E.F. Cave, and G.W. Vangorder, *Intracapsular fractures of the neck of the femur: treatment by internal fixation*. Archives of Surgery, 1931. **23**(5): p. 715-759.
28. Thakur, A.J., *Intramedullary nailing*, in *Elements of fracture fixation*, A.J. Thakur, Editor 2007, Elsevier Health Sciences: New Delhi, India. p. 127-166.
29. Russell, T.A., *Intramedullary nailing: evolutions of femoral intramedullary nailing: first to fourth generations*. Journal of Orthopaedic Trauma, 2011. **25**(12): p. S135-S138.
30. Hermawan, H., D. Ramdan, and J.R.P. Djuansjah, *Metals for biomedical applications*, in *Biomedical engineering – From theory to applications* R. Fazel-Rezai, Editor 2011, INTECH Open Access Publisher: Rijeka, Croatia. p. 411-430.
31. Venable, C.S. and W.G. Stuck, *Three years' experience with vitallium bone surgery*. Annals of Surgery, 1941. **114**(2): p. 309-315.
32. Venable, C.S., W.G. Stuck, and A. Beach, *The effects on bone of the presence of metals; based upon electrolysis: an experimental study*. Annals of Surgery, 1937. **105**(6): p. 917–938.
33. Collins, D.H., *Structural changes around nails and screws in human bones*. Journal of Pathology and Bacteriology, 1953. **65**(1): p. 109-121.
34. Danis, R., *Théorie et pratique de l'ostéosynthèse* 1949, Paris, France: Masson & Cie.
35. Müller, M.E., et al., *Medullary nailing of femur and tibia*, in *Manual of internal fixation: techniques recommended by the AO-ASIF group*, M. Allgöwer, Editor 1992, Springer - Verlag: Berlin, Germany.
36. Vécsei, V. and L.L. Negrin, *Küntscher—a historical vignette*. Trauma, 2013. **15**(4): p. 331-335.
37. Speitling, A., *Intramedullary nail systems*, in *Practice of intramedullary locked nails: scientific basis and standard techniques recommended by AIOD*, I. Kempf, et al., Editors. 2002, Springer - Verlag: Heidelberg, Berlin p. 51-60.
38. Vécsei, V., S. Hajdu, and L.L. Negrin, *Intramedullary nailing in fracture treatment: History, science and Küntscher's revolutionary influence in Vienna, Austria*. Injury, 2011. **42**(4): p. S1-S5.
39. Court-Brown, C.M., *An atlas of closed nailing of the tibia and femur*. 1st ed 1991, New York, USA: Springer Verlag.
40. Küntscher, G., *Die marknagelung von knochenbrüchen*. Langenbecks Archiv für Chirurgie, 1940. **200**: p. 443-55.
41. Samiezadeh, S., et al., *Biomechanical assessment of composite versus metallic intramedullary nailing system in femoral shaft fractures: A finite element study*. Clinical Biomechanics, 2014. **29**(7): p. 803-810.
42. Beer, F.P., et al., *Mechanics of materials*. 6th edition ed, ed. M. Lange 2011, New York, USA: McGraw-Hill.
43. Browner, B.D. and J.D. Cole, *Current status of locked intramedullary nailing: A review*. Journal of Orthopaedic Trauma, 1987. **1**(2): p. 183-195.
44. Furman, B.R. and S. Saha, *Torsional testing of bone*, in *Mechanical Testing of Bone and the Bone-Implant Interface*, Y.H. An and R.A. Draughn, Editors. 2000, CRC Press: Florida, United States of America. p. 219-239.
45. Stedtfeld, H.-W., *Rationale of Intramedullary Nailing*, in *Intramedullary nailing: A comprehensive guide*, P.M. Rommens and M.H. Hessmann, Editors. 2015, Springer London: London, United Kingdom. p. 13-25.

46. Ingrassia, T. and A. Mancuso, *Virtual prototyping of a new intramedullary nail for tibial fractures*. International Journal on Interactive Design and Manufacturing, 2013. **7**(3): p. 159-169.
47. Brückner, M., M. Unger, and M. Spies, *In vitro biomechanical comparison of a newly designed interlocking nail system to a standard DCP. Testing of cat femora in an osteotomy gap model*. Tierärztliche Praxis Kleintiere, 2014. **42**(2): p. 79-87.
48. DeCoster, T., *A brief history of medullary nailing, New Mexico perspective*. University of New Mexico Orthopaedics Research Journal, 2012. **1**: p. 46-54.
49. Gimeno, M.S., et al., *Biomechanical study of the Grosse-Kempf femoral nail*. International Orthopaedics, 1997. **21**(2): p. 115-118.
50. White, G.M., et al., *The treatment of fractures of the femoral shaft with the Brooker-Wills distal locking intramedullary nail*. Journal of Bone and Joint Surgery. American Volume, 1986. **68**(6): p. 865-876.
51. Dagrenat, D. and I. Kempf, *Biomechanics of locked intramedullary fixation of fractures*, in *Practice of intramedullary locked nails: Scientific basis and standard techniques recommended by AIOD*, I. Kempf, et al., Editors. 2002, Springer - Verlag: Heidelberg, Berlin p. 43-50.
52. Street, D.M., H.H. Hansen, and B.J. Brewer, *The medullary nail: Presentation of a new type and report of a case*. Archives of Surgery, 1947. **55**(4): p. 423-432.
53. Born, C.T., *75 Years of contemporary intramedullary nailing*. Journal of Orthopaedic Trauma, 2014. **28**(8): p. S1-S2.
54. *Medicine: Amazing thighbone*, in *Time1945*: United States of America.
55. Fischer, A.W. and R. Maatz, *Weitere Erfahrungen mit der Marknagelung nach Küntscher*. Archiv für klinische Chirurgie, 1942. **203**: p. 531.
56. Küntscher, G., *The Küntscher method of intramedullary fixation*. Journal of Bone and Joint Surgery. American Volume, 1958. **40**(1): p. 17-26.
57. Smith, J., I. Greaves, and K. Porter, *Oxford desk reference - Major trauma* 2010, New York, United States of America: Oxford University Press.
58. Hofmann, A., et al., *The role of intramedullary nailing in treatment of open fractures*. European Journal of Trauma and Emergency Surgery, 2015. **41**(1): p. 39-47.
59. Wong, M.K., *Intramedullary techniques*, in *Techniques and principles for the operating room*, M. Porteous and S. Bäuerle, Editors. 2010, Thieme: Davos Platz, Switzerland. p. 157-161.
60. Sumita, M., et al., *Failure processes in biometallic materials*, in *Comprehensive structural integrity*, I. Milne, R.O. Ritchie, and B.L. Karihaloo, Editors. 2003, Elsevier: London, United Kingdom. p. 131-168.
61. Schennitsch, E.H., et al., *Comparison of the effect of reamed and unreamed locked intramedullary nailing on blood flow in the callus and strength of union following fracture of the sheep tibia*. Journal of Orthopaedic Research, 1995. **13**(3): p. 382-389.
62. Klein, C., et al., *Unreamed or RIA reamed nailing: An experimental sheep study using comparative histological assessment of affected bone tissue in an acute fracture model*. Injury, 2010. **41**(2): p. S32-S37.
63. Wehner, T., et al., *Improvement of the shear fixation stability of intramedullary nailing*. Clinical Biomechanics, 2011. **26**(2): p. 147-151.
64. Högel, F., et al., *Fracture healing after reamed and unreamed intramedullary nailing in sheep tibia*. Injury, 2011. **42**(7): p. 667-674.
65. Forster, M.C., A.S. Aster, and S. Ahmed, *Reaming during antegrade femoral nailing: is it worth it?* Injury, 2005. **36**(3): p. 445-449.
66. Hoegel, F., et al., *Bone debris: dead matter or vital osteoblasts*. Journal of Trauma and Acute Care Surgery, 2004. **56**(2): p. 363-367.
67. Green, J., *History and development of suction-irrigation-reaming*. Injury, 2010. **41**(S2): p. S24-S31.

68. Danckwardt-Lilliestrom G and G.L. Lorenzi, *Intramedullary nailing after reaming – an investigation on the healing process in osteotomized rabbit tibias*. Acta Orthopaedica Scandinavica, 1970. **41**(S134): p. 1-78.
69. Devine, D.M., et al., *Healing pattern of reamed bone following bone harvesting by a RIA device*. European Cells and Materials, 2015. **29**: p. 97-104.
70. Danckwardt-Lillieström, G., *Reaming of the medullary cavity and its effect on diaphyseal bone: A fluorochromic, microangiographic and histologic study on the rabbit tibia and dog femur*. Acta Orthopaedica Scandinavica, 1969. **40**(S128): p. 1-165.
71. Synthes, *Reamer/Irrigator/Aspirator (RIA) for intramedullary reaming and bone harvesting - Technical guide*, 2008: Pennsylvania, United States of America. p. 1-8.
72. Green, J.M., A.N. Perrier, and S.J. Kmiec, *Surgical reamer and method of using same*, U.S.P.a.T. Office, Editor 2001, Synthes USA: Washington DC, USA.
73. Green, J. and S.J. Kmiec, *Attachable/detachable reaming head for surgical reamer*, U.S.P.a.T. Office, Editor 2004, Synthes USA: Washington DC, USA.
74. Porter, R.M., et al., *Osteogenic potential of reamer irrigator aspirator (RIA) aspirate collected from patients undergoing hip arthroplasty*. Journal of Orthopaedic Research, 2009. **27**(1): p. 42-49.
75. Quintero, A.J., I.S. Tarkin, and H.-C. Pape, *Technical tricks when using the reamer irrigator aspirator technique for autologous bone graft harvesting*. Journal of Orthopaedic Trauma, 2010. **24**(1): p. 42-45.
76. Kuhn, K.M., B.T. Barlow, and D. Dromsky, *The Reamer-Irrigator-Aspirator: Roles and evidence supporting its use in current orthopaedic practice*. Surgery: Current Research, 2014. **4**(2): p. 1-5.
77. Hsu, J.R. and K.F. Dickson, *Advances in tibial nailing*, in *Practice of intramedullary locked nails: New developments in techniques and applications*, K.-S. Leung, G. Taglang, and R. Schnettler, Editors. 2006, Springer: Berlin, Germany. p. 99-108.
78. Modny, M.T. and J. Bambara, *The perforated cruciate intramedullary nail: Preliminary report of its use in geriatric patients*. Journal of the American Geriatrics Society, 1953. **1**(8): p. 579–588.
79. Wu, C.-C. and C.-H. Shih, *Biomechanical analysis of the mechanism of interlocking nail failure*. Archives of Orthopaedic and Trauma Surgery, 1992. **111**(5): p. 268-272.
80. Eveleigh, R.J., *A review of biomechanical studies of intramedullary nails*. Medical Engineering and Physics, 1995. **17**(5): p. 323-331.
81. Hernigou, P. and D. Cohen, *Proximal entry for intramedullary nailing of the tibia: The risk of unrecognized articular damage*. Journal of Bone and Joint Surgery. British Volume, 2000. **82-B**(1): p. 33-41.
82. Seifeldin, A.F. and A. Khedr *History and evolution of intramedullary nailing*. 2014.
83. Herzog, K., *Nagelung der Tibiaschaftbrüche mit einem starren Nagel*. Langenbecks Archiv für Klinische Chirurgie, 1953. **276**(1): p. 227-229.
84. Ingrassia, T., A. Mancuso, and V. Ricotta. *Design of a new tibial intramedullary nail*. in *International Conference on Innovative Methods in Product Design*. 2011. Venice, Italy: Libreria Internazionale Cortina Padova.
85. Dai, K., *Rational utilization of the stress shielding effect of implants*. 1st ed. Biomechanics and biomaterials in orthopedics, ed. D.G. Poitout 2004, London, United Kingdom: Springer - Verlag.
86. Lucas, G.L., F.W. Cooke, and E. Friis, *A primer of biomechanics* 1999, New York, United States of America: Springer.
87. Zhou, X., et al. *Finite element analysis of mechanical properties of wooden club shaped and general screws with interlocking intramedullary nail* in *IEEE International Conference on Mechatronics and Automation*. 2014. Tianjin, China.

88. Morawska-Chochół, A., et al., *Influence of the intramedullary nail preparation method on nail's mechanical properties and degradation rate*. Materials Science and Engineering: C, 2015. **51**: p. 99-106.
89. Leong, J.C.Y. and W.W. Lu, *Biomechanics and biomaterial*, in *Biomechanics and biomaterials in orthopedics*, D.G. Poitout, Editor 2004, Springer - Verlag: London, United Kingdom. p. ix-xv.
90. Synthes, PFNA. *Proximal Femoral Nail Antirotation - Technique Guide*, 2014: Oberdorf, Switzerland. p. 5.
91. Borrelli, J., *Intramedullary nailing of the tibia*, in *Practical procedures in orthopaedic trauma surgery*, P.V. Giannoudis and P. Hans-Christoph, Editors. 2014, Cambridge University Press: New York, United States of America. p. 346-354.
92. Al-Omari, A., P. Kendrick, and C.S. Roberts, *Antegrade intramedullary nailing of the humerus*, in *Practical procedures in orthopaedic trauma surgery*, P.V. Giannoudis and P. Hans-Christoph, Editors. 2014, Cambridge University Press: New York, United States of America. p. 48-52.
93. Al-Omari, A., P. Kendrick, and C.S. Roberts, *retrograde intramedullary nailing of the humerus*, in *Practical procedures in orthopaedic trauma surgery*, P.V. Giannoudis and P. Hans-Christoph, Editors. 2014, Cambridge University Press: New York, United States of America. p. 52-56.
94. Gaebler, C., et al., *The fatigue strength of small diameter tibial nails*. Injury, 2001. **32**(5): p. 401-405.
95. Lacroix, D. and P.J. Prendergast, *Three-dimensional simulation of fracture repair in the human tibia*. Computer Methods in Biomechanics and Biomedical Engineering, 2002. **5**(5): p. 369-376.
96. Ouyang, X., et al., *Interlocking intramedullary nails in fracture treatment*. Cell Biochemistry and Biophysics, 2015. **73**(1): p. 261-265.
97. Lichte, P. and P. Hans-Cristoph, *Tibia shaft fractures*, in *Bone and joint injuries: Trauma surgery III*, H.-J. Oestern, O. Trentz, and S. Uranues, Editors. 2014, Springer - Verlag: London, United Kingdom. p. 341-346.
98. Zirkle, L.G., *Technique manual of SIGN IM Nail & interlocking screw system insertion & extraction guide*, S.F.C. International, Editor 2012: Washington, USA. p. 1-47.
99. Sié, E.J.B., et al., *Primary unreamed and unlocked intramedullary nailing of femoral shaft fractures*. Malaysian Orthopaedic Journal, 2012. **6**(3): p. 13-17.
100. Shah, R.K., et al., *Surgical Implant Generation Network (SIGN) intramedullary nailing of open fractures of the tibia*. International Orthopaedics, 2004. **28**(3): p. 163-166.
101. Steiner, M., et al., *Disadvantages of interfragmentary shear on fracture healing—mechanical insights through numerical simulation*. Journal of Orthopaedic Research, 2014. **32**(7): p. 865-872.
102. Dresing, K., *Diaphyseal fractures*, in *Techniques and principles for the operating room*, M. Porteous and S. Bäuerle, Editors. 2010, Thieme: Davos Platz, Switzerland. p. 170-175.
103. Kaspar, K., et al., *Angle stable locking reduces interfragmentary movements and promotes healing after unreamed nailing*. Journal of Bone and Joint Surgery. American Volume, 2005. **87**(9): p. 2028-2037.
104. Bailón-Plaza, A. and M.C.H. van der Meulen, *Beneficial effects of moderate, early loading and adverse effects of delayed or excessive loading on bone healing*. Journal of Biomechanics, 2003. **36**(8): p. 1069-1077.
105. Goodship, A.E., T.J. Lawes, and C.T. Rubin, *Low-magnitude high-frequency mechanical signals accelerate and augment endochondral bone repair: Preliminary evidence of efficacy*. Journal of Orthopaedic Research, 2009. **27**(7): p. 922-930.
106. Leung, K.S., et al., *Low-magnitude high-frequency vibration accelerates callus formation, mineralization, and fracture healing in rats*. Journal of Orthopaedic Research, 2009. **27**(4): p. 458-65.

107. Zhang, X., et al., *In vivo assessment of the effect of controlled high-and low-frequency mechanical loading on peri-implant bone healing*. Journal of the Royal Society Interface, 2012. **9**: p. 1697-1704.
108. Gómez-Benito, M.J., et al., *Influence of high-frequency cyclical stimulation on the bone fracture-healing process: Mathematical and experimental models*. Philosophical Transactions of the Royal Society of London A: Mathematical, Physical and Engineering Sciences, 2011. **369**(1954): p. 4278-4294.
109. Claes, L., et al., *Influence of size and stability of the osteotomy gap on the success of fracture healing*. Journal of Orthopaedic Research, 1997. **15**(4): p. 577-584.
110. Hak, D.J., et al., *The influence of fracture fixation biomechanics on fracture healing*. Orthopedics, 2010. **33**(10): p. 752-755.
111. Granta - Material Intelligence, *CES EduPack*, 2015: Cambridge, United Kingdom.
112. Perren, S.M., *Physical and biological aspects of fracture healing with special reference to internal fixation*. Clinical Orthopaedics and Related Research, 1979. **138**: p. 175-196.
113. Yamaji, T., et al., *The effect of micromovement on callus formation*. Journal of Orthopaedic Science, 2001. **6**(6): p. 571-575.
114. Perren, S.M., *Evolution of the internal fixation of long bone fractures. The scientific basis of biological internal fixation: choosing a new balance between stability and biology*. The Bone and Joint Journal, 2002. **84**(8): p. 1093-1110.
115. Comiskey, D.P., et al., *The role of interfragmentary strain on the rate of bone healing—A new interpretation and mathematical model*. Journal of Biomechanics, 2010. **43**(14): p. 2830-2834.
116. Augat, P., et al., *Interfragmentary movement in diaphyseal tibia fractures fixed with locked intramedullary nails*. Journal of Orthopaedic Trauma, 2008. **22**(1): p. 30-36.
117. Wu, X., et al., *A biomechanical comparison of two intramedullary implants for subtrochanteric fracture in two healing stages: a finite element analysis*. Applied Bionics and Biomechanics, 2015. **2015**: p. 1-7.
118. Filardi, V., *The healing stages of an intramedullary implanted tibia: A stress strain comparative analysis of the calcification process*. Journal of Orthopaedics, 2015. **12**(1): p. S51–S61.
119. Morgan, E.F. and J. Lei, *Toward clinical application and molecular understanding of the mechanobiology of bone healing*. Clinical Reviews in Bone and Mineral Metabolism, 2015. **13**(4): p. 256-265.
120. Horn, J., et al., *Angle stable interlocking screws improve construct stability of intramedullary nailing of distal tibia fractures: A biomechanical study*. Injury, 2009. **40**(7): p. 767-771.
121. Verlag Stahlschlüssel, *Stahlschlüssel: Key to steel*. 23th edition ed2013, Marbach, Germany.
122. EUROFLEX GmbH, *Stainless steel turbing for surgical implants - 316L medical grade, ASTM F 138, material data*, 2016: Pforzheim, Germany.
123. Fort Wayne Metals, *316 LVM - Material data*, 2016: Co Mayo, Ireland.
124. Breme, J. and V. Biehl, *Metallic biomaterials*, in *Handbook of Biomaterial Properties*, J. Black and G. Hastings, Editors. 1998, Springer Science & Business Media: London, United Kingdom. p. 135-213.
125. Ramakrishna, S., et al., *Biomedical applications of polymer-composite materials: A review*. Composites Science and Technology, 2001. **61**(9): p. 1189–1224.
126. ASM International, *Materials and Coatings for Medical Devices: Cardiovascular*. ASM Materials and Processes for Medical Devices 2009, Ohio, USA: ASM International.
127. Disegi, J., *Implant materials – Titanium-6% Aluminum-7% Niobium* Synthes, Editor 2008: Pennsylvania, United States of America. p. 1-19.
128. Koyun, A., E. Ahlatcioğlu, and Y.K. İpekYıldız, *A roadmap of biomedical engineers and milestones*. Biosensors and Theory Principles, 2012: p. 115-143.

129. Montes de Oca, H. and I.M. Ward, *Structure and mechanical properties of poly(L-lactic acid) crystals and fibers*. Journal of Polymer Science Part B: Polymer Physics, 2007. **45**(8): p. 892-902.
130. Patel, N.R. and P.P. Gohil, *A review on biomaterials: Scope, applications and human anatomy significance*. International Journal of Emerging Technology and Advanced Engineering, 2012. **2**(4): p. 91-101.
131. Bagheri, Z.S., et al., *Biomechanical properties of an advanced new carbon/flax/epoxy composite material for bone plate applications*. Journal of the Mechanical Behavior of Biomedical Materials, 2013. **20**: p. 398-406.
132. Liang, S., P.B. Gning, and L. Guillaumat, *Fatigue behavior of flax/epoxy composite*, in *18th International Conference on Composite Materials* 2011: Jeju Island, Korea. p. 1-6.
133. Teoh, S.H., Z.G. Tang, and G.W. Hastings, *Thermoplastic polymers In biomedical applications: Structures, properties and processing*, in *Handbook of Biomaterial Properties*, J. Black and G. Hastings, Editors. 1998, Springer Science & Business Media: London, United Kingdom. p. 270-301.
134. Lewis, D., et al., *Low cost polymer intramedullary nails for fracture fixation: a biomechanical study in a porcine femur model*. Archives of Orthopaedic and Trauma Surgery, 2009. **129**(6): p. 817-822.
135. Lerch, B.A., J.C. Thesken, and C.T. Bunnell, *Polymethylmethacrylate (PMMA) material test results for the capillary flow experiments (CFE)*, 2007, NASA STI Program: Ohio, United States of America. p. 1-16.
136. Sorbie, C., R. Zdero, and J.T. Bryant, *Normal and prosthetic hip biomechanics*, in *Biomechanics and Biomaterials in Orthopedics*, D.G. Poitout, Editor 2004, Springer-Verlag: London, UK. p. 528-249.
137. Boger, A., et al., *Variation of the mechanical properties of PMMA to suit osteoporotic cancellous bone*. Journal of Biomaterials Science, Polymer Edition, 2008. **19**(9): p. 1125–1142.
138. Mantripragada, V.P., et al., *An overview of recent advances in designing orthopedic and craniofacial implants*. Journal of Biomedical Materials Research Part A, 2013. **101**(11): p. 3349-3364.
139. Farraro, K.F., et al., *Revolutionizing orthopaedic biomaterials: The potential of biodegradable and bioresorbable magnesium-based materials for functional tissue engineering*. Journal of Biomechanics, 2014. **47**(9): p. 1979-1986.
140. Petrini, L. and F. Migliavacca, *Biomedical applications of shape memory alloys*. Journal of Metallurgy, 2011. **2011**: p. 1-15.
141. Sun, Q.-P. and Z.-Q. Li, *Phase transformation in superelastic NiTi polycrystalline microtubes under tension and torsion—from localization to homogeneous deformation*. International Journal of Solids and Structures, 2002. **39**(13): p. 3797-3809.
142. Schwartz, M., *New Materials, Processes, and Methods Technology*, ed. M. Schwartz 2005, Florida, United States of America: CRC Press.
143. Ryhänen, J., *Biocompatibility evaluation of nickel-titanium shape memory metal alloy*, in *Department of Surgery* 1999, Oulu University: Oulu, Finland. p. 28-30.
144. Byrne, D.P., D. Lacroix, and P.J. Prendergast, *Simulation of fracture healing in the tibia: Mechanoregulation of cell activity using a lattice modeling approach*. Journal of Orthopaedic Research, 2011. **29**(10): p. 1496-1503.
145. Wang, X., et al., *Fundamental biomechanics in bone tissue engineering*, ed. K.A. Athanasiou 2010, California, United States of America: Morgan & Claypool.
146. Currey, J., *Cortical bone*, in *Handbook of Biomaterial Properties*, J. Black and G. Hastings, Editors. 1998, Springer Science & Business Media: London, United Kingdom. p. 3-13.
147. Hench, L.L. and J. Wilson, *Introduction*, in *An Introduction to Bioceramics*, L.L. Hench and J. Wilson, Editors. 1993, World Scientific: London, UK. p. 1-24.

148. Hak, D.J., et al., *Use of carbon-fiber-reinforced composite implants in orthopedic surgery*. Orthopedics, 2014. **37**(12): p. 825-830.
149. Maniscalco, P., *Preliminary experience with carboFix - Radiolucent distal fibula*, 2014, AOFAS meeting: Chicago, USA.
150. Steinberg, E.L., et al., *Carbon fiber reinforced PEEK Optima—A composite material biomechanical properties and wear/debris characteristics of CF-PEEK composites for orthopedic trauma implants*. Journal of the Mechanical Behavior of Biomedical Materials, 2013. **17**: p. 221–228.
151. Pichler, K., et al., *Cellular reactions to biodegradable magnesium alloys on human growth plate chondrocytes and osteoblasts*. International Orthopaedics, 2014. **38**(4): p. 881-889.
152. Rössig, C., et al., *In vivo evaluation of a magnesium-based degradable intramedullary nailing system in a sheep model*. Acta Biomaterialia, 2015. **25**: p. 369-383.
153. Dai, K. and C.Q. Ning, *Shape memory alloys and their medical application*. 1st edition ed. Biomechanics and Biomaterials in Orthopedics, ed. D.G. Poitout 2004, London, UK: Springer-Verlag.
154. Prymak, O., et al., *Morphological characterization and in vitro biocompatibility of a porous nickel–titanium alloy*. Biomaterials, 2005. **26**(29): p. 5801-7.
155. Kujala, S., et al., *Bone modeling controlled by a nickel–titanium shape memory alloy intramedullary nail*. Biomaterials, 2002. **23**(12): p. 2535-2543.
156. Niinomi, M., *Recent metallic materials for biomedical applications*. Metallurgical and Materials Transactions A, 2002. **33**(3): p. 477-486.
157. Da, G.Z., et al. *Surgical treatment of tibial and femoral fractures with TiNi shape-memory alloy interlocking intramedullary nails*. in *International Conference on Shape Memory and Superelastic Technologies and Shape Memory Materials 2001*. Kunming, People's Republic of China
158. Da, G.Z., et al. *Surgical treatment of tibial and femoral fractures with TiNi shape-memory alloy interlocking intramedullary nails*. in *Materials Science Forum*. 2002. Switzerland: Trans Tech Publications Inc.
159. Cheung, G., et al., *Finite element analysis of a femoral retrograde intramedullary nail subject to gait loading*. Medical Engineering and Physics, 2004. **26**(2): p. 93-108.
160. Laflamme, G.Y., et al., *Proximal tibial fracture stability with intramedullary nail fixation using oblique interlocking screws*. Journal of Orthopaedic Trauma, 2003. **17**(7): p. 496-502.
161. Penzkofer, R., et al., *Influence of intramedullary nail diameter and locking mode on the stability of tibial shaft fracture fixation*. Archives of Orthopaedic and Trauma Surgery, 2009. **129**(4): p. 525-531.
162. Höntzsch, D., *Angular stable locking of intramedullary nails (ASLS) - A new system*, 2010, AO Foundation: Davos, Switzerland.
163. Flanagan, B.P., et al., *A Method to modify angle-stable intramedullary nail construct compliance*. The Iowa Orthopaedic Journal, 2014. **34**: p. 68.
164. Garlock, A.N., et al., *A modified intramedullary nail interlocking design yields improved stability for fatigue cycling in a canine femur fracture model*. Proceedings of the Institution of Mechanical Engineers, Part H: Journal of Engineering in Medicine, 2012. **226**: p. 469-476.
165. Dell'Oca, A.A.F., *Intramedullary nail including stable locking bolts*, 2009, Synthes USA, LLC: Montevideo, Uruguay.
166. Kuhn, S., et al., *A new angle stable nailing concept for the treatment of distal tibia fractures*. International Orthopaedics, 2014. **38**: p. 1255-1260.
167. Wähnert, D., et al., *The primary stability of angle-stable versus conventional locked intramedullary nails*. International Orthopaedics, 2012. **36**(5): p. 1059-1064.

168. Höntzsch, D., et al., *Evaluation of the Effectiveness of the Angular Stable Locking System in Patients with Distal Tibial Fractures Treated with Intramedullary Nailing*. Journal of Bone and Joint Surgery. American Volume, 2014. **96A**(22): p. 1889-1897.
169. Heiney, J.P., et al., *Distal femoral fixation: A biomechanical comparison of retrograde nail, retrograde intramedullary nail, and prototype locking retrograde nail*. Clinical Biomechanics, 2012. **27**(7): p. 692-696.
170. Smith & Nephew, *Trigen meta-nail system, tibial and retrograde femoral nail*, 2011, Smith & Nephew: London, UK.
171. Thelen, S., et al., *Angle stable locking nails versus conventionally locked intramedullary nails in proximal tibial shaft fractures: a biomechanical study*. Archives of Orthopaedic and Trauma Surgery, 2012. **132**(1): p. 57-63.
172. Zimmer, *Zimmer® Natural Nail® System*, 2010, Zimmer, Inc.: Indiana, USA.
173. Dailey, H.L., et al., *The Flexible Axial Stimulation (FAST) intramedullary nail provides interfragmentary micromotion and enhanced torsional stability*. Clinical Biomechanics, 2013. **28**: p. 579-585.
174. Lascombes, P., *Flexible intramedullary nailing in children: The Nancy University manual* 2009, Berlin, Germany: Springer-Verlag.
175. Ingman, A.M. and D.A. Waters, *Locked intramedullary nailing of humeral shaft fractures. Implant design, surgical technique, and clinical results*. Journal of Bone and Joint Surgery. British Volume, 1994. **76**(1): p. 23-29.
176. Steriopoulos, K.A., et al., *Placement of the distal locking screws of the femoral intramedullary nail without radiation*. Archives of Orthopaedic and Trauma Surgery, 1996. **115**(1): p. 43-44.
177. Durham, A.A. and D.P. Crickenberger, *Magnetic distal targeting for modular intramedullary nails*. Techniques in Orthopaedics, 1998. **13**(1): p. 71-78.
178. Al-Naemi, H.M., *Assessment of radiation dose for non-radiation workers in the medical field practices*. International Journal of Medical Physics, Clinical Engineering and Radiation Oncology, 2015. **4**(2): p. 85-95.
179. Ebrahimi, H., A. Yee, and C. Whyne, *Surgical process analysis identifies lack of connectivity between sequential fluoroscopic 2D alignment as a critical impediment in femoral intramedullary nailing*. International Journal of Computer Assisted Radiology and Surgery, 2015. **10**(69): p. 1-9.
180. Madan, S. and C. Blakeway, *Radiation exposure to surgeon and patient in intramedullary nailing of the lower limb*. Injury, 2002. **33**(8): p. 723-727.
181. Finestone, A., et al., *Do physicians correctly estimate radiation risks from medical imaging?* Archives of Environmental Health: An International Journal, 2003. **58**(1): p. 59-62.
182. Committee, B.E.I.R., *Health effects of exposure to low levels of ionizing radiation: BEIR V*, in 0-309-03995-9, E.N. Society, Editor 1990, The National Academies Press: Washington D.C., United States of America.
183. Müller, L.P., et al., *Radiation exposure to the hands and the thyroid of the surgeon during intramedullary nailing*. Injury, 1998. **29**(6): p. 461-468.
184. De Smet, K., et al., *Closed intramedullary tibial nailing using the Marchetti–Vincenzi nail: its use in closed and open fractures*. Injury, 2000. **31**(8): p. 597-603.
185. Anastopoulos, G., *Distal locking with mechanical jig (author's own technique)*, in *Practice of intramedullary locked nails: New developments in techniques and applications*, K.-S. Leung, G. Taglang, and R. Schnettler, Editors. 2006, Springer: Berlin, Germany. p. 271-274.
186. Liu, B., et al., *Comparison of our self-designed rotary self-locking intramedullary nail and interlocking intramedullary nail in the treatment of long bone fractures*. Journal of Orthopaedic Surgery and Research, 2014. **9**(47): p. 1-9.

187. Dursun, M., et al., *Does the magnetic-guided intramedullary nailing technique shorten operation time and radiation exposure?* European Journal of Orthopaedic Surgery and Traumatology, 2014. **24**(6): p. 1005-1011.
188. Londei, R., et al., *Intra-operative augmented reality in distal locking*. International Journal of Computer Assisted Radiology and Surgery, 2015. **10**(9): p. 1395-1403.
189. Cunningham, J.L., J. Kenwright, and C.J. Kershaw, *Biomechanical measurement of fracture healing*. Journal of Medical Engineering and Technology, 1990. **14**(3): p. 92-101.
190. Akkus, O., et al., *Relation between mechanical stiffness and vibration transmission of fracture callus: an experimental study on rabbit tibia*. Proceedings of the Institution of Mechanical Engineers, Part H: Journal of Engineering in Medicine, 1998. **212**(5): p. 327-336.
191. Joslin, C.C., et al., *Weight bearing after tibial fracture as a guide to healing*. Clinical Biomechanics, 2008. **23**(3): p. 329-33.
192. Augat, P., et al., *Biomechanical methods for the assessment of fracture repair*. Injury, 2014. **45**: p. S32-S38.
193. Claes, L.E. and J.L. Cunningham, *Monitoring the mechanical properties of healing bone*. Clinical Orthopaedics and Related Research, 2009. **467**(8): p. 1964-1971.
194. Faroug, R., et al., *Strain response of an instrumented intramedullary nail to three-point bending*. Journal of Medical Engineering and Technology, 2011. **35**: p. 275-282.
195. Nikiforidis, G., et al., *Monitoring of fracture healing by lateral and axial vibration analysis*. Journal of Biomechanics, 1990. **23**(4): p. 323-330.
196. Protopappas, V.C., et al., *Ultrasonic monitoring of fracture healing*, in *Bone quantitative ultrasound*, P. Laugier and G. Haïat, Editors. 2010, Springer: New York, United States of America. p. 361-80.
197. Richardson, J.B., J. Kenwright, and J.L. Cunningham, *Fracture stiffness measurement in the assessment and management of tibial fractures*. Clinical Biomechanics, 1992. **7**(2): p. 75-79.
198. Wade, R.O. and J. Richardson, *Outcome in fracture healing: A review*. Injury, 2001. **32**(2): p. 109-14.
199. Morshed, S., et al., *Outcome Assessment in Clinical Trials of Fracture-Healing*. J Bone Joint Surg Am, 2008. **90**(1): p. 62-7.
200. Dijkman, B.G., et al., *When is a fracture healed? Radiographic and clinical criteria revisited*. Journal of orthopaedic trauma, 2010. **24**: p. S76-S80.
201. Greve, D.W., I.J. Oppenheim, and A.F. Chen. *An instrumented intramedullary implant to monitor strain in fracture healing*. in *Ultrasonics Symposium (IUS), 2012 IEEE International*. 2012. Dresden, Germany: IEEE.
202. Guda, T., et al., *Quality of bone healing: Perspectives and assessment techniques*. Wound Repair and Regeneration, 2014. **22**: p. 39-49.
203. Lowet, G., X. Dayuan, and G. Van der Perre, *Study of the vibrational behaviour of a healing tibia using finite element modelling*. Journal of Biomechanics, 1996. **29**(8): p. 1003-10.
204. Tower, S.S., R.K. Beals, and P.J. Duwelius, *Resonant frequency analysis of the tibia as a measure of fracture healing*. Journal of Orthopaedic Trauma, 1993. **7**(6): p. 552-7.
205. Benirschke, S.K., et al., *The use of resonant frequency measurements for the noninvasive assessment of mechanical stiffness of the healing tibia*. Journal of Orthopaedic Trauma, 1993. **7**(1): p. 64-71.
206. Lippmann, R.K., *The use of auscultatory percussion for the examination of fractures*. Journal of Bone and Joint Surgery. American Volume, 1932. **14**(1): p. 118-126.
207. Anast, G.T., T. Fields, and I.M. Siegel, *Ultrasonic Technique for the evaluation of bone fractures*. American Journal of Physical Medicine, 1958. **37**(3): p. 157-9.
208. Saulgozis, J., et al., *The effect of fracture and fracture fixation on ultrasonic velocity and attenuation*. Physiological Measurement, 1996. **17**(3): p. 201-211.

209. Foldes, A.J., et al., *Quantitative ultrasound of the tibia: A novel approach for assessment of bone status*. Bone, 1995. **17**(4): p. 363-367.
210. Machado, C.B., et al., *Experimental and simulation results on the effect of cortical bone mineralization in ultrasound axial transmission measurements: A model for fracture healing ultrasound monitoring*. Bone, 2011. **48**: p. 1202–1209.
211. Gerlanc, M., et al., *Ultrasonic study of normal and fractured bone*. Clinical Orthopaedics and Related Research, 1975. **111**: p. 175-180.
212. Njeh, C.F., et al., *The use of quantitative ultrasound to monitor fracture healing: a feasibility study using phantoms*. Medical Engineering and Physics, 1998. **20**: p. 781–786.
213. Barbieri, G., et al., *Ultrasonometric evaluation of bone healing: Experimental study using a model of diaphyseal transverse osteotomy of sheep tibiae*. Ultrasound in Medicine and Biology, 2006. **32**(6): p. 875–882.
214. Ryu, J., et al. *Diagnosis of dental cavity and osteoporosis using terahertz transmission images*. in *Ultrafast Phenomena XII: Proceedings of the 12th International Conference*. 2000. Charleston, USA: Springer Science & Business Media.
215. Sun, Y., et al., *A promising diagnostic method: Terahertz pulsed imaging and spectroscopy*. World Journal of Radiology, 2011. **3**(3): p. 55-56.
216. McFadyen, I. and S. Gallivan, *Metal removal*, in *Intramedullary nailing: A comprehensive guide*, P.M. Rommens and M.H. Hessmann, Editors. 2015, Springer: London, United Kingdom. p. 95-101.
217. Boerger, T.O., G. Patel, and J.P. Murphy, *Is routine removal of intramedullary nails justified?* Injury, 1999. **30**(2): p. 79-81.
218. Yadav, D., et al., *Removal of a broken distal cannulated intramedullary femoral nail with solid reamer with closed methods and without using C-arm: A case report*. Journal of Arthroscopy and Joint Surgery, 2015. **2**(1): p. 9-11.
219. Kumar, V., et al., *Removal of broken femoral intramedullary nail using Arthroscopic Flipcutter: A novel technique*. Techniques in Orthopaedics, 2014. **29**(3): p. 171-173.
220. Davidson, J.A. and N.B. Beals, *Fatigue resistant orthopaedic implant and method of manufacture*, 1991, Davidson, JA, Beals, NB, Smith & Nephew Richards Inc.: United States of America.
221. Brewster, N.T., G.P. Ashcroft, and T.R. Scotland, *Extraction of broken intramedullary nails - An improvement in technique* Injury, 1995. **26**(4): p. 286.
222. Metikala, S. and R. Mohammed, *Closed retrograde retrieval of the distal broken segment of femoral cannulated intramedullary nail using a Ball-Tipped Guide Wire*. Indian Journal of Orthopaedics, 2011. **45**(6): p. 347-350.
223. Middleton, R.G., et al., *Multiple guide wire technique for removal of the short distal fragment of a fractured intramedullary nail*. Injury, 1995. **26**(8): p. 531-532.
224. Steinberg, E.L., et al., *Removal of a broken distal closed section intramedullary nail*. Journal of Orthopaedic Trauma, 2004. **18**: p. 233–235.
225. Charnley, G.J. and W.J. Farrington, *Laparoscopic forceps removal of a broken tibial intramedullary nail*. Injury, 1998. **29**(6): p. 489-490.
226. Kim, Y.-M., Y.-B. Joo, and K.-Y. Leeb, *Use of a Nancy nail to remove a broken intramedullary nail: A technical note*. Injury, 2015. **46**(12): p. 2498–2501.
227. Rosa, N., et al., *From mechanical stimulus to bone formation: A review*. Medical Engineering and Physics, 2015. **37**(8): p. 719-728.
228. Metsemakers, W.-J., et al., *Influence of implant properties and local delivery systems on the outcome in operative fracture care*. Injury, 2016. **47**(3): p. 595-604.
229. Goodman, S.B., et al., *The future of biologic coatings for orthopaedic implants*. Biomaterials, 2013. **34**(13): p. 3174–3183.
230. van Baardewijk, L.J., et al., *Circulating bone morphogenetic protein levels and delayed fracture healing*. International Orthopaedics, 2013. **37**(3): p. 523-527.

231. Bergsma, E.J., et al., *Foreign body reactions to resorbable poly (L-lactide) bone plates and screws used for the fixation of unstable zygomatic fractures*. Journal of Oral and Maxillofacial Surgery, 1993. **51**(6): p. 666-670.
232. Morawska-Chochół, A., et al., *Gentamicin release from biodegradable poly-L-lactide based composites for novel intramedullary nails*. Materials Science and Engineering: C, 2014. **45**: p. 15-20.
233. Wildemann, B., et al., *Local BMP-2 application can rescue the delayed osteotomy healing in a rat model*. Injury, 2011. **42**: p. 746-752.
234. Raschke, M.J., S.B. Rosslenbroich, and T.F. Fuchs, *Antibiotic coated nails, in Intramedullary nailing: A comprehensive guide*, P.M. Rommens and M.H. Hessmann, Editors. 2015, Springer: London, United Kingdom. p. 555-564.
235. Craveiro-Lopes, N., *Treatment of open fractures of the tibia with a locked intramedullary nail with a core release of antibiotics (SAFE DualCore Universal): Comparative study with a standard locked intramedullary nail*. Journal of Limb Lengthening and Reconstruction, 2016. **2**(1): p. 17-22.
236. Raschke, M.J., S.B. Rosslenbroich, and T.F. Fuchs, *Gentamicin-coated Tibia Nails: Can We Afford NOT to Use Them?* Techniques in Orthopaedics, 2014. **29**(2): p. 62–68.
237. D'Lima, D.D., B.J. Fregly, and J.C.W. Colwell, *Implantable sensor technology: Measuring bone and joint biomechanics of daily life in vivo*. Arthritis Research and Therapy, 2013. **15**(203): p. 1-8.
238. Heinilä, H., et al., *Low cost miniaturization of an implantable prototype*. Circuit World, 2009. **35**(1): p. 34-40.
239. McGilvray, K.C., et al., *Implantable microelectromechanical sensors for diagnostic monitoring and post-surgical prediction of bone fracture healing*. Journal of Orthopaedic Research, 2015. **33**(10): p. 1439–1446.
240. Seide, K., et al., *Telemetric assessment of bone healing with an instrumented internal fixator: A preliminary study*. Journal of Bone and Joint Surgery. British Volume, 2012. **94**(3): p. 398-404.

“A clear understanding is critical to those managing bony injuries, as it is over this that the orthopaedic surgeon will ultimately have most control”

Paul J. Hardwood

3. Bone-intramedullary nail system stability

Tibial fractures are one of the most common serious musculoskeletal system injuries [1, 2]. Most fractures occur at the mid-shaft region and at the distal third of the tibia (where the smallest cross-section and moment of inertia are found) and for which interlocking intramedullary nails is considered the preferable method for stabilization and treatment [3-6]. The advantage of this method includes small operative scars [3], low infections rate [7], decreased blood loss [7], minimal disturbance to the fracture site and the surrounding soft tissues [8, 9], early patient ambulation [10] and an overall good results (decreased rates of delayed and non-union cases) [7] when compared to other stabilization methods.

Currently, intramedullary nailing is considered a very successful technique; nonetheless there is still space for improvement in order to enhance fracture healing. The quality and healing rate are strongly determined by the mechanical conditions at the fracture site. From all the mechanical factors involved, the width and fracture configuration and most decisively the type and amount of interfragmentary motion determine in the final outcome. The latter, results from bone-implant construct stability and the nature and quantity of the external loads applied [11, 12]. Unlike in engineering where the term stability denotes for the “ability of a structure to support a given load without experience a sudden change in its configuration” [13], in the medical science, however, deformation is of paramount importance where stable fracture fixation/bone systems should allow strain to the healing tissue on the fracture gap under physiological loading [14]. Any effort to optimize the stability of the intramedullary nailing techniques and improve fracture recovery requires a good understanding of the fracture fixation mechanics and its relation to physiological healing [15]. Computational and experimental mechanics are useful investigative techniques in biomechanical research and their potential are increased when anatomically contoured bone

models are used to evaluate the fixation method stability such as cadaveric and synthetic bone specimens where both models present strengths and weakness [16, 17].

Cadaveric specimens, by virtue of being human bone, and more accurately mimicking the *in vivo* behaviour, have long been used in orthopedic research [16]. However, these bone models are associated with a high cost - nearly three times more per specimen than the fourth-generation composite equivalents - and their mechanical properties have been shown to vary significantly between samples and are strongly dependent upon storage and handling procedures (*e.g.* removal of the tissue from the body), where variation as high as 10% have been registered. The cadaveric models available do not always allow for the study of young healthy bone cases. In addition, there is also a strong ethically, religiously and culturally controversy associated with experimentation on these models [18, 19]. By trying to overcome cadaveric test specimen's limitations, composite bone models which mimic the complex properties of physiological human bones were developed. The great improvement suffered by synthetic bone models in terms of composition and manufacturing process, since their introduction in 1987, led to the increase in their potential to be used as replacement of cadaver models in orthopaedic and biomechanical research [18, 20]. The first-generation composite bones models were poorly representative of the bone biomechanical behaviour. They were composed of a polyurethane foam core to mimic the trabecular bone and an epoxy-reinforced braided glass fiber was used as a cortical bone analog. Although the rigid polyurethane foam core presented mechanical properties in the range of human cancellous bone, its structure was not representative of the complex trabecular bone arrangement (*e.g.* in terms of porosity, structural orientation and connectivity) [19, 21]. The epoxy-reinforced braided glass fibre, cortical bone analog, was constituted by a weak bonding between the glass fibre and the epoxy components, as a result of glass sizing and which led to structure delamination. The second-generation composites bones were first presented in 1991 and replaced the previous cortical bone analogue with fiberglass fabric reinforced epoxy. However, the cortical layer required manual craftsmanship which restricted the manufacturing technique efficiency and consequently the model anatomic details and mechanical properties uniformity. Regardless of this limitation, the upgraded composites bone models were capable of successfully resembling cadaveric bones diaphyseal lateral bending rigidity values [18, 22]. In 1997, the third-generation composite bones were developed. The bone replicates were entirely manufactured with a pressure technique by which short glass fiber reinforced epoxy was injection-molded (cadaveric bone cast-based) around the polyurethane foam core to form the cortical wall [18]. In a comparative study between the second- and third-generation synthetic bones, Anneliese Heiner and Thomas Brown [22] demonstrated that the more recent model

presented improved characteristic when compared to the second-generation one, namely in terms of inter-specimen's uniformity structural properties and mean stiffness values that fall within the range of the ones obtained for cadaveric bones. However, this model was prone to crack nucleation and propagation leading to failure in fatigue or repeated quasistatic loading [23]. The fourth-generation composite bone, the most recent developed model so far, has the same geometry and manufacturing process as the previous generation bone replicate. The cortical bone analog, however, benefit from an optimized epoxy component to improve tensile and compressive modulus and strength, thermal stability and moisture resistance. Anneliese Heiner [20] validated this latest model through the evaluation of femur and tibia composites stiffness under bending, axial, and torsional loading and also the strain distribution along the femur proximal-medial diaphysis. With the exception of tibial flexural rigidity with the anterior surface in tension and femur compressive longitudinal strain at the second lowest strain gauge location, the fourth-generation composite bones biomechanical properties improved when compared with the previous composite model and were closer to the values measured for natural bones under the same testing conditions. Also the inter-specimen variability of the fourth-generation composites was demonstrated to be much less than that of natural bone. Gardner *et al.* [24] reported for the fourth-generation composite tibia an intra-specimen variability 10% from a total of 30 cases considered were negligible differences may be attributed to productions variations in size and composite quality. The results obtained in a study developed by Chong *et al.* [23], also demonstrated the fourth-generation composite model enhanced biomechanical properties through the comparison of the cortical bone analogue material with the E-glass-fiber-epoxy used in the previous generation model. This study also demonstrated an increase in the tensile properties, an increase of up to 48% in fracture toughness values and a decrease in the threshold stress intensity factor for crack propagation and in the fatigue crack growth rate. Hence, there was an improvement of fracture performance and an increase in fatigue lives of the latest generation model. The fourth-generation synthetic femurs composites models also approximated human femurs with respect to screw purchase behaviour when pull-out force, shear stress, and energy-to-pull-out were measured on cancellous [25] and cortical bone [26]. Nicayenzi *et al.* [27] also reported that composite human femurs accurately replicate human cortical properties during screw insertion. There is no general agreement as to whether the fourth-generation composite tibia should be used as a substitute for cadaveric specimens in bone and orthopaedic fixation implants constructs biomechanical studies. However, the physiological or near physiological stiffness values in torsional, axial compression and bending stiffness, the model low inter-specimen variability, consistent mechanical properties for long time periods and the easy availability and unlimited

number of samples which require no special handling or preservation demands [15, 16, 18, 22], led to the selection of the fourth-generation composite bone, in detriment of the highly complex and challenging to use, cadaveric bone models, for the study of the tibia-intramedullary nail construct stability presented in this chapter.

The assessment of the intramedullary nailing fixation stability *in vivo* is difficult if not impossible, which limits the success of orthopedic biomechanical research to be achieved by combining the *in vitro* and *in silico* analysis for system evaluation and improvement [28]. In most bone-intramedullary nail studies (see Table 3.1), finite element analysis and experimental mechanical testing have been conducted more often separately than combined. There is a clear advantage in using the finite element analysis since it provides detailed information of strain and stress field on the entire structure and in sites which are difficult to measure through *in vivo* experimentation. However, the accuracy and prediction ability of the finite element model is solely and reliably guaranteed by mechanical experimental validation [29, 30].

Various stiffness determination studies have been reported in literature (see Table 3.1). These biomechanical studies conducted comprehensive analysis on the influence of intramedullary nail fixation parameters (*e.g.* compliance, clearance and nail diameter in conjugation with the appropriate interlocking mode on the overall bone-implant complex stability) [11, 31]. However, there is a considerable variability among the procedure used for stiffness evaluation. The experiments parameters varied from bone alignment, the manner and amount of loads applied, the method used for displacement measurements and the way that stiffness values are calculated. These variabilities are present not only among bone-intramedullary nail system stability evaluation but also in tibiae whole-bone biomechanical behavior studies (see Table 3.1). Therefore, there is no standardized method for bone-implant stiffness determination. Some of the major problems in determining tibia stress patterns and fracture interfragmentary translations result from some restrictions imposed by the bone itself, such as its size, its irregular geometry, difficulties in the specimens gripping and also the relatively low loads that can be applied. And although, the experimentation methods are based in the fundamental principles of mechanics, the tibia intrinsic limitations have jeopardized the generalization of an engineering testing method for tibia bone as an organ [32].

Table 3.1 - Review on in vitro mechanical experimentation (ME) and/or finite element analysis (FE) of tibia bone with or without an intramedullary nail implanted. M – Medium size, L - Large size, S – Sagittal plane, C - Coronal plane, IR - Internal rotation, ER - External rotation, AT - Anterior surface in tension, PT - Posterior surface in tension, LT - Lateral surface in tension, NIA – No information available

| Study | Bone model (No. samples) [Sample dimension] | Intramedullary nail diameter, type, brand | Fracture location (width) | Load mode | | | | Load/Moment (Rate) [Sample orientation/ direction of rotation] | Data acquisition | Reference |
|-------|---|---|------------------------------|-------------------|-----------------|---------|-------|--|-----------------------------------|-------------------|
| | | | | Axial compression | 4-Point Bending | Torsion | Shear | | | |
| ME | Metallic tube with polyurethane washers | 7 mm, aap Biorigid Nail® 8 mm, aap Biorigid Nail® 8 mm, Ace UTN® 8 mm, RT Tibial Nail® 8 mm, Synthes UTN® | Distal (55 mm) | | | | | 1920 N | Load cell | [33] ¹ |
| ME | Cadaveric tibiae (5) | 9 mm, T2 tibia nail, Stryker | Central (8 mm) | | | | | 100 N | Ultrasound-based motion system | [31] |
| | | | | | | | | ±20 Nm [S,C] | | |
| | | | | | | | | 5 Nm [IR,ER] | | |
| | | | | | | | | ±100 N [S,C] | | |
| ME | 3G composite (1)[L] | 9 mm, Expert Tibial Nail, Synthes | Distal (10 mm) | | | | | 1300 N | Displacement transducers | [34] |
| ME | Cadaveric tibiae (8) | 10 mm, Expert Tibial Nail, Synthes | Distal (7 mm) | | | | | 500 N | Video optical measurement system | [8] |
| ME | Cadaveric tibiae (12) | 9 mm, T2 tibia nail, Stryker | Central (8 mm) | | | | | 100 N | Ultrasound-based 3D motion system | [11] |
| | | | | | | | | ±20 Nm [S,C] | | |
| | | | | | | | | 5 Nm [IR,ER] | | |
| | | | | | | | | ±100 N [S,C] | | |
| ME | Cadaveric tibiae (8) | 10 mm ≥, modified Synthes nails | Central (2 mm) | | | | | 147 N (0.25 mm/s) | Extensometers | [35] |
| FE | Cadaveric tibiae (5) | Synthes UTN® | NIA | | | | | 500 N | - | [32] |
| | | | | | | | | 15 Nm | | |
| FE | Human tibia (1) | No information | Central (-) | | | | | 250, 500, 1000 and 1500 N | - | [36] |
| FE | Human tibia (1) | 8 to 10 mm, Expert tibial nails, Synthes | Central (9 mm) | | | | | 700 N | - | [28] |

| | | | | | | | | | | |
|---------|--|-------------------------------|----------------|--|--|--|--|---|------------------|------|
| FE | Human tibia (1) | 11 mm, T2 tibia nail, Stryker | Central (8 mm) | | | | | ±100 N [S,C] | - | [37] |
| FE | Human tibia (1) | - | - | | | | | - | - | [38] |
| | | | | | | | | 500 N (0.05 mm/s)[AT,MT] | | |
| | | | | | | | | Until 5°reach (0.23 mm/s)[IR] | | |
| FE | Human tibia (-) | - | - | | | | | 800 N | - | [39] |
| | | | | | | | | 4.8 Nm | | |
| FE | Human tibia (1) | - | - | | | | | 750, 900 and 1000 N | - | [40] |
| ME | 3G composite (8)[M] Cadaveric tibiae (8) | - | - | | | | | - | Load cell | [41] |
| | | | | | | | | 31 Nm (0.05 mm/s) | | |
| | | | | | | | | 5 N/m (0.2 deg/s) | | |
| ME | 4G composite (6)[M] 3G composite (6)[M] Cadaveric tibiae (-) | - | - | | | | | 60 to 600 N (60 N/s) | 5 strain gauge | [20] |
| | | | | | | | | 500 N (0.025 mm/s) | | |
| | | | | | | | | 0.5 to 7.5 Nm (0.25°/s) | | |
| ME | 3G composite (6)[M] 2G composite (6)[M] | - | - | | | | | 60 to 600 N (60 N/s) | Load cell | [22] |
| | | | | | | | | 500 N (0.025 mm/s) | | |
| | | | | | | | | 0.5 to 15 Nm (0.25°/s) | | |
| ME | 4G composite (30)[L] Cadaveric tibiae based in [41] | - | - | | | | | 60 to 600 N → failure (60 Nm/s → continuously) | Load cell | [24] |
| | | | | | | | | 50 to 500 N → failure (50 N/s → 0.025 mm/s) | | |
| | | | | | | | | 0 Nm to failure (0.25°/s) [ER] | | |
| FE & ME | Cadaveric tibia (1) | - | - | | | | | 300 N | 17 strain gauges | [29] |
| | | | | | | | | 500 N | | |
| | | | | | | | | 20 Nm | | |
| FE & ME | 3G composite (2)[M] | - | - | | | | | 700 N (35 N/s) | Strain gauges | [42] |
| | | | | | | | | 500 N (0.05 mm/s) | | |
| | | | | | | | | 20 Nm (1 Nm/s) | | |

¹Only Gaebler *et al.* [33] used solid intramedullary nails, all the other authors used cannulated nails models

According to Raunest *et al.* [32] a realistic representation of the bone-implant complex behavior requires mimicking the physiological conditions in terms of type of load and tibia orientation. Most of the studies concerning the intramedullary nails system stability considered only axial compression loading mode [8, 28, 33-36, 43] while only a reduced number of studies considered a greater range of tests [11, 31, 32]. In the present work, all the load components typically applied to the tibia in physiological activity were considered: axial compression, bending, torsion, and shear loading mode. Performing the full range of loading mode on the whole-tibia model has the added difficulty of attaching the specimen to the testing machine and also aligning it according to its physiological orientation [19].

Several authors have claimed [20, 22, 24, 41] high set-up variability and difficulty in obtaining reproducible bone alignment between mechanical experimentations. During axial and torsional loading tests some authors [11, 31, 35], oriented the tibiae vertically, according to its long axis parallel to the base plate of the testing machine. The proximal bone was fixed with a fast-curing resin embedding it in a cardiac hinge where a water level was used for the long axis adjustment. In other studies, [20, 22], where composite tibia models, instead of cadaveric ones, were used, it was possible to align the bone using a rigid, centrally located rod, which went up into the intramedullary shaft. In these experiments the tibiae were also oriented vertically, however there is a greater degree of alignment reproducibility between mechanical experiments. However, it is not always possible to replace cadaveric models by composite replicates. More accurately realistic experiments demand anatomical samples. Gray *et al.* [29, 42] in a rougher approach defined a set of reference axes (a bone coordinate system), which were marked on the surface of the cadaveric tibia to help align the bone during experiments and correlate the alignment with the finite element model experiments. In 4-point bending and shear loading tests, the tibia non-uniform cross section sets a challenge in loading identically all points along the bone. This could infer additional error to the results [44]. For the whole-bone 4-point bending behavior analysis, Cristofolini and Viceconti [41], used four rollers, where the geometry of two of the inner rollers were adjustable in height to allow for equal load distribution between them and the other two external rollers presented clamps to prevent the tibia from rotating. For the bending and shear tests, Augat *et al.* and Penzkofer *et al.* [11, 31], design the fixing jigs with a generic central triangular gap to help align the biased tibia triangular cross-section in the coronal and sagittal planes during loading. Although, there is a higher control on the bone orientation, different bones samples may not always be placed with the same precise orientation and loading application may not always be applied in the same region since the triangular shaped-bone contact jig site will align the tibia according to its anterior border.

The goal in this Chapter is to propose a simple methodology to evaluate the stiffness of the tibia-intramedullary nail construct under different loading conditions that occur during the patient's early healing phase where partial-weight bearing on the fracture would be expected as a result of the patient's motion with crutches. It is important to highlight that the procedure described does not aim to be defined as a standardized method for bone-implant stiffness determination. However, a description of a comprehensive and reproducible set of testing conditions for finite element analysis and validation by mechanical experimentation is expected. Special fixtures were developed to guarantee physiological tibia orientation and load application and reproducible alignment between different mechanical experiments and between mechanical and finite element experimentation.

3.1. Material and methods

3.1.1. Tibia finite element model construction

i) Geometry acquisition, axis determination and tibia planes-based alignment

The computed-aided jig design started with the acquisition, through a 3D scan (ATOS Triple Scan from GOM, Braunschweig, Germany), of a realistic computational external surface from the synthetic human tibia model (4th generation, medium left, model #3401, from SawBones Europe AB, Malmö, Sweden). This composite tibia model was used throughout the study in both finite element simulation and mechanical experimentation. The data obtained was imported into SolidWorks (Dassault Systèmes, Concord, Massachusetts, USA) using stereolithography file format. SolidWorks software was used for surface preparation (*e.g.* topographic cleanup of surface) and solid model construction. The bone's microstructure was ignored and it was treated as a continuum medium. The tibia was physiologically aligned by its three planes, coronal, sagittal and transverse which were determined based in its two main axis lines: anatomical and mechanical. The coronal plane was defined by the anatomical and mechanical axis [45]. In normal aligned lower limb, from a frontal view, the anatomical axis - the mid-diaphyseal line through the tibia medullary canal [45, 46] - is parallel and only few negligibly millimeters medially to the mechanical axis of the lower limb [47-49]. The mechanical axis is defined as the line passing through the center of the knee to the center of the ankle [50]. Also but not very relevant for this specific case, the tibia anatomic axis thus subtends an angle of 3° with the vertical axis, which is the vertical line drawn downwards from the symphysis pubis [46]. The sagittal plane was defined by the mechanical axis [45] and from an anatomical and functional perspective, the orientation of the tibia is best described by the bone's mechanical axis [49]. The knee moves in the sagittal plane during locomotion and other physical activities so the

orientation of the mechanical axis reflects the alignment in stance [45, 49]. The transverse plane describes the foot position during stance [45] and it was defined parallel to the coronal and sagittal planes. The anatomical axis was determined based on the method suggested by Han *et al.* [51] where it was considered as the line connecting the upper and lower midpoints of the shaft at 7 cm below the tibial plateau and 7 cm above the plafond (see Figure 3.1). The mechanical axis was determined through the method described by Yoshioka *et al.* [50] where the knee center at the tibial plateau was considered as the midpoint between the medial and lateral intercondylar eminences and the center of the ankle was defined as the intersection point of two diagonals drawn from the corners of the weight-bearing area of the tibia plafond (distal articular surface). For validation, the method described by Ruth and Hayes [52] was also used. Positive X,Y,Z directions are anterior, lateral and proximal, respectively. The XY plane was settled parallel to the tibia transverse plane (as it is oriented vertically according to its mechanical axis and the Z-axis) and the X-axis was formed by the intersection of the sagittal and the transverse plane (see Figure 3.1).

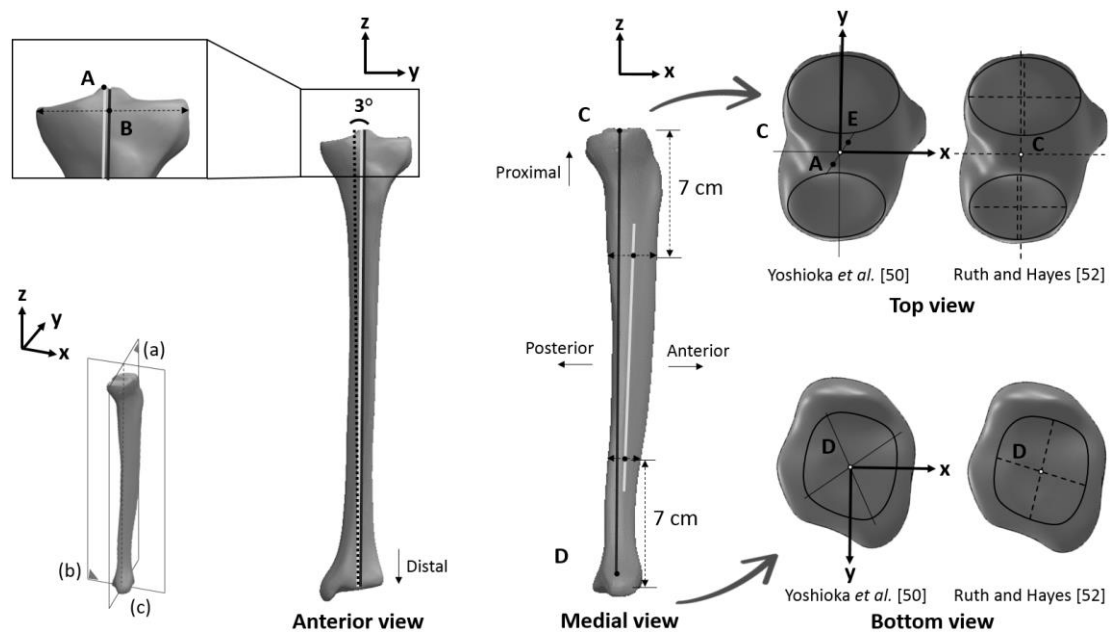


Figure 3.1 - Diagram showing the physiological orientation of the tibia. Where the orientation planes - coronal (a) and sagittal (b) - and the tibia reference axes: the vertical axis (dark dotted line), the mechanical axis (dark gray continuum line or (c)) and the anatomical axis (light gray continuum line), are represented. A - Medial spine (or medial intercondylar eminence), B - Center of the tibia, C - Knee center, D - Ankle center, E - Lateral spine (or lateral intercondylar eminence)

ii) Cortical and trabecular sites definition, intramedullary nail model design and placement

To obtain physiologically more realistic model, cortical and trabecular bone portions were considered. The bone composite structure was obtained by assembling the cortical shell to the trabecular nucleus (result of the subtraction of the cortical shell from the tibia original volume).

Tibia cortical tissue thickness varies along the bone. Since no detailed information on cortical bone thickness distribution along the composite model was provided by the manufacturer and there was only one bone sample available for test (refuting the possibility of cross-section cutting for thickness measurement), physiological-like values were considered (see Figure 3.2). In a simplified approach, the bone was divided in six distinct segments considered at 10, 20, 40, 60 and 80 percent of the tibia total length from the bottom of the medial malleolus to the top of the intercondylar eminence according to the standard tibial measures (see Figure 3.3) [53]. For each segment, cross-sections of 5% apart from each other were considered and were all obtained as transverse cuts perpendicularly to the tibia anatomical axis. Each of the cross-section images and scale information were obtained in SolidWorks and the cortical wall thickness measurements were developed in a java-based image processing software, ImageJ (National Institutes of Health, Maryland, USA). The cortical wall thickness for each segment was determined as the total average of the widths values measured around each 5% cross-sections.

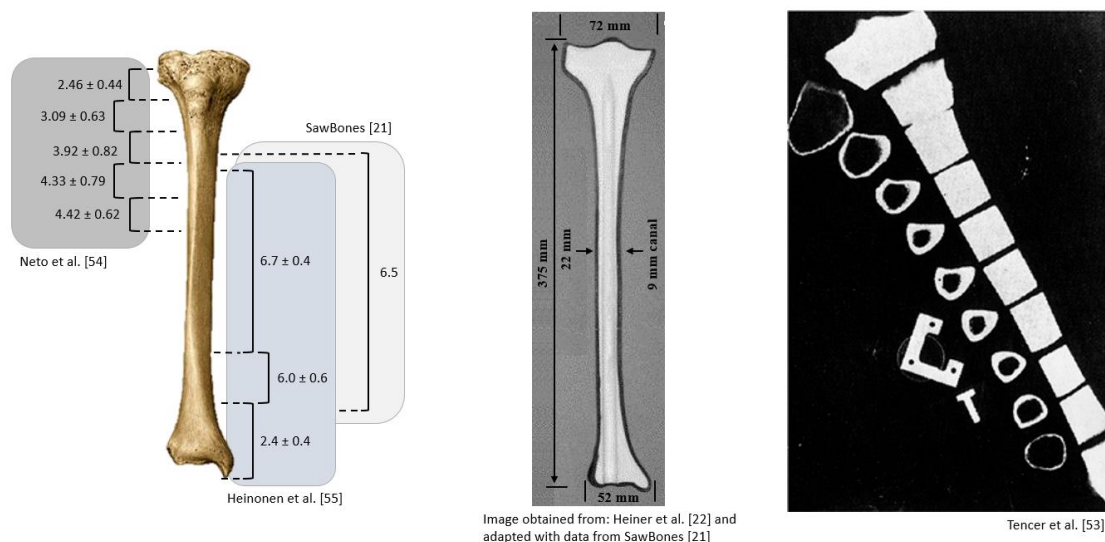


Figure 3.2 - SawBones manufacture information [21] and physiological values from literature [22, 54-56] on cortical bone thickness distribution along the tibia

The intramedullary nail implant used was the same during the mechanical experimentation and finite element simulations. The suitable nail length range was determined from the subtraction of between 30 to 40 mm to the tibia length [57, 58]. The composite tibia length - defined as the distance measured parallel to the longitudinal axis, between the plafond and the tibia plateau - was 375 mm. Thus an appropriate nail for this composite tibia should present a length between 340 to 350 mm. Considering the fixation implant dimensions supplied by the manufacture, a cannulated AISI 316L ASTM F318 stainless steel intramedullary nail (model M596222 AB0366 T, L.A. Medicals, Albergaria-a-Velha, Portugal) with 9-mm-diameter per 345 mm length, was

selected. The intramedullary nail structure was modeled in SolidWorks after accurate measurements obtained from the original metallic implant. The SolidWorks intramedullary nail structure design was validated through the comparison between the model and the real implant resonance frequencies which is the system natural frequency. For the real intramedullary nail the values were obtained through an acoustic resonance analysis. In this method the nail, placed on soft tips to avoid damping effects, was suitably stimulated by creating a surface impact with a small metal hammer. This mechanical stimulation made the nail vibrate in its characteristic frequency and forms. The vibrations were then measured by a microphone mounted close to the nail surface which collected these frequencies and converted them into electrical signals and then into numerical values. The finite element model intramedullary nail harmonics were obtained through free-free boundary condition simulation in ANSYS Workbench 15.0 (ANSYS Inc., Canonsburg, Pennsylvania, USA). Based on the resulting percentage error variation of 7.6, 5.5 and 6.4 for the natural frequency, second and third harmonic, respectively, the intramedullary nail modeled in SolidWorks was considered a valid approximation. Locking screws were modeled with a simplified geometry as 5.0 mm cylindrical shaped solid body (screw threads were not modeled) and positioned to protrude approximately 2 mm out of the bone. Assemblage of the intramedullary nail in the bone was accomplished in SolidWorks and accurate clinical scenario replication was possible by following the manufacturer's instructions [58]. To accommodate the larger proximal portion of the nail, a nail entry site of 12.7 mm diameter and 60 mm length was considered. Although, reaming to a diameter of 0.5 to 1.5 mm greater than the nail diameter is advised [59], according to Augat *et al.* [31], the presence of toggling during the reaming process should be considered and which would result in the generation of an average total 2 mm more reaming than the nail diameter if 1 mm larger than the nail diameter reamers would be used. Hence, by considering a reaming diameter of 1 mm more than the nail size and expecting toggling to occur, an 11 mm diameter reaming procedure was applied throughout the anatomical axis. The intramedullary nail was inserted and 2 proximally and 2 distally locking screws were assembled. The proximal locking screws were placed parallel to each other from the anterior-medial and the anterior-lateral direction. The upper and lower distal locking screws were also placed parallel to each other, both from lateral-medial direction. No motion was considered between the screws and the bone and the screw and the nail hole. The correct position of the intramedullary nail was validated by an experienced orthopedic surgeon. After assembly, similarly to Duda *et al.* [60], an osteotomy (a cutting or incision of bone [61]) of 11 mm in the mid-diaphyseal region (along the longitudinal axis), was created. This bone gap simulates a "worst-case-scenario" by resembling a type C3 complex fracture (according to AO Müller classification, see Table 2.3 in Chapter 2) where the main fragments have no contact after

reduction [62]. In the end of this procedure, two finite element models were obtained: the tibia whole-bone structure and the osteotomized tibia with the intramedullary nail implanted. Both models were verified to identify possible penetration between the components of the construct. In the end the files were saved in a workable format for the finite element analysis.







| | Expected cortical wall thickness (mm) | SolidWorks method used | Measured cortical wall thickness | | Cross-section obtained |
|---|---------------------------------------|------------------------|----------------------------------|---------------------------|---|
| | | | Number of measurements | Average (\pm std) (mm) | |
| 6 | 2 | Shell | - | 2 |  |
| | 80% | | | | |
| 5 | 3 | Cut-Loft | 414 | 2.6 (\pm 1.1) |  |
| | 60% | | | | |
| 4 | 6.5 | Cut-sweep | 345 | 5.7 (\pm 3.0) |  |
| | 40% | | | | |
| 3 | 6 | Cut-sweep | 539 | 4.1 (\pm 1.5) |  |
| | 20% | | | | |
| 2 | 2.5 | Shell | - | 2.5 |  |
| | 10% | | | | |
| 1 | 2 | Shell | - | 2 |  |

Figure 3.3 - Illustration of the segmentation adopted, the theoretical cortical wall-thickness considered based on literature and the average wall-thickness obtained after appropriate SolidWorks canal-formation tools were applied

iii) Computer-aided jigs design, analysis and production

The bone was oriented in the standardized position as described above, during finite element jig design. The jigs were design based on the model tibia with the intramedullary nail implanted to assure that no direct contact between the jig and the nail would occur. The jigs were design using SolidWorks software.

For axial compression experimentation, an upper ball-and-socket grip was designed. This grip is constituted by a cylindrical jig which establishes an inferior contact with the tibia plateau and at the upper portion presents a ball-and-socket joint region. This joint jig allows for the proximal tibia in conjugation with the ball structure to freely rotate in the actuation cup (or socket) to guarantee the bone position adjustment, self-alignment, to compensate for non-parallel load-bearing surfaces and reduce misalignment error during the experimental tests [19, 63]. For similar alignment of the tibia in the finite element model and in the experimental set-up, the central portion of the cylindrical upper and lower jig were molded to conform to the tibia plateau and tibia plafond, respectively. This will guarantee precise positioning of the bone on the jigs

and consequent will control the tibia alignment and guarantee the precise orientation and load application between the finite element model and mechanical experimentation and between mechanical experimentations. The jigs allowed a tibia exposed length of approximately 330 mm.

In the torsion experimentation the distal jig was the same as the one used for the axial compression loading mode. The proximal jig, also maintained the concept previously described by presenting a central portion molded to conform to the tibia plateau. The jigs allowed a tibia exposed length of approximately 340 mm.

In the four-point bending experiment, spans width between loading points similarly to the ones used in the study develop by Penzkofer *et al.* [11] were adopted. The span width for the inner loading points was 70 mm and the outer loading points was 200 mm. The jigs were design for the bent of the tibia in coronal and sagittal plane with the lateral side and the posterior side in tension, respectively. The jigs had their central portion molded to conform to the tibia surface and fixation and to allow for the coronal and sagittal essays to be developed using the same jigs and only requiring tibia rotation; see an example in Figure 3.4(A). The position selected guaranteed tibia physiological orientation and that the shaft fracture would be placed at the same distance from the two upper supports. A set of horizontal cross-nails was fitted between the rod and the loading ram in order to ensure that the load on the bone was purely vertical [11].

For the determination of the shear stiffness, jigs were designed with the same concept used for four-point bending experimentation. However, in this loading mode, there were two loading elements and two fixing element at a distance between them of 30 mm, again similarly to Penzkofer *et al.* [11]. The determination of shear stiffness was in the coronal and the sagittal plane with the loading points applied in the medial and anterior site.

To avoid any undesirable damage to the composite bone model and to verify potential flaws associated with the jigs design and test apparatus, besides the development of finite element tests simulations, a three-dimensional sized copy of the tibia was used to test acrylonitrile butadiene styrene (ABS-P430, Stratasys, Minnesota, USA) 3D printed replicate versions of the jigs obtained from fused deposition modelling (FDM) technology (uPrint SE™, Minnesota, USA). To guarantee some consistence, the 3D printed replicate versions of the jigs were filled with equal portions of HB R19 polyol and isocyanate polyurethane resins (Axson Group Iberica S.L., Barcelona, Spain) (see an example in Figure 3.4(B)).

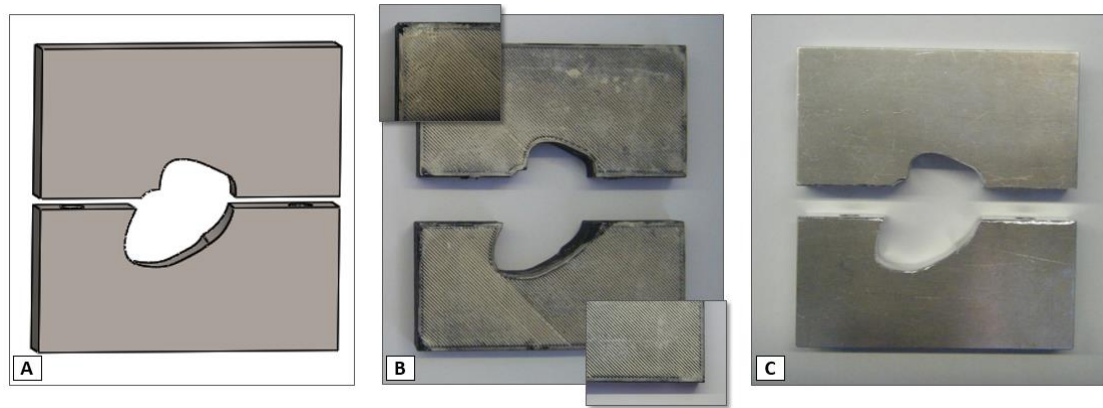


Figure 3.4 - A 4-point bending jig at different process stages: (A) 3D SolidWorks version, (B) 3D printed ABS replicate version and (C) Aluminium alloy AA6082-T6 machined final version

The mold-based tibia replicate was produced in INEGI (Institute of Science and Innovation in Mechanical and Industrial Engineering, Porto, Portugal [64]) through the mixture of equal portions of HB R19 polyol and isocyanate polyurethane resins (Axson Group Iberica S.L., Barcelona, Spain) at a temperature above 18 °C with 2h post-curing inside the mold at 80 °C. Friction in the printed jigs was avoided by coating it with lubricant grease.

The bone contact portion in the final jigs version were all machined from aluminium alloy AA6082-T6 (Rio Tinto Alcan Inc., Quebec, Canada) through a computer numerically controlled (CNC) milling machine and at the Vocational Training Centre of the Metal Industry (CENFIM, Trofa, Portugal [65]) (see example in Figure 3.4(C)). For the torsional experiment, a molded bone-jig personalized contact zone was 3D printed, using the same material and technique described previously, and was press-fixed into a trapezoid section of the aluminium jig as demonstrated in Figure 3.5. The ball and socket joint jig used in the axial compression loading system was polytetrafluoroethylene coated (TEFLON® 958G-414, Dupont, Hertfordshire, UK) by Flupol - Surface Engineering S.A. [66], for low coefficient friction and good abrasion resistance acquisition.



Figure 3.5 - Image of the torsional test top jig with the 3D printed personalized bone contact zone

3.1.2. Mechanical experimentation

All the mechanical experiments developed have a specimen gripping and loading mechanism and two apparatus to record general and local specimen deformation. Mechanical testing in axial compression, 4-point bending, torsional and shear modes were performed first with the intact whole bone specimen and then with the intramedullary nail implanted in the osteotomized tibia. All the mechanical experimentation was developed at the Adhesive Laboratory (translated as *Laboratório de adesivos*) with the exception of the electronic speckle pattern interferometry (ESPI) analysis which was developed at the Laboratory of Optics and Experimental Mechanics (translated as *Laboratório de Óptica e Mecânica Experimental* - LOME).

i) Mechanical test set-up on the intact whole tibia bone

To enable the tibia to be rigidly fix to the jigs during axial and torsional testing, after perfectly aligning the bone in the especially designed jigs, transverse screws (see Figure 3.6) were placed to prevent sliding and to guarantee bone correct orientation during embedding in plaster (Plaster Gesso standard, Axton, UK). The plaster at a fluid state was obtained from gypsum powder mixing with appropriate water proportions, being afterwards poured until the space between the grip and the bone was filled. The structure was left to solidify at room temperature for 3 days. For the bending and the shear tests, the specimen was mounted in the jigs system without over-containing the tibia, for loading in the two planes.

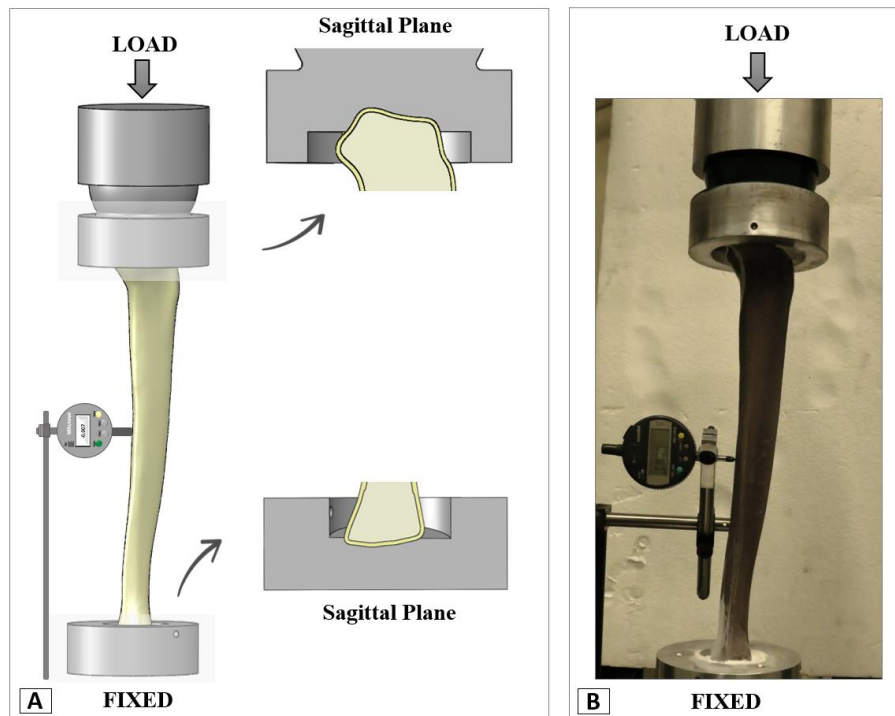


Figure 3.6 -Testing configuration, grips designs and the measurement devices used in the axial compression assay on the intact composite tibia model: (A) Illustration of the test set-up with detailed information of the jigs from a sagittal section and (B) Image of the test set up

A 30 kN electromechanical universal testing machine (Instron® Model 3367, Buckinghamshire, England) was employed for axial compression, 4-point bending and shear testing were load and deformation within the principal loading directions were measured at a sampling rate of 100 Hz within the machine system. In axial compression the distal end of the tibia was rigidly fixed, while the proximal end was connected to the load cell through the ball-and-socket joint jig. As a complementary measuring method a dial indicator (ZERO/ABS series, Mitutoyo Europe GmbH, Neuss, Germany) was positioned at the tibia mid-shaft region, to register any bending that may occur on the specimen, as exemplified in Figure 3.6. This measuring method was also used in the 4-point bending loading mode where it was positioned at the tibia mid-diaphysis to measure its vertical deflection with respect to the two loading grips (see Figure 3.7). In the shear testing, the grips proximity enabled the adoption of any other measuring method besides the data obtained from the testing machine system (see Figure 3.8).

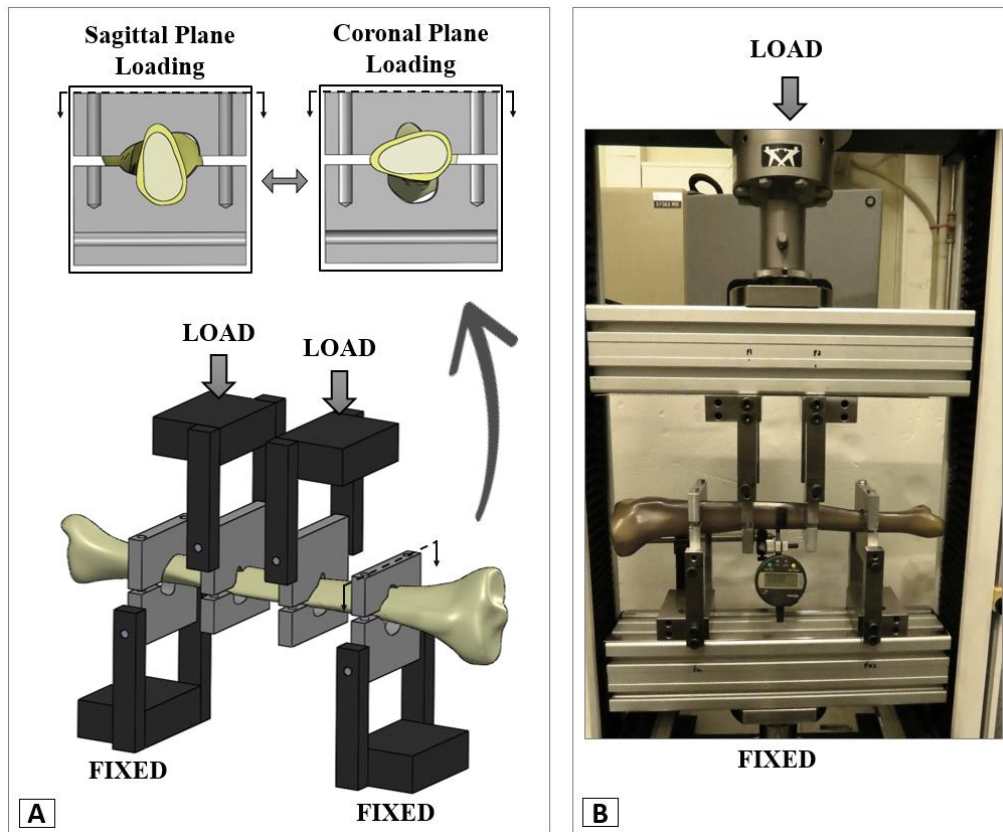


Figure 3.7 - Testing configuration, grips design and the measurement devices used for the 4-point bending assay on the intact composite tibia model: (A) Illustration of the test set-up with the tibia on coronal orientation and with an exemplification of the switching mechanism used between the coronal and sagittal loading mode and (B) Image of the test set up for 4-point bending with the tibia sagittal orientation

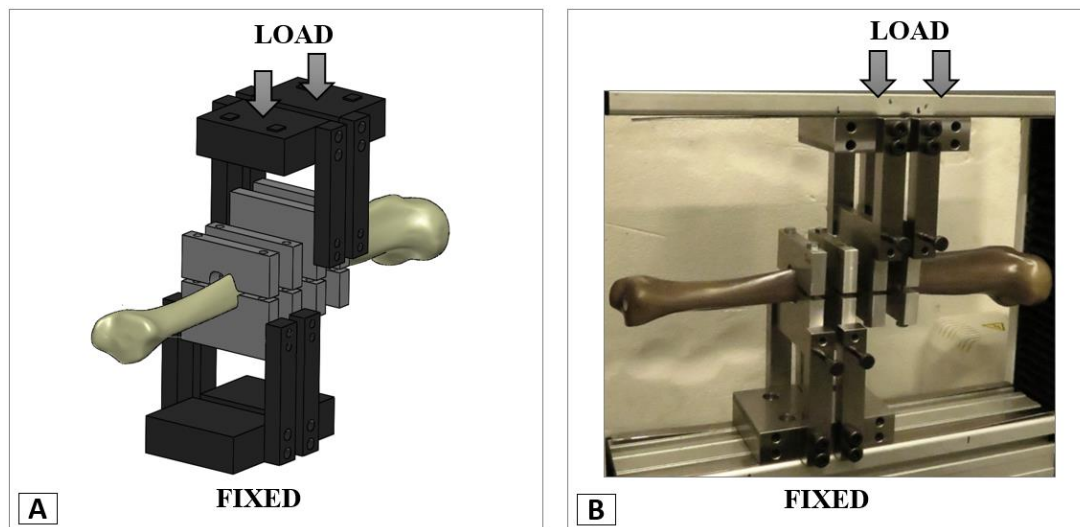


Figure 3.8 - Testing configuration used for the shear assay on the intact composite tibia model with the bone on sagittal orientation: (A) Illustration of the test set-up and (B) Image of the test set-up

Considering the inexistence, at the national wide level, of an electromechanical torsional testing machine capable to fit the whole tibia composite model, a custom set-up had to be developed for the torsional loading mode mechanical testing. In this set-up the tibia distal end was rigidly fixed and the upper extremity was only allowed to rotate. The bone upper rotational motion

was guaranteed with the specimen positioning in an electromechanical universal testing machine (Instron® Model 3367, Buckinghamshire, England) and through the use of a thrust ball bearing (51406 model, SKF, Germany) between the upper grip and the load cell (see Figure 3.9). A torque was generated through the application of weights by virtue of an apparatus where they were connected by a thread (Cucirini International S.P.A., Italy) to a pin bonded to the upper jig. Considering that no information on the tibia rotation in response to the torque application could be acquired from the machine system (since it only had a positioning purpose), two measuring methods were considered. The tibia rotation was calculated based on the measurement of the distance travelled by the weights and their support structure as they go down upon load application. For that purpose, a ruler was placed behind the hanging weights and measurements were obtained from several photographs taken with a digital camera (PowerShot SX40 HS model, Canon Inc., Tokyo, Japan) during the torque application. The other method was based on the use of a wireless laser (R400, Logitech) which was fixed onto the top container pin and which was projected onto a graph paper placed at a considerable distance on the wall. By applying a torque, there is an increase on the moment load which drags the top grip pin and moves it horizontally and in tandem with the projected laser on the graph paper. The distance covered on the graph paper can be related to the rotation suffered by the tibia bone.

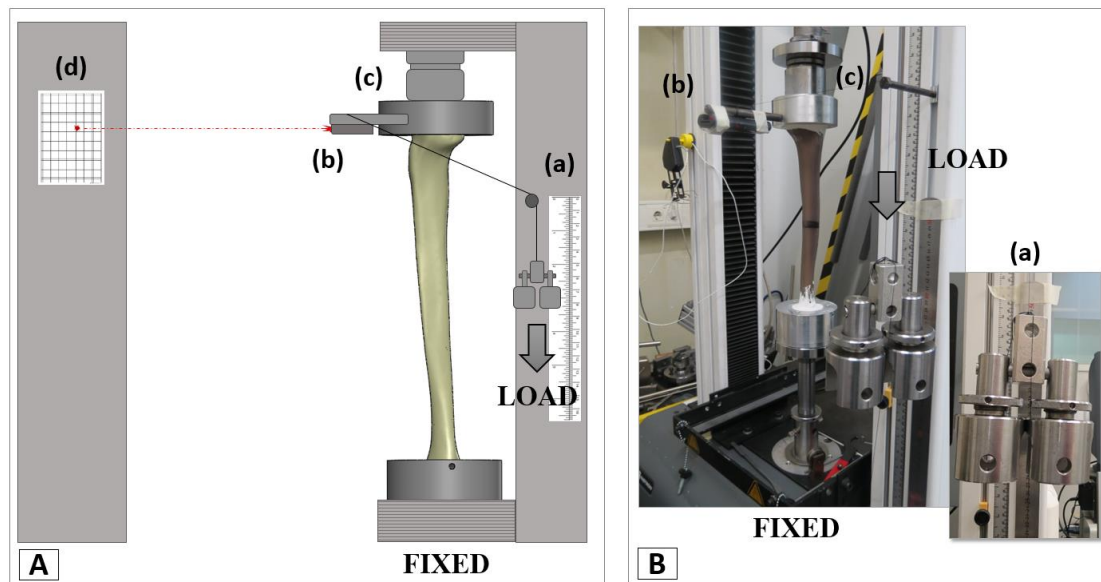


Figure 3.9 - Custom testing configuration and the measurement devices used for the torsional assay on the intact composite tibia model where: (A) Simplified illustration of the torsional test set-up and (B) Image of the test set-up. The measuring apparatus used to record the system rotation - (a) weight and their support structure fall and (b) laser projected and motion registration – and the (c) thrust ball bearing and (d) graph paper, are also represented

To guarantee stabilization of the test apparatus, a preload was applied until the resulting load-displacement plot appears to converge towards a stable curve. Also, as advised by some authors [19, 44], in all the tests, the recorded cycles were preceded by pre-conditioning loading cycles

(between 3 to 5 loading cycles for each experiment) to improve the stiffness. To validate the test method, repeated measurements were performed for a total of five runs for each load mode. Although the models were loaded within their elastic region, and therefore repeated measurements were allowed, after every loading mode, the test specimen was inspected to analyse physical damage caused by the experiments.

With the exception of the torsional test where the torque rate applied could not be controlled, a physiological displacement rate of 1 mm/min, similarly to Horn *et al.* [8], was adopted in all the experiments. After the load application the test specimen was unloaded at a reduced speed to allow recovery of the viscoelastic deformation [41] and to relief any residual strains [19]. In the axial loading test, a vertically compressive load to a maximum of 150 N was applied in load control. This value was selected based in Dailey *et al.* [35], which claimed that during walking with crutches, at bone fracture early healing phase, a 20% of body weight “toe tap” axial compression load is achieved and by considering the Portuguese average body weight as being 74 kg [67]. The load/torque applied in the torsional, 4-point bending and shear experiments, were based in the Augat *et al.* [31] and Penzkofer *et al.* [11] studies for partial weight bearing cases. Torsional testing was performed at a constant axial load of 30 N (weight of the upper grip and the thrust ball bearing, plus the axial load applied by the machine system) [11, 31], and a maximum torque of 5 Nm in internal rotation torsional. The four-bending test was performed with the tibia in antero-posterior plane (or sagittal plane) and in medio-lateral plane (or in coronal plane) with the posterior side and lateral side in tension, respectively, and by applying a 20 Nm bending moment through load-controlled application. The shear loading (in the coronal and sagittal plane) was achieved, through load-controlled application of a maximum axial load of 100 N.

Considering the influence of structural properties (*e.g.* size and shape) and mechanical properties in the intact bone mechanical behaviour [68], the arithmetic means stiffness values for each loading mode were calculated according to Heiner *et al.* [22], and based on the data collected from the machine system, the laser projected and motion registration technique. The average axial compression stiffness was determined through a regression line obtained from the load-displacement curve. The average torsional rigidity was calculated by multiplying the torque-rotation slope - also using the regression line - with the specimen exposed length which in this case is 340 mm (or 0.34 m). The 4-point bending load/deflection slope was converted to apparent rigidity which is translated by the product between the modulus of elasticity (E) equation and the moment of inertia (I) as demonstrated by equation (3.1) where S is the slope

of the tangent of the initial straight line portions of the load-deflection curve and C is the distance between the inner and outer support (65 mm or 0.065m).

$$EI = \frac{5}{12} \cdot S \cdot C^3 \quad (3.1)$$

The average shear stiffness was determined through a regression line obtained from the load-displacement curve. The slope of the elastic region of the load-deformation curve represents the stiffness (extrinsic rigidity) meaning the value obtained will be influenced by extrinsic factors like specimen size and shape. The rigidity (or intrinsic rigidity) considered corresponds to a property of a system or of a material itself or within [19, 63].

ii) Electronic Speckle Pattern Interferometry (ESPI) system

Factors affecting the accuracy of mechanical experimentation measurement are usually related to the test machine, the bone specimen, and/or the interface between the grip and the test specimen [19]. Considering that the error associated with the test machine and the bone specimen are known, the electronic speckle pattern interferometry (also known as ESPI) was chosen as the most suitable technique for experimental evaluation the coupling quality of the bone/jig relation during the application of axial compression load in the intact tibia. The ESPI is a highly sensitive technique, which allows detection of displacements as small as tens of nanometers (the limit of detection is approximately $\lambda/2$, where λ is the wavelength of the laser light; typically half a hundreds of nanometer) and has ability to independently discriminate the three principle orthogonal displacement vectors [69, 70]. This interferometry evaluation was development on the tibia whole bone model, instead to the bone-implant system, in order to reduce the number of variables and to allow quantify the quality between the tibia and the custom-design grip.

Since the appearance of the first ESPI system in 1971 [71], this technique has suffered great improvement, however its potential on the measurement of bone surface deformations has only recently been started to be considered [69, 72, 73]. The ESPI technique is an optical method where there is a complete absence of contact with the test specimen and full-field visualization is allowed. Figure 3.10 shows a schematic representation of the ESPI measuring system used.

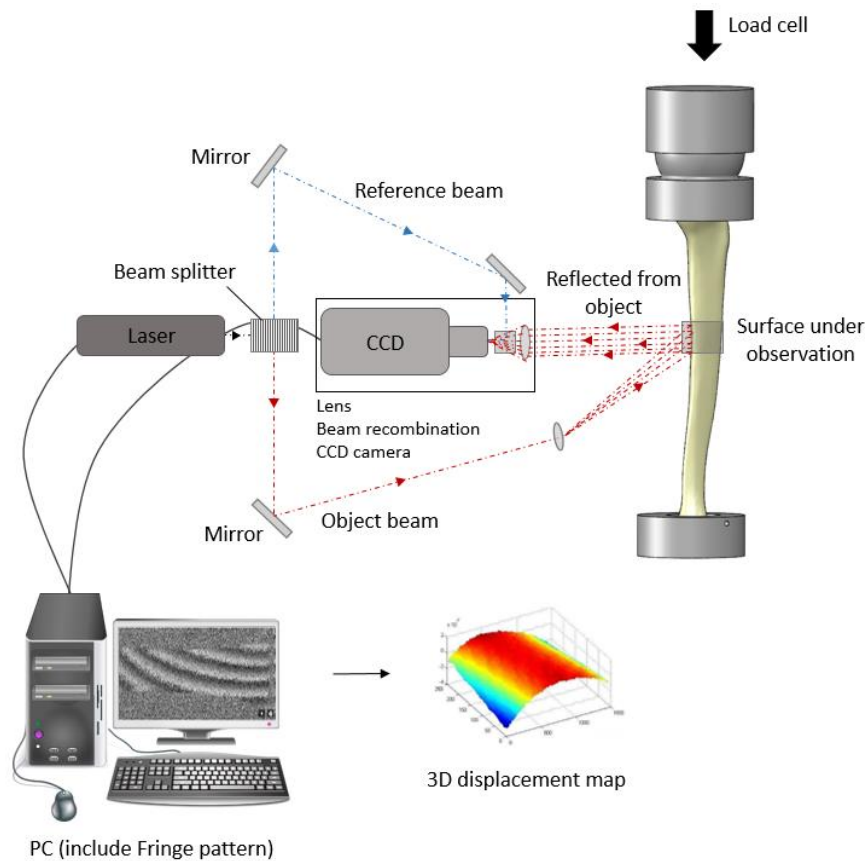


Figure 3.10 - Schematic representation of the electronic speckle pattern interferometry (ESPI) experimental arrangement system. Image constructed based in information from [69, 70, 74, 75] and the image of the computer was obtained from [76]

Using a specific constructed modular ESPI device and custom-written software, surface displacements fields were recorded along two axes (x and y) at the region of bone that presented a considerably simple geometry, the intact tibia mid-section. This method consisted of a 532 nm wave length laser beam produced by Nd-YAG diode-pumped laser which through a *beam splitter* was divided into two beams of the same wave form: object and reference beam. An expanded object laser beam illuminates the target surface and produces a speckle field. This field is produced by the natural roughness of the specimen surface (roughness is greater than the wave length of the beam used) under illumination which produces tiny spots of light and dark called 'speckles'. Hence, the light scattered from the optically rough surface of the bone forms a speckled image which interferes with the reference beam derived from the same laser, creating a grainy image termed *speckle pattern*. Any change in the shape of the object results in local changes in the intensity distribution in the speckle pattern. The object is imaged on the charged coupled device (or CCD) camera with a 50 nm resolution, which records the speckle images of the surface under observation and transferred the corresponding data to a computer. The speckled images were then superimposed and fringes which correspond to the degree of correlation of the speckle patterns that contour the changes in shape of the surface, were

obtained [69, 72, 77-79]. To avoid large displacements that could lead to de-correlation [70], a series of small and consecutive incremental axial loads of 10 N (up to 80 N) were applied through a load cell on the axial compression assay custom-designed grip, as showed in Figure 3.10. The displacement field were determined for each increment and the differences between patterns of consecutive speckle images taken before and after applying the load are used to detect shifts in the phases of the speckles. The ESPI analysis was developed in an isolated environment that included an acoustically-insulated system mounted on top of a vibration isolation table.

iii) Intramedullary nail surgical implantation

Once all the mechanical tests on the intact composite tibia had been completed, the intramedullary nail was implanted by an experienced orthopedic surgeon according to the manufactures' instructions and using all the tools recommend for this specific nail model. For best comparability with the finite element model, similar parameters were considered. From the entry point and up to 60 mm of the proximal metaphysis, a 12.7 mm in diameter drill was used. The entry point for the nail was on the central line, directly anterior to the articulating surface, between the tibial medial and lateral condyle. The medullary canal was reamed in sequential steps by increments of 0.5 mm up to a diameter of 10 mm using the flexible intramedullary reamer. The nail was locked with two screws distally and two proximally. A 4.0 mm drill was used for all the 4.8 mm in diameter fully threaded locking screws. The upper and lower distal locking screws were placed from lateral direction. The proximal locking screws were placed perpendicular to each other from the anterior-medial and the anterior-lateral direction. At the centre of the tibial mid-shaft - around 182 mm upwards from the tibial platform - two transverse osteotomies were performed with an oscillating saw, creating an 11 mm osteotomy gap. The full description of the implantation procedure is presented in Chapter 8 in Appendix A.

After nail implantation, a full length radiograph on the bone-implant construct was taken to document the correct position of the nail in the medullary canal and to infer on parameters variation which may alter the mechanical results in relation to the finite element model.

iv) Mechanical test set-up on the tibia-intramedullary nail system

After the intramedullary nail was implanted the bone-implant construct was studied. However, and taking in consideration the increased complexity of this system when compared with intact bone specimen, an accurate local osteotomy site ("fracture" zone) displacement measurements, was required. Considering the limitations of the most popular measurement technique used, the strain gauges (device whose electrical resistance varies in proportional to the amount of

strain [80]), such as the difficulty to measure bone fragment motion due to the absence of a solid structure at the osteotomy site and the fact that it is often not possible to assume with certainty that the presence of the strain gauges will not affect the measurement made [79], an optical measurement technique was selected. The method of preference was the high resolution digital image correlation (often referred to as "DIC") technique associated with virtual extensometers. The DIC method was developed by a group of researchers at the University of South Carolina in the 1980s, when digital image processing and numerical computing were still in their infancy [81]. In the last thirty years, it has become a popular and powerful technique for full-field motion, deformation and shape measurement [82]. The selection of this method in association with virtual extensometers was based on its ability to perform the measurements without the need to destroy the test sample or interfere with the resulting outcome. Also, although only fracture site information was considered in this study where virtual extensometers were associated to the DIC technique, this method has the additional advantage to develop full-field surface measurements. A large area measurement grants this method with the ability to identify local displacements which could be missed by traditional method measurements - where only data from few strategic strain gauges placed are obtained - and to more easily compare the results with the ones obtained in an equivalent the finite element simulation. When compared with the ESPI technique, the DIC method benefits from a lower sensitive to environment vibrations. However, it still presents a high resolution and is capable of detecting displacements up to the order of $0.3\ \mu\text{m}$ [69, 82-84]. The concept behind the DIC measurement technique is based on matching the first image (also known as the reference image), of the speckled pattern study object surface and which is captured before any load is applied, with the images generated during load application and where deformation is generated at the study object surface. Hence, the system splits the image into small subsets and the patterns within each subset of subsequent images are compared to the reference image. Subsequently, the software determines the displacement values of the centre of the subsets, which yields an entire displacement field [69, 82, 85, 86].

As it is possible to see in Figure 3.11, the set-up used was composed of two fixed camera-lens optical system with a CCD to record the digital images of the test specimen surface before and during deformation at a constant sampling frequency of 50 Hz and which out-of-plane specimen displacement was limited to the depth of field of the camera lens, one light source and a VIC-2D™ commercial computer software (Vic-Gauge™, Correlated Solutions Inc., Irmo, USA) that controls image capture and conducts the post-test analysis. The fractured region including the exposed nail was coated with a speckle pattern suitable for the DIC assay. This was constituted

by a white-based thin layer applied with an aerosol spray paint and on top a fine layer of black paint that was airbrushed onto the composite tibia to create the DIC characteristic speckle pattern. To understand the bone-implant system stability, the displacement tracking of each bone fragment and its relation to the intramedullary nail was considered to distinguish between the global and each component displacement. Each extensometer was characterized by two gauges which were defined in the software reference image, since virtual extensometers require no physical setup, and their orientation was according to the direction of the tibia long axis. A total of three extensometers were considered which measure displacement between: bone fragments, upper bone fragment and intramedullary nail and intramedullary nail and the bottom bone fragment. The motion of each single gauge was also considered, thus allowing the displacement profile of each component in the bone-implant system at fracture site to be evaluated (see Figure 3.12 as an example).

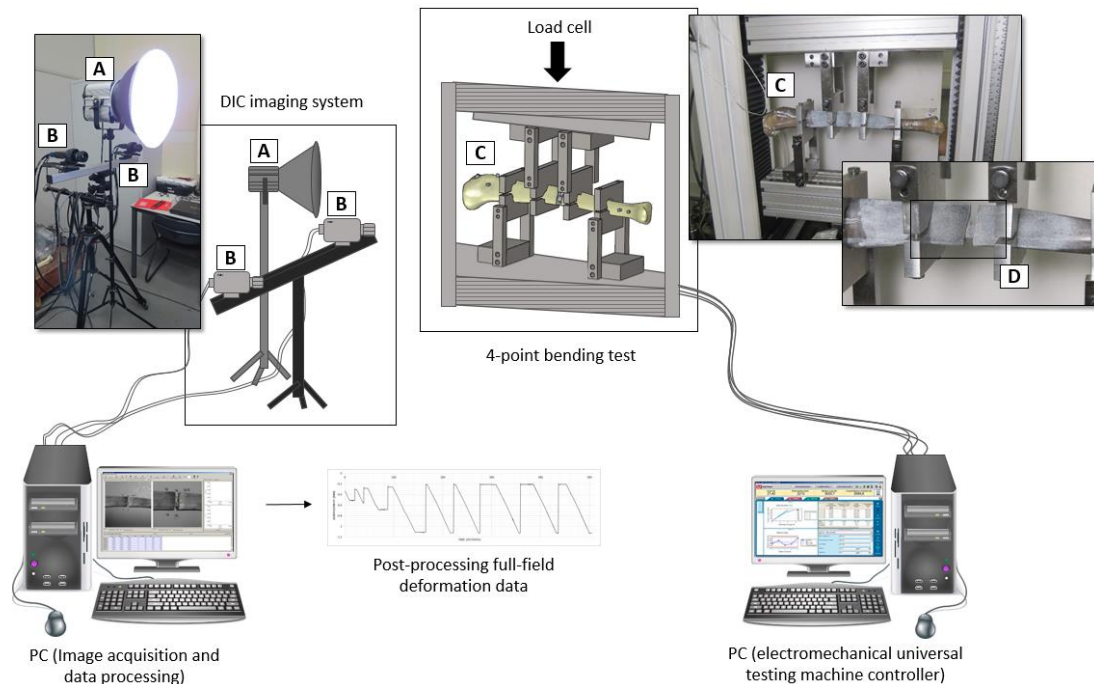


Figure 3.11 - Schematic representation of the digital image correlation (DIC) technique using virtual extensometers experimental arrangement system where: (A) Light source, (B) CCD digital camera, (C) Speckled composite tibia under 4-point bending loading and (D) speckled surface under analysis. Image constructed based in information from [87] and the image of the computer was obtained from [76]

Axial compression, torsion, 4-point bending and shear tests were performed on the tibia bone as standard, using the same protocol that was previously considered during the mechanical experiments on the intact tibia model. The general bone-implant system displacement and the local fracture/osteotomy displacement field were recorded through the mechanical system and the DIC measurement method using virtual extensometers, respectively. Similarly to Penzkofer *et al.* [11], interfragmentary motion was defined as the amplitude of the fracture-end

displacements at the fracture gap in the direction of the applied load, during a complete load cycle. The arithmetic means stiffness values based on the data collected from the machine system and DIC using virtual extensometer measurements were determined over the regression line obtained from the load-displacement or load/deflection curve at the linear elastic range for the axial compression, 4-point bending and shear assay. For the 4-point bending assays, the load/deflection slope was converted to apparent rigidity as previously done on the intact tibia experiment. The average torsional stiffness was also determined based on the regression line obtained from the torque/rotation curve. However, considering the two-dimensional displacement data obtained from the DIC method and the tibia out-of-plane interfragmentary rotation, a different strategy was adopted to determine the components rotation. The method adopted is described in Figure 3.12. If the situation is analyzed from a cross-section view and if the principle behind the DIC measurement method is taken into consideration, the tibia rotation will lead to “a” speckle point motion from its initial position (t_i) to the final position (t_f) and which will translate in a displacement (δ - information given by the DIC method). Through SolidWorks “Point-to-Point” measure tool it is possible to approximately determine the speckle point initial and final positions and the distance from those point to the center of rotation (A and B , respectively). This information, together with the displacement data (δ), forms a triangle where all sides lengths are known. Hence, the rotation angle (represented by β) can be determined with the use of the cosine formula and based on the triangle side lengths, as stated by equation (3.2).

$$\delta^2 = A^2 + B^2 - 2AB \cdot \cos(\beta) \quad (3.2)$$

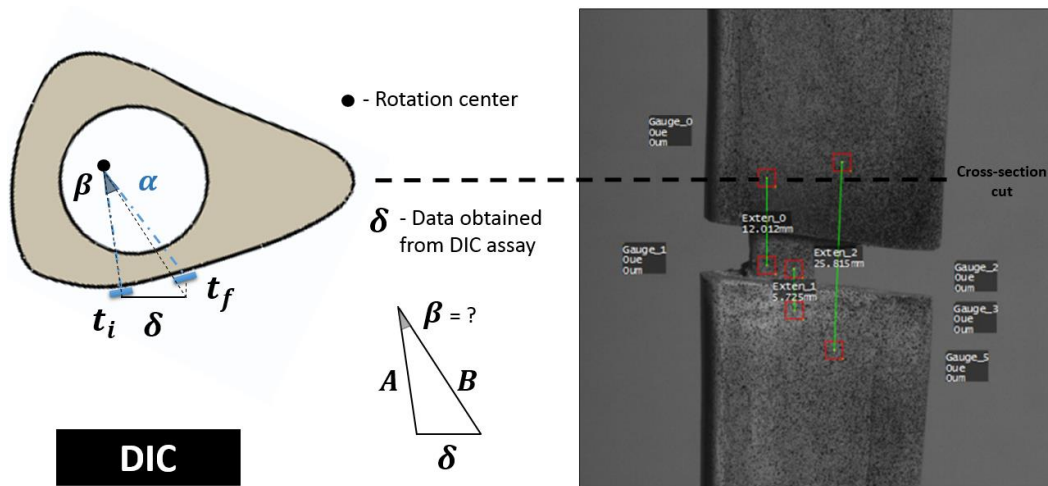


Figure 3.12 - Schematic representation of the strategy used for the calculation of the horizontal and vertical gauges displacements variations during torsional assays

The horizontal (Δx) and vertical (Δy) displacements variations were also calculated for every loading mode.

3.1.3. Finite element simulation

The intact tibia and osteotomized tibia with the implanted intramedullary nail and respective jigs assembled CAD models, were imported with parasolid file format into ANSYS Workbench 15.0 (ANSYS Inc., Canonsburg, Pennsylvania, USA), to generate the finite element models. The models stiffness was analyzed in ANSYS through a sequence of stages. Studies have showed that material properties, boundary conditions and contact surfaces in finite element computation have great impact on the study structure resultant biomechanical behavior [12]. Therefore, each of these parameters were carefully defined in the preprocessing stage. A three dimensional Cartesian coordinate system oriented according to the tibia physiological positioning (as described previously) was used in the finite element model.

i) Material properties and meshing

The tibia cortical and cancellous bone properties were obtained from the manufacture [21]. The tibia cortical material was considered to present linear, elastic, orthotropic properties, a density of 1 640 kg/m³, a Young's modulus of 10,000 MPa for transverse load (E_x and E_y) and 16,700 MPa for longitudinal load (E_z) and a Poisson's ratio of 0.3 for any directional load applied (v_x , v_y , v_z). The cancellous portion presents a density of 270 kg/m³ and was assumed to behave as an isotropic linear elastic material with a Young's modulus of 155 MPa and a Poisson's ratio of 0.225. Since the study considered the initial stage of bone healing, the existence of granulation tissue was assumed and it was analyzed as an isotropic linear elastic material with a Young's modulus of 0.2 MPa and a Poisson's ratio of 0.167, similarly to Byrne *et al.* [5]. The 316L stainless steel material for the nail and the screws was modeled as linear elastic, isotropic and homogeneous material with a density, Young's modulus and Poisson's ratio of 8000 kg/m³, 200,000 MPa and 0.27, respectively [88-90]. The titanium alloy for the nail and the screws was also modeled as linear elastic, isotropic and homogeneous material with a density, Young's modulus and Poisson's ratio of 4400 kg/m³, 114,000 MPa and 0.27, respectively [91]. For the grips common steel conditions was considered.

The number of selected finite elements nodes in each component was based on the geometry complexity and the region of interest in the overall system. The tibia cortical bone was meshed with varying refinement 10-node tetrahedral elements (150326 - 244782 nodes), with three degrees of freedom at each node (translations in the nodal x, y, z directions) since several studies

[15, 40, 92] claimed the ability of tetrahedral meshes to approximate very complex structures. Critical geometric sites and contact areas of cortical bone and interlocking screws had high density of nodal points. Albeit, the trabecular bone in the tibia model may be considered a complex structure, meshing was done using less tetrahedral elements (15278 - 47311 nodes) in a manner to avoid excessively long computational running time. The intramedullary nail and screws were meshed with hexahedral elements (7965 - 19462 nodes) as well as all the jigs. The quality of the mesh generated greatly influences the results accuracy and the model predictive capability. In the finite element models development, the mesh quality obtained was analyzed - in terms of aspect ratio, Jacobian ratio and skewness parameters - and the stress results convergence level (*i.e.* until the differences in calculated displacements at the point of application of the loads from one iteration to the next was low) was verified and evaluated for its reliability to be used in the design [93].

ii) Contact surface definition

Next in the preprocessing phase the contact surfaces were defined. Moreover, to reduce the simulation time without reducing the result accuracy, only particular selected areas (and not the all components surfaces) have been used as contact pairs. These steps were carefully carried out to correctly simulate the mechanical testing essays. The cortical and trabecular bone were considered as being bounded ("glued contact"). Because a relative tangential motion may occur between the cancellous bone inner wall and the fixation implant, contact elements with a friction coefficient of 0.2 were used and described with a Penalty algorithm or augmented Lagrange algorithm depending upon the contact typology, as suggested by several authors [37, 94, 95]. The screws were tied to the bone and to the nail simulating thread locking action. The other contact surfaces between the bone/containers were also assumed to be bounded ("glued contact").

iii) Boundary conditions

Finally, to complete the finite element model preparation, the suitable boundary conditions (loads and displacements) were imposed on model. All finite element simulations were performed on the intact model first and then on the tibia model with the intramedullary nail and transverse osteotomy. The load levels applied were equal to the ones used in the mechanical experimentation, the loads were applied on the jig surface and its displacement was limited to the direction of the applied load to best approximate the experimental scenario.

iv) Finite element analysis validation and models adequacy evaluation

The finite element models were validated through the comparison of the stiffness or rigidity values predicted and the ones measured which resulted from the mechanical tested reproduced under the same conditions. The models' adequacy was verified through their comparison with published studies.

3.1.4. Statistical analysis

The results were expressed as arithmetic means \pm standard deviation (\pm SD) for experiment.

3.2. Results

3.2.1. Intact tibia model

The averages stiffness and standard deviations obtained from axial compression, torsion, 4-point bending and shear loading modes as a result of mechanical experimentation on the intact composite tibia and the correspondent finite element simulation, as well as the mechanical experimental results obtained in the study developed by Anneliese Heiner [20], are presented in Table 3.2. The agreement (or percentage difference) between the finite element and experimental stiffness/rigidity data for all loading modes was evaluated as percentage difference, as suggested by Zdero *et al.* [96] and according to equation (3.3).

$$\text{Percentage difference} = \left(\frac{FE_{stiffness} - ME_{stiffness}}{ME_{stiffness}} \right) \times 100 \quad (3.3)$$

In general, most stiffness/rigidity values predicted by the finite element model were similar to the ones obtained from the mechanical experimentation when all loading modes are considered. The exception refers to the axial compression loading, where there is 51% variation between the stiffness value determined experimentally and the average stiffness value measured. The data obtained, from the dial indicator measurements, demonstrated a posterior-anterior motion of the tibia mid-section portion in 0.015 ± 0.001 mm during axial compression. The existence of motion was confirmed through the finite element analysis, however a higher value, up to 0.023 mm, was obtained. In the torsional loading mode, only data from the laser projected and motion registration method was considered and used to determine the rotation generated at the top grip and to calculate the torsional rigidity values. The weight and support system fall measurement technique was associated to a high error. When comparing both models, the predicted torsional rigidity presents a 15% variability in relation to the measured one. In the 4-point bending loading mode, the apparent rigidity was in good agreement to the

mean values of the *in vitro* results with a maximum deviation of 7 and 3% for the loading in sagittal and coronal plane, respectively. Also, in the 4-point bending loading mode, mean deflection measured by the dial indicator on the tibia mid-section portion in response to the maximum bending load application, was 0.16 ± 0.01 mm in the posteroanterior plane and 0.30 ± 0.003 mm in the mediolateral plane. These values were corroborated with the finite element model when simulated under the same loading conditions. Simulated results showed motions in the magnitude of 0.12 mm and 0.21 mm, in the sagittal and coronal plane, respectively. The tibia mid-diaphyseal region shear stiffness value, showed a deviation of 20 and 17% between the mechanical experimentation and finite element simulation, for the loading in sagittal and coronal plane, respectively. When comparing the finite element model stiffness/rigidity values with the mechanical experimentation results from other authors [20] (see Table 3.2), the predicted axial stiffness and 4-point bending rigidity in the sagittal plane, were within the published experimental range values and the torsional and 4-point bending rigidity in the coronal plane were close to the published values. No studies reporting results on intact composite or cadaveric tibia shear loading or shear stiffness determination were found.

Table 3.2 - Comparison between the 4th generation composite intact tibia mechanical experimentation (ME) and finite element simulation (FE) with published experimental data from the study developed by Anneliese Heiner [20] where the same tibia model was considered. NIA – No information available

| Loading mode | Stiffness | | |
|---|-----------------|------|-----------------------|
| | ME | FE | Anneliese Heiner [20] |
| Axial compression (N/ μ m) | 4.76 ± 0.02 | 7.20 | 7.48 ± 0.7 |
| Torsional (Nm ² /deg) | 2.07 ± 0.13 | 1.75 | 1.93 ± 0.07 |
| 4-Point bending sagittal (Nm ²) | 186 ± 0.08 | 197 | 199 ± 9.95 |
| 4-Point bending coronal (Nm ²) | 121 ± 0.08 | 124 | 146 ± 5.11 |
| Shear sagittal (N/mm) | 1009 ± 2 | 1207 | NIA |
| Shear coronal (N/mm) | 1399 ± 3 | 1634 | NIA |

ESPI investigations on the tibia midsection site under axial compressive loading were developed and the results obtained are presented in Figure 3.13.

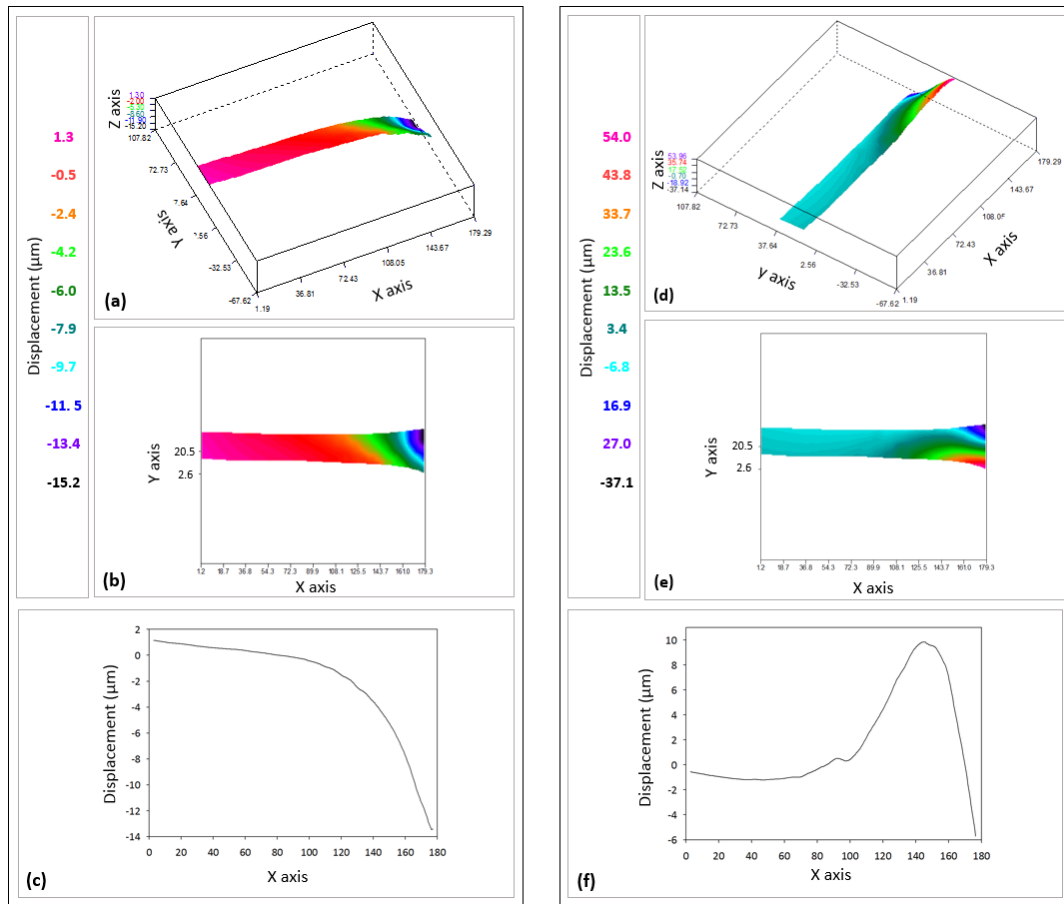


Figure 3.13 - ESPI analysis on the tibia midsection site displacement from the whole bone structure axial compression at (A) 20 and (B) 80 N. The results are presented as a (a) three-dimensional displacement map, (b) two-dimensional displacement map and the (c) displacement along the x-axis at position $y = 24.6 \mu\text{m}$

Figure 3.13 shows the generation of torsional motion in the most proximal portion of the analyzed mid-section area.

3.2.2. Tibia-intramedullary nail system

The comparison of the finite element simulated stiffness values for the osteotomized composite tibia-intramedullary nail system under pure load cases to the *in vitro* results based on registers from the machine system and DIC measurement method are presented in Table 3.3. The finite element model was conducted considering two types of intramedullary nail materials, stainless steel and titanium alloy. Hence, the finite element model could be compared and validated based on the *in vitro* results where a stainless steel intramedullary nail was implanted in the composite tibia and by considering a titanium alloy intramedullary nail in the finite element simulation the predicted stiffness values could also be compared with published mechanical experimentation data where titanium alloy is the standard material of choice for intramedullary nails (see Table 3.3).

Table 3.3 - Stiffness (mean value \pm SD) of the composite tibia-intramedullary nail based on mechanical experimentation with data from the machine system and DIC measurement method and from the finite element (FE) simulation and their comparison to published data from the study developed by Penzkofer et al. [11]. SS - stainless steel, TA - titanium alloy, UNCOMP - uncompressed bone-intramedullary nail construct system and COMP - compressed bone-intramedullary nail construct system

| Loading mode | Stiffness | | | | |
|---|----------------|-----------------|------|------|---|
| | ME (SS) | | FE | | Penzkofer et al. [11] UNCOMP/COMP (TA) |
| | Machine system | DIC | (SS) | (TA) | |
| Axial compression (N/mm) | 2838 \pm 46 | - | 3007 | 2500 | 723 \pm 421 / 2257 \pm 358 |
| Torsional (Nm/deg) | - | 2.34 \pm 0.22 | 2.34 | 1.44 | 0.8 \pm 0.1 / 2.8 \pm 2.4 |
| 4-Point bending sagittal (Nm ²) | 126 \pm 20 | 151 \pm 8 | 113 | 93 | 37 \pm 8 / 83 \pm 15 |
| 4-Point bending coronal (Nm ²) | 76 \pm 1 | 71 \pm 3 | 96 | 65 | 37 \pm 7 / 58 \pm 15 |
| Shear sagittal (N/mm) | 176 \pm 1 | 186 \pm 1 | 201 | 164 | 131 \pm 30 / 1136 \pm 244 |
| Shear coronal (N/mm) | 187 \pm 1 | 202 \pm 2 | 213 | 182 | 164 \pm 89 / 1040 \pm 139 |

By analysing Table 3.3, it is possible to notice that there are inconsistencies among the stiffness values measured by the machine system and by the DIC virtual extensometer method during each loading mode and difference as high as 20% were obtained. Also, with the exception of the coronal plane 4-point bending loading mode, in all the other loading cases the stiffness calculated based on DIC measurements showed a higher value than the ones determined based on data from the machine system measurements. Although the data was not presented in this chapter, the finite element simulation stiffness values were calculated considering data from the jigs and the interfragmentary site. When compared, and for all loading modes with the exception of the 4-point bending, similar values were obtained. For the 4-point bending loading mode and as showed by Figure 3.14, larger motions were registered at the interfragmentary site when compared with the loading jigs.

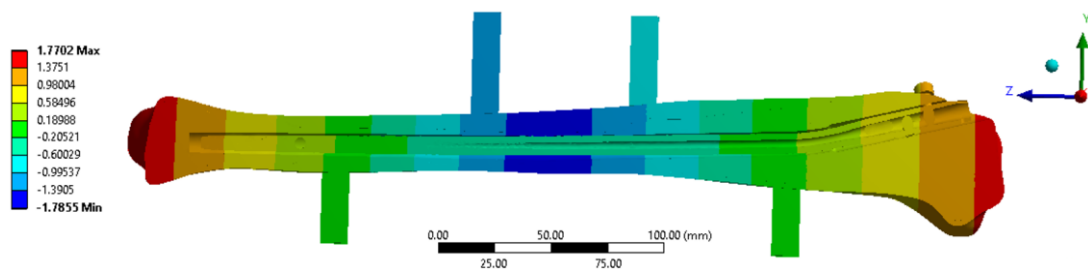


Figure 3.14 - Cross-section of the tibia-intramedullary nail finite element model displacement distribution in yy direction (mm) during 4-point bending load in the sagittal plane and in response to 20 Nm bending moment

In relation to the axial compression loading mode, the excessive preloading applied led to the structure displacements associated with error. Hence, the experiment had to be repeated. However, it was no possible to complement the study using DIC measurement and only data

from the machine system could be considered. With the exception of axial compression, the stiffness values obtained from the DIC measurement methods were used as the basis for the validation of the finite element simulation method.

During torsional loading mode the measurements obtained from the laser projected and motion registration method was not considered throughout the bone-implant system evaluation. The DIC extensometer measurement method set-up arrangement interfered with the previously adopted directional orientation of the laser projected and motion registration method. Hence, the only available option was to adjust the laser to be positioned in the same direction but with the opposite orientation in order for real-time data acquisition to be achieved. The measurement system rearrangement led to a reduce distance between the laser tip and the graph paper and which caused the measurements registered to not be considered valid.

There was a 6% difference between the axial compression stiffness value predicted by the finite element model when compared with the one obtained from *in vitro* machine system measurement-based data. There was a perfect agreement between the simulated torsional stiffness and the one obtained from the *in vitro* experimentation. There was also congruence between the simulated bending stiffness and the ones obtained from the mechanical experimentation DIC measurements and where a maximum deviation of 25% and 35% were obtained from loading in sagittal and coronal plane, respectively. The simulated shear stiffness values were also in good agreement with the mean stiffness values of the *in vitro* results were deviations of 8% and 5% were obtained from loading in the sagittal and coronal direction, respectively. For an accurate/rigorous validation of the finite element model, the system constitutive components deformation at the fractured bone critical site, were compared with the mechanical experimentation DIC-measurements in all the loading modes. The comparative results are present in Figure 3.15, 3.16, 3.17 and 3.18 for loading in axial compression, torsion, 4-point bending and shear, respectively.

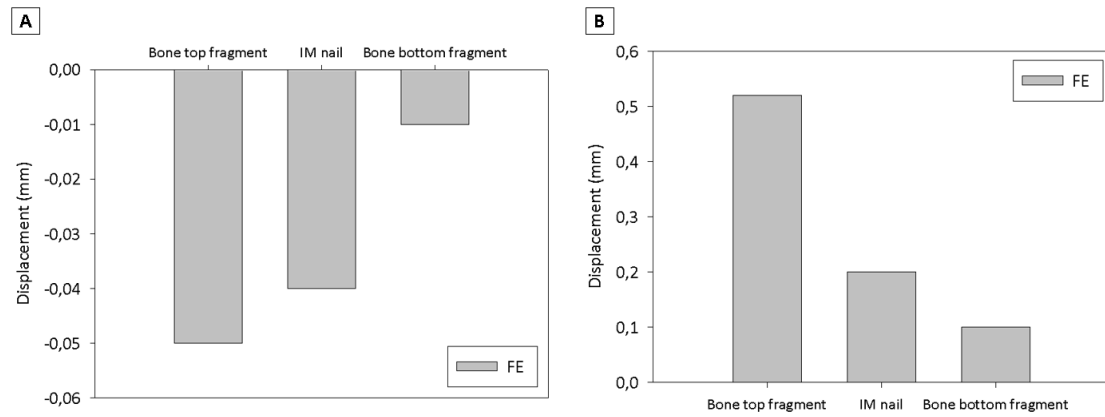


Figure 3.15 - Comparison of the bone fragments (upper and lower portion) and intramedullary nail deformation from finite element simulation (FE) at the (A) axial and (B) anteroposterior direction and in response to 150 N axial compression loading of the osteotomized composite tibia fixed with the intramedullary nail system

As it is possible to notice from Figure 3.15, the finite element model predicted that, in the axial direction, most of the total bone-implant complex compression was from the motion of the upper bone fragment and the intramedullary nail, where the latter contributed in 80% to the total interfragmentary motion. The bone lower fragment shows the least amount of motion (see Figure 3.15(A)). The motion in the anteroposterior direction followed the same principle (see Figure 3.15(B)).

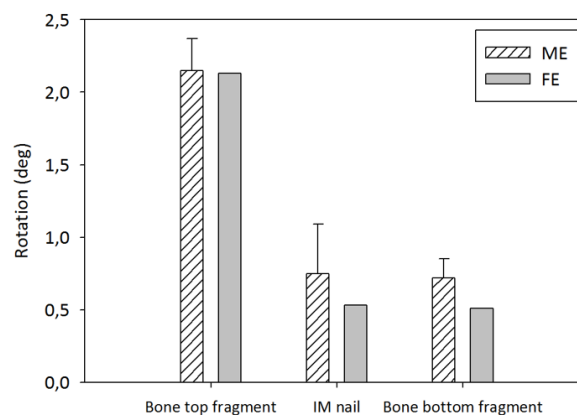


Figure 3.16 - Bone fragments (upper and lower portion) and intramedullary nail rotation registers from finite element simulation (grey) and mechanical experimentation DIC-measurements (diagonal stripes) in response to 5 Nm torsional loading of the osteotomized composite tibia fixed with the whole intramedullary nail system. FE - Finite element simulation, ME - Mechanical experimentation DIC measurements

From Figure 3.16 analysis, it is possible to identify that both finite element and *in vitro* mechanical experimentation presented similar bone interfragmentary and intramedullary nail rotations. Based on the results from the mechanical experimentation, the intramedullary nail contributed in average 35% for the fracture gap final torsion.

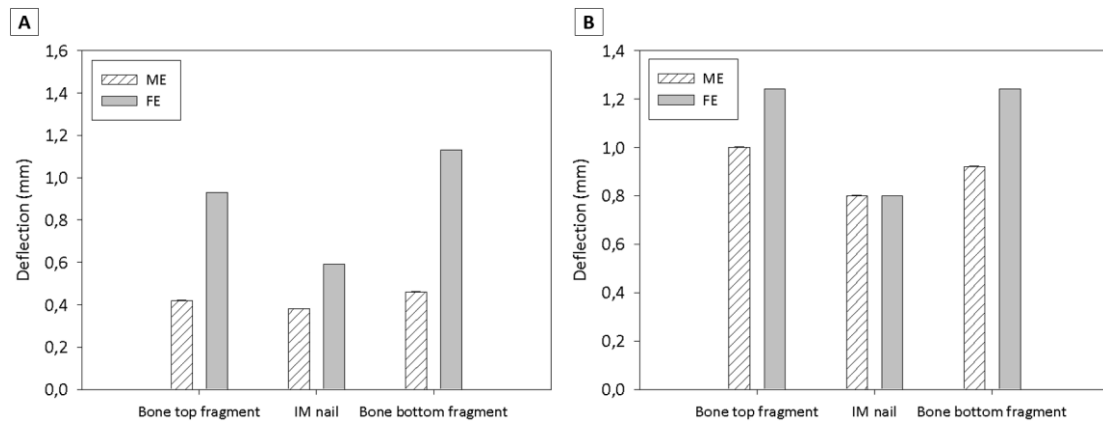


Figure 3.17 - Bone fragments (upper and lower portion) and intramedullary nail deflection registers from finite element simulation (grey) and mechanical experimentation DIC-measurements (diagonal stripes) as a response to 20 Nm N 4-point bending loading in the (A) sagittal and (B) coronal plane of the whole osteotomized composite tibia fixed with the intramedullary nail system. FE - Finite element simulation, ME - Mechanical experimentation DIC measurements

In the sagittal direction 4-point bending load finite element simulation shows a higher deflection of the bone fragments in relation to the intramedullary nail (see Figure 3.17(A)). In the mechanical experimentation all components exhibited the same amount of deflection. Based on the results from the *in vitro* mechanical experimentation, the intramedullary nail greatly contributes (around 82%) to the total amount of motion generated at the fracture site.

In both finite element simulation and mechanical experimentation coronal direction 4-point bending loading (see Figure 3.17(B)), there was a higher deflection of the bone fragments in relation to the intramedullary nail. However, the different models showed a significant difference in the amount of motion registered for the intramedullary nail. A higher intramedullary nail deflection was registered for the in the *in vitro* experiment. The deflection magnitude difference between the upper and lower bone fragment, is minor and can be considered of negligible importance. Based on the results from the *in vitro* mechanical experimentation, the intramedullary nail greatly contributes (about 82%) to the total amount of motion generated at the fracture site.

It is possible to verify from the results on the shear loading mode, Figure 3.18(A) and (B), that the system components - upper and lower bone fragments and the intramedullary nail - present a similar behavior between the finite element simulation and *in vitro* mechanical experimentation, in both the sagittal and coronal loading direction. However, overall lower deflection values were registered in the *in vitro* experimentation. There was also a greater discrepancy between the amounts of deflection of both upper bone fragment and intramedullary nail when compared to the amount generated by the lower bone fragment. Based on the information from the *in vitro* mechanical experimentation, the intramedullary nail

contributed in average 85% and 24%, during the sagittal and coronal bone orientation, respectively.

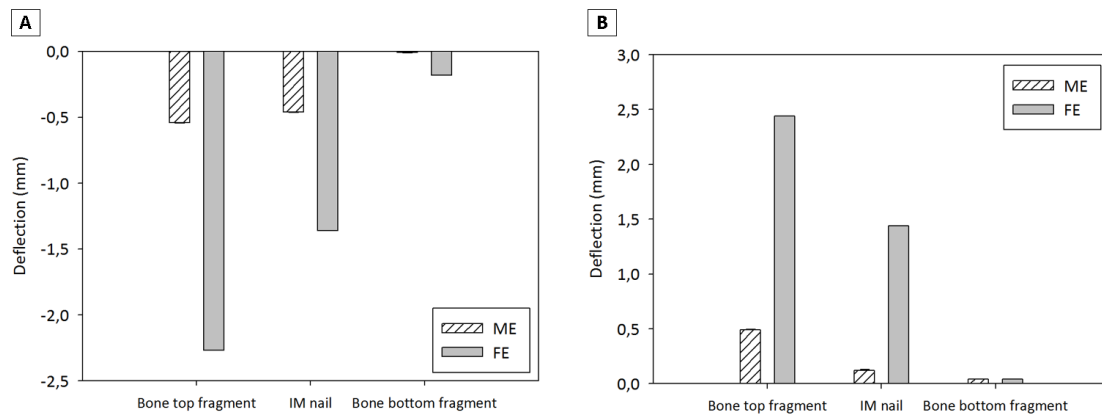


Figure 3.18 -Bone fragments (upper and lower portion) and intramedullary nail deflection registers from finite element simulation (FE) and mechanical experimentation DIC-measurements (ME) as a response to 100 N shear loading in the (A) sagittal and (B) coronal plane of the whole osteotomized composite tibia fixed with the intramedullary nail system

No prior published data was found in the literature on intramedullary nail fixation to an osteotomized fourth-generation composite tibia system mechanical evaluation which study conditions - *e.g.* load mode and magnitude applied as well as intramedullary nail parameters - fully matching the currently developed study. However, the study developed by Penzkofer *et al.* [11] and which research was later continued by Augat *et al.* [31], presented similar loading conditions and values as well as similar bone-implant system characteristics (8 mm length mid-diaphyseal bone fracture and a 9 mm diameter intramedullary nail with conventional locking mode). This level of correlation allowed the stiffness values, for all loading modes, obtained in the latter studies to be compared with one predicted in this chapter and by considering the bone-titanium alloy intramedullary nail finite element model (see Table 3.3).

The finite element predicted axial compression stiffness is higher than the one obtained by Penzkofer *et al.* [11] when the uncompressed bone-implant construct stiffness case was considered (723 ± 421 N/mm). However, the stiffness value obtained more closely resembles the ones registered when the compressed construct system was considered (2257 ± 358 N/mm). In regard to the predicted axial compression stiffness value (2500 N/mm), an axial interfragmentary narrowing of 0.08 mm is achieved which corresponds to 1% displacement of the fracture gap width, when a partial weight-bearing axial compression loading is applied. This interfragmentary movement was lower than the 10 mm obtained by Augat *et al.* [31] when the same amount of load was applied.

In respect to the torsional loading mode, the predicted stiffness value (1.44 Nm/deg), falls within Penzkofer's torsional stiffness values wide range for the compressed bone-implant construct (2.8 ± 2.4 Nm/deg). The finite element model led to an interfragmentary rotation of 4 degree of the proximal fragment in relation to the distal one, when 5 Nm moment is applied. The amount of rotational movement generated is below the 15 degrees achieved by Augat *et al.* [31].

For the 4-point bending in sagittal and coronal loading direction, the flexural stiffness predicted by the finite element model (93 Nm² and 65 Nm², respectively) were closely similar to the compressed bone-implant construct average flexural stiffness in sagittal and coronal loading direction (83 ± 15 Nm² and 58 ± 20 Nm², respectively). The amount of motion generated when 20 Nm bending moment was applied, 1.3 and 1.63 mm respectively, was also around 20% of the total deflection obtained by Augat *et al.* [31].

In regard to stiffness in sagittal and coronal loading direction obtained in this chapter (164 Nm² and 182 Nm², respectively), when a 100 N shear load was applied, a deflection of 2.34 and 2.53 mm was generated, respectively. The predicted interfragmentary motions were below the 5 mm deflection measured by Augat *et al.* [31] when the same amount of load was applied in shear mode, however the shear stiffness predicted closely related to the ones measured by Penzkofer *et al.* [11], when the uncompressed bone-implant construct stiffness case was considered (131 ± 30 N/mm and 164 ± 89 N/mm).

3.3. Discussion

Finite element models for a composite tibia before and after an intramedullary nail was implanted, were created and validated against a comprehensive set of mechanical experiments in which the models' stiffness/rigidity were measured and compared under axial compression, 4-point bending, shear and torsion loads considering a patient's early healing phase conditions and the results were evaluated against published experimental data. Special attention was given to the jigs with personalized bone-jig contact interface that were developed with the goal of guaranteeing bone physiological orientation during load application and a reproducible alignment between different mechanical experiments and between mechanical and finite element experimentation.

3.3.1. Intact tibia

This study started with the intact tibia finite element model validation through the comparison of the stiffness/rigidity values for all loading modes with those obtained from *in vitro* mechanical experimentation developed under the same test conditions. As it is possible to see in Table 3.2,

with the exception of the axial compression loading case, there was a considerably good agreement between all loading modes stiffness/rigidity values predicted by the finite element model and the ones determined from *in vitro* mechanical experimentation. In axial compression loading mode, a higher percentage difference of 51%, was registered. In a study developed by Zdero *et al.* [96], a finite element model of a fourth-generation composite femur was considered and validated to study the influence of cortical wall thickness on the biomechanical characteristics. In this study, an average percentage difference of 8% was obtained between finite element and experimental data and was used to validate the finite element predictability efficiency. The higher average percentage difference obtained in this work, 12%, did not allow to accurately claim the predictability in torsional, 4-point bending and shear loading mode of the intact tibia finite element model. The stiffness/rigidity variations encountered between the finite element and mechanical experimentation models most probably would be due to differences in the material properties, the boundary conditions and in the cortical bone thickness adopted for the tibia finite element model. Considering the manufacturer's reduced information regarding the composite tibia cortical thickness distribution, a physiological cortical bone thickness along the tibia and based on data obtained from literature, was adopted. The average measurements on the cortical bone thickness, in both planes, obtained from the x-ray taken after intramedullary nail implantation (see Figure 8.2 in Appendix A), were 2.60 ± 0.80 , 5.31 ± 3.42 , 6.62 ± 4.32 , 5.25 ± 1.35 , 3.54 ± 0.78 and 1.91 ± 0.73 which reflected on a difference of 23%, 40%, 14%, 22%, 29% and 5% between the measured values and the ones assumed on the finite element model throughout each of the six distinct segments considered at 10, 20, 40, 60 and 80 percent of the tibia total length (from the tibia bottom to the top), respectively. As previously stated in Sub-chapter 2.1., the cortical bone layer is considered to be the main weight-bearing component and not the cancellous bone [97], hence this component geometry and thickness greatly influences the bone structure stiffness. Besides the variation registered, the low average percentage difference can be considered as an indication of the designed set-up ability to guarantee a reproducible tibia alignment and load application between the mechanical and finite element experimentation.

Considering the intact tibia model relative simplicity, when compared to the bone-implant system, and the fourth-generation composite tibiae characteristic low inter-specimen mechanical properties variability, the *in vitro* mechanical experimentation results were compared to published data from the study developed by Anneliese Heiner [20] where the same size and model composite tibiae were tested under the axial compression, torsional and 4-point bending loading modes (see Table 3.2). Again with the exception of the axial compression

loading mode, the *in vitro* average flexural (in sagittal and coronal plane) and torsional rigidity values obtained in this chapter are reasonably similar with those in the reference study. The variations are most likely due to differences in the experimental technique setup (e.g. bone orientation, contact between bone and grips, location of the specimen support, fixation embedding material used), loading value and rate applied and motion data measurement method. No comparative analysis could be developed regarding the shear stiffness values obtained since this loading mode was not considered in the reference study. However, considering that the interlocking contact to bone loading jigs strategy was based on the same principle as the 4-point bending ones, it is possible to speculate that most probably similar results could have been obtained with literature, if this loading mode had been considered. Since the finite element axial stiffness value ($7.20 \text{ N}/\mu\text{m}$) is not in agreement with the *in vitro* mechanical experimentation values ($4.76 \pm 0.02 \text{ N}/\mu\text{m}$), but reasonably coincided with the one obtained in the reference study ($7.48 \pm 0.7 \text{ N}/\mu\text{m}$), where *in vitro* experimentation was developed, we are led to believe on the occurrence of a flaw in the axial compression *in vitro* experimentation. To analyze this hypothesis, the alignment between the tibia bone and the axial compression personalized grips were evaluated through the ESPI technique. As demonstrated in Figure 3.13 when axial compression load was applied, besides the bending (compression and tension) and pure axial motion expected, a torsional movement was generated at the tibia proximal portion. The generation of an additional motion type in the specimen proximal portion, indicates that there is a misalignment between the tibia plateau surface and the top grip personalized interface. The non-perfect contact between the grip and the bone may have caused the application of uneven stress on the specimen proximal surface during loading, which in turn caused a triaxial stress field in the tibia proximal portion and consequently additional non-physiological motion was generated [19]. Although the bone-grip contact interface site was machined through CNC technique, where a computer software controls the movement of the cutter and therefore the shape of the interface, the occurrence of a slight mistake during the conversion of the design into an information code can cause a considerable alteration in the machined structure. This phenomenon may explain the non-full contact between the bone and the machined interface site at the grip. The impossibility of a comparison between the predicted and measured stiffness values, limited the conclusions taken on the axial compression grips potential of maintaining the bone alignment between the mechanical and finite element experimentation.

As stated previously, the bending rigidity is influenced by the cross-sectional moment of inertia of the test specimen which is a measurement of the material distribution around a given axis

[63]. Hence, the value considered for this parameter can influence the bending rigidity, such that the greater the cross-sectional moment of inertia the higher is the resistance to buckling [98]. Similarly to Heiner *et al.* [20, 22] and Gardner *et al.* [24], in this study the moment of inertia equation adopted for the tibia bone case was the same as for a rectangular shaped beam. Such approximation is associated with an error. As demonstrated by Rittweger *et al.* [98], by considering beams with different cross-sections but with the same cross-sectional area as a human tibia, variations in the moment of inertia of approximately 157%, 64% and 3% can be obtained if a rectangular, circle or ring cross-section are considered, respectively. Also, as stated in sub-chapter 2.1, the cross-sectional moment of inertia varies greatly among tibiae (due to factors such as genetic differences and patterns of physical activity) and exhibits marked changes with age [99]. Hence, when the personalized grip technique is considered, by precisely knowing the positioning of the grips and through the use of the Solidworks software it will be possible to accurately determine the cross-sectional moment of inertia and hence standardize the bending rigidity calculation method and facilitate results comparison between studies.

3.3.2. Tibia-intramedullary nail system

After the intact tibia finite element model was validated and considered to have potential predictive abilities in 4-point bending (in sagittal and coronal plane), torsional and shear (in both planes) loading modes and the corresponding personalized designed grips evaluated and after the set-up was considered to be capable of guaranteeing reproducible bone alignment between mechanical and finite element simulation, the same composite tibia was osteotomized and fixed with an intramedullary nail to mimic a diaphyseal bone fracture recovery early scenario. The finite element model of the bone-implant complex system was developed and validated using the same strategy adopted for the intact tibia. Considering this system increased complexity when compared to the simple intact tibia model, besides the machine system global data acquired, local fracture site motion measurement through DIC virtual extensometer was included in the study, to guarantee that the maximum information from the bone-implant system *in vitro* mechanical experimentation would be obtained. As expected there were differences between the stiffness values registered with the DIC virtual extensometer and the ones measured by the machine system and where a percentage difference up to 20% was obtained. The machine system is associated with systematic errors. The machine system measurements are obtained from the mechanical testing machine internal transducers which register the displacement of the loading plate throughout the test. However, the specimen displacement and machine displacement are never exactly equal [63]. Besides the possible existence of 'end artifacts' (*e.g.* platen-specimen friction and machining-related damage of the

specimen ends), the machine system displacement measurements are also associated with displacements in the machine components during the test (*e.g.* internal test machine compliance and loading plate displacement) which compromise the accuracy of measurements obtained. Hence, the displacement measurements based upon machine system will always be overestimated to a certain extent which will lead to the underestimation of the stiffness determined [19, 63, 69, 100, 101]. This explains the DIC measurements-based higher stiffness values when compared with the ones determined from the machine system measurements. Hence, the stiffness values determined from the DIC optical methods local displacement measurements were considered more accurate and were used as the basis for the validation of the finite element simulation method. Although the DIC method using virtual extensometers technique was considered a more reliable measurement method it is important to highlight that this technique is also associated with error. The DIC method takes in-plane displacement measurements from a non-planer structure, that is the tibia, and this association is always correlated with a certain amount of measuring error. Also, the virtual extensometers technique considers selected points at the interfragmentary site where displacement information from a very limited amount of speckle points is considered, and which again is associated with a certain amount of error. Such approximations should always be taken into consideration when the results are analysed. For the finite element model, in all loading modes, with the exception of the 4-point bending, similar stiffness/rigidity values were obtained when data from the jig or the interfragmentary site was considered. The four-point bending test is only able to produce pure bending between the internal loading point for specimens with constant cross section and stiffness [102].

In all loading modes the stiffness values predicted by the finite element model were similar to the ones obtained from the *in vitro* mechanical experimentation, where a percentage variation between the models below 35% was registered (see Table 3.3). Although, according to Shore *et al.* [99], differences between the finite element and experimental stiffness values can differ by as much as 2-fold when cadaveric bone models are considered. It is possible to assume that for composite bone samples, the tolerance limit would be considerably lower. The percentage difference obtained in this study was considered low and could be due to differences in regard to the material properties considered in the finite element model, the existing differences between the models medullary canal reaming diameter (11 mm and 10 mm diameter, respectively), boundary conditions and more importantly to the different cortical bone thickness adopted in the finite element model. Therefore, the bone-implant model was considered predictive potential in 4-point bending (in sagittal and coronal plane), torsional and shear (in

both planes) loading modes. Since the same grips were used in both studies, it is reasonable to assume that the misalignment between the bone and the grip due to machined error at the grip interface (and which was identified during the intact tibia model *in vitro* mechanical experimentation) would also manifest during the bone-implant system mechanical experimentation study. Despite the importance of the axial compression loading conditions, which according to Gray *et al.* [42] were considered to be predominant when compared to 4-point bending and torsion loading, the validation of the bone-implant system finite element model in this loading mode was not possible. In addition to the models stiffness values comparison, a more rigorous evaluation of the predictability potential of the finite element model was also achieved through the analysis and comparison between the upper and lower bone fragments and intramedullary nail displacements registers from *in vitro* mechanical experimentation DIC measurement method using virtual extensometers data and the ones predicted by the finite element model simulation. In all loading cases, the upper and lower bone fragments showed similar behaviours between the models, although differences were found between the predicted and measured stiffness values. In most *in vitro* tests the intramedullary nail showed a high percentage contribution (up to 85%) for the total fracture site motion, when compared to the results obtained by Augat *et al.* [31]. In the finite element model, however, the percentage contribution of the nail for the total motion of the interfragmentary bone fragments was reduced and more closely resembled those obtained by Augat and his co-workers. An explanation for the difference between the *in vitro* and the finite element model developed in this study is that during *in vitro* mechanical experimentation, the bone fragments are presenting a low motion as a result of the bone fragments inner cancellous bone analog approximation to the intramedullary nail as a result of set-up preload during the test system “settling” phase. This reduces the overall motion expected from the bone fragments which are in direct contact with the loading grips and consequently increases the contribution of the nail in the interfragmentary motion [31, 37]. It is important to highlight that in a real case scenario the presence of soft tissue would stabilize the bone fragments reducing their motion and increasing the intramedullary nail contribution for the fracture site overall motion. Based on the system evaluation the bone-implant model developed is considered close to valid and having predictive potential in 4-point bending (in sagittal and coronal plane), torsional and shear (in both planes) loading modes.

The adequacy of the bone-implant finite element model was verified through the comparison of the predicted stiffness values and interfragmentary gap motion with the ones obtained from previous studies. The stiffness values, obtained from the bone-intramedullary nail (titanium alloy) construct finite element, in almost all loading modes, more closely resembled the ones

measured from the mechanical experimentation developed by Penzkofer *et al.* [11], where a compressed construct model was considered in relation to conventional intramedullary nail fixation construct. Also the amount of interfragmentary gap motion was below the values registered by Augat *et al.* [31] when osteotomized cadaveric tibiae were equipped with interlocked intramedullary nails. Several factors contributed for the higher stiffness values obtained in bone-implant systems finite element such as the lower reaming diameter, the fully bonded contact between the nail and the screws (*i.e.* resembling the case where screws are threaded into the threads on the bone and on the implant creating an angle-stable nail-screw fixation [37, 103]), differences in the mechanical properties of the implant material and the fact that the finite element model considered an orthotropic cortical bone and isotropic cancellous bone with mechanical properties from healthy adult bone in contrast to the anisotropic mechanical properties behaviour of human bone. In this chapter, the goal was not to analyze the biomechanical behavior of this particular intramedullary nail design, but to experiment and consolidate the knowledge on the principle of bone-intramedullary nail stability. However, it is possible to claim that the finite element model studied is a representation of a more stable construct as a result of the system higher stiffness values in all loading modes and which translates in a reduced amount of motion generated at the fracture gap. This study also demonstrated that the interfragmentary site will always be subjected to some amount of motion and that during early healing phase the nail will support most of the load applied on the lower limb.

3.3.3. Limitations

This study has several limitations and assumptions which should be discussed. In this study, the intact tibia model was validated based on the stiffness values obtained from the machine system load applying grip displacement registers obtained during mechanical experimentation and the bone-implant system finite element model was validated based on the assumption that if selected points at the interfragmentary site were similar between the finite element and the mechanical experimentation, the overall displacements between the models would also be. However, both validation strategies lack in the detection of local errors through the finite element models, therefore they could be considered as global indicators of the accuracy of the predictions. A more rigorous evaluation method would be to compare the finite element model stiffness values to the experimental measured ones in correspondent sites along the tibia through the analysis of the coefficient of linear regression R^2 , the slope and interception of the linear regression line obtained from measured and predicted values curve, as suggested by Gray *et al.* [29, 42] and Taddei *et al.* [104]. The surface displacement measurements methods

available, ESPI and DIC, showed restrictive limitation in their application for this particular purpose. The experiment developed in this chapter with the ESPI technique where it was used for the detection of all the small displacements in order to identify any slight misalignments between the bone and the grip, was a good example of the potential and high sensitivity of this technique. However, the ESPI technique high resolution makes it extremely sensitive to ambient vibrations which decreases the signal-to-noise ratio and limits the use of this technique to environments with controlled conditions. Another limitation for the use of ESPI is that the load applied to the test specimen must be small to avoid large displacement that could lead to de-correlation. The interpretation of the resulting in-plane fringes can also be difficult and to gain an understanding of the overall movement is not always straightforward [70]. All these characteristics limited the application of the ESPI technique for the measurement of the displacements along the entire tibia model. The use of the DIC measurement method without the virtual extensometers approach requires individual measurements for each component in the bone-implant system since it is not possible to measure the entire construct at the same time, which limits its use for this specific application. An interesting alternative measurement method would be the highly accurate non-contact laser extensometers which scan a laser beam along the length of the test specimen and tracks record of marks along the structure [105, 106]. Unfortunately, this method technique was no available in the Faculty of Engineering.

There are many reasons which have contributed for the differences between the finite element model and the mechanical experimentation stiffness/rigidity values obtained. Considering that variations in the bone alignment between the models were not present, details assumed or simplified in the finite element model could have greatly contributed for the variations registered. As stated previously, there were differences between the mechanical experiment boundary conditions and the ones considered in the finite element model. The most common suggested strategy and which was also adopted in this chapter, for the development of a model that satisfies the practical requirements, is to modify the modelling assumptions and parameters until there is a correlation between the analytical predictions and the experimental results [107]. From this iterative approach it was possible to notice that both models (bone and bone-implant) were very sensitive to slight boundary and parameters variations. The study developed in this chapter was not concerned with the understanding of how changes of parameters may influence the structural responses. It is important that the influence of each assumption is understood in order to determine whether the results are still reliable [108]. Hence, in order for the location of the error(s) and for deviations between test and mechanical analysis to be minimized a sensitive analysis should have been developed. Another important parameter which contributed

for the percentage variation between the models was the distribution of the cortical bone thickness through the tibia. The determination of the cortical thickness based on the method suggested in this chapter was a very challenging task. However, the geometric modeling of this layer could have been done in a more easily manner and with more accurate results, if computer tomography (or CT) [28, 29, 37-39, 42] or magnetic resonance imaging (or MRI) [28, 32] data was obtained from the intact tibia and was used as the basis for the construction of the finite element model. The use of a CT also allows obtaining anisotropic specific properties of the bone tissue under study for the mechanically complex cadaveric bone. It is believed that this strategy would have improved the model predictive capabilities [104].

Another limitation of the study was that although a huge concern was expressed in relation to physiological bone orientation and even load application, the tibia as a support structure of the body system is subjected to a more complex loading *in vivo* than the simplified representations adopted in this study [68, 97, 99]. Hence, in order to replicate a physiological representative biomechanical behavior of the bone-implant system and to obtain clinically relevant insights on this subject, the influence of the soft tissue, muscles and hematoma in the fracture gap motion [31, 35] should prospectively be included in the study tools developed. Another limitation was in the use of the gypsum plater during the mechanical experimentation. In comparison to the more commonly used poly(methyl methacrylate) (PMMA) bone cement as mounting/embedding material [35], the gypsum plater was selected based on its good availability, simple application and more importantly the ease to remove which allowed different grips to be applied to the same bone test sample. However, the solidification process involves water evaporation where mould shrinkage may occur. There is also no proof of the material stability under load since this component has not been used in previous bone mechanical test experiments. Another remark can be made regarding the torsional loading mode where a cardanic hinge (saddle joint) should have been coupled to the upper grip in order to avoid transmission of any load other than the intended torque and to allow tibia self-alignment during the essay. However, such improvements were not possible due to the torsional loading set-up adaptation required.

Despite these limitations, this study provided a tool for simulating mechanical experimental conditions with a composite tibia, where the standardized geometry and low inter-specimen mechanical properties variability of the synthetic bones, facilitated the study design and validation process. However, although it may be agreed upon that the composite bones are able to establish a baseline which allow a direct comparison to physiological conditions [16], it is of

general consent that an accurate study on bone-implant system and its relation to the bone healing process, demands the use of cadaveric bone samples. If the cadaveric tibiae are to be considered the study samples, the tools developed in this study present severe limitations. The grips' stainless steel personalized interface only allows their use for the specific tibia to which they were designed based on. When composite tibia is used, this drawback may be bypassed due to the synthetic tibia similar geometries, however, high inter- and intra-individual geometric variability characteristic of human tibiae, completely jeopardize their study through this strategy [109]. Also, the study of cadaveric tibia samples, obligates to test a high number of specimens to obtain satisfactory statistically significant comparisons as a result of their large variability in terms of quality and mechanical property [14, 100]. A simple and reproducible strategy to use the models developed in this chapter to studies based on the use of cadaveric bones, would be to apply the 3D-printing techniques to obtain personalized bone-implant interface for each of the cadaver specimens under test and shift the personalized interface in the grips between the test specimens. This approach would allow the development of finite element analysis studies based on cadaveric bone and their validation through mechanical experimentation while guaranteeing reproducible bone alignment and load application.

3.4. Conclusion

The acquisition of an optimal mechanical environment for bone fractures is a determinant issue in the recovery process and the ability to study the bone-intramedullary nail system biomechanical stability with data that closely resembles the physiological ones is a key strategy in this process. Thus, in this research a strategy considering both finite element analysis and mechanical tests for the overall evaluation of intact bone and/or bone-implant system under simple and reproducible conditions while reflecting physiological load and bone orientation, was developed.

Through the analysis and validation of the study tools, a bone-intramedullary nail stiff construct was developed and when loaded, in different modes, it positively responded with the generation of interfragmentary motion. However, the impact of such stimulus in the healing process is greatly limited by the still controversial and not fully understood ideal mechanical environment at the fracture site and how this concept evolves throughout the healing progress. Until the relation between bone-intramedullary nail stability and optimal interfragmentary motion for fracture healing is not established, it is difficult to determine performance goals for the intramedullary nail fixation method and to develop strategies in order to improve the fixation method and enhance the healing process quality and recovery time. The tools developed in this

study still need to be improved in order for cadaveric bone samples to be studied. However, considering the high sensibility of the model to slight variation in the parameters, it is possible to claim that the finite element model developed presents a satisfactory level of reliability in relation to the tibia experimental behaviour. Hence, it can already be used for bone-implant studies, *e.g.* by considering that the shape and the mechanical properties of bone are greatly determined by the strain to which it is subjected, the question arises if any interesting insights could be obtained with the application of the tools developed in this study to analyze the stress and strain generated at the fracture site when intramedullary nail system was used and how it resembles the pattern generated at the same location in physiological healthy bone when exposed to the same mechanical loading conditions. Hopefully the strategy developed in this chapter will contribute to assist in the physiological description of the bone-implant construct stability and its role in the healing process. Also with the use of the tools developed and by varying the axis lines, it may be possible to represent and analyze limb deformity cases (*e.g.* valgus knee, varus knee, hamstring contracture, hyper-extended knee and knee arthritis) [45, 46]. While no new groundbreaking disclosure on the intramedullary nail stability subjected is introduced, the application of additional physiological micromotion, to the already generated motion from the use of the intramedullary nail, in the early healing phase post-fracture (up to 3 weeks according to Dailey *et al.* [35] suggestions) when patients normally have very low activity levels, is an interesting strategy which may reinforce the fracture healing process without additional risks to the patients.

3.5. References

1. Claes, L., S. Recknagel, and A. Ignatius, *Fracture healing under healthy and inflammatory conditions*. Nature Reviews Rheumatology, 2012. **8**(3): p. 133-143.
2. Trafton, P.G., et al., *Tibial shaft fractures*, in *Skeletal Trauma: Basic Science, Management, and Reconstruction*, B.D. Browner, Editor 2009, Elsevier Health Sciences: Philadelphia, United States of America. p. 2319-2452.
3. Ouyang, X., et al., *Interlocking Intramedullary Nails in Fracture Treatment*. Cell Biochemistry and Biophysics, 2015. **73**(1): p. 261-265.
4. Madadi, F., et al., *Adult tibial shaft fractures—different patterns, various treatments and complications*. Medical Science Monitor, 2011. **17**(11): p. CR640-CR645.
5. Byrne, D.P., D. Lacroix, and P.J. Prendergast, *Simulation of fracture healing in the tibia: mechanoregulation of cell activity using a lattice modeling approach*. Journal of Orthopaedic Research, 2011. **29**(10): p. 1496-1503.
6. Schmitt, K.-U., et al., *Trauma Biomechanics: Introduction to Accidental Injury* 2013 New York, United States of America: Springer Science & Business Media.
7. Lewis, D., et al., *Low cost polymer intramedullary nails for fracture fixation: a biomechanical study in a porcine femur model*. Archives of orthopaedic and trauma surgery, 2009. **129**(6): p. 817-822.

8. Horn, J., et al., *Angle stable interlocking screws improve construct stability of intramedullary nailing of distal tibia fractures: a biomechanical study*. Injury, 2009. **40**(7): p. 767-771.
9. Yadav, D., et al., *Removal of a broken distal cannulated intramedullary femoral nail with solid reamer with closed methods and without using C-arm: A case report*. Journal of Arthroscopy and Joint Surgery, 2015. **2**(1): p. 9-11.
10. Letechipia, J., et al., *Design and preliminary testing of an active intramedullary nail*. Revista de Investigación Clínica, 2014. **66**(1): p. S70-S78.
11. Penzkofer, R., et al., *Influence of intramedullary nail diameter and locking mode on the stability of tibial shaft fracture fixation*. Archives of Orthopaedic and Trauma Surgery, 2009. **129**(4): p. 525-531.
12. Samiezadeh, S., et al., *Biomechanical assessment of composite versus metallic intramedullary nailing system in femoral shaft fractures: A finite element study*. Clinical Biomechanics, 2014. **29**(7): p. 803-810.
13. Beer, F.P., et al., *Mechanics of Materials*. 6th ed2012, New York, USA: Mc-Graw-Hill.
14. Dutta, S.K. and D. Dutta, *Applied Orthopaedic Biomechanics*. 1st ed2008, New Delhi, India: BI Publications Pvt Ltd.
15. Cheung, G., et al., *Finite element analysis of a femoral retrograde intramedullary nail subject to gait loading*. Medical Engineering & Physics, 2004. **26**(2): p. 93-108.
16. Papini, M., et al., *The biomechanics of human femurs in axial and torsional loading: comparison of finite element analysis, human cadaveric femurs, and synthetic femurs*. Journal of Biomechanical Engineering, 2007. **129**(1): p. 12-19.
17. Martens, M., et al., *The Geometrical Properties of Human Femur and Tibia and Their Importance for the Mechanical Behaviour of These Bone Structures*. Archives of Orthopaedic and Trauma Surgery, 1981. **98**: p. 113-120.
18. Elfar, J., et al., *Composite bone models in orthopaedic surgery research and education*. Journal of the American Academy of Orthopaedic Surgeons, 2014. **22**(2): p. 111-120.
19. Keller, T.S. and M.A.K. Liebschner, *Tensile and Compression Testing of Bone, in Mechanical Testing of Bone and the Bone - Implant Interface*, Y.H. An and R.A. Draughn, Editors. 1999, CRC Press: London, United Kindom. p. 175-206.
20. Heiner, A.D., *Structural properties of fourth-generation composite femurs and tibias*. Journal of Biomechanics, 2008. **41**(15): p. 3282-3284.
21. SawBones, *Mechanical test materials*, 2015: Malmö, Sweden. p. 1-8.
22. Heiner, A.D. and T.D. Brown, *Structural properties of a new design of composite replicate femurs and tibias*. Journal of Biomechanics, 2001. **34**(6): p. 773-781.
23. Chong, A.C.M., et al., *Fracture toughness and fatigue crack propagation rate of short fiber reinforced epoxy composites for analogue cortical bone*. Journal of Biomechanical Engineering, 2007. **129**: p. 487-493.
24. Gardner, M.P., et al., *Mechanical evaluation of large-size fourth-generation composite femur and tibia models*. Annals of Biomedical Engineering, 2010. **38**(3): p. 613-620.
25. Zdero, R., et al., *Cancellous bone screw purchase: a comparison of synthetic femurs, human femurs, and finite element analysis*. Proceedings of the Institution of Mechanical Engineers, Part H: Journal of Engineering in Medicine, 2008. **222**(8): p. 1175-1183.
26. Zdero, R., et al., *Cortical screw purchase in synthetic and human femurs*. Journal of Biomechanical Engineering, 2009. **131**(9): p. 094503.
27. Nicayenzi, B., et al., *Biomechanical measurements of cortical screw stripping torque in human versus artificial femurs*. Proceedings of the Institution of Mechanical Engineers, Part H: Journal of Engineering in Medicine, 2012: p. 1-7.
28. Filardi, V., *The healing stages of an intramedullary implanted tibia: A stress strain comparative analysis of the calcification process*. Journal of Orthopaedics, 2015. **12**(1): p. S51-S61.

29. Gray, H.A., et al., *Experimental validation of a finite element model of a human cadaveric tibia*. Journal of Biomechanical Engineering, 2008. **130**(3): p. 1-9.
30. Zdero, R. and H. Bougherara, *Orthopaedic biomechanics: a practical approach to combining mechanical testing and finite element analysis*, in *Finite Element Analysis*, D. Moratal, Editor 2010, INTECH Open Access Publisher.
31. Augat, P., et al., *Interfragmentary movement in diaphyseal tibia fractures fixed with locked intramedullary nails*. Journal of Orthopaedic Trauma, 2008. **22**(1): p. 30-36.
32. Raunest, J., et al., *Geometric properties of the fractured tibia stabilized by unreamed interlocking nail: development of a three-dimensional finite element model*. Computers and Biomedical Research, 1996. **29**(4): p. 259-270.
33. Gaebler, C., et al., *The fatigue strength of small diameter tibial nails*. Injury, 2001. **32**(5): p. 401-405.
34. Tschegg, E.K., et al., *Stiffness analysis of tibia-implant system under cyclic loading*. Materials Science and Engineering: C, 2008. **28**(8): p. 1203-1208.
35. Dailey, H.L., et al., *A novel intramedullary nail for micromotion stimulation of tibial fractures*. Clinical Biomechanics, 2012. **27**(2): p. 182-188.
36. Zhou, X., et al. *Finite element analysis of mechanical properties of wooden club shaped and general screws with interlocking intramedullary nail*. in *IEEE International Conference on Mechatronics and Automation (ICMA)*. 2014. Tianjin, China: IEEE.
37. Wehner, T., et al., *Improvement of the shear fixation stability of intramedullary nailing*. Clinical Biomechanics, 2011. **26**: p. 147-151.
38. Taheri, E., B. Sepehri, and R. Ganji, *Mechanical Validation of Perfect Tibia 3D Model Using Computed Tomography Scan*. Engineering, 2012. **4**: p. 877-880.
39. Tarnita, D., et al., *CAD method for three-dimensional model of the tibia bone and study of stresses using the finite element method*. Romanian Journal of Morphology and Embryology, 2006. **47**(2): p. 181-186.
40. Yardimeden, A., et al., *The stress analysis of human tibia under axial loading using finite element method*, in *12th International Research/Expert Conference* 2008: Istanbul, Turkey.
41. Cristofolini, L. and M. Viceconti, *Mechanical validation of whole bone composite tibia models*. Journal of Biomechanics, 2000. **33**(3): p. 279-288.
42. Gray, H.A., et al., *Experimental validation of a finite element model of a composite tibia*. Proceedings of the Institution of Mechanical Engineers, Part H: Journal of Engineering in Medicine, 2007. **221**(3): p. 315-324.
43. Gaebler, C., et al., *A new modular testing system for biomechanical evaluation of tibial intramedullary fixation devices*. Injury, 2001. **32**(9): p. 708-712.
44. Goodyear, S.R. and R.M. Aspden, *Mechanical properties of bone ex vivo*, in *Bone Research Protocols, Methods in Molecular Biology*, M.H. Helfrich and S.H. Ralston, Editors. 2012, Springer Science+Business Media: London, UK. p. 555-572.
45. Mündermann, A., *The use of Anthropometry for the measurement of lower extremity alignment*, in *Handbook of Anthropometry. Physical Measures of Human Form in Health and Disease*, V.R. Preedy, Editor 2012, Springer Science & Business Media: London, United Kingdom. p. 2951-2970.
46. Pickering, S. and D. Armstrong, *Focus on alignment in total knee replacement*. The Bone & Joint Journal, 2012: p. 1-3.
47. Paley, D., *Normal lower limb alignment and joint orientation*, in *Principles of Deformity Correction*, D. Paley and J.E. Herzenberg, Editors. 2002, Springer Berlin Heidelberg: New York, United States of America. p. 1-18.
48. Paley, D., *Principles of Deformity Correction*, in *Skeletal Trauma: Basic Science, Management, and Reconstruction*, B.D. Browner, et al., Editors. 2014, Elsevier Health Sciences: Philadelphia, United States of America. p. 2779-2843.

49. Cooke, T.D.V., E.A. Sled, and R.A. Scudamore, *Frontal plane knee alignment: a call for standardized measurement*. Journal of Rheumatology, 2007. **34**(9): p. 1796-1800.
50. Yoshioka, Y., et al., *Tibia anatomy and functional axes*. Journal of Orthopaedic Research, 1989. **7**(1): p. 132-137.
51. Han, H.S., et al., *Evaluation of anatomic references for tibial sagittal alignment in total knee arthroplasty*. Knee Surgery, Sports Traumatology, Arthroscopy, 2008. **16**(4): p. 373-377.
52. Ruff, C.B. and W.C. Hayes, *Cross-sectional geometry of Pecos Pueblo femora and tibiae—A biomechanical investigation: I. Method and general patterns of variation*. American Journal of Physical Anthropology, 1983. **60**(3): p. 359-381.
53. White, T.D., M.T. Black, and P.A. Folkens, *Leg: Femur, patella, tibia, and fibula*, in *Human Osteology*, T.D. White, M.T. Black, and P.A. Folkens, Editors. 2012, Academic press: Oxford, UK. p. 254-263.
54. Tencer, A.F., *Biomechanics of fixation and fractures*, in *Rockwood & Green's Fractures in Adults*, R.W. Bucholz, J.D. Heckman, and C. Court-Brown, Editors. 2006, Lippincott Williams & Wilkins. p. 4-43.
55. Neto, R.B., J.D.M.B. Rossi, and T.P. Leivas, *Experimental determination of bone cortex holding power of orthopedic screw*. Revista do Hospital das Clínicas, 1999. **54**(6): p. 181-186.
56. Heinonen, A., et al., *Mineral mass, size, and estimated mechanical strength of triple jumpers' lower limb*. Bone, 2001. **29**(3): p. 279-285.
57. Apivatthakakul, T., et al., *Tibial shaft 42-C1 CRIF*, P. Trafton, Editor 2012, AO Foundation.
58. L.A. Medical, *Surgical technique operation manual for intramedullary tibial nails ACCU – NAIL®*, 2013: Albergaria-a-Velha, Portugal. p. 1-14.
59. DePuy Synthes Trauma, *Opening the tibia*, in *Expert Tibial Nail - Surgical Technique* 2015, Synthes GmbH: Oberdorf, Switzerland. p. 18.
60. Duda, G.N., et al., *Mechanical conditions in the internal stabilization of proximal tibial defects*. Clinical Biomechanics, 2002. **17**(1): p. 64-72.
61. Nelson, F.R.T. and C.T. Blauvelt, *A manual of orthopaedic terminology*. 8th ed 2015, Philadelphia, USA: Elsevier Saunders.
62. AO Foundation, *Müller AO Classification of Fractures - Long Bones*, in *AOTrauma* 2010: Switzerland. p. 1-10.
63. Turner, C.H. and D.B. Burr, *Experimental techniques for bone mechanics*, in *Bone Mechanics Handbook*, S.C. Cowin, Editor 2001, CRC Press LLC: London, United Kingdom. p. 1-35.
64. Institute of Science and Innovation in Mechanical and Industrial Engineering. Available from: <http://www.inegi.pt/inicial.asp?k=z&LN=EN>.
65. Centro de Formação Profissional da Indústria Metalúrgica e Metalomecânica (CENFIM). Available from: <http://www.cenfim.pt/>.
66. Flupol - Surface Engineering S.A.; Available from: <http://flupol.pt/>.
67. Arezes, P., et al., *Anthropometric study of the Portuguese population* 2006, Lisbon, Portugal: Portuguese Institute for Safety and Health at Work (ISHST).
68. Morgan, E.F., G.F. Barnes, and T.A. Einhorn, *The bone organ system: Form and function*, in *Osteoporosis*, R. Marcus, et al., Editors. 2013, Elsevier: London, UK. p. 3-20.
69. Barak, M.M., A. Sharir, and R. Shahar, *Optical metrology methods for mechanical testing of whole bones*. The Veterinary Journal, 2009. **180**: p. 7-14.
70. Tyrer, J.R., C. Palou-Heras, and T. Slater, *Three-dimensional human femoral strain analysis using ESPI*. Optics and Lasers in Engineering, 1995. **23**: p. 291-303.
71. Butters, J.N. and J.A. Leendertz, *Speckle pattern and holographic technique in engineering metrology*. Optical Laser Technology, 1971. **3**: p. 26-30.

72. Chattah, N.L.-T., et al., *Determining the elastic modulus of mouse cortical bone using electronic speckle pattern interferometry (ESPI) and micro computed tomography: A new approach for characterizing small-bone material properties*. Bone, 2009. **45**: p. 84-90.
73. Novitskaya, E., et al., *Recent advances on the measurement and calculation of the elastic moduli of cortical and trabecular bone: a review*. Journal of Theoretical and Applied Mechanics, 2011. **38**(3): p. 209-297.
74. František, Š., K. Matúš, and O. Martin, *The Verification of Fixture for Shear Load with Optical Method ESPI*. American Journal of Mechanical Engineering, 2013. **1**(7): p. 180-184.
75. Huang, Y.-H. and C.-C. Ma, *Forced vibration analysis of piezoelectric quartz plates in resonance*. Sensors and Actuators A Physical, 2009. **149**(2): p. 320-330.
76. OpenClipart-Vectors, *Computer/Communication*, computer-158675_960_720, Editor 2013: Pixabay.
77. Maji, A.K., J.L. Wang, and J. Lovato, *Electronic speckle pattern interferometry for fracture mechanics testing*. Experimental Techniques, 1991. **15**(3): p. 19–23.
78. Lu, B., et al., *Measurement of a three-dimensional temperature field applying ESPI and CT techniques*. Optics Communications, 1988. **69**(1): p. 6-10.
79. Facchini, M. and P. Zanetta, *Estimation of masonry mechanical characteristics by ESPI fringe interpretation*. Optics and Lasers in Engineering, 1995. **23**: p. 277-290.
80. Sękalski, P., *Smart materials as sensors and actuators for Lorentz force tuning system*, in *Department of Microelectronics and Computer Science* 2006, Technical University of Łódź: Lodz, Poland.
81. Pan, B., et al., *Two-dimensional digital image correlation for in-plane displacement and strain measurement: a review*. Measurement Science and Technology, 2009. **20**(6): p. 1-18.
82. Pan, B. and K. Li, *A fast digital image correlation method for deformation measurement*. Optics and Lasers in Engineering, 2011. **49**(7): p. 841-847.
83. Xavier, J., et al., *The region of interest of the model was painted to create a carrier speckle pattern suitable for DIC technique*. Optical Engineering, 2012. **51**(4): p. 1-12.
84. Robert, L., et al., *Use of 3-D digital image correlation to characterize the mechanical behavior of a fiber reinforced refractory castable*. Experimental Mechanics, 2007. **47**: p. 761–773.
85. Lecompte, D., et al., *Quality assessment of speckle patterns for digital image correlation*. Optics and Lasers in Engineering, 2006. **44**(11): p. 1132-1145.
86. Bailey, D., *Full field strain*, Instron®, Editor 2016: Buckinghamshire, England. p. 1-2.
87. Harris, D., *MOB Lab and VT collaborate on testing Westbound spans of Hampton road bridge tunnel bridges*, in *Digital Image Correlation*, U.o. Virginia, Editor 2016.
88. *Stahlschlüssel: Key to steel*. 23th ed 2013, Marbach, Germany: Verlag Stahlschlüssel.
89. Morawska-Chochół, A., et al., *Influence of the intramedullary nail preparation method on nail's mechanical properties and degradation rate*. Materials Science and Engineering: C, 2015. **51**: p. 99-106.
90. EUROFLEX GmbH, *Stainless steel tubing for surgical implants and devices - Material data*, 2015: Pforzheim, Germany.
91. Disegi, J., *Implant materials – Titanium-6% Aluminum-7% Niobium Synthes*, Editor 2008: Pennsylvania, United States of America. p. 1-19.
92. Parthasarathy, V.N., C.M. Graichen, and A.F. Hathaway, *A comparison of tetrahedron quality measures*. Finite Elements in Analysis and Design, 1994. **15**(3): p. 255-261.
93. Sinclair, G.B., J.R. Beisheim, and S. Sezer. *Practical convergence-divergence checks for stresses from FEA*. in *In Proceedings of the 2006 international ANSYS conference*. 2006. Pittsburgh, USA.

94. Begum, F., *Experimental and Numerical Analysis of Augmented Locking Plate Fixation Repair for Proximal Humeral Fractures*, in *Civil and Environmental Engineering Department* 2011, University of Alberta: Alberta, Canada.
95. Cordey, J., et al., *Importance of the friction between plate and bone in the anchoring of plates for osteosynthesis. Determination of the coefficient of metal-bone friction in animal in vivo*. *Helvetica chirurgica acta*, 1979. **46**: p. 183-187.
96. Zdero, R., et al., *The effect of cortex thickness on intact femur biomechanics: a comparison of finite element analysis with synthetic femurs*. *Proceedings of the Institution of Mechanical Engineers, Part H: Journal of Engineering in Medicine*, 2010. **224**(7): p. 831-840.
97. Minns, R.J., G.R. Bremble, and J. Campbell, *The geometrical properties of the human tibia*. *Journal of Biomechanics*, 1975. **8**(3): p. 253-255.
98. Rittweger, J., et al., *Bone-muscle strength indices for the human lower leg*. *Bone*, 2000. **27**(2): p. 319-326.
99. Shore, S.W., et al., *Bone biomechanics*, in *Orthopaedic Biomechanics*, B.A. Winkelstein, Editor 2012, CRC Press: Florida, USA. p. 3-48.
100. Currey, J., *Cortical bone*, in *Handbook of Biomaterial Properties*, J. Black and G. Hastings, Editors. 2013, Springer Science & Business Media: Dordrecht, Netherlands. p. 3-14.
101. Keaveney, T.M., *Cancellous bone*, in *Handbook of Biomaterial Properties*, J. Black and G. Hastings, Editors. 2013, Springer Science & Business Media: Dordrecht, Netherlands. p. 15-23.
102. Saffar, K.P., N. JamilPour, and S.M. Rajaai, *How does the bone shaft geometry affect its bedding properties?* *American Journal of Applied Science*, 2009. **6**(3): p. 463-470.
103. Heiney, J.P., et al., *Distal femoral fixation: A biomechanical comparison of retrograde nail, retrograde intramedullary nail, and prototype locking retrograde nail*. *Clinical Biomechanics*, 2012. **27**: p. 692-696.
104. Taddei, F., et al., *Subject-specific finite element models of long bones: an in vitro evaluation of the overall accuracy*. *Journal of Biomechanics*, 2006. **39**(13): p. 2457-2467.
105. Dillard, D.A., *Physical properties of adhesives*, in *Handbook of Adhesion Technology*, L.F.M. da Silva, A. Öchsner, and R.D. Adams, Editors. 2011, Springer: Heidelberg, Germany. p. 393-414.
106. Shah, V., *Handbook of plastics testing and failure analysis*. 3rd ed 2007, New Jersey, USA: Wiley.
107. Mottershead, J.E., M. Link, and M.I. Friswell, *The sensitivity method in finite element model updating: A tutorial*. *Mechanical Systems and Signal Processing*, 2011. **25**: p. 2275-2296.
108. McCurry, M.R., A.R. Evans, and C.R. McHenry, *The sensitivity of biological finite element models to the resolution of surface geometry: a case study of crocodilian crania*. *PeerJ*, 2015. **3**: p. 988-1004.
109. Hrdlicka, A., *Study of the normal tibia*. *American Anthropologist*, 1898. **11**(10): p. 307-312.

“Roughly 90% of the useful information about magnets can be learned in 25 minutes.

The remaining 10% takes a lifetime to learn”

Anonymous

4. Actuator selection

In this chapter, the potential of different material actuators for the purpose of bone healing enhancement, as well as their ability to perform in association with the intramedullary nail, and to be implanted in the medullary cavity, were evaluated. There is constant search for excellence in medical technologies, which increases patient's quality of life by reducing the required healing time in a simple and effective manner and at a possibly reduced cost. This demanding's, requires the existence of materials with superior performance characteristics [1]. A material that generates a motion - strain or vibration - throughout the intramedullary nail, transmitting it to bone fragments and consequently to the interfragmentary healing site, should be considered. Movements with different amplitudes and frequencies that are capable of inducing at least 5 μe at the fracture site and performs at frequencies between 10 to 100 Hz (or slightly higher), are desired. The actuator will be in direct contact with the cannulated intramedullary nail's interior or the exterior surface. Hence, actuator sizes can vary but are preferred to be in the millimeter range. The actuator is expected to perform during at least several weeks in response to a stimulus, and at an average temperature of 37 °C (in the absence of tissue inflammation). The actuator should be biocompatible during a considerably long time range, which may go from months - if the intramedullary nail is removed after the fracture as healed - to years - in cases where the physicians decide not to remove the stabilization device (strategy normally adopted among elderly patients). The goal is to find a material with unique requirements according to its functions and implantation location [2]. In such case, a device, which is any equipment that transforms one type of energy into another, should be considered [3]. The appropriate type of transducer would be an actuator which transforms some type of energy into kinetic energy or motion. Progress in material science brought a new generation of materials which outperform the conventional structural and functional ones - the smart materials [1]. Although, there is no worldwide general definition for these materials, according to Przemysław Sękalski [4] they can be described as 'materials' where one or more properties might be dramatically altered with a specific stimulus (*e.g.* electricity, heat, or magnetic field).

Also, according to Addington and Schodek [5], all smart materials are capable of real-time response and of responding to more than one environmental state and have discrete and predictable response to the triggering event. This is the case of piezoelectric, pyroelectric, electrostrictive, magnetostrictive, piezoresistive, or electroactive materials [4, 6, 7]. From all the available smart materials, and considering the actuator's desired features, piezoelectric stacks and permanent magnets were considered due to the desired motion range, reduced size and general known good reputation. Section 4.1. is dedicated to piezoelectric materials and Section 4.2., to the evaluation of permanent magnets.

4.1. Piezoelectric stacks

4.1.1. Introduction

Coupling between electrical and mechanical phenomena is commonly experienced by a broad range of materials and constitute the basis for multiple applications [8]. Piezoelectricity was first discovered by Pierre and Jacques Curie, in 1880, after crystal tourmaline showed an electrical polarization when subjected to mechanical force [4, 7, 9-11]. Soon after this finding, it was discovered that, conversely, when such crystals were exposed to an electrical field they experienced an elastic strain, and lengthened or shortened according to the polarity and in proportion to the strength of the field. These behaviors were labelled as piezoelectric effect (or effect of piezoelectricity) and inverse piezoelectric effect (or piezo-mechanics), respectively [10]. However, when actuators are required, the inverse piezoelectrical effect should be considered. The piezoelectric actuators' good reputation is a result of properties such as the small shifts, high force generation, high mechanical load capability and high stiffness [12]. These, combined with their reliability and availability, made piezoelectric actuators a successful practical option with application in the modern technology field as motors and devices for precise positioning control, and for sonic and ultrasonic signals generation [13-15]. Medical applications of piezoelectric devices involve drug delivery, surgery, diagnosis, and therapy [16]. The fabrication of most bulk piezoelectric ceramics follows the mixed oxide route. This method starts with the powder preparation through the mixture of metal oxides at stoichiometric proportions. Then the mixture is calcinated at temperatures between 700 and 1100 degrees and which causes volatiles removal and crystallization occurrence. Afterwards, the particles are reduced to the micrometer range through a milling process (*e.g.* dry-ball milling, vibration milling and/or wet ball milling). The fine powder is then mixed with a binder - usually a combination of polymers - and shaped and sized as desired (*e.g.* dry-pressing, extrusion, casting and injection molding). The rough shapes are then sintered for binder burn-out and to obtain a mechanically strong and dense crystalline structure. The next steps are: cutting and machining into a more refined shape,

electroding where electrodes are applied to the appropriate surface and poling (or polarizing) [7, 10, 11, 13]. Piezoelectric ceramics (or piezoceramics) are polycrystalline materials where each crystal with determined chemical composition is made of negatively and positively charged atoms occupying specific positions in repeated small units called unit cells. The manufactured ceramic, composed of randomly oriented piezoelectric crystallites, produced a composition of random orientated dipoles with reciprocally cancelling effects. Hence, the overall element has no polarization and no piezoelectric behavior. The regions of like-oriented dipole moments are referred to as domains. Also, the presence of piezoelectricity in a crystal is related to the lack of center of symmetry in the structure, meaning that the movement of the positive and negative ions with respect to each other produces an electric dipole. During the manufacturing process, the poling method is used to orient the domains through the application of a strong, direct current electric field at a certain temperature. During this process, nearly all domains will align with the external electric field and the ceramic will slightly lengthen along the poling axis and contract in both direction perpendicular to it. When the electric field is removed, most of the dipoles are kept fixed. This gives the material a permanent polarization, called the remnant polarization, and a permanent elongation that makes it anisotropic. If a voltage of the same polarity as the poling voltage is applied to a piezoelectric element, parallel to the direction of the poling voltage, the element will lengthen and a slight contraction perpendicular to the field will occur. If an alternating voltage is applied, the disk will lengthen and shorten cyclically, according to the frequency of the applied voltage [4, 7, 9-11, 13, 17].

After the previous brief description of the piezoelectric concept [18], a sequential strategy to try to adapt a piezoelectric actuator to a distinct application was considered. It started with the unavoidable task of selecting the most suitable lead zirconate titanate (or PZT) material or materials, while considering a reliable accommodation site for the piezoactuator (in/at the intramedullary nail) and with concerns towards environmental hazards (*e.g.* sealing for corrosion and resistance to shock). Finally, the selected accommodation site was evaluated towards the mechanical impact it may represent for the actuator and the actuator itself was also evaluated in terms of driving conditions (voltage applied, displacement generated, force generated and interfragmentary site motion produced) in systems resembling as close as possible the real scenario.

4.1.2. Piezoactuator and accommodation site selection

Piezo-mechanics is a composition-dependent property in which the chemically complex piezoceramics fall into different categories. Starting with the barium titanate (chemical formula: $BaTiO_3$) introduced as a replacement of the primordial piezoelectric single crystals such as quartz and tourmaline, the lead zirconate titanate, lead metaniobate (popular for its high anisotropy and lower acoustic impedance) and more recent materials such as modified lead titanate and bismuth strontium titanate (commonly used for higher temperature applications) [13]. PZT, represented by the general molecular formula $Pb(Zr_{1-x}Ti_x)O_3$, is currently one of the most widely used piezoelectric materials. Its popularity was obtained from the continuous excellent actuator and transducer performance that resulted from its advantageous properties such as its superior dielectric, piezoelectric and electromechanical coupling coefficients [7, 19-21]. Similarly to other commercially available ceramics, PZT is based on a perovskite crystal structure where each unit consist of a tetravalent metal ion, titanium, in a lattice of large divalent metal ions, such as lead and O^{2-} ions [13]. A noticeable feature of PZT is that it lies near a morphotropic phase boundary. This allows a coupling between two equivalent energy states, tetragonal and rhombohedral phases, and an optimum domain reorientation during the poling process, which results in an enhanced polarizability and consequently in an anomalously high dielectric and piezoelectric properties [19, 20]. Considering its outstanding performance and availability, PZT materials will be considered for evaluation.

Piezoelectric actuators from a few manufactures, namely, Noliac, Face® International Corporation, Piezomechanik GmbH, PiezoDrive, Johnson Matthey Piezo Products, PI Ceramic Piezotechnology and NEC/TOKIN, were investigated, as suggested by Niezrecki *et al.* [22] and Uchino [23], in terms of the actuators' design, size, weight, displacement generated, force exerted, frequency, biocompatibility, electrical induced current and operating life. The information's gathered from the different companies' manufacture guides, are summarized in Table 8.1 (in Appendix B).

To select the most suitable actuator design and size, it's positioning in or at the intramedullary nail should first be considered. The concern with the actuator protection against mechanical impact (*e.g.* during intramedullary implantation), to avoid its deterioration due to the surrounding *in vivo* conditions (*e.g.* body fluids) and to guarantee a desirable level of reproducibility during a satisfying operating lifetime, led to the consideration of the circular cannulated interior of the intramedullary nail as the best site for the placement of the actuator. There, the actuator should be placed between two blocks rigidly linked to the inner

intramedullary wall so that the displacement generated by the actuator could be propagated along the nail and into the healing interfragmentary site. Assuming the worst scenario where a small diameter intramedullary nail (according to manufacturers corresponds to the 9 mm) would be considered, the available space for the actuator placement would be reduced to 6 mm diameter which corresponds to the nail interior dimension. However, when selecting the actuator dimensions, the existence of an air gap between element side-faces and the surrounding mechanics should be considered. So that no damage to the actuator surface insulation occur over time [12]. This limitation greatly reduces the actuator design and size admitted.

There is a limited variety of commercially available actuator designs. Common designations are: thick film, rectangular, tube, ring, film, laminar, stack, bender- and shear-type [17, 22]. Although, PZT thick films (thickness between 1 and 100 micrometers) actuators were not selected for evaluation and were not displayed in Table 8.1 (in Appendix B), according to literature [13] there is an increase popularity in the use of these devices due to their improved capabilities when compared to bulk actuators (thickness equal or superior to 100 micrometers). The bulk components are the most common commercially established actuator designs, whose availability and variability edge led to their consideration for use in the project. The bender-type actuators design consists of two joint small beams with interdependence motion where their different expansion or contraction will lead to the overall structure bending [17]. From the different designs presented in Table 8.1 (in Appendix B), the bender-type actuators are the ones in which the smaller sized components allowed a larger free motion, with range between 30 μm to 4 cm. However, there seems to be an inverse relation between the amount of free motion and the maximum force exerted by the actuator. Hence, the force applied by the bender-type is reduced, with a maximum value of 5.50 N for the products presented. Also the increase in the free stroke is associated with an increase of the actuator size, which again limits its application in the nail. By excluding the latter design, the suitability of the shear-type and plate models are compared. Both designs have actuators with reduced dimensions, which allows their application inside the intramedullary nail. Although, similar in shape, the great difference between the actuators are the type of motion generated. The shear-type actuator exploits the transverse motion while the plate actuator the axial motion. As stated previously (in Chapter 1), there is no particular preference in the type of motion generated at the fracture site, since there is no general agreement in which type of motion most greatly benefits the healing process. Hence, both actuator types can be considered. However, the free motion magnitude generated by the smaller sized actuators is very low. To improve the traditional single bulk piezoactuators reduced

strain levels, internally, externally or frequency leveraged strategy can be adopted. The simplest form of internally leveraged amplification is obtained by stacking several layers of PZT elements one on top of the other, in the direction of the applied electrical field, leading to a multilayer structure [16, 22]. The final structure obtained is known as a piezo-stack actuator and is represented in Figure 4.1. According to manufacturers [12, 18], the axial strain enhancement can rate up to 0.2% of the stack's length (L) (in comparison to the 0.1% strain characteristic of the single ceramic actuators) and may lead to a range of motion between 2 μm and 0.1 mm depending in the stack length and the actuation conditions while maintaining a low voltage requirement. Although this strategy may induce dielectric hysteresis, meaning that there is a non-linear relationship between the applied voltage and the resulting mechanical displacement, in most cases actuator behavior can be considered linear and the resolution is still maintained very high. Another strategy to amplify the piezo actuator stroke is to use an external leverage, which relies on a mechanism external to the piezoelectric input (*e.g.* lever arm actuator and hydraulic amplification). Even though a significant strain amplification can be achieved with this method, it normally requires an apparatus that increases the actuator system dimension and costs. Frequency leveraging is a completely different approach and theoretically leads to infinite stroke, but it suffers from limited force generation due to frictional effects [9, 22, 24]. Therefore, the piezo-stacks were considered for evaluation in this work.

In the piezo-stack actuator the faces of each PZT ceramic element are electrodes, being the alternate faces electrically connected. When a voltage is applied to the stack, an electrical field within each ceramic layers is generated, the adjacent elements are poled in opposite directions and the resulting mechanical strain of the stack (ΔL) will be the sum of each of the elements strain. The high actuation force (F) will also result from the accumulation of the force produced by each single piezoelectric element. Similarly to what is verified in single PZT elements, in stack actuators the axial expansion in the direction of the electric field will be accompanied by a lower contraction/shrinking in the opposite direction. However, for the sake of simplicity, this phenomenon was not represented in Figure 4.1 [4, 15, 24].

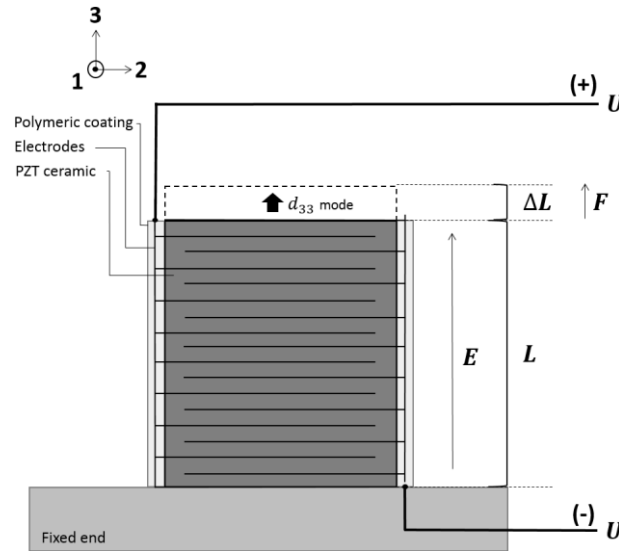


Figure 4.1 - Schematic cross-sectional representation of a multilayer PZT piezo-stack with longitudinal expansion, built up from individually contacted piezoceramic discs. Based on [9, 16, 18, 24].

Other essential characteristics of the actuator are the displacement capability, force generated and operation frequency. When the piezoelectric stack expands freely, in the absence of external forces, the actuator strain (S_{ij}) will be proportional to the electric field strength (E) as demonstrated by equation (4.1).

$$S_{ij} = \frac{\Delta L}{L} = d_{ij}E \quad (4.1)$$

The proportionality between the electric field applied and strain generated is given by the piezoelectric coefficient (d_{ij}) constant. Furthermore, these properties are directional quantities being subscripts to identify the conditions under which they are determined. Hence, the first subscript indicates the direction of the applied electrical field and the second is the direction of the induced strain. The piezoelectric stack free expansion will correspond to the material maximum displacement. The maximum electric field allowed, however, will depend on the breakdown voltage of the ceramic. Commonly, PZT piezo-stacks present a maximum field strength of 2 kV/mm [7, 9, 11, 12, 18, 19]. However, this situation does not always occur. For this project the actuator device should reflect in an interfragmentary site motion, meaning, it will act upon a mechanical partner so the motion can be propagated along the nail and into the healing site. In the presence of a mechanical partner, the piezo-actuator expands generates an external force (F) which not only compresses the mechanical partner, but the force will act back on the stack it-self. This phenomenon reduces the effective external stroke of a piezoelectric stack. When placed against an infinitely rigid body it is not capable of creating a motion, however the actuator maximum force (also known as blocking force) will be generated. The transfer of

energy from the actuator to the mechanical system is maximized when the stiffness of the actuator and the mechanical system are similar [12, 22]. The motion, in static behaviour in the longitudinal field (with a 33 subscript), in a simplified manner, can be described by equation (4.2), where T represents the stress (*e.g.* caused by external forces), s_{33}^E the material compliance (inverse of Young modulus) and c_T the material stiffness. The superscripts indicate a quantity held constant and in this case the electric field is held constant.

$$S_{33} = \frac{\Delta L}{L} = s_{33}^E \cdot T + d_{33} \cdot E = \frac{F}{c_T \cdot L} + d_{33} \cdot E \quad (4.2)$$

From the information available in the Table 8.1 (in Appendix B), and by limiting the design to piezo-stack actuators to reduce dimensional size, high axial displacement and load generated, there is a reduced amount of commercially available models. From the piezo-stacks displayed in Table 8.1 (in Appendix B), the Pst 150/2x3/5 and Pst 150/2x3/7 models from Piezomechanik GmbH were selected for evaluation based on the fact that they presented the dimension below the maximum accepted to fit the intramedullary nail interior space, they are lightweight - with average weight is 0.43 ± 0.004 and 0.66 ± 0.013 g, respectively - and present the higher free stroke to blocking force rate at a lower price. In relation to the operating frequency parameter, similarly to every body of mass, piezoceramics have an intrinsic characteristic frequency, known as resonance frequency, at which it prefers to vibrate. When the actuator is excited at this resonant frequency, it will vibrate freely with greater amplitude than at other frequencies and it will convert more efficiently the electrical energy into mechanical energy [4, 7]. However, according to manufacturer information [12], in several cases the real operating frequency of a piezomechanical system is far below the actuator's resonance frequency. As anticipated for this project, the physiological frequencies, between 10 to 100 Hz, are also below the resonance frequency of the selected actuators, 100 and 150 Hz, respectively. The selected piezo-stacks samples resonance frequency difference is a result of the actuators structure size, where a lower frequency is expected from a larger length-to-diameter ratio actuator.

The selection of these actuators was also influenced by the work developed by Clara Frias [25-27]. Based on the concept that extracellular mechanical forces induce bone adaptation and reconstruction, several studies tested the use of piezoelectrical inverse effect to prompt bone cells growth *in vitro* and *in vivo*. Tanaka *et al.* [28, 29], used bimorph-type piezoelectrical actuator which through bending motion, mechanically stimulates cultured osteoblastic-like bone cells growth. The device developed was capable of generating physiological strains, frequencies and waveforms making it an interesting tool for bone cells activities study. Konno

et al. [30] also developed a research device based on a PZT vibrator piezoelectric beam with clamp-free boundary conditions to enforce local mechanical stimulation onto cultured living adhesive cells. With the aim of developing an implantable device to improve bone formation, Clara Frias [25, 26] tested polymeric PVDF (also known as polyvinylidene fluoride) films coated with poly (methyl methacrylate) (or PMMA) and micro-particles of Bonelike to stimulate osteoblast-like cells growth through tri-dimensional displacement of the piezoelectric film. To further evaluate the potentiality of Frias' actuator, an *in vivo* study was developed by Reis *et al.* [27] in sheep femur and tibia osteotomy cuts. The study demonstrated that after one-month implantation, the total bone area and bone deposition rate were significantly higher around actuators when compared to static controls. However, the development of a fibrous capsule was also detected. This phenomenon may have been triggered by piezoactuator coating damage which expose the *in vivo* environment to hazardous effects of the actuator device constitutive materials (PVDF and silver nitrate from the electrode) and electrical current. This calls our attention to the variables biocompatibility and electrical field generated.

It is of general acceptance that the biocompatibility of the implanted material is vital for the application of actuators *in vivo*. The behavior of PZT materials in a body fluid environment is not clearly established yet. PZT itself does not seem to be toxic to the cells but concern arises from the possible lead release from the material dissolving/corrosion in the body fluid presence. Titanium and zirconium are considered highly biocompatible; however, there is a concern with lead oxide toxicity since it is known to accumulate in the organism, causing damage to the brain and nervous system [31]. Considering this burden, strategies where piezoelectric non-toxic materials have been investigated. A popular approach is the use of lead-free piezoelectric ceramics, which are reported to offer comparable properties to that of PZT ceramics, making them viable candidates for *in vivo* applications [19, 20]. According to the initial strategy the actuator would already be hermetically isolated from the *in vivo* body fluids and protected from mechanical impact by its positioning in the cannulated interior of intramedullary nail and between two blocks coupled to the nail interior wall. However, the possibility of the additional application of a biocompatible resistant coating is always a safe approach. Some companies are capable of providing such special sealing [9, 13].

The electrical driving field needed to produce the piezo-stack displacement should also be evaluated and will allow design issues to be addressed. From an electrical point of view, piezo-actuators behave like electrical capacitors where the induced motion can also be described as the consequence of the variation of the electrical charge content of the piezo-actuator. These

charge change and actuator displacement is connected with a charge transport that requires the electrical current (I) and which depends on the actuator capacitance (C), as described by equation (4.3) [12, 16, 18, 32].

$$I(t) = \frac{dQ}{dt} = C \cdot \frac{dV}{dt} \quad (4.3)$$

Based on this relation the current required for sinusoidal operation will be given by equation (4.4) where f represents the operating frequency and V_{p-p} the peak-to-peak drive voltage.

$$I(t) = C \cdot V_{p-p} \cdot 2 \cdot \pi \cdot f \quad (4.4)$$

To have a framework of the maximum current required by the piezo-stack actuators, it was necessary to assume that the actuators would perform at the maximum semi-bipolar activation voltage, *i.e.* 180 V (-30/+150 V). Although, the maximum bone physiological frequency is 100 Hz, an alternating current (or AC) between 50 and 60 Hz sinusoidal waveforms currents are considered, since this is the frequency for which the human bone and other signal sensitive tissues (*e.g.* nerve controlling the heart) are more responsive [33]. The actuators capacitance is a material-inherent property and for the Pst 150/2x3/5 and Pst 150/2x3/7 models the values are 70 and 170 nF, respectively. Hence, each model operates at a maximum electrical current of approximately 4.8 and 11.5 mA. The PZT piezoelectric actuators electrical driving field has been pointed-out as one of the limitation of these transducers [14].

Some strategies should also be adopted in order to guarantee the actuator's high reliability, reproducibility and long operating life. These parameters will depend on the operating conditions, such as the parameters used (*e.g.* voltage applied) and the actuator surrounding conditions (*e.g.* temperature, humidity and compressive stress) [13]. According to literature [2, 9, 16-19, 34] there are strategies which may contribute to maintain the piezoelectric effect and increase the PZT piezo-stack actuator lifetime. The piezoelectric effect can be lost if a strong electric field is applied opposite to the direction of polarization, and which, normally, should not exceed 500 V/mm. Also if an extended lifetime is desirable, maximum voltages should be avoided by using operating voltages as low as possible, for example in the case of a 150 V actuator, instead, a 100 to 130 V would be advisable. However, the reduction in the applied voltage will also reduce the maximum stroke applied by the actuator. Furthermore, the piezoelectric effect will be lost if the actuator is heated above the Curie temperature. However, to avoid reduction in the piezoelectric activity the operating temperature should be approximately 50% of the Curie temperature (temperature to which the piezoelectric material

will suffer depolarization). Being this parameter material-dependent, in the case of multilayer actuators such as piezo-stacks their Curie temperature are around 150 degrees. Hence, it may be advisable only to heat piezo-stacks up to 80 degrees. This boundary allows the implantation and performance of PZT piezoceramics inside the human organisms since the average temperature is 37 degrees. Also, the actuators would not be sterilized with high temperature. According to a national orthopedic device company *Artur Salgado S.A.* the γ -irradiation is the preferable method used for intramedullary nails. Since the PZT piezoceramics are not degraded by radiation, the actuator can be sterilized with the same method used for the fixation implants and again the temperature limit does not represent a restriction. Another strategy used to increase the lifetime of piezoactuators is to apply appropriate coating or to encapsulate the actuator into a hermetic metal casing. The latter would improve the reliability and stability by protecting the ceramic against the human body harsh environment with highly conductive and chemically aggressive body fluids (*e.g.* body fluid corrosion properties) and against mechanical impact (*e.g.* higher shock resistance). However, the metal casing piezo-stack designs available are for larger sized actuators which hinder their use for this project. Piezoelectric materials are brittle components, are sensitive to shear, cross-bending, torsional forces and have low resistance to tensile load. Hence, the compressive strength of piezo-stacks is more than one order of magnitude larger than their tensile strength. The resistance to tension is especially low when multiple piezoceramic layers are glued together. Tensile forces can cause layer separation and ceramic material cracking which can lead to a weakening of the electrical “stability” of the ceramics. A common strategy used to compensate for tensile loads is to subject the actuator to a pre-loading condition. This method will also increase the stability of larger length to diameter ratio piezo-stacks and will maintain the actuator in position. Manufacturers often suggest the application of a compressive mechanical pre-loading between 10 to 12% of the maximum load capability and in push configurations levels of up to 50% can also be recommended.

4.1.3. Actuator performance

To properly evaluate the piezoelectric actuators potential for bone healing process enhancement when intramedullary nails fixation method are used, it is essential to evaluate the selected accommodation site in terms of its capability to guarantee the actuator’s mechanical protection during demanding surgical procedures, such as intramedullary nail implantation and nail removal after full bone recovery. According to manufacturers [10, 12, 13, 18], the product information on the piezoactuators performance was obtained from studies developed by the companies under particular test conditions. Thus, a distinct behavior can be expected when operated in different experimental settings. It is essential to evaluate the selected

piezoactuators samples under as close as possible realistic operational conditions in order to understand and predict its behavior. The piezo-stack actuator converts electrical energy into the generation of deformation and force, and the mechanical interaction between the actuator and the mechanics is ruled by the stiffness of the two system parts. Hence, the actuator's displacement and force generation in response to voltage variation should be determined to obtain a simple first characterization of the actuators performance. Unfortunately, the direct measurement of force in relation to electric voltage or strain is challenging due to the short-range nature of the force generated in the selected actuators. To obtain this information a combination of a sensitive force detection method with a precise control of distance on the sub-micrometer scale or voltage application would be crucial [35]. Hence, the relationships between the applied electric voltage and the actuator displacement response through the increase of the mechanical partner load applied were evaluated. Another approach to better predict the behavior of the actuator in a host structure was through the development of a finite element model of the system to understand the relation between the actuator force applied and the interfragmentary displacement generated, as suggested by Flint *et al.* [16].

i) Material and methods

Accommodation site evaluation

The accommodation site selected was evaluated through a finite element analysis in ANSYS Workbench 15.0 (ANSYS Inc., Canonsburg, PA, USA). The finite element tibia model based on the synthetic human tibia structure (4th generation, medium left, model #3401, from SawBones Europe AB, Malmö, Sweden), which was developed in Chapter 3, was also used throughout the "Accommodation site evaluation" experiment. No reaming was applied throughout the medullary canal, in order to simulate a worst case scenario of nail implantation (very narrow medullary canal with difficulty in nail sliding) and removal (new bone formation around the nail after fracture has healed). No osteotomy/fracture was assumed. Top and bottom jig with contact region between the jig and the bone surface guaranteed the physiological orientation of the bone and physiological movement limitation to which the tibia would be subjected when pressed by joints. The intramedullary nail used in this study, was also based on the 9-mm-diameter per 345 mm length, cannulated AISI 316L ASTM F318 stainless steel intramedullary nail (model M596222 AB0366 T, L.A. Medicals, Albergaria-a-Velha, Portugal). The nail was not fixed with screws. A proximal positioning of the piezostack (10 mm below the end of the nail proximal portion curvature) in the straight portion of the intramedullary nail was considered. The piezo-stack Pst 150/2x3/5 model actuator was represented by a 2x3x5 block, restricted above and

below by 2 mm length per 6 mm diameter intramedullary nail discs. The discs were considered as an extension of the interior wall. Similarly, to Chapter 3, cortical bone was considered as a linear, elastic, orthotropic material with a density of 1 640 kg/m³, a Young's modulus of 10 000 MPa for transverse load (Ex and Ey) and 16 700 MPa for longitudinal load (Ez) and a Poisson's ratio of 0.3 for any directional load applied (vx, vy, vz). The cancellous portion presents a density of 270 kg/m³ and was assumed to behave as an isotropic linear elastic material with a Young's modulus of 155 MPa and a Poisson's ratio of 0.225. The stainless steel material for the nail and the discs was modelled as linear elastic, isotropic and homogeneous material with a density, Young's modulus and Poisson's ratio of 8000 kg/m³, 200 000 MPa and 0.27, respectively [36, 37]. The piezoelectric stack was assumed to behave as an isotropic linear elastic material with a Young's modulus of 37 500 MPa based on manufacture's information and the Poisson's ratio of 0.27 was assumed similar to stainless steel material. The upper and lower jigs presented common steel properties. The mesh adopted throughout the finite element model was similar to the one used in the Chapter 3 model. The actuator part was meshed with hexahedral elements (16319 nodes) and with element size of 0.2 mm. All contact surfaces between the cortical/trabecular bone; bone/containers and intramedullary nail/actuator and intramedullary nail/bone (cortical and trabecular) were assumed to be bounded ("glued contact"). The upper and lower jigs were assumed as fixed parts. The loads considered aimed to mimic nail implantation through hammering and nail removal and were selected based in mechanical experimentation studies. A hammering performance depends on the impulse force and accuracy [38]. By assuming that a Slide Hammer through a Hammer Guide apparatus would be used, the accuracy variable would not be included. Considering that the force applied to the nail would be very large and act for a very short time [39], the hammering maximum impulse force was assumed as 2224 N [40] and it was applied at the tip of the intramedullary in the direction of the nail proximal portion. Similarly to the study developed by Sonoma Orthopedic Product [41], for the nail removal procedure a tension of 900 N was considered. Again the load was applied at the tip of the intramedullary and in the inner wall of the proximal curved portion of the nail and was applied in the direction of the nail proximal portion. The actuator upper surface stress and the actuator strain (normal and shear) during the mechanically demanding procedures were registered.

Displacement versus voltage analysis

The test set-up of Figure 4.2 was used to measure the displacement versus voltage of the actuators under different loads. The piezo-actuators displacement in real-time was measured

through the use of a single-point laser Doppler vibrometer system. This system comprises an optical sensor head (model OFV-303, Polytec Ltd., Hertfordshire, UK) and a controller (model OFV-3001, Polytec Ltd., Hertfordshire, UK) which provides power for the measuring head and processes the vibration signal. In this method, the actuator displacement magnitude is obtained through the comparison between the incident laser beam used as reference beam and the frequency shift of the scattered laser light due to the Doppler effect in response to the motion of the surface [42-44]. The mounting and motion transfer in piezo-stacks is always done through the endfaces. Therefore, the actuators models tested, Pst 150/2x3/5 and Pst 150/2x3/7 (Piezomechanik GmbH, Munich, Germany), were fixed through their bottom endface to the top of a stable supporting base with the use of an acrylic adhesive and it was fixed in series with a mechanical press. The different load applied to the actuator with the mechanical press was manually adjusted and its magnitude determined by a feedback control obtained through a specially adapted battery operated top loader scales (or portions scale). The actuators voltage/deflection behavior was evaluated with the piezo-stacks under three different loads of approximately 3, 10 and 30 N. After each set-up assembling, the end-faces contacts were verified for misalignment between the actuator top surface and the mechanical press arm, to assure that the load vector coincided with the actuators' axis and that it was equally distributed across the actuator's cross section to avoid high local pressure. Since the laser Doppler vibrometer can only measure the motion component in out-to-plane direction parallel to the optical axis sensor head [42-44], a mirror system strategy was adopted to direct the laser light to the actuator free end surface, or more precisely, to the surface (right above the actuator) of the mechanical press arm.

Piezo-stack actuators fine movements were controlled with the use of a single-channel, open-loop piezo controller (model MDT694A, Thorlabs, New Jersey, USA) which provided precise low-noise output voltages to the actuator. The electrical polarity of the piezo-stacks was indicated by the color of their wires where the positive pole was identified by a red wire. Although, semi-bipolar activation with a minimum reversal voltage on the order of 10% of the maximum voltage is recommended in order to increase the stack stroke between 20 to 30%, the use of piezoelectric controllers only allowed for the adoption of a unipolar activation [9, 12, 18]. The piezo-stacks motion responded to the applied voltage signal when it passed from 0 to 150 V. The motion was reversed when the actuator was discharged. The data acquisition was synchronized with the specimen oscillation and stimulation. Three experiments were used to allow system small re-adjustments and only afterwards was the actuators displacement/voltage

curve, for the different loads, registered. The data presented was the average result from five experimental repetitions.

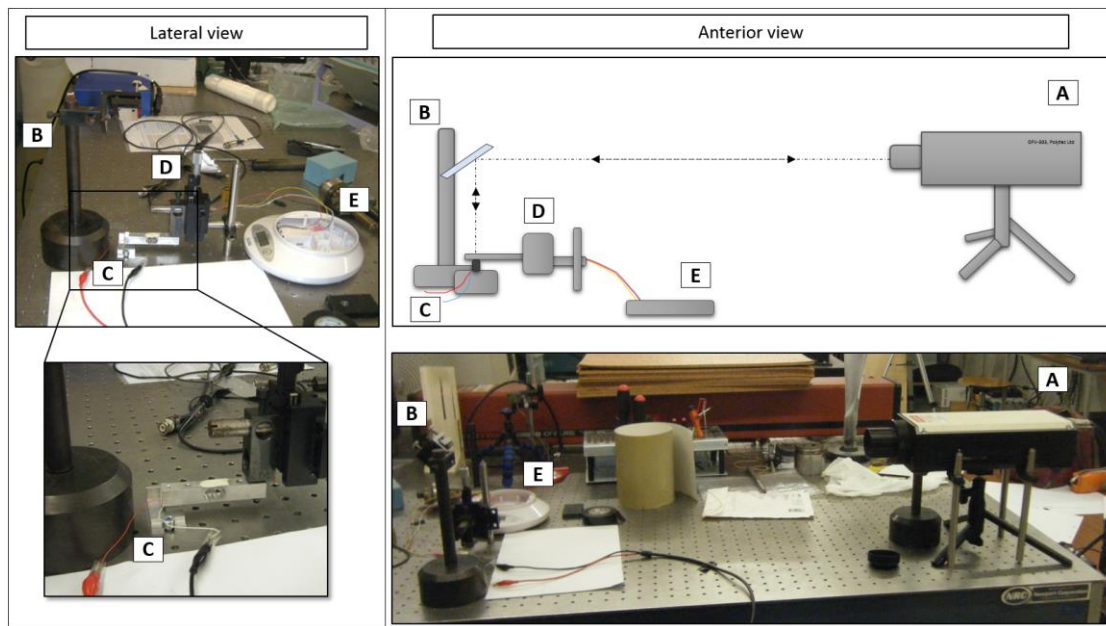


Figure 4.2 - Schematic representation from the anterior and lateral perspective of the set-up system based on a piezo stack (C) which was placed on a solid base and was mounted into a mechanical press (D) with known load (E), moving the attached mechanics (D) by electrical voltage stimulation. The strain of the stack is measured with the use of a laser Doppler vibrometer optical sensor head (A) which laser beam direction is controlled by mirror system (B)

Interfragmentary site motion versus actuator force application finite element analysis

The piezostack actuators act mainly like an expanding element generating a compressive force on the mechanical partner which at the same time will be connected to the general structure, propagating the deformation throughout the intramedullary nail and into the bone interfragmentary site. Hence, to better understand the actuator performance and the relation between the force applied and the interfragmentary fracture motion, a finite element analysis of the system was developed in ANSYS Workbench 15.0 (ANSYS Inc., Canonsburg, PA, USA). The tibia with intramedullary nail finite element model used in this experiment adopted the same nail implantation parameters that were used in Chapter 3 and which resembles a real case situation (e.g. reaming diameter, 12.7 mm nail entry site diameter and fracture width). The intramedullary nail used in this study, was also based on the 9-mm-diameter per 345 mm length, cannulated AISI 316L ASTM F318 stainless steel intramedullary nail (model M596222 AB0366 T, L.A. Medicals, Albergaria-a-Velha, Portugal). However, an upper disc as an extension of the interior wall (similar to and in the same position as the one considered in the “Accommodation site evaluation” study) was considered. As in Chapter 3., the tibia cortical material was treated as having a linear, elastic, orthotropic behavior with a density of $1\,640\text{ kg/m}^3$, a Young’s modulus

of 10 000 MPa for transversal load (E_x and E_y) and 16,700 MPa for longitudinal load (E_z) and a Poisson's ratio of 0.3 for any directional load applied (v_x , v_y , v_z). The cancellous portion presents a density of 270 kg/m³ and was assumed to behave as an isotropic linear elastic material with a Young's modulus of 155 MPa and a Poisson's ratio of 0.225. By considering the actuator performance during the first healing phase, the presence of granulation tissue between the bone fragments was included in the model. This material was assumed to present a isotropic linear behavior with a Young's modulus of 0.2 MPa and a Poisson's ratio of 0.167 [45]. The intramedullary nail and the screws were considered as being of stainless steel and were modelled as linear elastic, isotropic and homogeneous material with a density, Young's modulus and Poisson's ratio of 8000 kg/m³, 200 000 MPa and 0.27, respectively [36, 37, 46]. For the jigs, common steel mechanical conditions have been used. The mesh adopted for the finite element model was the same as in Chapter 3. In contact surfaces definition, the cortical and trabecular bone were considered as being bounded ("glued contact"). Because a relative tangential motion may occur between the cancellous bone inner wall and the fixation implant, contact elements with a friction coefficient of 0.2 were used, as suggested by [47-49]. The screws were tied to the bone and to the nail simulating thread locking action. Other contact surfaces between the bone/containers and granulation tissue/bone (trabecular and cortical) were also assumed to be bonded ("glued contact"). Different piezoelectric actuator expansion loads - including 50, 100, 150, 300, 500, 1000, 2000, 5000 and 10000 N - were evaluated. This load was applied upwards, in the direction of the nail straight portion, to the intramedullary nail inner disc lower surface. The upper jig displacement was limited to the direction of the applied load to best approximate a real scenario. The lower jig was assumed as a fixed support. The average bone interfragmentary displacement for each actuator expansion load considered was registered.

ii) Results

Accommodation site evaluation

The finite element results for the actuator stress and strain during intramedullary nail implantation through mechanically demanding procedures such as hammering and implant removal are present in Figure 4.3 and 4.4, respectively.

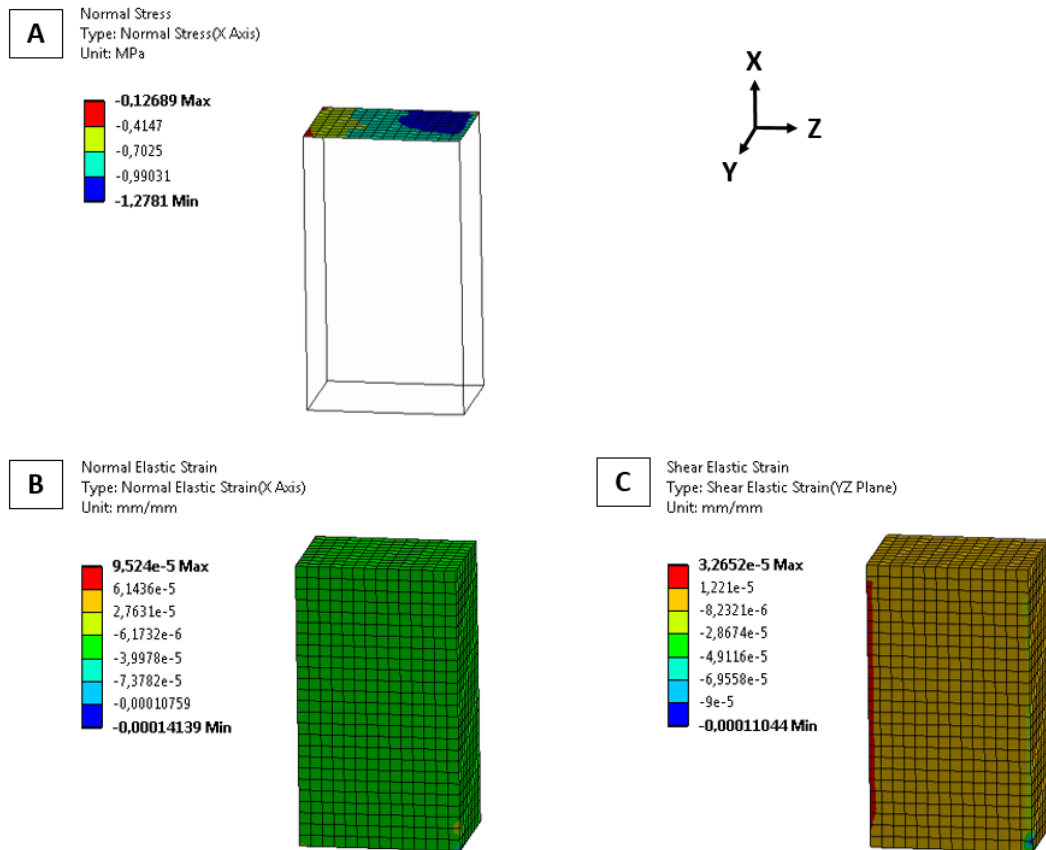


Figure 4.3 - Actuator finite element model simulation during intramedullary nail hammering where (A) is the normal stress distribution at the piezo-stack surface in direction X (direction of the piezoelectric effect), (B) in the normal strain distribution in direction X and (C) is the normal shear strain distribution in the YZ plane

According to Figure 4.3, the intramedullary nail implantation through hammering leads to the generation of a maximum compressive stress of 1.3 MPa and consequently maximum compressive load of 7.8 N to the piezo-stack. The maximum normal (in the direction of the load applied) and shear (parallel to the direction of the load applied) strain suffered by the actuator, during this mechanically demanding task, was approximately 0.0001 in both strain directions considered.

As demonstrated in Figure 4.4, the maximum tensile stress to which piezo-stack model would be subjected during a nail removal process is 0.4 MPa which corresponds to a 2.4 N tensile load. The normal and shear strain suffered by the actuators are in the order of 10^{-6} .

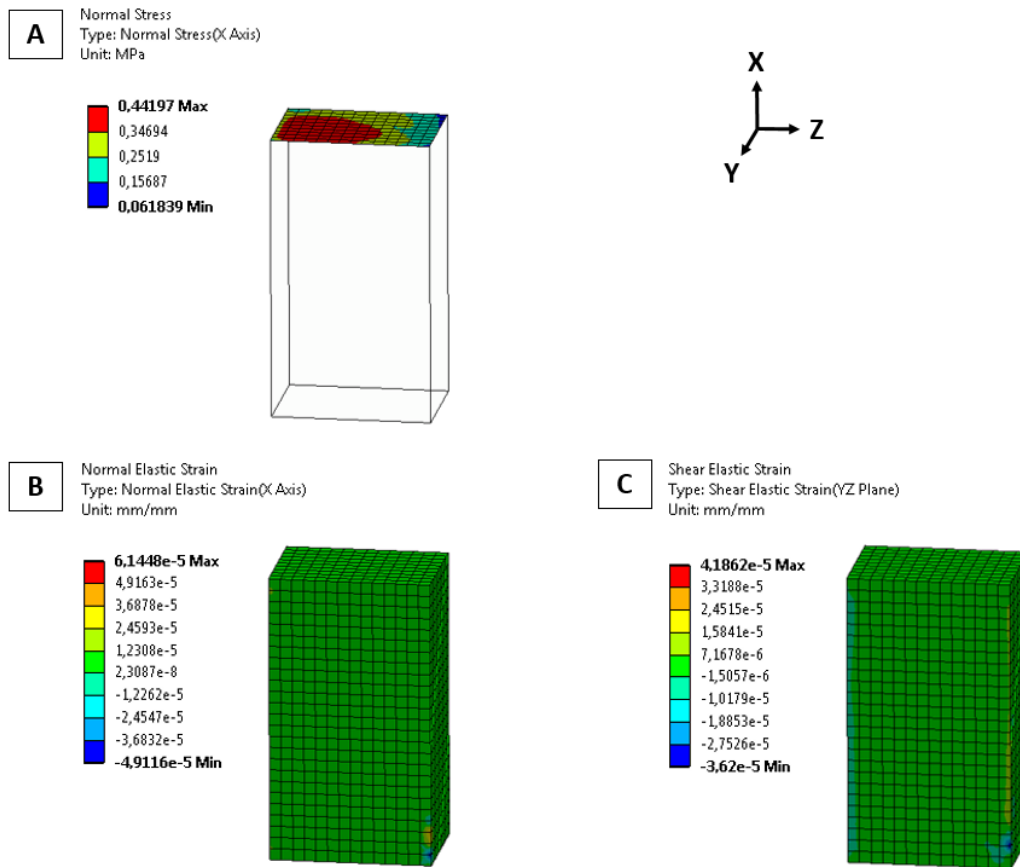


Figure 4.4 - Actuator finite element model simulation during intramedullary nail removal where (A) is the normal stress distribution at the piezo-stack surface in direction X (direction of the piezoelectric effect), (B) in the normal strain distribution in direction X and (C) is the normal shear strain distribution in the YZ plane

Displacement versus voltage analysis

Figure 4.5 and 4.6, shows the relation between displacement and voltage stimulus for the two selected piezo-stacks models Pst 150/2x3/5 and Pst 150/2x3/7, respectively, when subjected to different axial compressive loads of approximately 3, 10 and 30 N. The piezoelectrical behaviour of the stack actuator will result from the mechanical interaction between the actuator and the mechanical partner where in the experiment the mechanical influence of the mechanical partner was expressed as mass load through weights applied on the actuator.

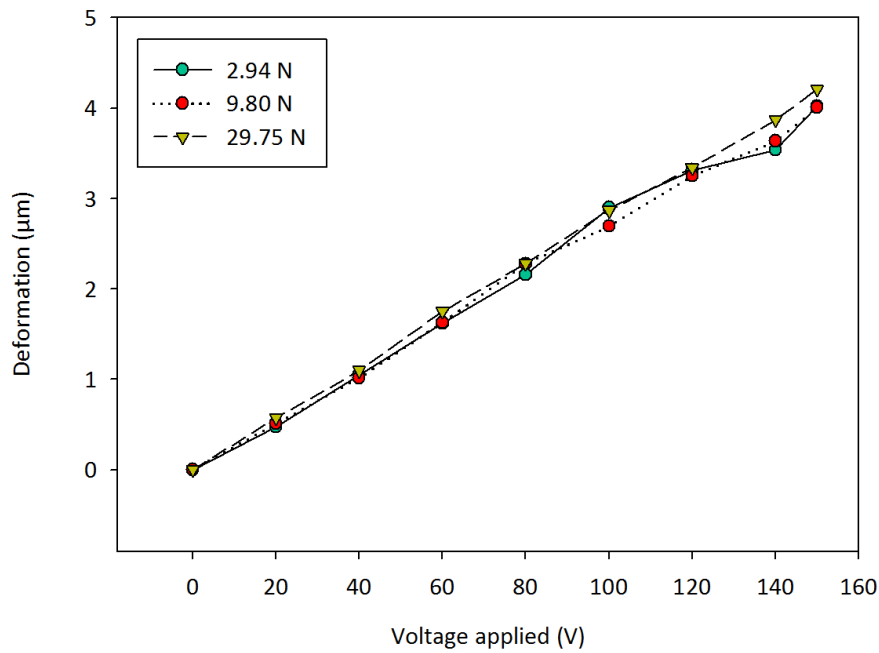


Figure 4.5 - Schematic voltage/stroke diagram for the model Pst 150/2x3/5 stack actuator under different loads

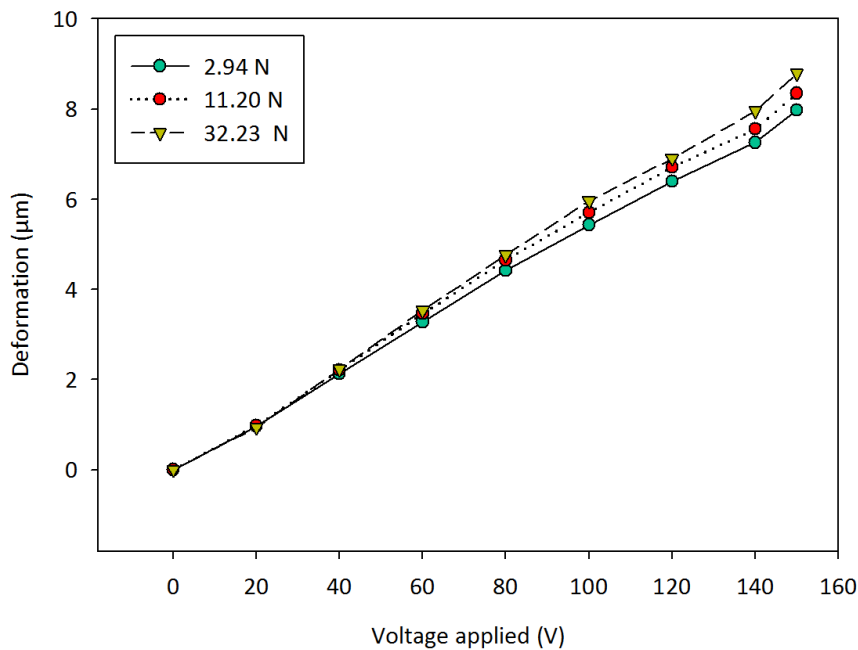


Figure 4.6 - Schematic voltage/stroke diagram for the model Pst 150/2x3/7 stack actuator under different loads

As demonstrated in Figure 4.5, the piezo-stack model 150/2x3/5 displacement response to voltage decreased with the increase in the load applied. Oppositely, in the actuator model Pst 150/2x3/7, the deformation generated increased with the rise of weight applied (see Figure 4.6). In both models, the relation between the load applied and the actuator deformation becomes more distinct at higher voltages, above 120 V. From the displacement/voltage curves, in Figure 4.5 and 4.6, it was possible to verify that both actuators demonstrate a slightly non-linear displacement behavioral response to the applied voltage.

Interfragmentary site motion versus actuator force application finite element analysis

The average interfragmentary site deformation as a result of different piezo-stack expansion force applied to the intramedullary-bone system, is presented in Table 4.1. From Table 4.1 data, it is possible to notice that a high force applied by the actuator will only generate a small amount of granulation tissue deformation.

Table 4.1 - Average interfragmentary displacement (μm) for each actuator force applied (N)

| Force (N) | Average interfragmentary deformation (μm) |
|-----------|--|
| 0 | 0 |
| 50 | 1.3 |
| 100 | 2.5 |
| 150 | 3.8 |
| 300 | 7.6 |
| 500 | 12.7 |
| 1 000 | 25.4 |
| 2 000 | 50.8 |
| 5 000 | 127.1 |
| 10 000 | 254.5 |

When the actuator generates the maximum force, *i.e.* the blocking force (data given by the manufacturer), as stated previously, it will suffer no expansion. Therefore, for a reasonable evaluation of the materials' potential, $\frac{1}{2}$ of the blocking force will be considered as corresponding to half of the free stroke expansion. Hence, for the Pst 150/2x3/5 model a 150 N force with 2.5 μm actuator stroke were considered. Figure 4.7 describes the finite element model simulation concept with focus on the deformation generated at the interfragmentary site by the application of 150 N actuator force.

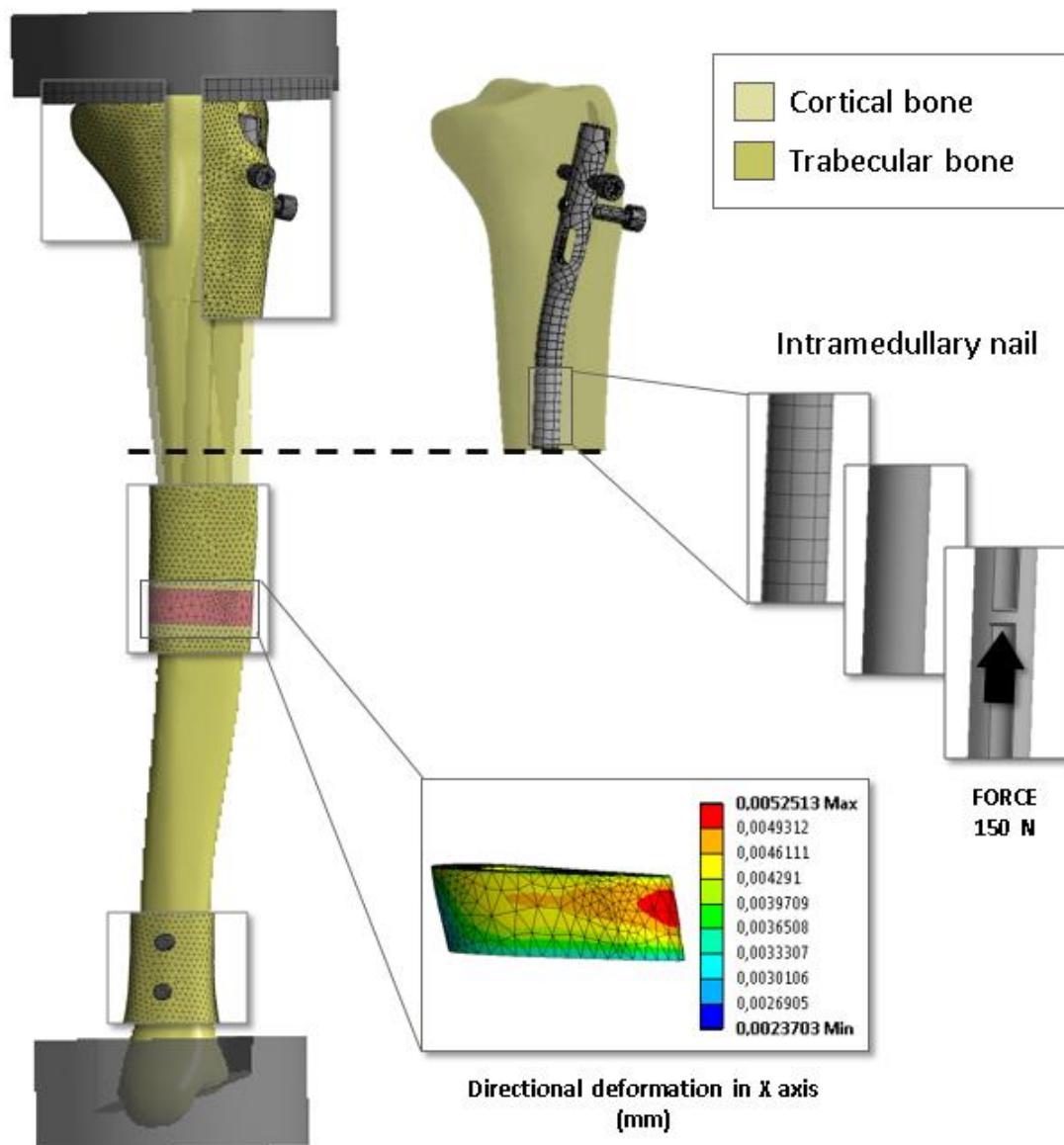


Figure 4.7 - Finite element analysis concept used for the understanding of the relation between the actuator force application and the generated interfragmentary site motion. The 150 N actuator force case was used for exemplification

iii) Discussion and conclusions

The application of piezoelectric actuators in the biomedical field has become increasingly popular. In this work, the capability of these actuators to, when linked to (or capable to be used simultaneously with) the intramedullary nail stabilization system, generate a physiological mechanical stimulation capable of accelerating the bone fracture-healing process. The greater limitation of this process is the challenge of fitting an actuator with particular characteristics in an already defined host structure, which is the intramedullary nail. Alterations in the original design should be avoided, and there is reduced space available for the actuator placement [15, 16]. Based on this problem, the strategy of placing the actuators along the cannulated intramedullary nail interior space was evaluated. Considering that the load

experienced by the piezo-stack would be expectably higher in the proximal region of the nail straight portion, this location was selected for evaluation. The maximum compressive load suffered by the piezo-stack actuator during intramedullary nail implantation through hammering, 7.8 N (see Figure 4.3), is below the maximum supporting load limit, which for this particular piezo-stack model is 300 N. If the actuator maximum supporting load limit is exceeded, its performance decreases as a consequence of de-poling effects. The mechanical damage threshold is normally at higher loads, up to 10 times larger than the de-poling limit [12]. However, such evaluation lacks the influence of the hammer/nail contact time on the material mechanical properties. As stated previously (in the material and methods subsection), the existence of a very small hammer time of action was recognized, but, for simplicity purposes, was not included as a variable in the simulation. When considering a brittle material such as the piezo-stacks, the response of the system to an impulse force (or Dirac- δ interaction) is determined. Therefore, the application of a highly time concentrated force on the piezoactuator would most certainly led to its fracture. In terms of tensile load, manufacturers often suggest a limit within 5 to 10% of the maximum compressive load, in order to avoid damage to the stack. Again, the maximum tensile stress to which piezo-stack model would be subjected during a nail removal process, 2.4 N, falls below the tensile load risk limit of 15 N (5% of 300 N). The strain (normal and shear) suffered by the piezo-stack during the nail removal task, are very low and do not appear to cause any risk to the actuator. The intramedullary nail removal is considered a slow procedure; therefore there is no Dirac- δ interaction in this case. Hence, the actuators positioning site considered cannot be assured as being capable of guaranteeing mechanical protection to the transducers during the intramedullary nail implantation procedure and considering the brittle nature of the material it would be difficult to find a location in the nail that could protect it from the strong hammering impact during implantation.

Another limitation of incorporating a piezoactuator component in an intramedullary nail structure is the difficulty to predict its performance and their influence on the overall system [15]. This led to the evaluation of piezoactuator displacement in response to voltage control and when subjected to different compressive loads. This analysis was carried on selected piezo-stacks samples which properties most closely satisfied the stipulated requirements - in terms of actuator design, size, weight, displacement generated, force applied, frequency, biocompatibility, electrical induced current and operating life. Actuators were selected from supplier companies which design their products to fit the standardized materials type and which actuators present characteristics that when perform well in some categories are typically poor in others [13, 22]. Although research has been made to improve the electromechanical

performance of commercial piezoelectric actuators, *e.g.*, through the development of advanced structural and functional composites (*e.g.* PZT composites incorporating zinc oxide nanoparticles), throughout this study only the commercially available products were considered [13, 14, 19, 21]. The actuator model Pst 150/2x3/5, reduced dimensions and displacement, could have led to a misalignment between the mechanical partner and the piezo-stack surface. Hence, this may have influenced the measurement of the actuator displacement in relation to the load applied. The influence of the applied load on the actuator displacement is more evident in the experiment performed with the Pst 150/2x3/7 piezo-actuator (2-fold higher length and displacement). Surprisingly, with this actuator model the increase in the applied load did not lead to a reduction in the actuator displacement. According to the manufacturers [12], often a heavy but constant load (mass load or a low stiffness preload) when applied to the piezo-stack before operating it will not reduce actuator's maximum stroke. Since this compression of the stack creates the necessary counterforce to bear the load, the system is in force equilibrium before starting the piezoaction. Also, based on the results obtained from the displacement/voltage relation, as expected, when placed in a close to real-case set-up, the maximum stroke generated by the actuators was lower than the free stroke capability presented in the manufacture's product information. The actuator also demonstrated a slightly non-linear displacement in relation to the voltage increase, which resulted from the material inherent hysteresis. To complement this study, the amount of displacement induced in the interfragmentary site by the actuator (based on the parameters from the selected actuator models) was evaluated through finite element simulation. Based on a simple finite element model and on a rough approximation of the actuator's force considered, an average interfragmentary site deformation of 3.8 μm was predicted. In this experiment, the displacement suffered by the mechanical partner is not conditioned by the actuator stroke limit. Depending on the fracture length considered this stimulus may be higher than the minimum 5 μm expected. However, in such a complex system such as the bone-implant structure, for an accurate conclusion to be taken, the influence of other variables cannot be omitted and details such as the clearance between the screw and screw hole, the reaming diameter, the nail thickness and the mechanical partner dimensions greatly influence the amount of strain generated at the healing site. Based on the different actuator loads considered (see Table 4.1) it is possible to conclude that a micro-level considerable interfragmentary deformation requires a high actuator load to be applied to the intramedullary nail. Besides the piezoactuator limitation and overall system relational characteristics, pointed-out so far, there are two essential drawbacks which restrict the use of this type of actuators for the project and which will be highlighted next.

There is a concern towards the actuator device safety limits in order to guarantee patient's safety. Although, the electrical current required by the actuator can generally be considered reduced, it may cause physiological effects in the human body [50]. According to literature [33, 50, 51], the estimated effects of 60 Hz AC currents in the human body are evaluated as 1 mA being the minimum humans can perceive, 16 mA as the maximum current an average man can grasp and "let go" and at 20 mA paralysis of respiratory muscle are already expected. Despite the lack of general consensus on the safe electrical current upper limit, according to the National Electrical Code, 5 mA may be considered as the limit value for adults and children [52]. Though the effects of electricity on the human body are more directly related to current strength, other variables such as contact voltage level, frequency, exposure time, total path resistance (with values as low as 550 Ω) and current path (if it passes through vital organs, *e.g.*, heart) also play an important role [33, 51, 52]. In terms of voltage, there is also no specific "safe voltage level", however, more stringent requirements are made for voltages above 71 V_{PEAK} [33]. The second limitation is on the direct connection between the power supplier and the actuator. At present, the majority of implants are battery-powered systems [53]. However, this particular case corresponds to an implanted actuator which most probably would be maintained inside the human body for a long time period and therefore should not present physical links to the environment outside the human body [54]. Although other power sources for implantable applications are being investigated, the batteries available in the market do not provide the energy density for the good performance of the actuator during a considerable amount of time. Also, the relation size to power supply of the batteries available, do not allow their implantation inside the human body together with the actuator. Hence, the power supply to the actuator system should come from the exterior of the body. This would demand a physical connection between the actuator (inside the human body) and the power supply (outside the human body). Such system would expose the interior of the organism to the exterior hazards (*e.g.* increase the risk of infection), would increase patient discomfort, increase the risk of circuit disconnection and the patient therapy would be restricted to hospital stay. Other actuators, (such as servo- or stepper-motor and the air or hydraulic actuators), show complex implementation procedures and falls under extremely tight design constraints which limits their availability and potentiality in terms of strain and force generated, biocompatibility and robust operation for considerable period time [28, 55]. All these limitations can be avoided if the actuator is used in association with other stabilization devices, such as the external fixators [56], where it actuates outside the human body and where the stimulus generated is propagated to the fixator and then to the bone. In such cases there is a wider variability in terms of system parameters such as actuator dimensions, strain and force generated increase through the use of more efficient leveraging

techniques, there is no concern with biocompatibility and the source of energy would not be a burden. However, this possibility is out of limits since one of the project's main goals is the exclusive use of intramedullary nails.

Other existing smart material actuators will be considered, based on the advantages of using a wireless energy source - such as actuation system robustness, the benefit of allowing the physician to constantly control and adjust the stimulus and the fact that the energy source and the actuator are not directly connected. This is the case of shape memory alloys and magnetostriction actuators. Shape memory alloys were described in sub-chapter 2.4. The amount of strain produced during transformation ranges from 3% to 8% of the shape actuator length (larger than in piezoelectric actuators). However, they also have various limitations which hinder practical application in this project [57]. These include transformation temperature hysteresis, the fact that the heating stimulus may not always be beneficial for the surrounding tissues and the slow dynamic cycles [6, 58]. The potential use of magnetostriction actuators will be evaluated in the next sub-chapter.

4.2. Electromagnetic vibration actuator

Magnetic actuators use voltage and current to produce magnetic fields and secondarily mechanical motion over external nearby localized materials [3]. The discovery of magnetic materials has its earliest record in the 12th century China, where the natural iron ore known as lodestone or magnetite (Fe_3O_4), was applied as mariner's compass during navigation [59-62]. However, it was the invention of the electromagnet, in 1825, triggered by the discovery of the connection between electricity and magnetism by Hans-Christia Oested - through the demonstration that a current-carrying wire produced circumferential field capable of deflection a compass needle – which allowed the production of powerful fields greater than the ones obtained from lodestone permanent magnets [63, 64]. Now-a-days these materials have a wide range of applications from transportation industries (*e.g.* automobiles have several hundred magnets from motor to sensor application) to electronics devices. In the medical field these materials have demonstrated utility for example in the MRI's instruments [4, 60, 65].

The intrinsic magnetic properties of a material are determined by the electronic structure, the crystal structure, and the microstructure namely the domains. Most crystal structures result in filled electron orbitals where all electrons are paired and the magnetic moment cancel. These materials are not magnetic. The ferromagnetic ceramic has all its dipoles in opposite directions, but they are not equal and do not cancel out. Ferromagnetic and ferromagnetic ceramics both contain domains that are not necessarily lined up, but can be aligned by application of a

magnetic field, and can be realigned by application of a reverse magnetic field. This results in a magnetic hysteresis loop. A magnetic field, H , is applied to the material. Domains began to align slowly at first. The slope of this initial magnetization curve is referred to as the initial permeability (μ_i). The magnetic field increases, the rate of domain alignment increases and the slope of the magnetization curve increases until a maximum is reached (maximum permeability, μ_{max}). The domain boundaries have all be displaced by this maximum. Further increase in magnetic field completes the alignment of the domains, reaching the saturation magnetization (also called the saturation flux density, B_s). Application of a reverse magnetic field reverses the direction of the magnetic dipoles. At zero-applied magnetic field, many of the domains are still aligned and residual or remanent magnetization exists. The Residual Induction, also called Flux Density (abbreviated as B_r), is the magnetic flux that remains permanent in a magnet, *i.e.*, it is the magnetic induction corresponding to zero magnetizing force in a magnetic material after saturation in a closed circuit. The Coercive Field (abbreviated as H_c) is a measure of the magnetic retentivity of magnetic materials, meaning it is equal to the magnetization force required to reduce the residual induction, to zero in a magnetic field after magnetizing to saturation. The Maximum Value of Energy Product (abbreviated as BH_{max}) is the maximum product of the Remanent Induction value by the Magnetic Field Strength corresponding to the Remanent Induction, which can be obtained on the Magnetic Induction and the Magnetic Field Strength demagnetization curve. This parameter is often used for comparison between different materials and is considered of interest in the permanent magnet material evaluation since it indicates the maximum magnetic energy [62, 65-67].

The ferrite actuator satisfies the goal of a physical connection absence between energy stimuli and the actuator. Such achivement would increase the safety standards since the interior human body enviroment would not be exposed to the exterior hazards, the actuator would be more robust and it would not be damaged as a result of broken interconnections. The implantable device, used in this study, receives its power via an electromagnetic field and it does not store the harvest energy. Increased patient safety and long-term implantation is achieved. Due to the complete isolation from the electrical network, wireless implants are also more robust.

Permanent magnets can be classified, accordingly to their composition, in three main categories: rare earth, alnico and ceramic magnets. The rare earth magnets are composed of alloys from the lanthanide group of elements. The most popular currently in use are: neodymium, also known as neodymium-iron-boron, with chemical composition is $Nd_2Fe_{14}B$, and samarium-cobalt (*e.g.* $SmCo_2$, Sm_2Co_{17}). The alnico magnet as indicated by its name stands for an alloy

mainly composed of aluminum (*Al*), nickel (*Ni*) and cobalt (*Co*) [3, 68]. Ceramic-like ferromagnetic materials are mainly composed of ferric oxide are called ferrites. Their crystalline structure has the general molecular formula is $M(Fe_xO_y)$, where *M* stands for the divalent metal (such as *Fe*, *Mn*, *Co*) [60, 65, 69]. The actuator selection was initiated with the identification of the magnet category and consequently the material which most satisfies the purpose of the study. Such analysis was based on a comparison study between the different magnets weight, mechanical and magnetic properties, temperature stability, corrosion resistance and pricing. In Table 4.2, the main type of permanent magnets and their typical properties are presented. However, it is important to highlight that as stated in literature [70, 71], in many cases an improved version of the magnets (after alloying with a variety of component) are used for the adjustment of the magnet properties to more suitable applications.

Table 4.2 - Permanente magnets types and typical properties. Data obtained from: [3, 66, 72-76]

| PROPERTIES | MATERIAL | | | |
|---|-------------|-----------------|-------------|------------|
| | Neodymium | Samarium-cobalt | Alnico | Ferrite |
| Density (g/cm ³) | 7.4 – 7.6 | 8.0 – 8.4 | 6.8 – 7.3 | 4.5 – 5.1 |
| Compressive strength (kg/m ²) | 9600 | 9100 | - | 9100 |
| Bending strength (kg/m ²) | 2950 | 1200 | - | 1400 |
| BH _{max} (kJ/m ³) | 119 – 398 | 119 – 255 | 11 – 52 | 6.5 – 35 |
| H _c (kA/m) | 780 – 1033 | 620 – 1194 | 39 – 52 | 125 – 300 |
| B _r (T) | 1.03 – 1.43 | 0.85 – 1.10 | 0.68 – 1.24 | 0.2 – 0.43 |
| Curie temperature (°C) | 310 – 350 | 720 – 825 | 890 | 450 |
| Maximum temperature (°C) | 80 – 180 | 250 – 350 | 425 | 250 |
| Corrosion resistance | Poor | Good | Good | Excellent |
| Cost | High | High | Medium | Low |

In agreement with the Standard Specifications for Permanent Magnets Material (MMPA Standard No. 0100-00) [66] the materials performance was evaluated based on the principal magnetic properties: The Residual Induction, the Coercive Field and the Maximum Value of Energy Product. As can be seen in Table 4.2, the magnetic properties of neodymium and samarium-cobalt magnets are very superior to the existing ferrite and alnico types, where neodymium has the best magnetic properties from all the current available materials. Hence, both magnets can be classified as magnetically very strong. Also, according to the compressive and bending strength values neodymium magnets present a higher bearing capability than samarium-cobalt and ferrite magnets. However, it is advisable to avoid exposing the magnets in mechanical stress conditions *e.g.* as a bearing components in an assembly. All magnets are

inherently brittle [65]. Hence, there should be precautions during handling and direct impact loads on the magnet must be avoided by appropriate design experimentation. Although ferrite magnets do not present the best magnetic properties they have advantageous characteristics favoring this material selection. 1) Among the permanent magnets families, the ferrite presents the lower density values meaning they are the lighter materials. This will avoid adding unnecessary weight to the stainless steel or titanium alloy intramedullary nails implants. 2) The ferrite materials are considered to have very good chemical stability in many solutions such as alkaline solutions, diluted acids, organic solvents and some hydroxides. Since they are made from oxides of iron, they do not present corrosion issues, not even in salt water conditions. This creates some expectation on its non-toxicity and also biocompatibility potential [77]. In contrast, neodymium-iron-boron suffers corrosion. Such limitation not only causes magnetic changes in the material, such as permanent performance weakening and total magnetism loss, but also makes it unacceptable to be placed in *in vivo* situations. There is always the possibility of covering the actuator with a biocompatible coating, however it is expected that the material by itself already shows some degree of biocompatibility. With a lower susceptibility to corrosion, but still prone to it, are the samarium-cobalt and alnico materials. 3) The Ferrite magnets are also the least expensive class of permanent magnets materials while still presenting good permanent magnet properties. 4) When considering the material temperature stability, both the maximum working temperature and the Curie temperature should be considered [65]. The ferrite magnet is considered to have the lowest thermal stability among the magnetic families. However, their performance is preserved in environment up to 250 °C. This temperature is well above the average body temperature of 37 °C and it is also above the temperature used for medical material sterilization. It is important to highlight that a material which satisfies all the parameters is a difficult if not an impossible task. Ferrite magnetic properties can vary depending on its size, the processing parameters (such as composition), additives, raw materials, production method and sintering conditions [78-80]. However, considering these materials general behavior, they were selected to be tested as actuators for bone enhancement and are expected to be capable to perform in a suitable way and to be placed inside the human body without creating any adverse reaction. However, these hypotheses will be tested next, in Chapter 5 and 6, respectively.

Although, early records from 1940, demonstrated research and technology on ferrite materials, the commonly accepted beginning of magnetic ceramics modern age was marked by the studies developed by J. L. Snoeck at the Holland Philips Laboratories, in 1946. Since then, there was a continuous progress in research and development of ferrite were it as found countless

application ranging from electronic to mechanical devices such as choke coils, loud speakers, noise filters, recording heads, broad band impulse transformers. It is often outlined that despite of their reduced size as part of a many pieces equipment, their importance is understatedly high [61, 62, 77, 78, 80]. On the medical field, new and exciting applications have emerged with ferrite size shifting from bulk to nano samples [6, 60, 77]. Magnetic nanoparticles are being actively used and investigated for *in vivo* applications, such as magnetic resonance imaging contrast enhancement, tissue repair, immunoassays, detoxications of biological fluids, drug delivery and cell separation techniques [81]. Promising results are also being obtained with ferrite nanoparticles for non-invasive localized magnetic hyperthermia when administrated together with other cancer treatment modalities. In this therapeutic procedure a region of interest affected by cancer is subjected to a temperature increase (above 40 °C) produced by applying an alternating magnetic field to a magnetic material [82, 83]. In an study developed by Qiang *et al.* [84], stainless steel and *NiTi* alloys coated with *TiO₂* film containing *SrFe₁₂O₁₉* powders showed an increase in the material blood biocompatibility due to its contact with charged particles reduction as a result a micro-magnetic field generation at the surface. Although only two examples were given, the ferrite has demonstrated interesting properties and advantageous applications in the medical field.

The manufacturing process of bulk ferrite is almost the same as that of other general ceramics. They can be obtained from different process, involving milling, mixing, pressing, sintering and finishing as basic operations. Firstly, the fine powders are compacted at high temperatures in a aligning magnetic field only after are they sintered into a solid shape [65, 77]. Independently of the method used they can be obtained in three different crystal systems: spinels, hexaferrites and garnets. Spinel, named after a mineral *MgAl₂O₄* is a class of ferrite characterized by the general molecular formula of $\alpha(Fe_2O_4)$, where α is usually a divalent cation such as manganese (Mn^{2+}), nickel (Ni^{2+}), cobalt (Co^{2+}), zinc (Zn^{2+}) or copper (Cu^{2+}). This structure is particularly stable, since there is an extremely large variety of oxides which adopt it, fulfilling the conditions of overall cation-to-anion ratio of $\frac{3}{4}$, a total valence of 8, and a relatively cation radii. However, its general cubic crystal structure characterized by oxide anions occupying a cubic close packed lattice and the cations occupying tetrahedral and octahedral sites. Hexaferrite (or hexagonal ferrites) named after its hexagonal crystal structure unique *c* axis (or vertical axis), has the general molecular formula $M(Fe_{12}O_{16})$, where *M* is usually barium (*Ba*), strontium (*Sr*) or lead (*Pb*). Garnets ferrites have the structure of the silicate mineral garnet (*Mn₃Al₂Si₃O₁₂*), where instead of *Al* and *Si* there is Fe^{3+} and rare earth cation (such as yttrium), α substitutes *Mn* to give the general formula $\alpha(Fe_5O_{12})$. The crystal structure as cubic symmetry and is relatively

complex. Ferrites are often classified according to the nature of their response to the magnetic field. When it is easy to change the direction of magnetization and when they are easily magnetized and demagnetized, ferrites are said to be “soft” magnetically and are named soft ferrites. Soft ferrites are generally of a spinel composition. These type of ferrites are present in a variety of electronic devices such as in televisions, radios, telephones, communications, electronic ignition systems, etc. Ferrites that have a strong permanent magnetization and does not easily demagnetize are called hard ferrites. Hard ferrites are generally of a hexagonal structure. Some of them are used in the household as magnets to latch cupboards or hang memos [60, 62, 69, 77, 85].



Figure 4.8 - Examples of different ferrite sizes and shapes

Ferrites appear in a dark gray color (when there is no coating present) and they are normally available in simple limited shapes such as discs, rings, blocks and cylinders as a result of the manufacturing process and the diamond cut or grind wheel finishing. However, specific shapes can also be produced (see Figure 4.8).

4.3. References

1. Gandhi, M.V. and B.S. Thompson, *Smart materials and structures*. 1st ed1992, London, UK: Chapman & Hall.
2. Ko, W., P. Wang, and S. Lachlman, *System integration and packaging*, in *Implantable Biomedical Microsystems: Design Principles and Applications*, S. Bhunia, S. Majerus, and M. Sawan, Editors. 2015, Elsevier: London, UK. p. 113-135.
3. Brauer, J.R., *Magnetic Actuators and Sensors*. 1st ed2006, New Jersey, USA: John Wiley & Sons.
4. SękalSKI, P., *Smart materials as sensors and actuators for Lorentz force tuning system*, in *Department of Microelectronics and Computer Science*2006, Technical University of Łódź: Lodz, Poland.
5. Addington, D.M. and D.L. Schodek, *Smart Materials and New Technologies: For the Architecture and Design Professions*. 1st ed2005, Massachusetts, USA: Architectural Press.

6. Kang, I., et al., *Introduction to carbon nanotube and nanofiber smart materials*. Composites Part B: Engineering, 2006. **37**(6): p. 382-394.
7. Jordan, T.L. and Z. Ounaies, *Piezoelectric Ceramics Characterization*, 2001, National Aeronautics and Space Administration in Langley Research Center Hampton: Virginia, USA. p. 1-23.
8. Kalinin, S.V., B. Mirman, and E. Karapetian, *Relationship between direct and converse piezoelectric effect in a nanoscale electromechanical contact*. Physical Review B, 2007. **76**(21): p. 212102.
9. Piezosystem jena, *Introduction - Instruction for using*, in *Piezoelectrical actuators* 2014: Massachusetts, USA.
10. APC International Ltd., *Piezoelectric Ceramics: Principles and Applications* 2nd ed 2011, Pennsylvania, USA.
11. Haertling, G.H., *Ferroelectric ceramics: History and technology*. Journal of the American Ceramic Society, 1999. **82**(4): p. 797-818.
12. APC International Ltd., *First Steps towards Piezoaction*, 2014: Pennsylvania, USA.
13. Wolny, W.W., *Application of piezoceramics - The manufacturer perspective*, in *Piezoelectric Materials in Devices*, N. Setter, Editor 2002, EPFL, Lausanne. p. 67-71.
14. Hai-Bo, L., et al., *Enhanced mechanical behaviour of lead zirconate titanate piezoelectric composites incorporating zinc oxide nanowhiskers*. Chinese Physics B, 2008. **17**(11): p. 4323-4327.
15. Main, J.A. and E. Garcia, *Piezoelectric stack actuators and control system design: Strategies and pitfalls*. Journal of Guidance, Control, and Dynamics, 1997. **20**(3): p. 479-485.
16. Flint, E., C. Liang, and C.A. Rogers, *Electromechanical analysis of piezoelectric stack active member power consumption*. Journal of Intelligent Material Systems and Structures, 1995. **6**(1): p. 117-124.
17. Iseman, R., *Mechatronic Systems: Fundamentals*. 2nd ed 2005, London, UK: Springer.
18. APC International Ltd., *Piezo-Mechanics: An Introduction*, 2014: Pennsylvania, USA.
19. Shrout, T.R. and S.J. Zhang, *Lead-free piezoelectric ceramics: Alternatives for PZT?* Journal of Electroceramics, 2007. **19**: p. 111-124.
20. Maeder, M.D., D. Damjanovic, and N. Setter, *Lead free piezoelectric materials*. Journal of Electroceramics, 2004. **13**: p. 385-392.
21. Promsawat, M., et al., *Effect of ZnO nano-particulates on structure and properties of PZT/ZnO ceramics*. Ferroelectrics, 2009. **382**(1): p. 166-172.
22. Niezrecki, C., et al., *Piezoelectric actuation: State of the art*. The shock and Vibration Digest, 2001. **33**(4): p. 269-280.
23. Uchino, K., *Piezoelectric Actuators and Ultrasonic Motors*. Electronic Materials: Science & Technology, ed. H.L. Tuller. Vol. 1. 1997, London, UK: Kluwer Academic Publishers.
24. Yi, K.A. and R.J. Veillette, *A charge controller for linear operation of a piezoelectric stack actuator*. IEEE transactions on control systems technology, 2005. **13**(4): p. 517-526.
25. Frias, C., *Materiais Inteligentes para prótese de Anca*, in *Department of Mechanical Engineering and Industrial Engineering and Management* 2009, University of Porto: Porto, Portugal.
26. Frias, C., et al., *Piezoelectrical actuator: Searching inspiration in nature for osteoblastic stimulation*. Composites Science and Technology, 2010. **70**: p. 1920-1925.
27. Reis, J., et al., *A new piezoelectrical actuator: induces bone formation in vivo: A preliminary study*. Journal of Biomedicine and Biotechnology, 2012. **2012**: p. 1-7.
28. Tanaka, S.M., *A new mechanical stimulator for cultured cells using piezoelectric actuator*. Journal of Biomechanics, 1999. **32**: p. 427-430.
29. Tanaka, S.M., et al., *Effects of broad frequency vibration on cultured osteoblasts*. Journal of Biomechanics, 2003. **36**(1): p. 73-80.

30. Konno, K.-I., T.N. Kowasada, and Z. Feng. *Piezoelectric micro device for mechanical stimulation and its detection for living cells*. in *6th World Congress of Biomechanics*. 2010. Singapore: Springer.
31. Sakai, T., S. Hoshiai, and E. Nakamachi, *Biochemical compatibility of PZT piezoelectric ceramics covered with titanium thin film*. *Journal of Optoelectronics and Advanced Materials*, 2006. **8**(4): p. 1435-1437.
32. PI Piezo Technology, *Electrical operation of piezo actuators*, 2016, PI Ceramic GmbH: Lederhose, Germany.
33. Bikson, M., *A review of hazards associated with exposure to low voltages*, 2004, The Pennsylvania State University: The Graduate School and University Center of the City University of New York. p. 1-18.
34. Krivts, I.L. and G.V. Krejnin, *Pneumatic Actuating Systems for Automatic Equipment: Structure and Design*. 1st ed2016, Florida, USA: CRC Press.
35. Butt, H.-J. and M. Kappl, *Surface and Interfacial Forces*2009, Weinheim, Germany: John Wiley & Sons.
36. EUROFLEX GmbH, *Stainless steel tubing for surgical implants and devices - Material data*, 2015: Pforzheim, Germany.
37. Morawska-Chochół, A., et al., *Influence of the intramedullary nail preparation method on nail's mechanical properties and degradation rate*. *Materials Science and Engineering: C*, 2015. **51**: p. 99-106.
38. Schoenmarklin, R.W. and W.S. Marras, *Effects of handle angle and work orientation on hammering: I. Wrist motion and hammering performance*. *Human Factors: The Journal of the Human Factors and Ergonomics*, 1989. **31**(4): p. 397-411.
39. Knudson, D., *Fundamentals of biomechanics*2013, New York, USA: Springer Science & Business Media.
40. Dobrjanski, D., *Experimental Parametric Study Of The Factors Leading To Elevated Femoral Intramedullary Pressure And Fat Embolus Syndrome In Orthopaedic Procedures*, in *Mechanical Engineering Department*2005, Ryerson University: Ontario, Canada.
41. Sonoma Orthopedic Products, *Sonoma HMRx™ - Humerus fracture repair device*, I. Sonoma Orthopedic Products, Editor 2011: California, USA. p. 1-16.
42. Sharma, V.K., *Laser Doppler Vibrometer for Efficient Structural Health Monitoring*, in *School of Aerospace Engineering*2008, Georgia Institute of Technology: Georgia, USA.
43. Rembe, C., et al., *Measuring MEMS in motion by Lazer Doppler Vibrometry*, in *Optical Inspection of Microsystems*, W. Osten, Editor 2016, CRC Press: Florida, USA. p. 245-292.
44. Lopes, H.M.R., *Estudo do Fluxo de Energia vibratória em Vigas e Placas*, in *Department of Mechanical Engineering*2001, School of Engineering at the University of Porto: Porto, Portugal.
45. Byrne, D.P., D. Lacroix, and P.J. Prendergast, *Simulation of fracture healing in the tibia: mechanoregulation of cell activity using a lattice modeling approach*. *Journal of Orthopaedic Research*, 2011. **29**(10): p. 1496-1503.
46. *Stahlschlüssel: Key to steel*. 23th ed2013, Marbach, Germany: Verlag Stahlschlüssel.
47. Wehner, T., et al., *Improvement of the shear fixation stability of intramedullary nailing*. *Clinical Biomechanics*, 2011. **26**: p. 147-151.
48. Begum, F., *Experimental and Numerical Analysis of Augmented Locking Plate Fixation Repair for Proximal Humeral Fractures*, in *Civil and Environmental Engineering Department*2011, University of Alberta: Alberta, Canada.
49. Cordey, J., et al., *Importance of the friction between plate and bone in the anchoring of plates for osteosynthesis. Determination of the coefficient of metal-bone friction in animal in vivo*. *Helvetica chirurgica acta*, 1979. **46**: p. 183-187.
50. Fish, R.M. and L.A. Geddes, *Conduction of electrical current to and through the human body: A review*. *Eplasty*, 2009. **9**: p. 407-421.

51. Calvas, R., *Residual current devices in LV*. Cahier Technique no. 1141999, Schneider Electric: Technical Collection.
52. Slaten, B.K. and F. Barnes, *Biological effect and electromagnetic fields*, in *Sensors, Nanoscience, Biomedical Engineering, and Instruments: Sensors Nanoscience Biomedical Engineering*, R.C. Dorf, Editor 2016, CRC Press: Florida, USA. p. 7-34.
53. Heinilä, H., et al., *Low cost miniaturization of an implantable prototype*. Circuit World, 2009. **35**(1): p. 34-40.
54. El-hami, M., et al., *Design and fabrication of a new vibration-based electromechanical power generator*. Sensors and Actuators A: Physical, 2001. **92**(1-3): p. 335-342.
55. Bhunia, S., S. Majerus, and M. Sawan, *Introduction*, in *Implantable Biomedical Microsystems: Design Principles and Applications*, S. Bhunia, S. Majerus, and M. Sawan, Editors. 2015, Elsevier: London, UK. p. 3-12.
56. Guzmán, A.I.A. and R.G. Lima. *Numerical Simulation of a mechanical pulse generating device for the induction of bone density increase*. in *5th Portuguese Congress on Biomechanics*. 2013. Espinho, Portugal.
57. Rao, A., A.R. Srinivasa, and J.N. Reddy, *Design of Shape Memory Alloy (SMA) Actuators* 2015, New York, USA: Springer.
58. Khan, A., *Characterization and Application of Shape Memory Alloy Wires for Micro and Meso Positioning Systems*, in *Mechanical and Aerospace Engineering* 2008, The George Washington University: Washington D.C., USA.
59. Coey, J.M.D., *Magnetism and Magnetic Materials*. 3rd ed 2010, New York, USA: Cambridge University Press.
60. Jaswal, L. and B. Singh, *Ferrite materials: A chronological review*. Journal of Integrated Science and Technology, 2014. **2**(2): p. 69-71.
61. Sugimoto, M., *The past, present, and future of ferrites*. Journal of the American Ceramic Society, 1999. **82**(2): p. 269-280.
62. Richerson, D., D.W. Richerson, and W.E. Lee, *Modern ceramic engineering: Properties, processing, and use in design*. 3rd ed. Materials Engineering 2006, Florida, USA: CRC Press.
63. Häfeli, U., *The mystery and history of magnetism*, in *Scientific and Clinical Applications of Magnetic Carriers*, U. Häfeli, et al., Editors. 1997, Springer: New York, USA. p. 1-10.
64. Cullity, B.D. and C.D. Graham, *Introduction to Magnetic Materials*. 2nd ed 2011, New Jersey, USA: John Wiley & Sons.
65. Alliance LLC, *Magnet guide & tutorial*, 2016: Indiana, USA.
66. Magnetic Materials Producers Association, *Standard specification for permanent magnet materials*, 2000: Illinois, USA. p. 1-28.
67. Kaufman, J.G., et al., *ASM ready reference: Properties and units for engineering alloys*. 1st ed 1997, Ohio, USA: ASM International.
68. Krishnamurthy, U., *Mitigation of vibration in a permanent magnet synchronous machine using field reconstruction*, in *Electrical Engineer Department* 2008, University of Texas: Arlington, USA.
69. Mason, T.O. *Magnetic ceramics*. 2016.
70. Campbell, P., *Permanent Magnet Materials and Their Application* 1996, Melbourne, Australia: Cambridge University Press.
71. Saura-Múzquiz, M., et al., *Improved performance of SrFe₁₂O₁₉ bulk magnets through bottom-up nanostructuring*. Nanoscale, 2016. **8**(5): p. 2857-2866.
72. Buschow, K.H.J., *Concise Encyclopedia of Magnetic and Superconducting Materials* 2005, London, UK: Elsevier.
73. *Characteristics of NdFeB magnets*, E.-m. UK, Editor 2016: Hertfordshire, UK.
74. IMA - Ingeniería Magnética Aplicada, S.L., *Technical Information - Magnetic materials*, 2016: Barcelona, Spain. p. 97.
75. Integrated Magnetics, *Magnetic Properties*, 2016: California, USA.

76. International Electrotechnical Commission, *Magnetic materials - Part 8-1: Specifications for individual materials - Magnetically hard materials*, 2015: Geneva, Switzerland.
77. Valenzuela, R., *Novel applications of ferrites*. Physics Research International, 2012. **2012**(2012): p. 1-8.
78. El-Badry, S.A., *Influence of processing parameters on the magnetic properties of Mn-Zn ferrites*. Journal of Minerals and Materials Characterization and Engineering, 2011. **10**(5): p. 397-407.
79. Chen, S.H., et al., *Improvement on magnetic power loss of MnZn-ferrite materials by V_2O_5 and Nb_2O_5 co-doping*. Journal of the European Ceramic Society, 2001. **21**(10): p. 1931-1935.
80. Nakamura, T. and Y. Okano, *Electromagnetic properties of Mn-Zn ferrite*. Journal of Physique IV, 1997. **7**(C1): p. 101-102.
81. Latorre-Esteves, M., et al., *Synthesis and characterization of carboxymethyl dextran-coated Mn/Zn ferrite for biomedical applications*. Journal of Magnetism and Magnetic Materials, 2009. **321**: p. 3061-3066.
82. Kim, D.-H., et al., *Cytotoxicity of ferrite particles by MTT and agar diffusion methods for hyperthermic application*. Journal of Magnetism and Magnetic Materials, 2005. **293**(1): p. 287-292.
83. Périgo, E.A., et al., *Fundamentals and advances in magnetic hyperthermia*. Applied Physics Reviews, 2015. **2**(041302).
84. Qiang, L., C. Xiaonong, and F. Huangxia. *Micro-magnetic field at the surface of surgical materials for biocompatibility improvement*. in *International Conference on Advanced Material Research* 2011. Chongqing, China: Trans Tech Publications.
85. Han, M.H., *Development of synthesis method for spinel ferrite magnetic nanoparticle and its superparamagnetic properties*, in *Chemistry2008*, Georgia Institute of Technology: Michigan, USA.

“If you can’t explain it simply, you don’t understand it well enough”

Albert Einstein

5. Cytocompatibility evaluation

A clinical device success requires a path towards regulatory approval, where the medical device materials have to undergo extensively testing, both *in vitro* and *in vivo* [1-3]. According to standards, it is essential to have a sufficient understanding of the *in vitro* system and of the relevant factors which could affect it prior to *in vivo* experimentation [3, 4]. The physical structure, chemical composition and corrosion resistance of implanted materials are determinant factors which influence the cellular responses and hence the level of biocompatibility of the implant [5, 6]. Although, the corrosion resistance of ferrite is considered excellent for most applications and its components are believed to be nontoxic, its biocompatibility is not fully studied. Several studies [7-9], have presented promising results on ferrite nanoparticles potential for non-invasive localized magnetic hyperthermia when administrated together with other cancer treatment modalities, the material influence on cell uptake, proliferation and functional activity still remain controversial [10]. The results obtained from this research allowed to evaluate the biocompatibility potential of the ferrite bulk material to be applied *in vivo* as a mechanical actuator for the enhancement of bone healing. This chapter is focused on the evaluation of cytocompatibility of ferrite samples under various conditions and through sequential experiments that are schematized in Figure 5.1. The study was initiated with the general evaluation of free, easily available, and non-homogenously shaped *Zn* ferrite samples through MTT assay, chorioallantoic membrane (CAM) angiogenesis assay, HET-CAM assay, optical and scanning electron microscopy, energy-dispersive X-ray spectroscopy (EDS) and contact angle measurement. To maximize the assays reproducibility, reliability and credibility, uniform ferrite samples were mandatory [4]. The samples should present a “plane” surface for cell adhesion and proliferation [4] and dimensions to fit the 48-well culture plates. These requirements reduced the materials availability to Sr-Ca ferrite testing samples. This new material biocompatibility was evaluated through cytotoxicity and cytocompatibility tests, such as the resazurin and MTT assays where cell viability, proliferation and metabolic activity were analysed. Cell attachment and morphology were evaluated by scanning electron microscopy. All experiments on cell adhesion and proliferation were carried out using a MG-63 osteoblastic-like

cell line as a cell model. Although, primary cells have obvious attractiveness in terms of more closely reflecting the *in vivo* behaviour, various cell culture models have been employed for the evaluation of osteoblastic cell behaviour under different conditions [11]. The MG-63 cell line, which was first introduced in 1977 by Billiau *et al.* [12] are osteosarcoma cells derived from malignant bone tumours and which are arrested in the pre-osteoblast state. Although, these osteosarcoma-derived cells have abnormal molecular and cellular functions due to chromosomal alterations, they are commonly used as osteoblastic models due to their advantages such as inexistence of interspecies differences, the cell high availability number, the similar to human osteoblastic cells hormonal response, the similarity to human integrin subunits profile and also their high growth and proliferation rate which makes them ideal for a preliminary experiments where a quick response evaluation is required [11, 13]. Besides their limitation as being inconsistent regarding cell mineralization they have been used in many studies to evaluate the biocompatibility of ferrite particles for *in vivo* implantation [14-16].

Considering that the cytocompatibility of materials is very closely related to cell behavior on contact and adhesion to their surface [17], the influence of using demagnetized samples where the demagnetization process was attained through different methods (strong external magnetic field of opposite polarity, Curie temperature under an oxygen environment and Curie temperature under a nitrogen environment) and the influence of chemical contaminants removal through abrasive mechanical cleaning and its consequent surface topography alteration were also considered and were evaluated through surface morphology and chemical composition characterization obtained from white light interferometry and EDS measurements, respectively.

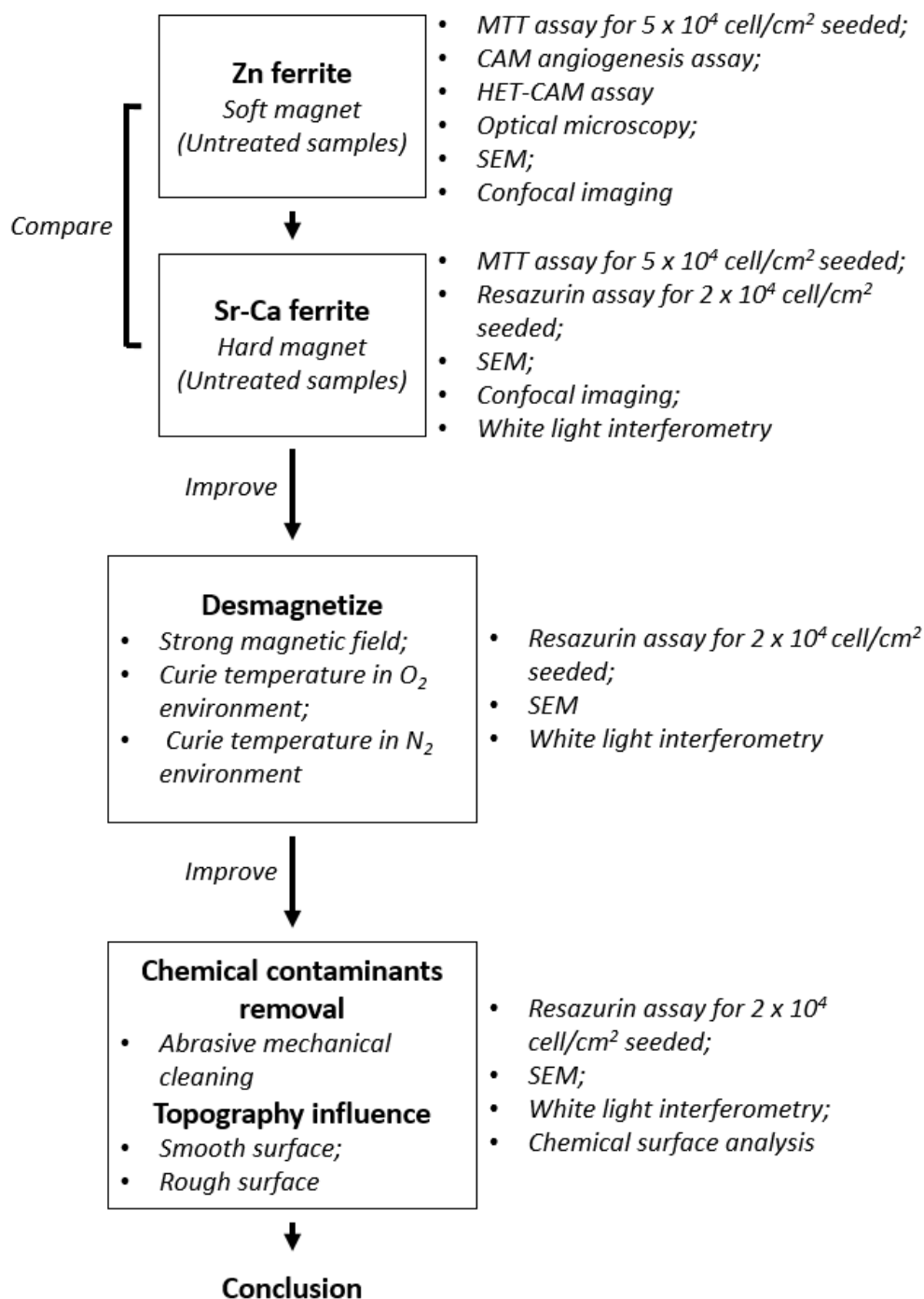


Figure 5.1 - Chart showing the overall structural organization of the experiments and the associated evaluation methods

5.1. Materials and methods

5.1.1. Materials, chemicals and reagents

Irregularly shaped soft magnetic *Zn* ferrite samples (see Figure 5.2(A)) with average surface area of 31.8 ± 17.3 mm² were obtained from the breakage of bulk materials available in the Technological Testing Laboratory (translated as *Laboratório de Ensaios Tecnológicos* - LET).

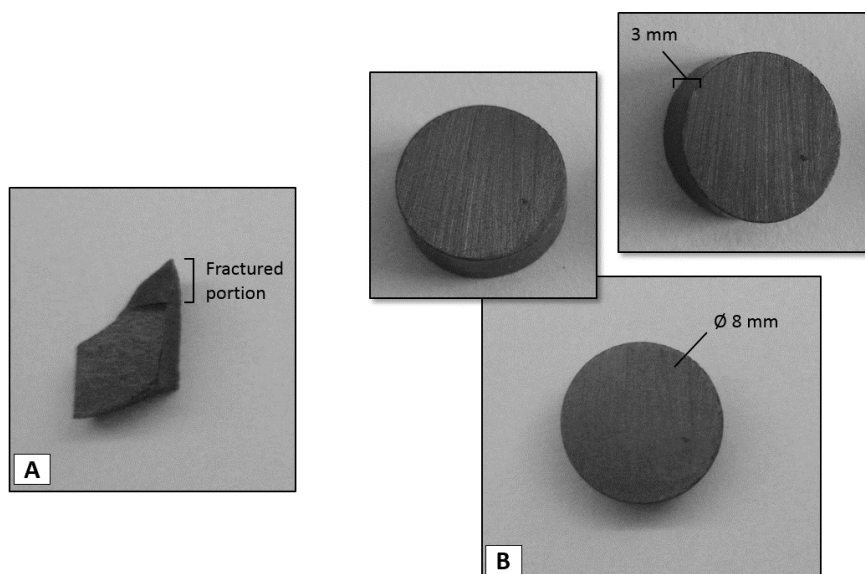


Figure 5.2 - The test materials considered in the study: (A) Zn irregular shaped ferrite sample and (B) Sr-Ca ferrite sample showed from different views

The hard magnetic Sr-Ca ferrite discs (axial magnetization, Y30BH quality) with 8 mm diameter and 3 mm width and 0.74 g weight (see Figure 5.2(B)) were purchased from IMA (Barcelona, Spain). This ferrite composition includes 85.6 wt% Fe_2O_3 , 13 wt% $SrCO_3$, 0.4 to 0.5 wt% Al_2O_3 and 0.5 to 0.6% $CaCO_3$.

5.1.2. Ferrite demagnetization

To understand the influence on cell adhesion and proliferation of permanent magnetic field removal, the Sr-Ca ferrite discs were subjected to demagnetization. To avoid inefficient permanent magnetization removal, three demagnetization process - Curie temperature under oxygen environment, Curie temperature under nitrogen environment and strong magnetic field - were considered.

For the samples demagnetization with Curie temperature in an oxygen environment, the magnets placed in a crucible were gradually heated slightly above the Curie temperature (which according to manufactures is 450 °C) at 458 °C, during 60 minutes in a high temperature thermal treatment chambers (Model E4, Maclife, Porto, Portugal). The samples cooling process was slow, during a time-period of 12 hours.

In the demagnetization through Curie temperature under nitrogen atmosphere, samples were placed inside a horizontal tubular TH furnace (Termolab, Águeda, Portugal), equipped with three different heating elements. These heating elements are actuated by three distinct control actions, using a Shimaden MR13 temperature digital controller (Tokyo, Japan). The samples

were heated at a slow rate at 2.4 °C/min after 30 minutes for full residual O_2 replacement by a 90 ml N_2 environment. Samples were then heated at an end temperature of 500 °C during 60 minutes. Samples cooling was done inside the furnace, slowly overnight. Both Curie temperature heating demagnetization process were developed in the Chemical Engineer Department at the Faculty of Engineer of the University of Porto.

The demagnetization of Sr ferrite discs by exposing them to a strong external magnetic field of opposite polarity was done by IMA Company (Barcelona, Spain). The materials were purchase already in the demagnetized form and no specific details on the demagnetization process were given by the company. This procedure is easily done by the material companies, since they normally have the appropriate machinery. Since Sr ferrites are hard magnet materials, *i.e.* are difficult to demagnetize, in the academic environment the magnetic fields strength generated would not allow proper demagnetization of the samples to be achieved.

5.1.3. Material biological and mechanical cleaning

It is important to work with pure system, *i.e.* free from chemical and biological contaminants since cells are greatly influenced by any external variable [4]. To avoid cell culture microbial contamination and false assessment of cytotoxicity, before cell culture, all ferrite samples were sterilized with medical autoclave at high-pressure saturated steam at 121°C during 45 minutes. The samples chemical contaminates removal was achieved with two abrasive mechanical cleaning: soft and the hard mechanical cleaning. In the soft mechanical cleaning samples were gently rubbed in gauze soaked with 70% ethyl alcohol (Agar, Prior Velho, Portugal). In the hard mechanical cleaning (MC was the abbreviation adopted throughout the chapter), samples surface were subjected to abrasion through circular movements applied in two sequential grid size silicon carbide sandpapers. First they were subjected to a very fine grain size P800 (average particle diameter of 22 µm [18]) sandpaper (Presi, Eybens, France) and afterwards to an ultrafine grain size P1200 (average particle diameter of 15.3 µm [19]) sandpaper (Luzostela, Aveiro, Portugal). The grid designation was according to the ISO/FEPA standards. The abrasive cleaning was only executed after the materials were demagnetized to avoid particles draw to the magnetic surface.

5.1.4. Cell culture

MG63 osteoblastic cells (ATCC® CRL-1427) were used in the biological evaluation of the ferrite samples. Cells were cultured in minimum essential medium, alpha modification (α -MEM, Gibco™, Thermo Fisher Scientific Inc., Massachusetts, USA) containing 10% v/v fetal bovine

serum (FBS, Gibco), 100 IU/mL penicillin, 100 µg/mL streptomycin and 2.5 µg/mL amphotericin B. Cultures were incubated at 37 °C in a 5% CO_2 humidified atmosphere. At 70% confluency, cells were harvested (0.05% trypsin – 0.25% EDTA solution) and the cell suspension was counted in a Neubauer haemocytometer chamber under the optical microscope (TMS-F model, Nikon, Japan). This cell suspension was used to test the ferrite samples.

Ferrite samples were placed in 48-well culture plates (Costar®) and incubated with complete cell-culture medium for at least 30 minutes, at 37 °C without agitation. Subsequently, cells were seeded over the materials at a density of 2×10^4 or 5×10^4 cells per cm^2 , in a working volume of 500 µl per well. Cells cultured on the standard 48-well culture plates were used as positive control. Also, ferrite samples were incubated with culture medium in the same experimental conditions, but in the absence of cells (negative control).

The seeded materials, the positive control and the negative control were incubated in the experimental conditions described above. Culture medium was changed every 3 days. Cultures were maintained for several culture times, and were characterized for cell viability/proliferation. All the experiments with cell cultures were developed in the Laboratory for Bone Metabolism and Regeneration at the Faculty of Dental Medicine of the University of Porto.

i) Cell viability/proliferation - Resazurin assay

The Alamar Blue or resazurin assay is a colorimetric test where a non-fluorescent blue resazurin compound is reduced to a pink highly fluorescent product, resorufin, by metabolically active cells enzymes such as NADP and FADH (see Figure 5.3). This is a sensitive, reproducible and non-destructive assay. Nonviable cells have no metabolic capacity and thus, will not reduce the dye. Therefore, the fluorescent intensity observed in this assay is a measure of the viable cells. Since resazurin is non-toxic and permeable through cell membranes, continuous monitoring of cells in culture is allowed [20-23]. In the first day of cell viability measurement, the ferrite samples were placed in new wells and a new medium with 10% resazurin sodium salt (Sigma-Aldrich, Missouri, USA) was added. The cultures were then incubated in the dark (since Alamar Blue is photosensitive) for 3 h under standard culturing conditions before collection of samples. Fluorescence readings in the culture medium were measured at an excitation/emission wavelength of $\lambda = 530/560$ nm using a Synergy^{MT} HT Multi-Detection Microplate Reader (BioTek, Bad Friedrichshall, Germany). All results were normalized in terms of macroscopic surface area and Fluorescence/ cm^2 .

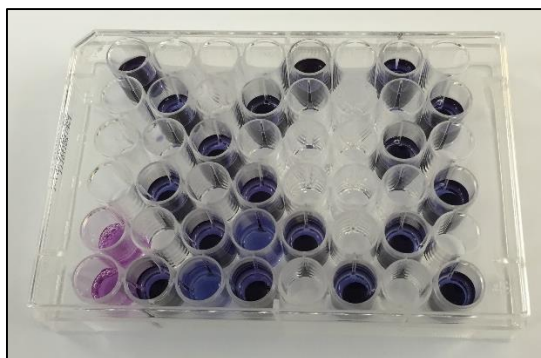


Figure 5.3 - Resazurin assay: non reduced blue resazurin compound is present in the wells with the ferrite samples and the fluorescent pink product in the positive control wells

ii) Cell viability/proliferation - MTT assay

MTT [3-(4,5-dimethylthiazol-2-yl)-2,5-diphenyltetrazolium bromide] assay is a colorimetric test to measure cell viability based on cells metabolic activity. In this assay, the ability of living cells to reduce a yellow tetrazolium salt solution to a violet-purple formazan product formation through active mitochondrial dehydrogenase enzymes, is evaluated. Hence, nonviable cells have no metabolic capacity and thus, will not reduce the tetrazolium salt. One of the limitations of this assay is that the formazan crystals produced must be solubilized, which destroys the cells under investigation so time-course experiments cannot be carried out. Control cultures and ferrite samples with seeded cells had the supernatant removed and replaced with culture medium containing 0.5 mg/ml MTT of solution (Sigma-Aldrich, Missouri, USA), with 50 μ l/well. After 3 h of incubation under standard culturing conditions, the medium was removed, and the crystallized formazan dye was solubilized with 200 μ l/well dimethyl sulphoxide (Sigma-Aldrich, Missouri, USA), also known as DMSO. After 5 min of slow shaking, the absorbance was measured at $\lambda = 550$ nm with Synergy^{MT} HT Multi-Detection Microplate Reader (BioTek, Bad Friedrichshall, Germany). All data was normalized in terms of macroscopic surface area and Absorbance/cm². Each irregularly shaped Zn ferrite samples area was obtained from the averaging of three measurements which were developed in a java-based image processing software, ImageJ (National Institutes of Health, Maryland, USA).

iii) Hen's egg test - Chorioallantoic membrane (HET-CAM) assay

The HET-CAM assay is a rapid, sensitive and inexpensive toxicity test, which gives information on the potential irritancy of the ferrite samples through the measurement of the material ability to induce toxicity in the chorioallantoic membrane of a chicken [24].

The *in vivo* HET-CAM assay procedure adopted followed the method suggested by the ICCVAM Recommended Test Method Protocols [25]. Fertilized white chicken eggs (Pintobar, Portugal)

were received and incubated at 37 °C and under 60% constant humidity. At incubation day 8, eggs are positioned with the large end of the eggs upwards for an additional day. On day 9 of incubation, the egg shell is scratched around the air cell with a rotating dentist saw blade and pared off. Caution on the eggshell removal was taken to ensure that the inner membrane was intact. The inner membrane was then moistened with a 0.9% *NaCl* solution through the use of a glass pipette. Afterwards the eggs were placed in the incubator. After 30 minutes incubation, the 0.9% *NaCl* solution was decanted, and the inner membrane was removed with forceps leaving the vascular CAM exposed. *Zn* ferrite bulk material was ground to a granulated state, were a 0.3 mL sample was applied directly onto the CAM so that at least 50% of the surface was covered. In each experiment a series of three eggs are used were two eggs are treated as a positive and negative control. For positive control, 0.1 N *NaOH* was used since it is a known irritant substance which does not induce an excessive reaction, hence ensuring a variability response across time. For negative control 0.9% *NaCl* solution was used. After the application of the ferrite test samples reactions for hemorrhage (bleeding from vessels), vascular lysis (blood vessels disintegration) and coagulation (intra- and extra-vascular protein denaturation), on the CAM were observed over a period of 5 minutes. The time for each reaction was recorded in seconds and an irritation score (IS) using equation (5.1) [26].

$$IS = 5 \times \frac{(301 - secH)}{300} + 7 \times \frac{(301 - secL)}{300} + 9 \times \frac{(301 - secC)}{300} \quad (5.1)$$

Where *secH* stands for hemorrhage, *secL* for vascular lysis and *secC* for coagulation reaction starting time. The 0.9% *NaCl* negative control was considered to have a 0 irritation assessment value and the *NaOH* positive control range to be between 9 to 21 values. For results validation, this experiment was repeated 6 times.

iv) Chorioallantoic membrane (CAM) angiogenesis assay

As stated in previous chapters, aside from the importance of the fracture fixation mechanical stability, it is essential to respect and maintain the biology of the healing process. Angiogenesis is defined as the formation of new blood vessels from existing ones which plays an important role in new tissue growth and therefore, is mandatory for a proper bone union to take place [27]. In order to evaluate the angiogenic response resulting from the presence of ferrite material, a well-established method for determining *the* angiogenesis response, known as the chick chorioallantoic membrane (CAM) assay, was adopted. The CAM assay is based on a highly vascularized structure with potential growth [27]. The selection of the CAM assay in detriment of other classic angiogenesis assays, such as rabbit ear chamber, mouse dorsal skin and air sac,

the iris and avascular cornea of the rodent eye and the zebrafish, was based on its simplicity, reduced cost, its availability and the high reproducibility rate. Also testing incubated eggs can be considered as a threshold system between the *in vivo* and *in vitro* model and does not cause any ethical and legal standards conflicts [24, 28-30].

The CAM is an extraembryonic membrane, formed on day 4 of incubation, by fusion of the chorion epithelium, derived from the ectoderm, with the allantois, a mesoderm derived-membrane which primitive blood vessels begin to take shape on day 3 of incubation [28, 31-33]. Until 8th day, this newly formed membrane primitive vessels (lacking a complete basal lamina and smooth muscles cells), continue to proliferate and differentiate into an extremely rich network of arteries and veins from which a delicate and intricate capillary plexus is formed. The network of capillaries migrates to occupy an area beneath the chorion and mediate gas exchanges with the outer environment, serving as the respiratory organ of the embryo until the time of hatching, actively transports sodium and chloride from the allantoic sac and calcium from the eggshell into the embryonic vasculature, and forms part of the wall of the allantoic sac, which collects excretory products [28, 31, 33, 34]. The rapid capillary proliferation goes until day 11 and from which the endothelial cell mitotic index declines rapidly and the vascular system attains its final arrangement on day 18, just before hatching [28, 31]. CAM's are cultured either *in ovo* or *ex ovo* as shell-less culture [32]. The *in ovo* CAM assay was selected a rapid and reliable evaluation method of tissue reaction to ferrite samples. According to Domenico Ribatti [28], there is no clear evidence of significant differences between data derived using *in ovo* or shell-less culture method. However, a part from the *in ovo* CAM assay significant accessibility limitation and the difficulty in the effects observation and photo documentation [35], this method presents a more physiological environment given by the presence of the egg shell which also confers an additional protection from temperature variation and any type of environmental hazards and reduces the amount of material motion at the CAM, when compared to the *ex ovo* shell-less culture method.

The *in vivo* angiogenesis assay procedure adopted followed the protocol described by Fábio Costa [36]. Fertilized white chicken eggs (Pintobar, Portugal) were received and incubated at 37 °C and under 60% constant humidity, as soon as embryogenesis starts. On embryonic day 4, post-incubated eggs surface was disinfected with 70% ethanol solution (Agar, Prior Velho, Portugal) and the eggs opening procedure was carried on. It started with the adhesion minimization of the shell membrane with CAM through withdraw of 2 to 3 ml of albumen with a 5-cc syringe inserted at a small hole created at the tip of the eggs (see Figure 5.4(A)).

Afterwards, the CAM was dissociated from the egg shell membrane with an 18-gauge needle. Further developmental time would result on CAM damage since the membrane tends to stick to the shell. Next, 1 ml of isotonic solution (to ensure the drop of the membrane) was injected through a small hole created at the top of the egg (see Figure 5.4(B)). To monitor the vessels development along the incubation time a square window with approximately 1 cm^2 was created in the shell surface, using sterilized dissection scissors (see Figure 5.4(C)). Prior to the window cutting an adhesive film was applied to prevent spilling of shell particles onto the CAM while cutting the window. Before incubation, the window was sealed with a transparent adhesive film to prevent dehydration (see Figure 5.4(D)). It was not necessary to cover the puncture sites. After 8 days of incubation, the square window was re-opened and 0.5 cm inner diameter sterile rings were laid on the CAM for the deposition of the testing samples. The samples for implantation in the chorioallantoic membrane were obtained by repeatedly hitting the bulk material, so small chips were obtained. The process was repeated in the smaller chips until a grain sided sample was produced. Only rounded edged samples were selected for CAM implantation. Each egg received a ring where one had a ferrite test sample and the other functioned as a control. The eggs were again closed using the same method and were then incubated. The overall assay was constituted by 5 experiments were 6 eggs were used in each one.

In ovo analysis, digital images were captured - with Inverted Phase microscopy (TMS model, Nikon, Japan) at 0.7x and 1x magnifications and with upper light application - immediately after material deposition (0 hour) and on embryonic day 11, *i.e.* 72 hours after material deposition (before which there is only vasodilation and no angiogenesis [37]). As a complementary method, *ex ovo* analysis images of the CAM implant were obtained. This was achieved by fixing the embryos and their membrane *in ovo* through the addition of a small volume of 3.7% formaldehyde solution, which makes the membrane stiffer and facilitates the cutting of the membrane, and afterwards frozen at 20 °C refrigerator during 10 minutes, so that blood vessels would stay unaffected. The CAM surrounding the rings was cut from the egg with aid of forceps and small dissection scissor. The harvested CAM was placed in 6-well plates containing formaldehyde solution so that the *ex ovo* images of the CAM implant could be directly obtained from the plates. In the *ex ovo* analysis, images were captured 3 days after material deposition with the Inverted Phase microscopy at 0.7x and 1x magnifications. The images obtained from both analysis methods (*in ovo* and *ex ovo*) were processed using WCIF ImageJ software (Wright Cell Imaging Facility, National Institutes of Health, Maryland, USA) to assist the progress of the angiogenetic response evaluation through the measurement of the number and diameter of all

blood vessels enclosed by the ring and the ones that converge towards the implanted ferrite. The blood vessels network was evaluated based on a classification method where the smallest vessels are defined as third-order vessels and are denominated as “type III” vessels and where only diameters between 30 and 66 μm were considered. When two third-order vessels converge, an order two vessel (or “type II”) is formed and only vessels with diameters between 65 and 110 μm were considered. Likewise, the convergence of second-order vessels forms a first-order vessel (or “type I”) and where only diameters between 110 and 240 μm were considered. When two unequal order vessels converge, the highest order is retained.

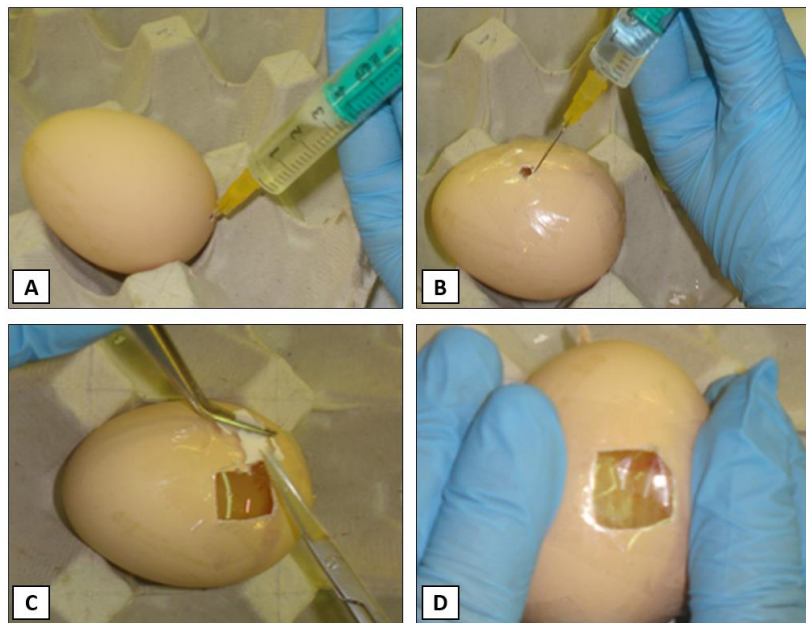


Figure 5.4 - Day 4 CAM assay protocol overview were: (A) albumin removal, (B) CAM dissociation from the egg shell membrane, (C) isotonic solution injection and (D) the square window creation for blood vessels development monitoring, are represented

v) Bright field microscopy

Light-optical microscopy is a more routine used technique for object amplification [38]. Standard bright field microscopy was performed with a Video-microscope with zoom XZ (Lan Optics, Labolan S. L., Spain) equipped with an image analysis system Gen5 Software (Version 3.0, BioTek, Bad Friedrichshall, Germany) at X0.7 to 2 resolution in MTT coloured ferrite samples.

vi) Scanning electron microscopy (SEM)

Scanning electron microscopy (SEM) is a well-known technique which allows surface qualitative analysis. In this method, a focused electron beam hits a test specimen surface which interaction allows several signals, such as secondary electrons, back-scattered electrons (known as BSE) and transmitted electrons, to be produced. The final image is dependent on the acquisition of signals produced from the electron beam and specimen interaction [39]. The SEM technique has unique

features such as: a flexible scalability range where magnification levels from less than 100X for up to 100000X allows image range from the order of 1 mm² to 1 μm² or on conductive surfaces a ultimate resolution of approximately 2 nm; large depth of field and the capacity of keeping simultaneously feature focus at different depths; the long usable working distance (distance of the specimen below the objective lens), and the facility in specimen preparation where there is no limitation to the use of thin test specimens [38, 40, 41].

For SEM observation, the specimens were rinsed with non-sterile PBS (Sigma-Aldrich, Missouri, USA), then fixed in 1.5% glutaraldehyde (Sigma-Aldrich, Missouri, USA) in 0.14 M sodium cacodylate buffer (pH 7.3) (Sigma-Aldrich, Missouri, USA) and then dehydrated in graded alcohols (70%, 80%, 90% and 100%). The specimens were then critical point dried at room temperature. Subsequently, the samples were sputter-coated with a *Au/Pd* thin film, using a Module Sputter Coater (SPI® Supplies, Pennsylvania, USA) equipment. The sputter-coating with a conductive material allows the surfaces of isolating materials, which otherwise may lead to electrostatic charging upon electron probe exposure, to be analysed using SEM. The prepared samples were observed under a high resolution (Schottky) environmental scanning electron microscope (FEI Quanta 400 FEG ESEM) equipped with EDS microanalysis capability (EDAX Genesis X4M), at an acceleration voltage between 5 and 15 kV. SEM observations were performed with the following magnifications: X 250, 2500 and 5000.

5.1.5. Surface evaluation

i) Surface topography

Ferrite samples surface topography was characterized using white light interferometry mapping (Bruker Corporation, Massachusetts, USA) equipped with Vision 64 Map software (Version 5.60, Bruker Corporation, Massachusetts, USA). The white light interferometry is a 3D-measurement technique resulting in absolute height values for the topography of a test object. Since it is based on electromagnetic waves of optical frequencies there is no physical contact with the surface being measured and therefore it does not represent a risk of surface damage. Another advantage of this method is that, as a result of its non-contacting nature must faster measurement are made than with contact scanning instruments [42, 43]. Since every surface is composed of different classes of irregularities [44], a filter cut-off (λ_c) was adopted. This filter defines where is the intersection between the roughness and waviness [45]. The filter length was 0.25 mm and its selection was based on the roughness value and according to ISO 4287 standard [46]. The white light interferometer had a vertical resolution of 1 nm and a lateral resolution in the order of micron. Standard engineering roughness values, namely average

surface roughness (R_a), root mean square roughness (R_q) and mean peak-to-valley roughness (R_z) (ISO 4287 definitions) were averaged from 12 different scans for each direction (x and y) and for a total of three samples per category. For each sample a topographic area of $(1.5 \times 1.5 \text{ mm})^2$ was mapped. The surface topography parameters were calculated and three dimensional images of the samples were taken. The surface topographic analysis was conducted at the Lubricant Analysis Laboratory (translated as *Laboratório de Analise de Lubrificantes*) in the Faculty of Engineering of the University of Porto.

ii) Energy dispersive X-ray spectroscopy (EDS)

The ferrite samples surface chemical analysis was achieved through the energy-dispersive X-ray spectroscopy (EDS). The EDS is a sensitive non-destructive elemental analysis technique that is based on the collection of energy dispersion of characteristics X-rays [47]. The x-rays are produced as a result of a collision between an electron of the incident beam and an electron in one of the inner shells of an atom and lead to an electron removal (or ionization) leaving an empty spot. To return the ionized atom to its ground state, an electron from a higher energy outer shell fills the vacant inner shell and, in the process, releases an amount of energy that is equal to the potential energy difference between the two shells and which is unique for every atomic transition. The X-ray spectrum consists of a series of peaks representative of the type and relative amount of each element in the sample. Some element, however, can present more than one peak, meaning that a single primary ionization has led to many emissions as a result of the atom many shells [47-51]. Contrary to other analytical techniques, EDS has the advantage of providing quantitative results in an absolute way. It can be applied to the characterization of very thin surface segregations (in low-voltage operation mode), or to the simultaneous determination of the composition of surface layers, buried layers or substrates [48, 52]. The EDS exam was performed on the prepared samples (previously coated with coated with an *Au/Pd* thin film) using a High resolution (Schottky) Environmental Scanning Electron Microscope (Quanta 400 FEG ESEM) with X-Ray Microanalysis (EDAX Genesis X4M) operating at 15 kV. A SUTW-Sapphire detector type with 132.58 resolution and life time of 60 secs (the real time that the instrument is available to for the measurements, *i.e.* without considering the dead time), was used.

iii) Contact angle measurement

The hydrophilicity of the ferrite samples was determined through the contact angle measurement technique. This powerful, but simple method to prone surface properties is based on establishing the tangent with the sessile drop profile at the point of contact with the solid

surface [53, 54]. Hence, the contact angle is defined as the angle between the substrate surface and the tangent line at the point of contact of the liquid droplet with the substrate [53]. The surface water contact angle was performed by using a Contact Angle System OCA (DataPhysics Instruments, Filderstadt, Germany) at room temperature. A drop of water was placed on the surface of the ferrite sample with a 500 μ syringe (Hamilton, Graubünden, Switzerland) at a dosing rate and volume of 4.00 μ l/s and 4.00 μ l. The contact angles were determined through image analysis using the SCA software (DataPhysics Instruments, Filderstadt, Germany). For each material the average from measurement based on four samples, was obtained. The contact angle measurements were conducted at the Science and Technology Park of University of Porto (translated as *Parque de Ciência e Tecnologia da Universidade do Porto* - UPTEC).

5.1.6. Statistical analysis

Surface characterizations were performed on two/three samples for each treatment group. For cell culture studies, each data presented is from a minimum of three individual cultures. The results were expressed as arithmetic means \pm standard deviation (\pm SD) for each group of samples. Analysis of the results were carried out using the t-test, with a significant level of $p < 0.05$.

5.2. Results

5.2.1. Zn Ferrite samples

i) Cell adhesion, viability and proliferation (MTT assay)

Figure 5.5 presents the MTT counts from days 1 and 3 after cell seeding on the irregularly shaped Zn ferrite samples.

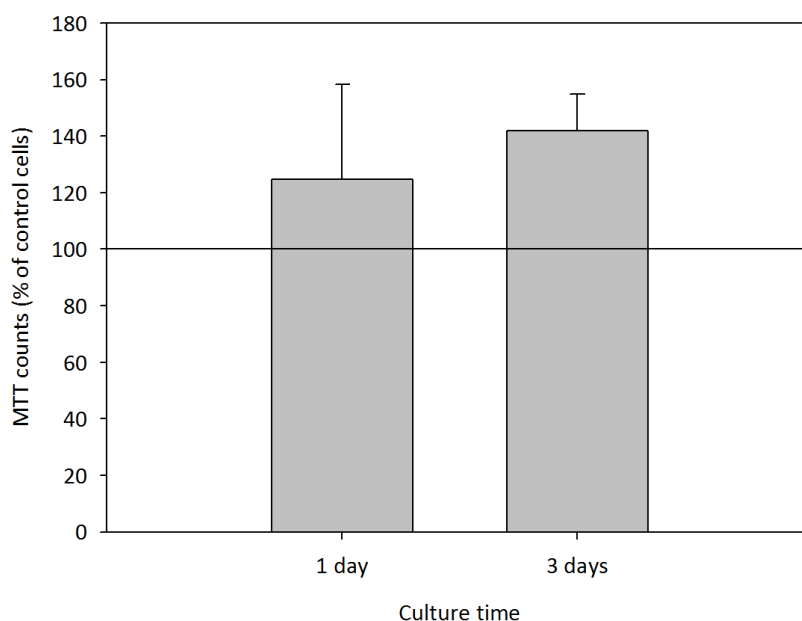


Figure 5.5 - MTT measurements of MG-63 cells cultured on Zn irregular ferrite samples after 1 and 3 days. The values are the mean \pm SD and expressed as percentage of positive controls (cell seeding density of 5×10^4 cell/ml)

As demonstrated in Figure 5.5, in the first day of culture, the number of cells on the Zn ferrite samples was already higher than that present in the control, where cells were not exposed to the ferrite material. However, values presented a high standard deviation. From day 1 to day 3 there was an increase of 17% in the number of cells in the ferrite surfaces in relation to the controls and a reduction of the standard deviation.

ii) Optical microscopy

Comparative optical microscopy images of the irregularly shaped Zn ferrite and negative control samples, after 72 hours from initial cell seeding, are presented in Figure 5.6. The ferrite materials present a poor optical transparency which limits the visualisation of the MG-63 cells at the samples surface. However, at the highest optical magnification (x2), dark purple patches could still be identified (see Figure 5.6(C)). This coloration resulted from the MTT reduction by viable cells. The Zn ferrite different surfaces, the fractured and non-fractured, are presented in Figure 5.6(A), on the left and right portion of the edge, respectively. Both surfaces are rough and irregular, still the fractured one appears to be slightly more uneven. Although, in the examples presented in Figure 5.6(A) and (C), cell adhesion and proliferation appears to be mostly limited to the non-fractured site; in the other tested samples (data not presented in this chapter), the cells surface preference is not so clear. Also there appears to be no evidence of surface oxidation during the material contact with the cell culture complete medium.

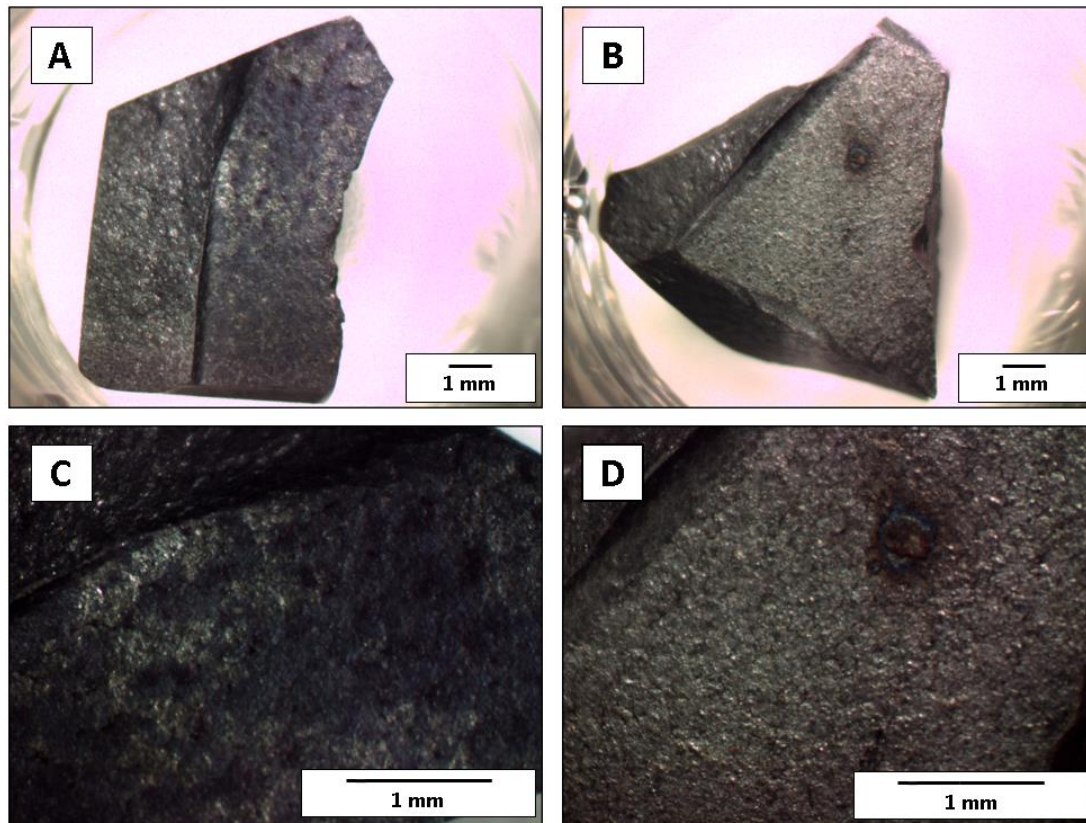


Figure 5.6 -Ferrite surface topographies after 3-day culture with MG-63 cells obtained from optical microscopy: (A and C) Cell adhesion and proliferation on ferrite samples and (B and D) Negative control samples which were not exposed to cells. Images magnification of 0.7X and 2X was used in the top and bottom images, respectively. Note the purple precipitates present on the seeded samples (A and C), compared to the non-seeded samples (B and D) (cell seeding density of 5×10^4 cell/ml)

iii) SEM

Figure 5.7 shows the SEM image of the Zn ferrite non-fractured portion surface.

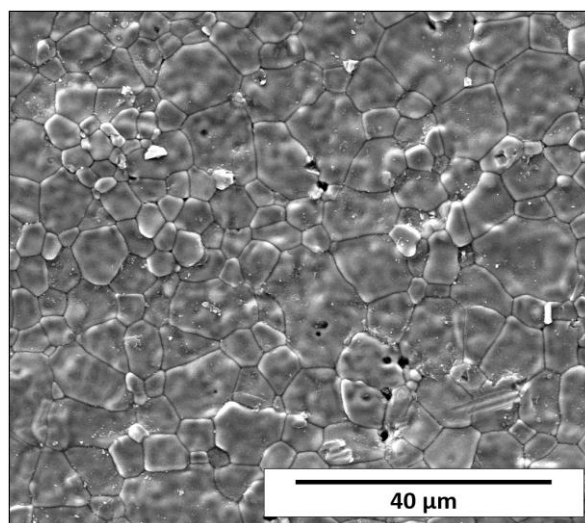


Figure 5.7 - SEM image of Zn ferrite non-fractured surface. Images were obtained from secondary electrons. Image magnification of 2500X

Figure 5.7 shows the heterogeneous grainy surface of the Zn ferrite surface.

iv) EDS

The X-ray spectrum of the *Zn* ferrite is present in Figure 5.8.

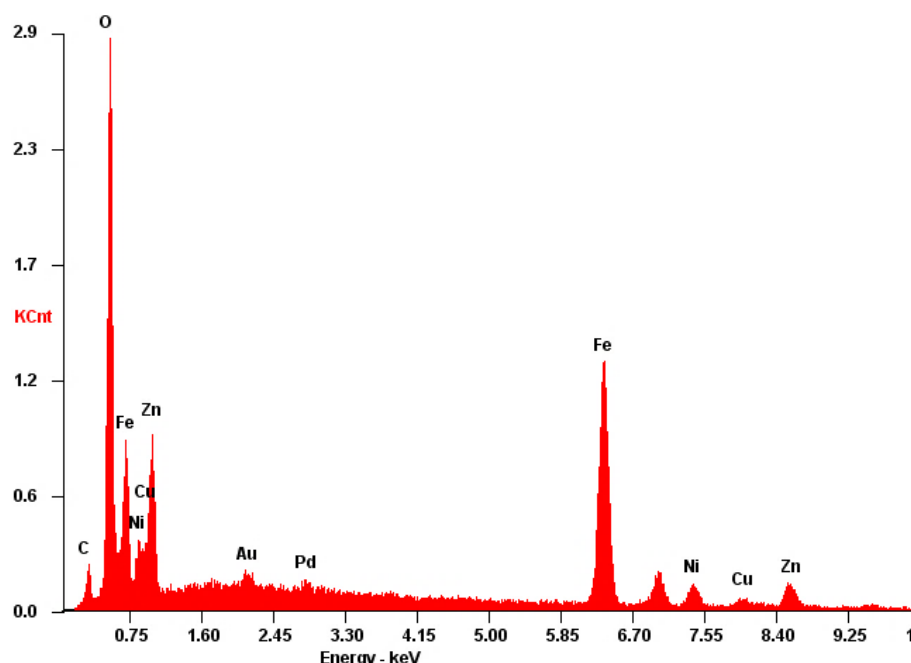


Figure 5.8 - X-ray spectrum of the *Zn* ferrite. The horizontal axis is the energy scale and the vertical axis is the number of photons per energy interval. The x-ray identification, element, is indicated in the vicinity of the peaks

In Figure 5.8 it is possible to visualize the *O*, *Fe*, *Zn*, *Ni* and *Cu* peaks. The *Au* and *Pd* peaks from the ferrite sample coating with an *Au/Pd* thin film, can also be identified. By not considering the presence of the *Au* and *Pd*, the elements proportions in the measured location was 22.90 wt% *O*, 49.42 wt% *Fe*, 16.55 wt% *Zn*, 7.35 wt% *Ni* and 3.78 wt% *Cu*.

v) Contact angle measurement

Figure 5.9 shows the average measurement of static contact angle of a water droplet on the non-fracture surface of *Zn* ferrite.

The average contact angle for the *Zn* ferrite surface was $86.1^\circ \pm 13.42$. Although, the average value obtained is an indication of a hydrophilic behaviour the standard deviation also points out for the fact that the surface is heterogeneous in terms of its hydrophilicity.

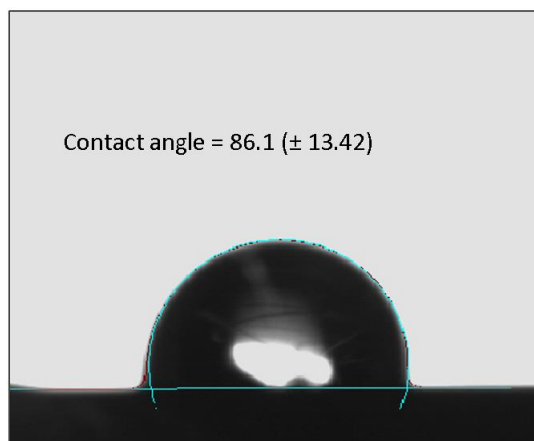


Figure 5.9 - Average measurement of static contact angle on Zn ferrite surface. The image represents a 103.5° contact angle

vi) Hen's egg test - Chorioallantoic membrane (HET-CAM) assay

Table 5.1 presents the results obtained on the HET-CAM irritation assay

Table 5.1 - Scoring scheme for irritation testing with hen's egg chorioallantoic membrane

| Effect | Time (min) | Score | | |
|----------------|------------|-------|---|---|
| | | 0.5 | 2 | 5 |
| Hemorrhage | | 0 | 0 | 0 |
| Coagulation | | 0 | 0 | 0 |
| Vascular lysis | | 0 | 0 | 0 |

Table 5.1 demonstrates that there was no evidence of hemorrhage, coagulation or vascular lysis on the CAM where the ferrite material samples were placed throughout the 5 minutes' evaluation time.

vii) Chorioallantoic membrane (CAM) angiogenesis assay

The influence of the Zn ferrite on the angiogenesis process was evaluated through the CAM assay. A comparative evaluation of the effect of material presence on the formation of blood vessels is present in Figure 5.10.

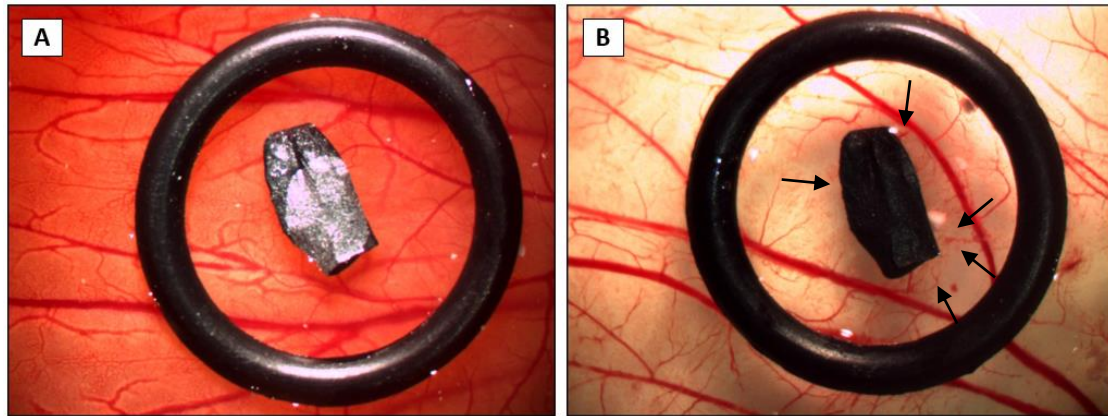


Figure 5.10 - Photographs of CAM (A) through in ovo analysis immediately after ferrite sample deposition and (B) after 11 days of incubation through ex ovo analysis. The arrow indicates the presence of new blood vessels sprouting towards the ferrite sample

By comparing Figure 5.10(B) with (A) it is possible to notice that after 3 days of CAM exposure to the ferrite material, there were a few new formed convergence capillary vessels around the ferrite sample. For a more quantitative evaluation of the effect of the ferrite material on the angiogenesis process, Figure 5.11 presents the total and convergence average number of blood vessels at the day of the material implantation and after 3 days of material exposure.

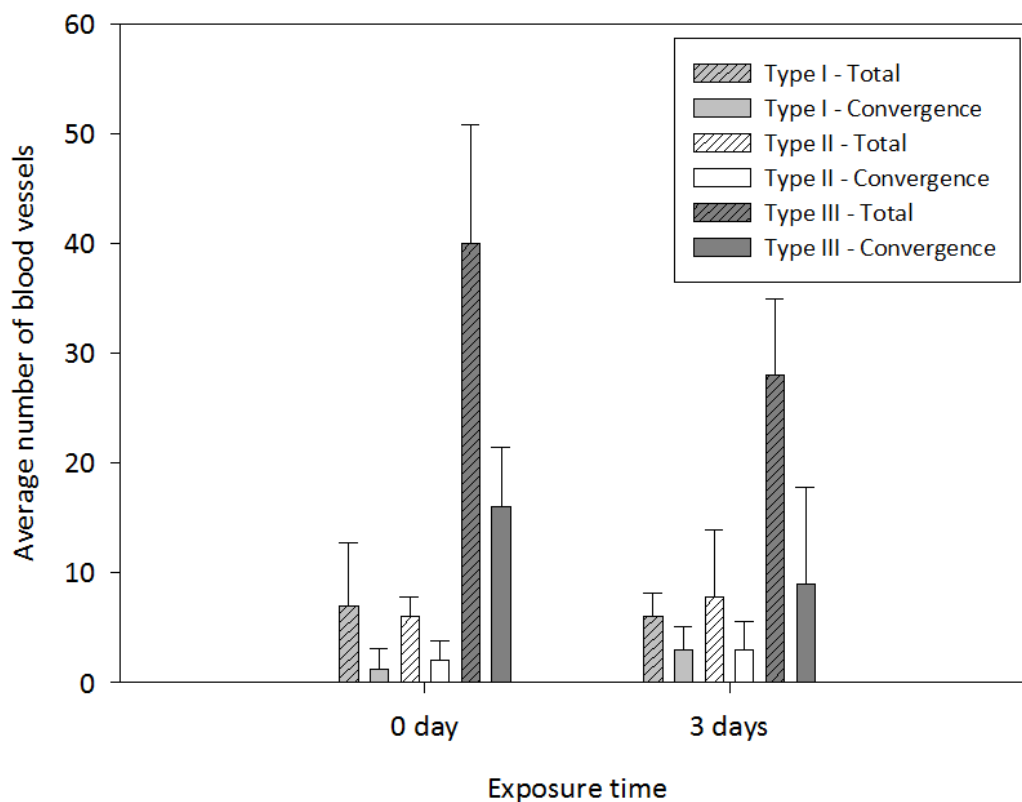


Figure 5.11 - Average number of CAM total blood vessels of type I (grey with diagonal stripes), II (diagonal stripes) and III (dark grey with diagonal stripes) and convergence blood vessels of type I (grey), II (white) and III (dark grey) on CAM images at day 0 and 3 from Zn ferrite sample deposition

As demonstrated in Figure 5.11, with the exception of type III capillaries, the average number of all blood vessels - total and convergence – increased after 72 hours' exposure to the ferrite samples. This is more prominent among the convergence type I blood vessels which registered a 2-fold increase in the average number after day 3 from material deposition. The total number of CAM type III blood vessels, reduced to half its amount at day 3. The number of type III convergence blood vessels also demonstrated a similar behaviour. In general, the number of blood vessels is associated with a high standard deviation. Figure 5.12 shows the blood vessels average diameter per type at the day of the ferrite sample implantation and after 3 days of exposure.

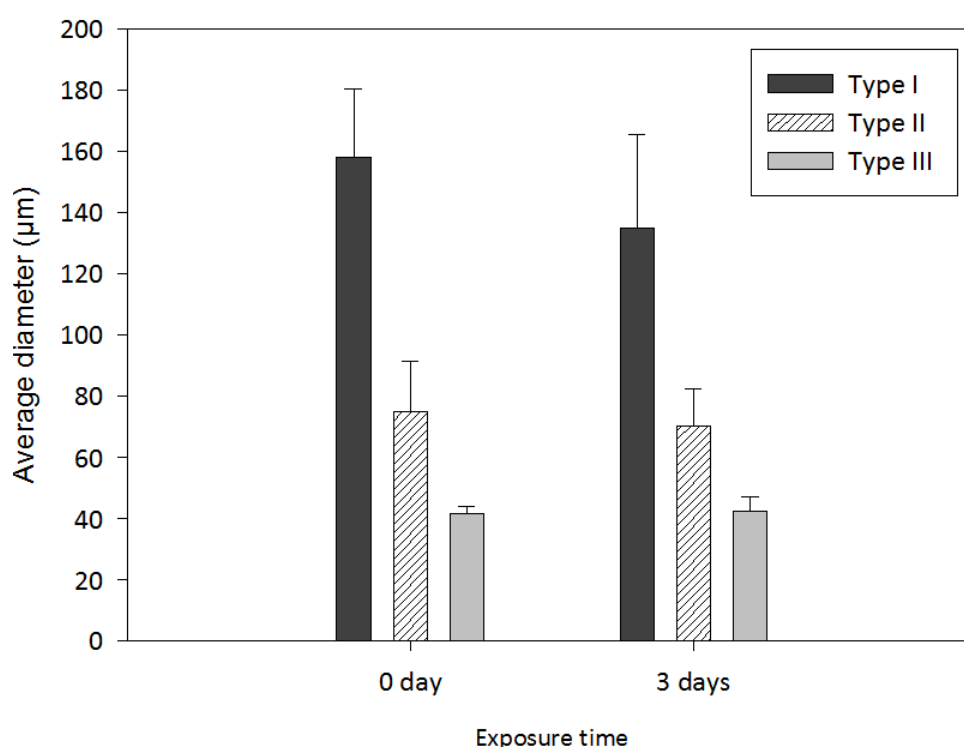


Figure 5.12 - Average blood vessels diameter of type I (dark grey), II (diagonal stripes) and III (grey) calculated from CAM images recorded at 0 and 72 hours after Zn ferrite sample deposition

From Figure 5.12 it is possible to verify that a 72 hours exposure to the ferrite materials did not significantly alter the convergence blood vessels average diameter in each capillaries type.

5.2.2. Zn Ferrite vs. Sr-Ca Ferrite

i) Cell adhesion, viability and proliferation (MTT assay)

Figure 5.13 displays the MTT counts measured on Zn and Sr-Ca ferrite samples for days 1 and 3 after cell seeding. At day 1, although still high, there were less cells attached to the Sr-Ca ferrite surfaces, 69.2%, than the amount found in the Zn ferrite samples, 124.9%.

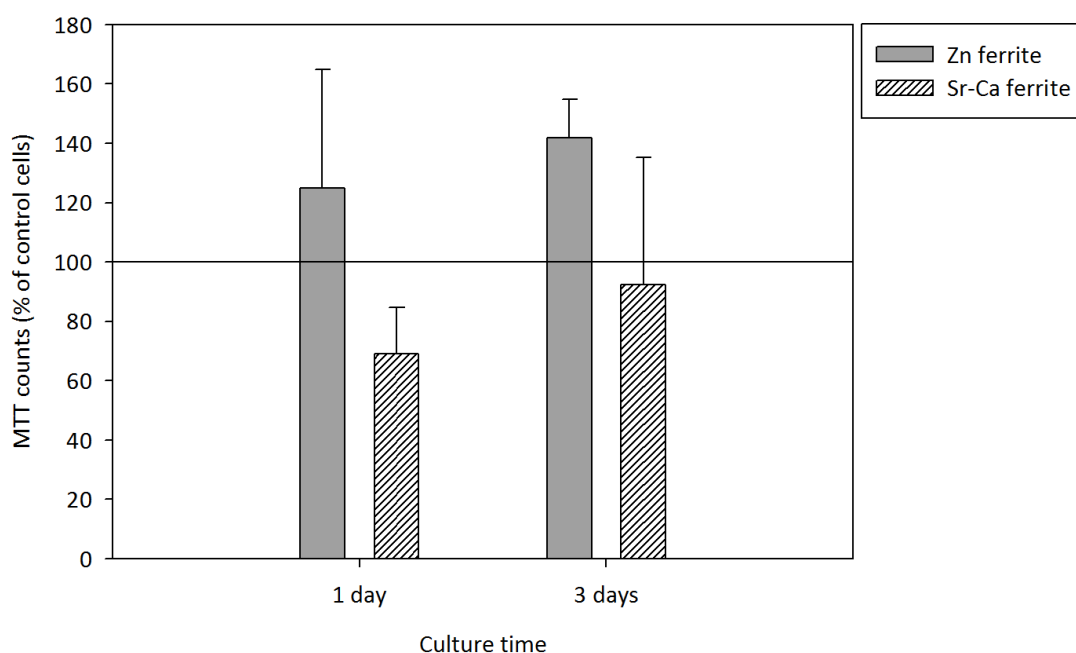


Figure 5.13 - MTT counts on MG-63 cells cultured on Zn (in grey) and Sr-Ca (diagonal stripes) ferrite samples, 1 and 3 days. The MTT counts are presented as the mean \pm standard deviation and expressed as percentage of positive controls (cell seeding density of 5×10^4 cell/ml)

5.2.3. Sr-Ca Ferrite discs

i) Cell adhesion, viability and proliferation (Resazurin assay)

Figure 5.14 presents the results on the resazurin measurement after 1, 3, 7 and 11 days in culture, regarding the cells attached to magnetic and demagnetized Sr-Ca ferrite samples. All samples used in this experiment were of Sr-Ca ferrite with the same rough surface (see Figure 5.2(B)) and subjected to medical autoclave sterilization followed by soft mechanical cleaning with 70% ethyl alcohol. Hence, no additional treatment besides the demagnetization process was adopted which could alter the surface composition and/or topography.

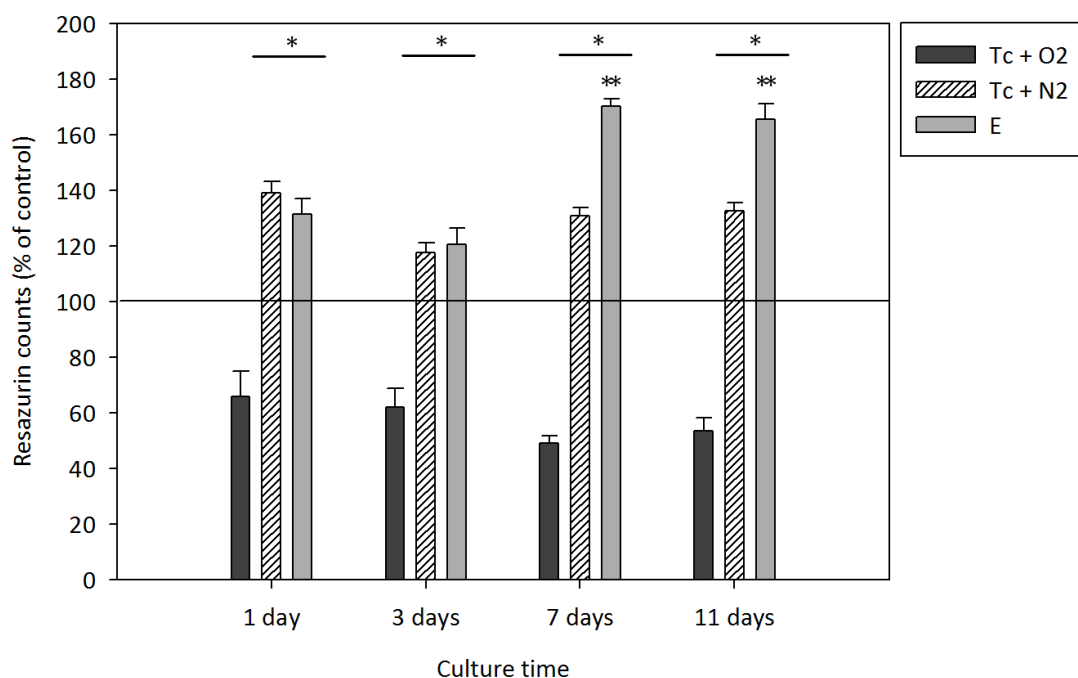


Figure 5.14 - Resazurin measurements at 1, 3, 7 and 11 days of MG-63 cells cultured on Sr-Ca ferrite at a demagnetized state through different methods: Curie temperature under an oxygen environment (dark grey - $T_c + O_2$), Curie temperature under nitrogen environment (diagonal stripes - $T_c + N_2$) and strong external magnetic field with opposite polarity (light grey - E). The resazurin counts are presented as the mean \pm standard deviation and expressed as percentage of control (cell seeding density of 2×10^4 MG-63 cell/ml). The results obtained from resazurin measurements on permanent magnetic samples were used as control. (* - Significantly different from control; ** - Significantly different from $T_c + N_2$)

In Figure 5.14, it is possible to verify the low affinity demonstrated by the MG-63 cells to the ferrite surface of the samples demagnetized through the Curie temperature under oxygen atmosphere when compared to the control magnetic samples. There was also no improvement on cell proliferation behavior in relation to the control with the increase of the incubation time. At day 1, the samples demagnetized with Curie temperature and under an nitrogen atmosphere and demagnetized through the application of a strong external magnetic field of opposite polarity showed an increase in the amount of cells attached to the Sr-Ca ferrite surfaces when compared to magnetic control samples. Differences of around 40 and 30%, respectively, were registered. Over the incubation time, the cells on the surfaces demagnetized with the Curie temperature and under a nitrogen atmosphere, showed a proliferation rate considerably similar to the amount registered in the control. However, at day 7 and 11 there was an almost 2-fold increase in the MG-63 attached to the external magnetic field demagnetized ferrite surfaces as a result of cell proliferation, in comparison to that measured on the permanent magnetic control surfaces. From all the samples tested and according to the results present in Figure 5.14, MG-63 cells show a preference to proliferate on Sr-Ca ferrite surfaces which demagnetization was achieved through the application of a strong external magnetic field of opposite polarity.

The results in Figure 5.15 depict the resazurin counts after 1, 3, 7 and 11 days in culture of MG-63 cells attached to Sr-Ca ferrite and where the influence of chemical contaminants removal through abrasive mechanical cleaning, was considered. All the samples tested in this experiment were demagnetized through Curie temperature and under a nitrogen atmosphere.

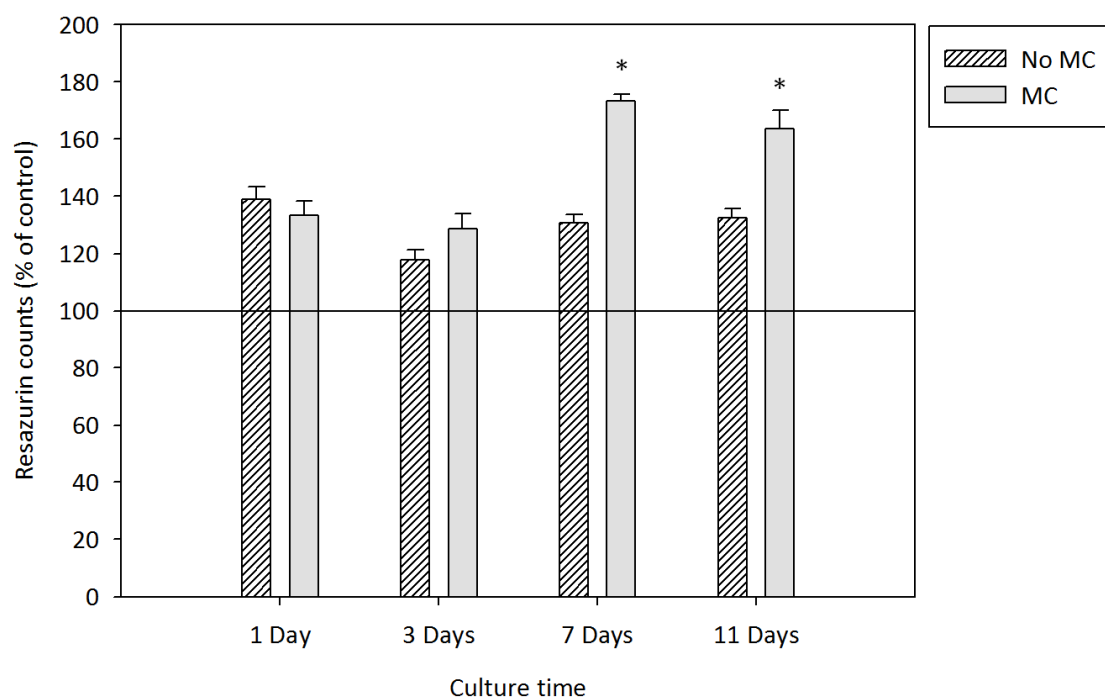


Figure 5.15 - Resazurin counts at 1, 3, 7 and 11 days of MG-63 cells cultured on Curie temperature and under nitrogen environment demagnetized Sr-Ca ferrite samples with additional mechanical cleaning (denoted as "MC") and without the mechanical cleaning (denoted as "No MC"). The resazurin counts are presented as the mean \pm standard deviation and expressed as percentage of controls (cell seeding density of 2×10^4 MG-63 cell/ml). The results obtained from resazurin measurements on permanent magnetic samples were used as control. (* - Significantly different from "No MC")

From Figure 5.15, it is possible to see, that there was no significant difference on the amount of cells adhesion between the surface non-subjected and the one subjected to the abrasive mechanical cleaning. However, on the 7th and the 11th day of incubation, an approximately 40 and 30% increase, respectively, in cell proliferation was registered on the abrasive mechanically cleaned surfaces when compared to the surfaces not subjected to this rough cleaning. The hard mechanical cleaning of the Sr-Ca ferrite surface appears to increase the MG-63 cells preference for Curie temperature and under a nitrogen atmosphere demagnetized ferrite surface.

ii) EDS

The X-ray spectrum of the Sr-Ca ferrite is present in Figure 5.16.

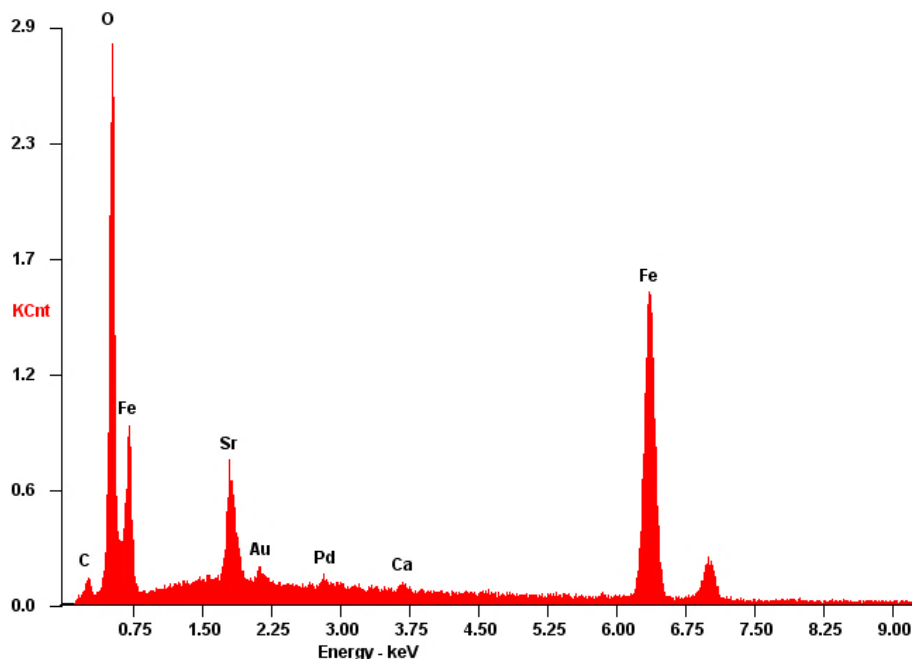


Figure 5.16 -X-ray spectrum of the Sr-Ca ferrite. The horizontal axis is the energy scale and the vertical axis is the number of photons per energy interval. The x-ray identification, element, is indicated in the vicinity of the peaks

In Figure 5.16 it is possible to visualize the *O*, *Fe*, *Sr* and *Ca* peaks. The *Au* and *Pd* peaks from the ferrite sample coating with a *Au/Pd* thin film, can also be identified. The spectrum also showed the existence of *C* on the samples which was associated with the presence of cells. By not considering the presence of the *C*, *Au* and *Pd*, the elements proportions in the measured location was 23.46 wt% *O*, 67.62 wt% *Fe*, 8.49 wt% *Sr* and 0.42 wt% *Ca*. All the Sr-Ca ferrite surfaces, demagnetized and the ones subjected to the hard mechanical cleaning, and with the exception of the permanent magnetic samples, were analyzed through EDS and similar X-ray spectra were obtained.

iii) Contact angle measurement

Figure 5.17 shows the average measurement of static contact angle of a water droplet on the surface of Sr-Ca ferrite samples. The average contact angle for the Sr-Ca ferrite surface was $79.5^\circ \pm 7.39$ which is an indication of a hydrophilic behaviour.

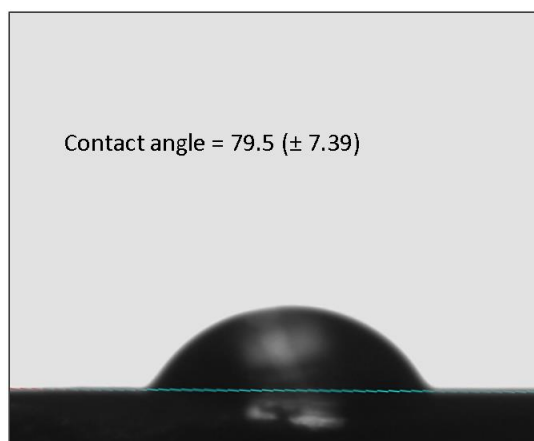


Figure 5.17 - Average measurement of static contact angle on Sr-Ca ferrite surface. The image is a representation of a 68.4° contact angle

iv) SEM

Figure 5.18 shows the SEM images of the MG-63 cells morphology when cultured for 1 day on Sr-Ca ferrite surfaces which were demagnetized under different conditions, namely, under a strong external magnetic field of opposite polarity and with a Curie temperature under an oxygen atmosphere. It was not possible to analyse the Sr-Ca ferrite in the magnetized state. There was also no demagnetized sample in the demagnetized state through Curie temperature under a nitrogen atmosphere, available from SEM analysis.

From Figure 5.18 it is possible to see that the MG-63 cells present a flatten and well spread morphology in both surfaces. However, in the Figure 5.18(C)(D) the cells cytoplasmic extensions are more prominent. Although, data on SEM images from lower magnifications were not presented in this chapter, on the demagnetized Sr-Ca ferrite through a strong external magnetic field of opposite polarity it was possible to verify that the disc surface was covered with regularly shaped cells. In the case of the demagnetized Sr-Ca ferrite through Curie temperature and under an oxygen atmosphere, the cells were unevenly scattered on the surface and clusters were even identified. Figure 5.18 SEM images, also allowed to confirm both Sr-Ca ferrite samples similar morphological surfaces which are marked by a rough and irregular appearance and contain several indentations, craters debris found over the entire surface

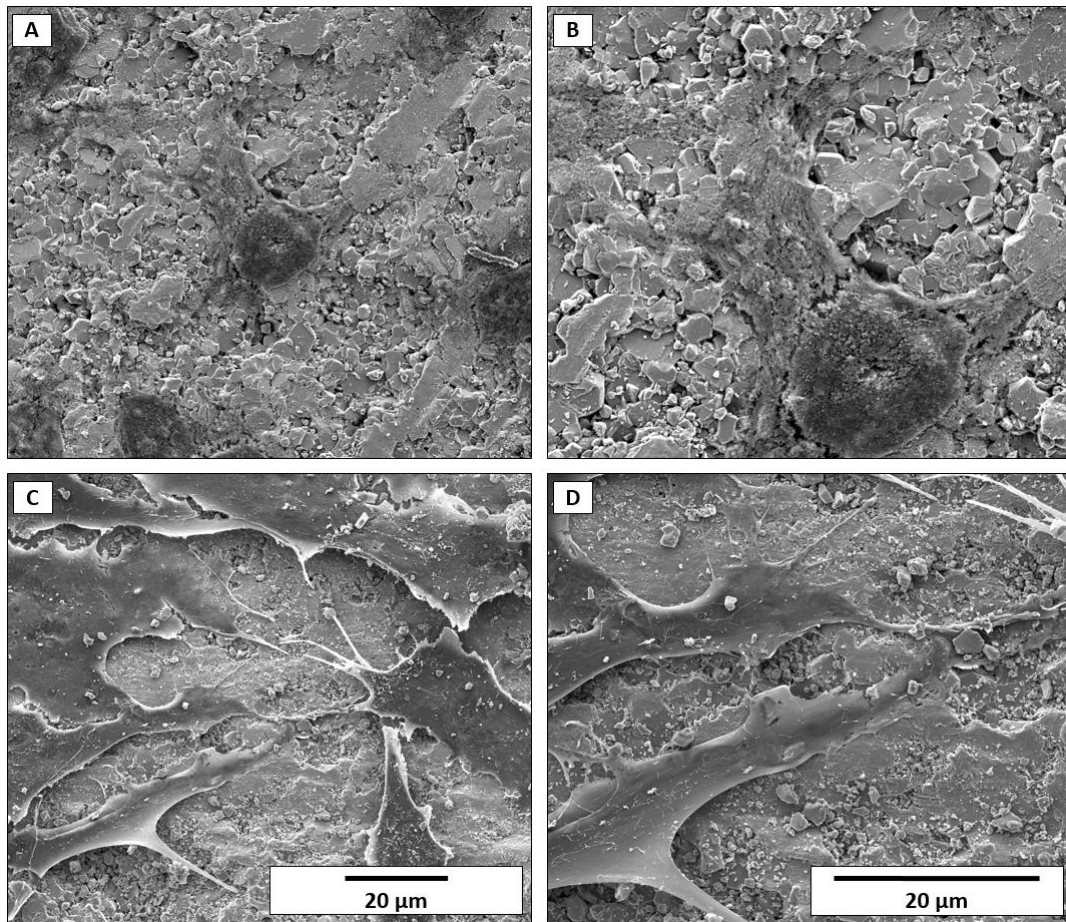


Figure 5.18 - SEM photographs from 1 day incubation of MG-63 cells cultured on Sr-Ca ferrite demagnetized surface through (A,B) strong external magnetic field of opposite polarity and (C,D) Curie temperature and under an oxygen atmosphere. Images were obtained from secondary electrons. Two magnifications are shown: 2500X (A,C) and 5000X (B,D)

SEM analysis was also used to evaluate MG-63 cells morphology after 1-day culture on hard mechanically cleaned Sr-Ca ferrite surfaces at a demagnetized state from its exposure to the Curie temperature under a nitrogen atmosphere (see Figure 5.19). The images in Figure 5.19, showed that the MG-63 cells also presented a flattened morphology on the surface altered by sandpaper abrasion. From Figure 5.19, the hard mechanically cleaned Sr-Ca ferrite surfaces appears to maintain its irregular grainy texture, however, it appears to be less irregular and more smoother. The microscope view selected was not very revealing on the ferrite surface morphology alteration as a consequence of the hard mechanical cleaning procedure. For more insight on this subject, a topographic analysis will be developed in the next section.

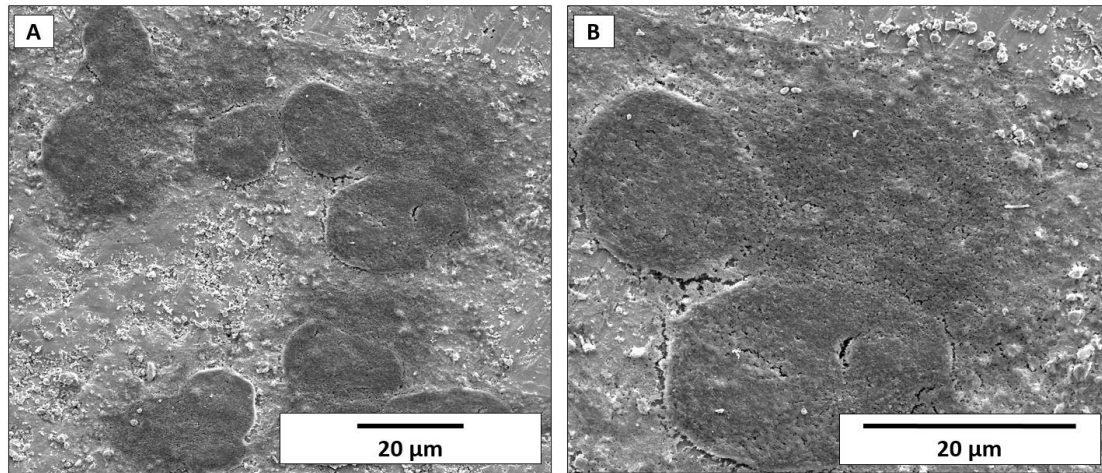


Figure 5.19 - SEM photographs from 1 day incubation of MG-63 cells cultured on Sr-Ca ferrite demagnetized surface through Curie temperature and under a nitrogen atmosphere and subjected to abrasive mechanical cleaning. Images were obtained from secondary electrons. Two magnifications are showed: 2500X (A) and 5000X (B)

v) White light interferometry

Surface interferometry analysis on the magnetic and demagnetized Sr-Ca ferrite samples, through the three dimensional topographic images of the samples surface and the calculation of the surface topography parameters, are presented in Figure 5.20 and Table 5.2, respectively.

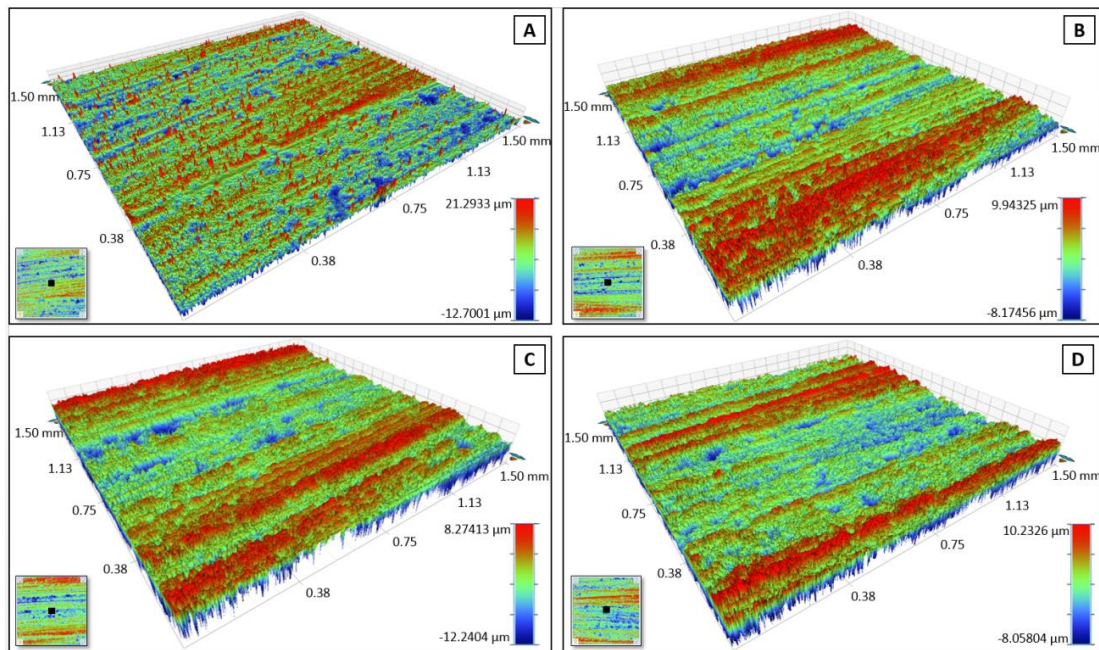


Figure 5.20 -Profilometry 3D images of the Sr-Ca ferrite surfaces as determined from microscope-based white light interferometry and where the influence of the de-magnetization process and the absence of it, was evaluated: (A) magnetic, (B) de-magnetized through the application of a strong electric field, (C) de-magnetized with Curie temperature in an oxygen atmosphere, and (D) ferrite de-magnetized with Curie temperature in a nitrogen atmosphere. Images magnification of 0.25X was used for (A) and 0.5X was used for (B), (C) and (D) samples

Table 5.2 - Surface roughness parameters measured in two directions (x and y) of the rougher magnetic and demagnetized ferrite samples through different methods (strong electric field (E), Curie temperature in an oxygen atmosphere ($T_c + O_2$) and Curie temperature in a nitrogen atmosphere ($T_c + N_2$)). Data is shown as arithmetic means \pm standard deviation ($\pm SD$) and expressed in μm . R_a : average surface roughness, R_q : root mean square roughness, R_z : mean peak-to-valley roughness

| Ferrite condition | Measured direction | Average \pm SD (μm) | | | |
|-------------------|--------------------|------------------------------------|-----------------|-----------------|-----------------|
| | | R_a | R_q | R_z | |
| Magnetic | x | 0.90 ± 0.11 | 1.27 ± 0.22 | 7.98 ± 1.80 | |
| | y | 1.15 ± 0.10 | 1.52 ± 0.17 | 9.02 ± 1.57 | |
| De-magnetized | E | x | 0.63 ± 0.06 | 0.81 ± 0.07 | 4.36 ± 0.40 |
| | | y | 0.86 ± 0.04 | 1.08 ± 0.05 | 5.34 ± 0.25 |
| | $T_c + O_2$ | x | 0.63 ± 0.03 | 0.80 ± 0.04 | 4.18 ± 0.12 |
| | | y | 0.88 ± 0.06 | 1.06 ± 0.11 | 5.14 ± 0.39 |
| | $T_c + N_2$ | x | 0.58 ± 0.04 | 0.74 ± 0.03 | 4.02 ± 0.14 |
| | | y | 0.85 ± 0.03 | 1.05 ± 0.01 | 5.31 ± 0.26 |

Both magnetized and demagnetized Sr-Ca ferrite discs were not subjected to any treatment which could alter the surface topography (e.g. hard mechanical cleaning), hence the results obtained can be considered as representative of the material original surface. From Figure 5.20, it was possible to verify that all samples present a surface with a striation pattern. With the exception of the magnetic sample (Figure 5.20(A)) which displays a larger scale range, all the samples present a similar maximum valley deepness and peak highs. This can be confirmed by comparing the results obtained in Figure 5.20 with Table 5.2 the surface roughness values. Again, the R_a , R_q and R_z values, were similar between the demagnetized materials and only slight variations were registered. However, when compared to the magnetic samples, higher surface roughness values were registered. Table 5.2 also allows to verify that, in all samples - magnetic and demagnetized, there is a clear difference between the surface roughness parameters values when measured perpendicular and parallel to the lay (meaning the direction of the pattern).

The surface interferometry analysis of the influence of sandpaper abrasive mechanical cleaning on the demagnetized Sr-Ca ferrite samples surface topography was achieved through the calculation of the surface topography parameters and the analysis of the three-dimensional topographic images of the samples surfaces. These results are presented in Table 5.3 and Figure 5.21, respectively. All the samples used in this particular experiment were in the demagnetized stated in which demagnetization was achieved through the material exposure to the Curie temperature and under a nitrogen atmosphere.

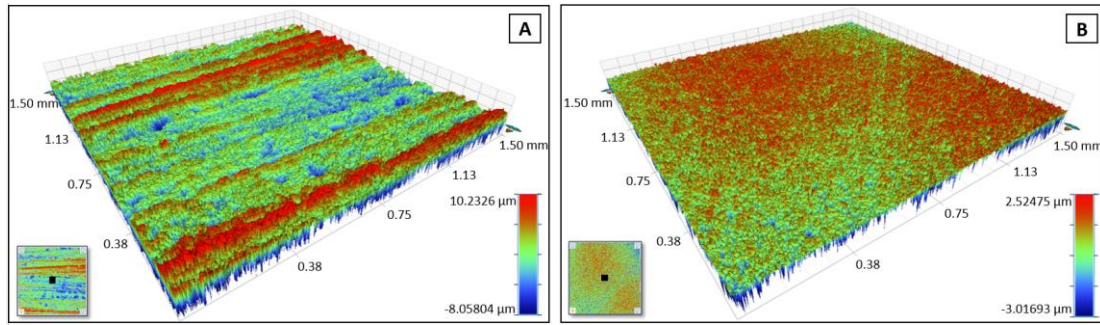


Figure 5.21 - Surface topographies of the Sr-Ca ferrite surfaces as determined from microscope-based white light interferometry and where the influence of the abrasion mechanical cleaning was evaluated: (A) demagnetized Sr-Ca ferrite through Curie temperature in a nitrogen atmosphere and not subjected to hard mechanically cleaned surface and (B) the same material however subjected to abrasive mechanical cleaning. Images magnification of 0.5X was used

Table 5.3 - Surface roughness parameters measured in two directions (x and y) of the demagnetized Sr-Ca ferrite through Curie temperature in a nitrogen atmosphere ($T_c + N_2$) and the ferrite material in the same conditions however subjected to additional mechanical cleaning (+ MC) surface treatment. Data is shown as arithmetic means \pm standard deviation (\pm SD) and expressed in μm . R_a : average surface roughness, R_q : root mean square roughness, R_z : mean peak-to-valley roughness

| Ferrite condition | Direction | Average \pm SD (μm) | | |
|-------------------------|-----------|------------------------------------|-----------------|-----------------|
| | | R_a | R_q | R_z |
| $T_c + N_2$ | x | 0.58 ± 0.04 | 0.74 ± 0.03 | 4.02 ± 0.14 |
| | y | 0.85 ± 0.03 | 1.05 ± 0.01 | 5.31 ± 0.26 |
| $T_c + N_2 + \text{MC}$ | x | 0.25 ± 0.06 | 0.34 ± 0.10 | 2.41 ± 0.77 |
| | y | 0.25 ± 0.05 | 0.34 ± 0.08 | 2.35 ± 0.59 |

A general analysis of the three dimensional topographic images presented in Figure 5.21(B), allows to identify that, oppositely to the samples evaluated in Figure 5.20(A), there appears to be no distinct characteristic pattern among these ones. This phenomenon was confirmed by the, low or no variation, in the surface roughness parameters values when measured in perpendicular directions (x and y) for the demagnetized through Curie temperature in a nitrogen atmosphere ferrite samples surface after mechanical cleaning was applied (see Table 5.3). By comparing Figure 5.21(A) and (B), it is possible to notice that the maximum peak heights and the valleys deepness were both reduced after the ferrite surfaces were subjected to the abrasive mechanical cleaning. The data presented in Table 5.3, and which more generally characterize the samples surface topographic behavior, corroborate these findings. According to the information in Table 5.3, after mechanical cleaning is applied to these samples, not only did R_a and R_q decreased from 0.85 to 0.25 μm and from 1.05 to 0.34 μm , respectively, but the average R_z value also decreased from 5.31 to 2.35 μm . Both results indicate a reduction in the surface roughness.

5.3. Discussion

The clinical application of a ferrite actuator requires that these materials are non-toxic and biocompatible. In this context, the cytocompatibility of two bulk ferromagnetic materials, *Zn* and Sr-Ca ferrite, were evaluated on MG-63 osteoblastic-like cell line.

The study started with the analysis of the most available material, *Zn* ferrite. Considering the inaccurate insights on the tested material surface chemical composition, an EDS analysis was performed. From the X-ray spectrum it was possible to identify, besides the expected zinc metal (*Zn*) compound, the presence of nickel (*Ni*) and copper (*Cu*). Considering the elements percentage by weight proportions, the material tested in this chapter is most probably a $Ni_{0.27}Cu_{0.14}Zn_{0.6}$ ferrite compound. According to Huq *et al.* [55], this is a well-known established ferrite chemical composition which is used in various electromagnetic devices due to their high resistivity, high permeability and comparatively low magnetic losses. From the MTT assay measurements of MG-63 cells cultured (cell seeding density of 5×10^4 cell/ml) on this material surface, at day 1, there was already a 25% more cells attached to the material surface when compared to the control (which presents the ideal surface for osteoblastic cells). After 3 days incubation, a 17% increase on cell proliferation, led to 42% more cells in relation to the control. In a study developed by Kim *et al.* [7], the MTT measurements of mouse fibroblast L929 cells viability in response to $Ni_{0.65}Cu_{0.1}Zn_{0.35}Fe_{1.9}O_4$ ferrite particles, were evaluated to infer on this material cytotoxicity for hyperthermia application. After 3 days exposure to the material, the cells viability reached between 75 and 80% in relation to the positive control. From the agar overlay method results the authors considered material tested to be mildly cytotoxic. The MTT assay percentage difference obtained between the studies could be due to the 2-fold higher content of the toxic element *Ni* in the ferrite compound tested by Kim and his co-workers. Those authors also considered that, despite the presence of toxic element in the ferrite composition, a percentage viability above 85% would be an indication of the material ability to be used for clinical application. Irrespectively of the authors' prediction, data based solely on the good MTT results obtained with $Ni_{0.27}Cu_{0.14}Zn_{0.6}$ during the 3 day study period, were not enough to confirm the material's cytocompatibility. However, these results allowed to determine that this ferrite material surface is favourable to cell adhesion and proliferation. There could be other factors influencing these good results. It was not possible to determine if the surface morphology contributed to the cell high affinity for this material, since it was not clear if the cell adhesion and proliferation was limited to the ferrite samples fractured or non-fracture area. From optical microscopy analysis and more conclusively through SEM analysis it was possible to determine that the ferrite material tested presented a heterogeneous and grainy surface. Also,

from the optical microscopy images it was possible to conclude that neither the autoclave sterilization method, nor the material contact for 3 days with cell culture complete medium led to surface alteration (*e.g.* surface oxidation) which could jeopardize cell adhesion and proliferation.

In order to evaluate the $Ni_{0.27}Cu_{0.14}Zn_{0.6}$ ferrite in terms of angiogenic activity, a CAM assay was performed. Through this experiment, after 72 hours CAM exposure to ferrite samples there was a significantly increase in the number of convergence blood vessels. A general blood vessels growth was also verified in the CAM area inside the reference ring. This behaviour was more evident among the type I convergence blood vessels which registered a 2-fold increase over the study period. This increase was also confirmed by the non-variation of the blood vessels average diameter for type, considered. Although, the CAM assay is perceived as an accurate method, its technique has the tendency to be overly sensitive and the results analysis is not always straightforward [29]. There are two limitations to this assay which may lead to false positive assumption on the convergence blood vessels growth. First, since the test materials were placed on already formed blood vessels an increased vascular density can be generated due to the rearrangement of existing vessels that follows contraction of the membrane. Also the presence of a foreign material onto CAM may develop a non-specific inflammatory reaction which can also lead to a misled conclusion [37]. It is important to highlight that the probability of developing a non-specific inflammatory reaction in the CAM is time-dependent. The lymphoid cells driven from the yolk and spleen are usually only detectable in the thymus on day 8 and in the Fabricius bursa on day 11, hence the host's immune system is relatively immature during CAM early development stages [31]. Considering that although vascular growth at the ferrite material site was registered, its increase rate was low and no dense blood vessels network was developed. Also, the blood vessels arrangement around the ferrite material appear to be distinctive of neoangiogenesis - sprouting vessels with branches and sub branches growing from larger existing ones and converging towards the ferrite sample, *i.e.* in a radial "spoke-wheel" arrangement of blood vessels [34]. Hence, it is believed that the capillaries formation was neither a result of tissue rearrangement nor non-specific inflammatory reaction. The existence of convergence blood vessels towards the ferrite material suggests that this material does not have an antiangiogenic effect. However, it also does not appear to enhance the angiogenesis process. Hence, it is possible to claim the $Ni_{0.27}Cu_{0.14}Zn_{0.6}$ ferrite showed a neutral effect on the angiogenesis process, behaving as an inert material. This behaviour also allows to speculate that when implanted in the human organism it will most likely not interfere with the physiological angiogenesis process at the fracture site. Corroborating with this behaviour were

the results obtained in the HET-CAM assay. This assay allowed concluding that the ferrite material does not present any irritancy properties since there was no evidence of haemorrhage, coagulation or vascular lysis during the study evaluation time.

The cytocompatibility study developed on the $Ni_{0.27}Cu_{0.14}Zn_{0.6}$ ferrite samples demonstrated promising results and consequently high expectations were created towards the potential biocompatibility of this material. However, in order to ensure assays reproducibility, reliability and credibility, some experimentation standards had to be respected (*e.g.* test material plane surface, uniformity size and dimensions to fit the 48-well culture plates). These requirements limited the material availability and led to the introduction of a ferrite material with a different composition, Sr-Ca ferrite. This also obligated to the development of a new cytocompatibility study for this new material.

Similar to the approach adopted for the $Ni_{0.27}Cu_{0.14}Zn_{0.6}$ study, in the hydrophilic surface Sr-Ca ferrite material, chemical composition was also confirmed through an EDS analysis. The X-ray spectrum allowed identification of the presence of strontium (*Sr*) and small portion of calcium (*Ca*) on the ferrite composition. In a first approach, in order to understand where the introduced material stands in relation to cell viability when compared to the previous one, the MTT assay results for the $Ni_{0.27}Cu_{0.14}Zn_{0.6}$ ferrite samples were compared to the ones obtained for the Sr-Ca ferrite material. At the first day of incubation, there were 38.8% less MG-63 cells attached to Sr-Ca ferrite surface than the amount registered in the positive control. After 3 days in favourable cell proliferation environmental conditions, there was an increase in 23% of the number of viable cells. The average reached around 93% when compared with the optimum positive control wells. Although this result was associated with a high standard deviation, the mean value was similar to the ones obtained in the studies performed by Lee *et al.* [56] and Kim *et al.* [7]. In both studies, Sr-ferrite particles showed more than 80% viability in response to mouse-fibroblastic L929 cells. According to ISO 10993-5:2009 [57] standards, if the viability is reduced below 70% of the blank, the material has cytotoxic potential. It is not possible to infer on the Sr-Ca ferrite samples cytocompatibility based on the results obtained from the MTT assay. However, the discrepancy registered when compared with the ones obtained with the $Ni_{0.27}Cu_{0.14}Zn_{0.6}$ ferrites samples, obligated further research for better understanding of the lower MG-63 cells affinity for this surface.

One of the factors which greatly determines the cytocompatibility and biocompatibility of ferrite materials are the magnetically responsive components [56], which in the case of the latter introduced material, are iron, strontium and calcium. As demonstrated in several studies [7, 58],

when compared to other ferrites, Fe_3O_4 has shown to allow high cell viability levels and is generally considered a biocompatible magnetic material. In relation to strontium, its similarities with calcium normally cause its deposition in bone [59]. This component is even used as therapeutic agent in bone disorders (*e.g.* osteoporosis), where it is claimed to increase osteoblastic activity [60]. In an experiment developed by Kirrane *et al.* [61] the intentional ingestion of strontium ferrite magnets resulted in very high urine strontium levels and no acute clinical toxicity. Also, large increments of serum strontium are considered to be possible without deleterious actions on organs or functions [59]. Based on this information, it is possible to claim that most probably none of the Sr-Ca ferrite constituents are responsible for causing cytotoxicity. Another factor which may influencing the MTT cells viability results obtained with this material and which also distinguishes it from the previously tested $Ni_{0.27}Cu_{0.14}Zn_{0.6}$ ferrites, is that these ferrites have a net magnetization which makes them a permanent magnet, *i.e.* they create a constant magnetic field. According to manufacturer's data, the Sr-Ca ferrite magnets residual induction (the magnetic flux that remains permanent in a magnet) is between 0.38-0.4 T. To study the influence of this variable on cell adhesion and proliferation, the Sr-Ca ferrite samples were demagnetized through the application of three methods: strong external magnetic field of opposite polarity, Curie temperature under an oxygen environment and Curie temperature under a nitrogen environment. The resazurin assay measurements during the 11 days' period study showed reduced MG-63 cell adhesion and proliferation on the surface demagnetized through the Curie temperature under oxygen atmosphere. The low cell affinity was also confirmed through SEM analysis. The occurrence of surface oxidation was not identified on the EDS analysis since there was no increase in the oxygen peak. However, the recognition of rust-coloured spots at the samples surface and the results obtained by Masahiro Amemiya [62], which demonstrate the occurrence of ferrite surface oxidation then this material is heat-treated in an oxidizing atmosphere, are both strong statements that justify the low cell viability measured in the resazurin assay when compared with the same material in the magnetized state. Despite the limitation shown by the demagnetization method through Curie temperature in oxygen atmosphere, the other two demagnetizations strategies - strong electric field and Curie temperature in oxygen atmosphere - led to an increased in the cell affinity towards the ferrite surface. A cell increase of 72 and 32%, respectively, was registered when compared with reference magnetic samples, during the 11 days study. The understanding of static magnetic field influence on bone cells has been the aim of several studies [63-67]. However, this issue has been subject of contradictive theories. According to Cunha *et al.* [63] the results from MTT assays showed a reduction in MG-63 human osteoblast-like cell proliferation after a continuously 7 days' exposure to a 0.32 T static magnetic field. The authors also verified that the

static magnetic field application during 1h/day increased the cell release of osteocalcin, which effect was reversed after 7 days. No influence on cellular distribution, morphology or cytoskeleton organization was verified. A different opinion was exposed by Chiu *et al.* [65], who studied the effects of a 0.4 T static magnetic field on MG-63 cell lines. This authors claimed that this stimulus, when applied during 6 hours, affected osteoblastic maturation by increasing the membrane rigidity and reducing the proliferation-promoting effects of growth factors at the membrane domain. However, both teams claim a reduction in the proliferation of MG-63 when exposed to a static magnetic field. Hence, this justifies the increase in the number of cells when the ferrite material was in a demagnetized state.

Considering that no procedure until now was adopted to assure an accurate chemical sterilization of the materials tested, the application of hard mechanical cleaning through sandpaper abrasion was adopted. From resazurin assay measurements it was possible to determine that the hard mechanical cleaning procedure increased cell proliferation, by a 40 and 30% at the 7th and the 11th day of incubation, respectively, in relation to the samples which were not subjected to this procedure. The EDS analysis showed no variation in chemical constitution of the Curie temperature under nitrogen atmosphere demagnetized Sr-Ca ferrite surface, before and after the mechanical cleaning procedure, was applied. Hence, the samples chemical “contaminants” removal did not appear to be responsible for the increase in cell growth.

Considering that the interface between the material and the surrounding environment plays a crucial role in cell adhesion and proliferation [68], the influence in surface morphology and topography alteration, were also evaluated. From the material surface morphological SEM analyses, it was possible to notice that the abrasively cleaned material presented a reduction in the surface irregularity and it also appeared slightly smoother when compared to the samples that were not subjected to the aggressive cleaning procedure. However, this variation did not appear to lead to any alteration in the MG-63 cell morphology (Figure 5.20 and 5.21, respectively). A quantitative surface analysis was achieved from white light interferometry topographic results. From the observation of Figure 5.20 and from the variation of the roughness parameters between the two measured directions (x and y), it was possible to confirm that all demagnetized Sr-Ca ferrites surfaces presented a striation pattern. This most probably resulted from the machining process (*e.g.* tool type, feed rate, machine type) [40]. The application of the abrasive mechanical cleaning altered the surface topography through: 1) reduction of the surface general roughness (see Figure 5.21 and Table 5.3) and which was characterized by a

decrease in the R_a values (gives a good general description of height variations but it does not differentiate between peaks and valleys and it is not sensitive to small changes in the profile [44, 69] and which was reduced to a typical value for polished surface, around $0.2\ \mu\text{m}$ [70]) and in the R_q values (more sensitive to peaks and valleys but it does not detect an isolated error or a general tendency towards the worsening of a surface [44, 69, 71]) and 2) the removal of the surface pattern with the general homogenization of the surface topography, which is not only clear from the 3D surface topography image but it is also confirmed by the reduction of the R_z value (usually used to verify if a profile has protruding peaks or valleys). It is difficult to compare the results attained in this study with the ones obtained in literature, due to the lack of similarity between the surfaces considered (*e.g.* chemical composition, topography and morphology) and the methods used to determine the roughness. However, few studies considering titanium surfaces were used to help interpret the results obtained. It is generally known that osteoblastic cells prefer rougher surfaces [72]. This idea was clearly demonstrated in a study developed by Kunzler *et al.* [70]. In this study, osteoblastic cells exposed to a roughness gradient (representative of the ones found in cell studies) in a single substratum, showed a similar osteoblastic attachment on the rough and smooth parts of the gradient, nonetheless the cell proliferation was almost two times higher on the rough end when compared to the smooth end of the gradients. However, and as stated by Kunzler, osteoblastic cells also tend to respond differently to changes in the surface roughness depending on their maturation state. The immature osteoblastic-behavioural MG-63 exposed to the Sr-Ca ferrite showed a morphology characteristic of their culture in a smooth surface and which according to Boyan *et al.* [73] in such environment flattened configuration is adopted. When cultured in rough surfaces (R_a between 4 and $7\ \mu\text{m}$), these cells assume a more cuboidal morphology with cytoplasmic extensions. Although, a significant reduction in the roughness values was generated with the sandpaper abrasive cleaning procedure (a minimum 2-fold reduction in all the roughness parameters) the range of roughness values obtained in both samples were all characteristic of what would be considered a smooth surface. This explains the non-variation of the MG-63 cells morphologies between the surfaces. Also the increase in the cell proliferation registered in this study is in accordance with the results obtained by Martin *et al.* [72] where the authors reported that the MG-63 cells proliferate better in smoother surfaces than in rough ones.

A better understanding of the ferrite morphology and topography relation to MG-63 cells adhesion and proliferation requires a more thorough study in order for proper conclusions on ideal cell surface, to be obtained. From this study it was possible to determine that MG-63 cells show a significant preference for proliferation on Sr-Ca ferrite surfaces demagnetized through

the application of a strong external magnetic field of opposite polarity, and that a decrease in surface roughness also appears to improve these cells proliferation rate.

5.4. Conclusions

The results obtained in the present study show strong evidences of both soft and hard ferrite, respectively $Ni_{0.27}Cu_{0.14}Zn_{0.6}$ and Sr-Ca ferrite materials, probability of being cytocompatible. However, this study is only a first approach in the determination of the materials cytocompatibility since time constraints limited the development of the additional essential assays (*e.g.* evaluation of functional parameters, as the alkaline phosphatase activity). It is important to highlight that all the ferrite materials tested during this study were originally designed for industrial applications (*e.g.* electronic circuits) and no strategies during their production and handling were adopted considering their application for *in vivo* purposes. Still it was interesting to show the high affinity of MG-63 cells for the $Ni_{0.27}Cu_{0.14}Zn_{0.6}$ ferrite material and how by the removal of the static magnetic field on the Sr-Ca ferrite the cells adhesion and proliferation was greatly increased. In relation to the magnetic ferrite material and the nature and degree of interaction with osteoblastic-type bone cells, it is a very complicated phenomenon [68, 74] and the study performed was not able to completely understand the set of parameters which govern the MG-63 cell adhesion and proliferation on the ferrite surfaces, and in which way they can be modified in order to improve cell affinity and guarantee material cytocompatibility. The path towards these materials full biocompatibility and the permission for their *in vivo* implantation is lengthy and difficult. In order for the ferrite material biocompatibility to be declared, it should present the ability to perform with an appropriate host response in a specific application, meaning the ferrite should be able to enhance fractured bone healing process, without inducing any undesirable local or systemic responses in the eventual host. Such property can only be validated with thorough *in vivo* assessment.

5.5. References

1. Sakai, T., S. Hoshiai, and E. Nakamachi, *Biochemical compatibility of PZT piezoelectric ceramics covered with titanium thin film*. Journal of Optoelectronics and Advanced Materials, 2006. **8**(4): p. 1435-1437.
2. Bhunia, S., S. Majerus, and M. Sawan, *Introduction*, in *Implantable Biomedical Microsystems: Design Principles and Applications*, S. Bhunia, S. Majerus, and M. Sawan, Editors. 2015, Elsevier: London, UK. p. 3-12.
3. Pérez, A.L., et al., *Osteoblast and MG-63 osteosarcoma cells behave differently when in contact with ProRoot™ MTA and white MTA*. International Endodontic Journal, 2003. **36**: p. 564-570.
4. Coecke, S., et al., *Guidance on good cell culture practice. a report of the second ECVAM task force on good cell culture practice*. Alternatives to laboratory animals: ATLA, 2005. **33**(3): p. 261-287.

5. Gu, X., et al., *In vitro corrosion and biocompatibility of binary magnesium alloys*. Biomaterials, 2009. **30**(4): p. 484-498.
6. Tan, J. and M. Saltzman, *Biomaterials with hierarchically defined micro- and nanoscale structure*. Biomaterials, 2004. **25**: p. 3593-3601.
7. Kim, D.-H., et al., *Cytotoxicity of ferrite particles by MTT and agar diffusion methods for hyperthermic application*. Journal of Magnetism and Magnetic Materials, 2005. **293**(1): p. 287-292.
8. Périgo, E.A., et al., *Fundamentals and advances in magnetic hyperthermia*. Applied Physics Reviews, 2015. **2**(041302).
9. Ansari, S.M., et al., *Size and chemistry controlled cobalt-ferrite nanoparticles and their anti-proliferative effect against the MCF-7 breast cancer cells*. ACS Biomaterials Science and Engineering, 2016. **in press**.
10. Hanini, A., et al., *Nanotoxicological study of polyol-made cobalt-zinc ferrite nanoparticles in rabbit*. Environmental Toxicology and Pharmacology, 2016. **45**: p. 321-327.
11. Czekanska, E.M., et al., *In search of an osteoblast cell model for in vitro research*. European Cells and Materials, 2012. **24**: p. 1-17.
12. Billiau, A., et al., *Human interferon: Mass production in a newly established cell line, MG-63*. Antimicrobial Agents and Chemotherapy, 1977. **12**(1): p. 11-15.
13. Pautke, C., et al., *Characterization of osteosarcoma cell lines MG-63, Saos-2 and U-2 OS in comparison to Human osteoblasts*. Anticancer Research, 2004. **24**: p. 3743-3748.
14. Saldívar-Ramírez, M.M.G., et al., *Study on the efficiency of nanosized magnetite and mixed ferrites in magnetic hyperthermia*. Journal of Materials Science: Materials in Medicine, 2014. **25**(10): p. 2229-2236.
15. Sampath, K.A., et al., *Structural, magnetic and in vitro bioactivity of Co-Cu ferrite and bioglass composite for hyperthermia in bone tissue engineering*. Bioceramics Development and Applications, 2016. **6**(1): p. 1-7.
16. Wei, Y., et al., *Magnetic biodegradable Fe₃O₄/CS/PVA nanofibrous membranes for bone regeneration*. Biomedical Materials, 2011. **6**: p. 1-15.
17. Anselme, K., *Osteoblast adhesion on biomaterials*. Biomaterials, 2000. **21**: p. 667-681.
18. Delhay, B., et al., *Texture-induced vibrations in the forearm during tactile exploration*. Frontiers in Behavioral Neuroscience, 2012. **6**(37): p. 60-69.
19. Golanski, L., et al. *New method for the characterization of abrasion-induced nanoparticle release into air from nanomaterials*. in *10th IEEE Conference on Nanotechnology*. 2010. Gyeonggi-Do, South Korea: Institute of Electrical and Electronics Engineers.
20. Frias, C., et al., *Piezoelectrical actuator: Searching inspiration in nature for osteoblastic stimulation*. Composites Science and Technology, 2010. **70**: p. 1920-1925.
21. Caballero-Díaz, E., *Analytical Nanotoxicology*, in *Encyclopedia of Analytical Chemistry*, R.A. Meyers, Editor 2006, John Wiley & Sons, Ltd. p. 1-28.
22. Anoopkumar-Dukie, S., et al., *Resazurin assay of radiation response in cultured cells*. The British Journal of Radiology, 2005. **78**: p. 945-947.
23. Rampersad, S.N., *Multiple applications of alamar blue as an indicator of metabolic function and cellular health in Cell viability bioassays*. Sensors, 2012. **12**(9).
24. Luepke, N.P., *Hen's egg chorioallantoic membrane test for irritation potential*. Food and Chemical Toxicology, 1985. **23**(2): p. 287-291.
25. NIH, *ICCVAM test method evaluation report: Current validation status of a in vitro test methods Proposed for identifying eye injury hazard potential of chemicals and products*, P.N. 10-7553, Editor 2010. p. Appendix B3 31-38.
26. Kishore, A.S., et al., *Hen egg chorioallantoic membrane bioassay: an in vitro alternative to draize eye irritation test for pesticide screening*. International Journal of Toxicology, 2008. **27**(6): p. 449-453.

27. Manjunathan, R. and M. Ragunathan, *In ovo administration of human recombinant leptin shows dose dependent angiogenic effect on chicken chorioallantoic membrane*. Biological Research, 2015. **48**(29): p. 1-13.
28. Ribatti, D., *The chick embryo chorioallantoic membrane as an in vivo assay to study antiangiogenesis*. Pharmaceuticals, 2010. **3**: p. 482-513.
29. Norrby, K., *In vivo models of angiogenesis*. Journal of Cellular and Molecular Medicine, 2006. **10**(3): p. 588-612.
30. Auerbach, R., et al., *Angiogenesis assay: Problems and pitfalls*. Cancer and Metastasis Review, 2000. **19**: p. 167-172.
31. Ribatti, D., et al., *The chick embryo chorioallantoic membrane as a model for in vivo research on angiogenesis*. International Journal of Developmental Biology, 1996. **40**: p. 1189-1197.
32. Chow, L.W., et al., *A bioactive self-assembled membrane to promote angiogenesis*. Biomaterials, 2011. **32**(6): p. 1574-1582.
33. Blacher, S., et al., *Quantification of angiogenesis in the chicken chorioallantoic membrane (CAM)*. Image Analysis and Stereology, 2011. **24**(3): p. 169-180.
34. Baiguera, S., P. Macchiarini, and D. Ribatti, *Chorioallantoic membrane for in vivo investigation of tissue-engineered construct biocompatibility*. Journal of Biomedical Materials Research Part B: Applied Biomaterials, 2012. **100**(5): p. 1425-1434.
35. Dohle, D.S., et al., *Chick ex ovo Culture and ex ovo CAM Assay: How it really works*. Journal of Visualization Experiments, 2009. **33**: p. 1-6.
36. Costa, F.M.S., *Biocompatibility assessment of calcium-silicate based endodontic sealers: In vitro studies*, in *Faculty of Engineering 2014*, University of Porto: Porto, Portugal.
37. Ribatti, D., et al., *Chorioallantoic membrane capillary bed: A useful target for studying angiogenesis and anti-angiogenesis in vivo*. The Anatomical Record, 2001. **264**(4): p. 317-324.
38. Egerton, R.F., *Physical principles of electron microscopy: An introduction to TEM, SEM, and AEM*. 2nd ed 2016, Switzerland: Springer.
39. Williams, D.B. and C.B. Carter, *The transmission electron microscope: A textbook for materials science*. 1st ed 1996, London, UK: Plenum Press.
40. Czichos, H., T. Saito, and L. Smith, *Springer handbook of materials measurement methods* 2006: Springer-Verlag Berlin Heidelberg.
41. Zhou, W., et al., *Fundamentals of Scanning Electron Microscopy*, in *Scanning Microscopy for Nanotechnology: Techniques and Applications*, W. Zhou and Z.L. Wang, Editors. 2007, Springer-Verlag: New York, USA. p. 1-40.
42. Leach, R., *Surface topography measurement instrumentation*, in *Fundamental Principles of Engineering Nanometrology*, R. Leach, Editor 2014, Elsevier: Oxford, UK. p. 131-204.
43. Berger, R. and W. Osten, *Analogy of white-light interferometry and pulse shaping*, in *Fringe 2009: 6th International Workshop on Advanced Optical Metrology*, W. Osten and M. Kujawinska, Editors. 2009, Springer-Verlag: Heidelberg, Germany.
44. Mummery, L., *Surface texture analysis: The handbook* 1992: Hommelwerke GmbH.
45. Leach, R., *Surface topography characterisation*, in *Fundamental Principles of Engineering Nanometrology*, R. Leach, Editor 2014, Elsevier: Oxford, UK. p. 241-294.
46. *ISO 4287:1997 - Geometrical Product Specifications (GPS) -- Surface texture: Profile method -- Terms, definitions and surface texture parameters*, 1997.
47. Geiss, R.H., *EDS : Energy-Dispersive X-Ray Spectroscopy*, in *Encyclopedia of Materials Characterization: Surfaces, Interfaces, Thin Films*, C.R. Brundle, C.A. Evans, and S. Wilson, Editors. 1992, Gulf Professional Publishing: London, UK. p. 120-134.
48. Pouchou, J.-L., *X-ray microanalysis of stratified specimens*. Analytica Chimica Acta, 1993. **283**(1): p. 81-97.

49. Laskin, A., J.P. Cowin, and M.J. Ledema, *Analysis of individual environmental particles using modern methods of electron microscopy and x-ray microanalysis*. Journal of Electron Spectroscopy and Related Phenomena, 2006. **150**(2): p. 260-274.
50. Sigee, D.C., *X-ray microanalysis in biology: Experimental techniques and applications* 1993: Cambridge University Press.
51. Russ, J.C., *Fundamentals of Energy Dispersive X-Ray Analysis: Butterworths Monographs in Materials* 2013, London, UKA: Butterworth-Heinemann.
52. Silver, E., et al., *Highresolution, broad-band microcalorimeters for x-ray microanalysis*. X-Ray Spectrometry, 1996. **25**(3): p. 115-122.
53. Rivero, S., M.A. García, and A. Pinotti, *Physical and chemical treatments on chitosan matrix to modify film properties and kinetics of biodegradation*. Journal of Materials Physics and Chemistry, 2013. **1**(3): p. 51-57.
54. Kwok, D.Y. and A.W. Neumann, *Contact angle techniques and measurements*, in *Surface Characterization Methods: Principles, Techniques, and Applications*, A.J. Milling, Editor 1999, CRC Press: New York, USA. p. 37-79.
55. Huq, M.F., et al., *Ni-Cu-Zn Ferrite research: A brief review*. Journal of Scientific Research, 2013. **5**(2): p. 215-233.
56. Lee, S.B., et al., *In vitro cytotoxicity of aginate-encapsulating ferrite particles using WST-1*. Key Engineering Materials, 2005. **284-286**: p. 815-818.
57. ISO 10993-5:2009(E), *Biological evaluation of medical devices - Parte 5: Tests for in vitro cytotoxicity*, 2009: Geneva, Switzerland.
58. Ghazanfari, M.R., et al., *Perspective of Fe₃O₄ nanoparticles role in biomedical applications*. Biochemistry Research International, 2016: p. 1-32.
59. Nielsen, S.P., *The biological role of strontium*. Bone, 2004. **35**(3): p. 583-588.
60. Almeida, M.M., et al., *Strontium ranelate increases osteoblastic activity*. Tissue and Cell, 2016. **48**(3): p. 183-188.
61. Kirrane, B.M., L.S. Nelson, and R.S. Hoffman, *Massive strontium ferrite ingestion without acute toxicity*. Basic and Clinical Pharmacology and Toxicology, 2006. **99**: p. 358-359.
62. Amemiya, M., *Oxidizing reaction of Mn-Mg-Cu ferrite accompanied with its decomposition*. Journal of Inorganic and Nuclear Chemistry, 1971. **33**(10): p. 3289-3295.
63. Cunha, C., et al., *Evaluation of the effects of a moderate intensity static magnetic field application on human osteoblast-like cells*. American Journal of Biomedical Engineering, 2012. **2**(6): p. 263-268.
64. Feng, S.W., et al., *Static magnetic field exposure promotes differentiation of osteoblastic cells grown on the surface of a poly-L-lactide substrate*. Medical and Biological Engineering and Computing, 2010. **48**(8): p. 793-798.
65. Chiu, K.-H., et al., *Static magnetic fields promote osteoblast-like cells differentiation via increasing the membrane rigidity*. Annals of Biomedical Engineering, 2007. **35**(11): p. 1932-1939.
66. Fassina, L., et al., *Effects of electromagnetic stimulation on calcified matrix production by SAOS-2 cells over a polyurethane porous scaffold*. Tissue Engineering, 2006. **12**(7): p. 1985-1999.
67. Denaro, V., et al., *Static electromagnetic fields generated by corrosion currents inhibit human osteoblast differentiation*. Spine, 2008. **33**(9): p. 955-959.
68. Barata, D., et al., *Surface micropatterning with zirconia and calcium phosphate ceramics by micromoulding in capillaries*. Journal of Materials Chemistry B, 2016. **4**: p. 1044-1055.
69. Gadelmawla, E.S., et al., *Roughness parameters*. Journal of Materials Processing Technology, 2002. **123**(1): p. 133-145.
70. P. Kunzler, T.P., et al., *Systematic study of osteoblast and fibroblast response to roughness by means of surface-morphology gradients*. Biomaterials, 2007. **28**: p. 2175-2182.

71. Pérez, L.C.J., *Analysis of the surface roughness and dimensional accuracy capability of fused deposition modelling processes*. International Journal of Production Research, 2002. **40**(12): p. 2865-2881.
72. Martin, J.Y., et al., *Effect of titanium surface roughness on proliferation, differentiation, and protein synthesis of human osteoblast-like cells (MG-63)*. Journal of Biomedical Materials Research, 1995. **29**: p. 389-401.
73. Boyan, B.D., et al., *Mechanisms involved in osteoblast response to implant surface morphology*. Annual Review of Materials Research, 2001. **31**: p. 357-371.
74. Liu, H.-C., et al., *Preparation of PLLA membranes with different morphologies for culture of MG-63 Cells*. Biomaterials, 2004. **25**(18): p. 4047–4056.

“Healing is a matter of time, but it is sometimes also a matter of opportunity”

Hippocrates (460 BC -375 BC)

6. Bone healing enhancement device:

Concept demonstration model

The global orthopedic trauma fixation devices market is witnessing a significant growth. In 2014, it was worth US\$6,1 billion (around 5,4 billion euros [1]) and it is projected to reach US\$9,3 billion (approximately 8,3 billion euros [1]) by 2020, by expanding at a 7.2% CAGR during the forecast period [2]. The market growth is also associated with an increased demand in the quality of the orthopedic implants. The slow healing process associated with the tibia shaft fractures stabilization using intramedullary nail technique presents a substantial burden to society and patients (see Chapter 3). Thus, exploring an efficacious and low-cost strategy to accelerate fracture healing can have an important impact in the improvement of currently used intramedullary nail devices [3]. It is of general acceptance that the healing site mechanical environment greatly determines the fracture healing process quality and progress [4]. However, only recently the underestimated low-amplitude high-frequency stimulus potential effect on bone fracture treatment enhancement has started to be evaluated. As presented in Chapter 1, there are numerous reports that demonstrate the positive influence provided by these stimuli. The results obtained in those studies provided the theoretical basis for the development of the actuator device.

In this Chapter, a new solution to enhance the fracture healing process is presented. The system concept was based on dynamically controlled magnetic fields applied through non-direct contact to the actuator which is connected to the bone fracture fixation device inside the patients. A time changing magnetic field when applied to a bulk conductive (*i.e.* low resistivity) medium, such as ferrite, results in the production of an electromotive force. These electromotive force causes eddy currents

(also called Foucault currents) to circulate inside the conductor and to generate a magnetic field. This magnetic field will, in turn, interact with the original one applied and cause the generation of magnetic force, repulsive or attractive. The drive signal needs to alternate the direction of current (*i.e.* an AC signal) and hence the magnetic field, so the permanent magnet oscillates back and forth. Also, if a continuously changing field is not applied to the conductor, the force will disappear because the eddy currents circulating inside the conductor will be dissipated into heat as a result of the conductor internal low resistance [5-8]. Figure 6.1 exemplifies the application of the bone healing enhancement device to an intramedullary nail fixation method. As illustrated in Figure 6.1, the actuator motions were generated by applying a time-changing magnetic field in close proximity to the conductive material. The control electric current used to produce the magnetic field through its passage in an open field circular coil was obtained from an amplified signal generated by an arbitrary frequency generator. The reduced wavelength produced magnetic field generated will not cross the bulk conductive actuator and eddy currents will develop at the conductor surface.

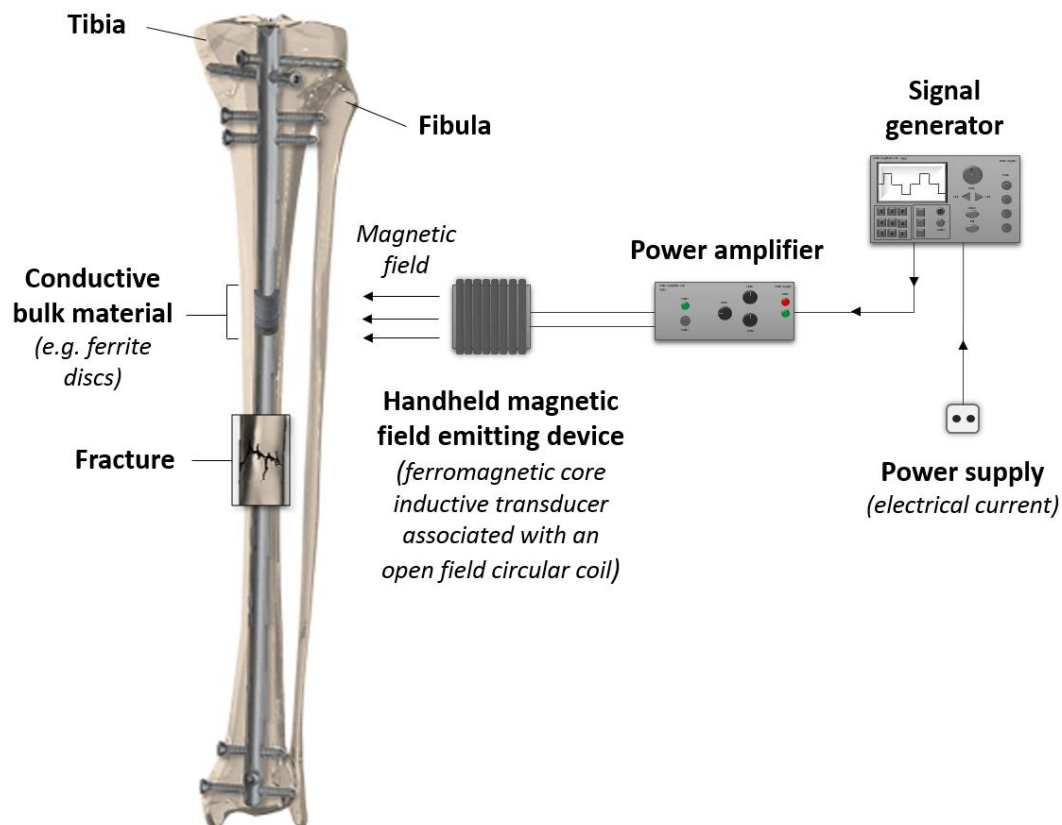


Figure 6.1 - Schematic representation of the proposed magnet actuator device linked to an intramedullary nail for bone healing enhancement. The implanted actuator is externally activated and controlled by a handheld emitting device which electrical current is obtained from a frequency generator amplified signal. Tibia with fibula and intramedullary nail image obtained from [9] and fracture image obtained from [10]

After the most suitable actuator material was selected (see Chapter 4) and its biocompatibility evaluated (see Chapter 5), the importance of securing the intellectual property rights of the original idea, required the development of a simple and easy to perceive model which allowed for principle demonstration. Although, the model satisfied the purpose to which it was developed, time constraints, implied it's used for theoretical basis study of the actuator device performance and to speculate on the potential extent of the idea. As suggested by C. Sujatha [11], there are three output parameters on actuator systems which should be considered such as the resonance frequency, waveform type and signal level or amplitude control. In this chapter, these parameters are studied and used to understand the actuation device system components relationship.

6.1. Materials and methods

The concept demonstration model was developed mostly based on materials available in the Technological Testing Laboratory with the exception of the electric apparatus components which were purchased. This model includes three examples for concept demonstration. However, only the one closer to the tibia and implant system case, model 2, was used for parameter study. Figure 6.2 shows a generalized block diagram of the test set-up used in the concept demonstration model. All models comprise an electrical power supply, an oscilloscope (model 33120A, Hewlett-Packard, California, USA) for signal generator, an amplifier for power amplification, a ferromagnetic core inductive transducer and a ferrite magnet linked to a central elongated body (which mechanical properties varies between models) and which, in turn, is connected from its extremities by 4 mm diameter stainless steel pins to a transparent acrylic tube that functions as a support structure (see Figure 6.3).

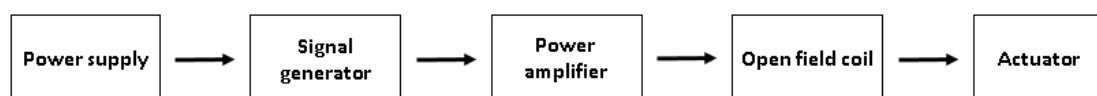


Figure 6.2 - Block diagram of the general constitutive components in the concept demonstration models

In model 1 (see Figure 6.3(1)) for the vibration to be visually perceived upon the application of the magnetic field, a ferromagnetic stripe with 10 mm width and 300 mm length was used.

In model 2 (see Figure 6.3(2)), which was used for the parameters testing and which more closely resembles the bone-implant system, a soft ferrite actuator (IMA, Barcelona, Spain) with inner and outer diameter of 9 and 19 mm, respectively and 30 mm length was fixed with cyanoacrylate adhesive (FORTE® Plus, Loctite®, Düsseldorf, Germany) to the exterior wall of a cannulated intramedullary nail with 9 mm diameter per 345 mm length made of AISI 316L ASTM F318

stainless steel (model SU-209-345, citieffe® S.r.l., Bologna, Italy) and which was provided by *Artur Salgado S.A.* The actuator was positioned at mid distance in the intramedullary nail straight portion. The intramedullary nail - “pin”-tube assembly resembles the intramedullary nail-screw-bone arrangement.

In model 3 (see Figure 6.3(3)), in replacement of the intramedullary nail and to increase the vibration effect, an 8 mm diameter polymeric rod was used. A same size and composition ferrite actuator was fixed with cyanoacrylate adhesive to the polymeric rod.

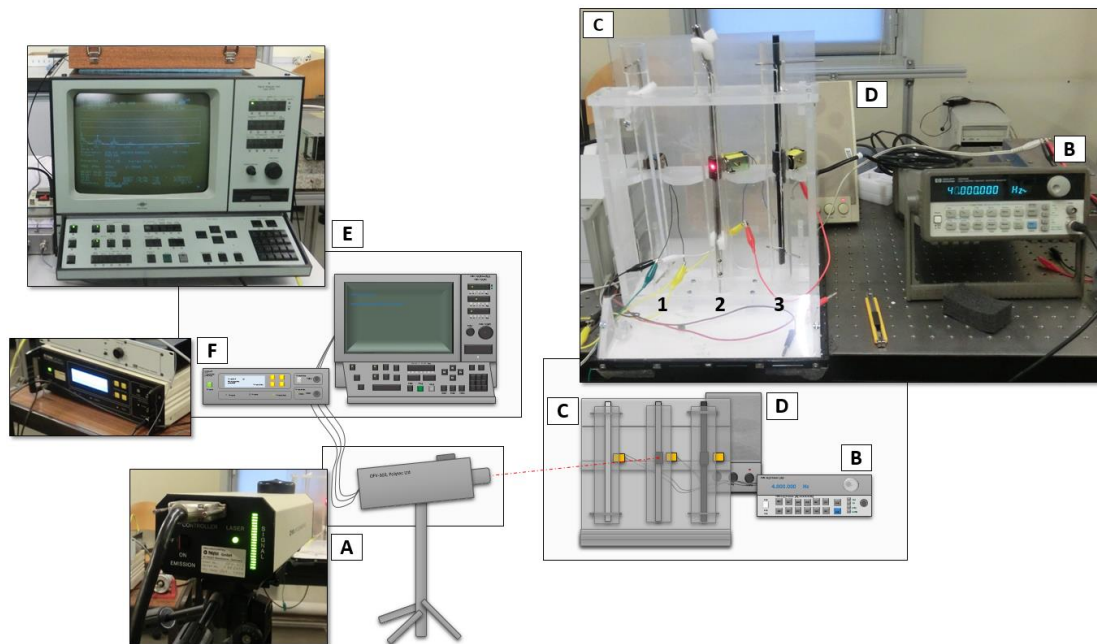


Figure 6.3 - Schematic representation of the (C) concept model developed for 'proof of concept' demonstration purpose and the set-up system used for the frequency measurements based in the model 2. The system electrical apparatus comprises: (A) laser Doppler vibrometer optical sensor head, (B) oscilloscope, (D) amplifier, (E) laser Doppler vibrometer controller and (F) laser Doppler vibrometer signal analyser unit

The model 2 test set-up was used to measure the intramedullary nail-actuator system resonance frequencies. For the frequencies to be determined considering the system free-free body conditions, the intramedullary nail extremities rigid pin fixation was replaced by a sponge-like material which guarantees the system positioning and at the same time allows its motion as a free body (*i.e.* not considering the influence of the overall set-up system). The actuator motion was generated by the application of a time-changing magnetic field, in close proximity to a conductive material which, in turn, was generated from the passage of the dynamic electric current in the open field circular coil. The resonance frequency was determined from the application of a physiological drive signal frequency between 10 and 200 Hz and with increments of 10 Hz. A rectangular waveform vibration in nature was applied. The ferromagnetic core inductive transducer was constituted by a neodymium-iron-boron conductive core - where the

high magnetic permeability of these materials will increase the magnetic field - associated with an open field circular copper wire coil. To avoid variation of the distance considered for the application of the magnetic field, the ferromagnetic core inductive transducer was fixed to the acrylic set-up. The ferrite actuator displacement in real-time was measured through the use of a single-point laser Doppler vibrometer system. This system comprises an optical sensor head (model OFV-303, Polytec Ltd., Hertfordshire, UK), a controller (model OFV-3001, Polytec Ltd., Hertfordshire, UK) which provides power for the measuring head and the signal analyser unit (model 2035, Polytec Ltd., Hertfordshire, UK) that processes the vibration signal and displays the results obtained. The single-point laser Doppler vibrometer system data acquisition method was previously described in Chapter 3.

6.2. Results and discussion

The concept model for principle demonstration purpose was used as a study-base for a better understanding of the actuator behaviour, the variables involved and their relation. The actuator performance is controlled by the applied magnetic field. Consequently, the AC drive signals and therefore, the magnetic field applied can be controlled by manipulating the frequency, its amplitude, shape and wavelength. The relation between the drive signal frequency and the actuator performance is not straightforward. As stated previously in Chapter 4, each system has a resonant frequency to which the input signal should operate in order to maximize the actuator energy absorbed, to magnify the actuator vibration and reduce the power required. The shifting of the input signal frequency away from the system resonant frequencies, cause the actuator vibration performance to be reduced significantly. Based on the previously described method, the intramedullary nail and actuator system in free-free body condition resonance frequencies were determined and the values obtained were between 28-30 and 39-46 Hz. The intramedullary nail and actuator system resonance frequencies, fall within the physiological ones. However, it is important to highlight that the actuator resonance frequency changes according to its dynamic constraints at the end boundary [12]. Differently from the frequency parameter, the driven signal amplitude has a linear relation to the actuator performance. Thus, the higher the amplitude the greater the actuator vibration output, for a given frequency. Hence, the strength of the eddy currents increases with the strength of the magnetic field [5-8]. Another magnetic field parameter is its time derivative. As stated previously, in order for the conductive actuator to oscillate back and forth, a pulsating (time-varying) magnetic field had to be applied [13]. For this effect to be increased, a rectangular waveform was considered. It is known that the size of the conductive actuator and its distance to the magnetic field also influences the final actuator performance. Although these parameters were not directly tested, it is known that the

distance between the magnetic field generator and the conductive material will depend on the intensity of the magnetic field [14]. Also, the density of the currents induced in the conductor will be directly proportional to the conductive material thickness and the reduce wavelength of the magnetic field will intentionally not cross the actuator and will cause the development of eddy currents on the ferrite conductor surface [5-8].

The principle demonstration concept model was also used to extrapolate on the bone enhancement actuator device features potentials and its comparison with competitive existing devices. Although, in this chapter, the actuator characteristics were considered in a general manner, based on the device functioning concept, it is possible to claim that the actuator can actually generate an almost unlimited range of interfragmentary mechanical stimuli, which can vary in the type of motion created, magnitude, frequency (or rate) type and intensity, duration and timing of initiation. The bone healing enhancement device actuation power supply and control is achieved by the magnetic field stimulus. The magnetic field can penetrate all tissues including epidermis, dermis, subcutaneous tissues as well as tendons, muscles and also bone, which allows it to be remotely supplied and this feature presents an additional advantage over the conventional wired actuators in terms of operating life but also in relation to safety. Contrarily to the controversy associated with the effect of static magnetic field influence on bone cells (see Chapter 5), *in vitro* experiments on low frequencies (up to 300 Hz) varying magnetic fields have demonstrated beneficial effects on osteogenic tissue, angiogenesis stimulation, osteogenic precursor proliferation, in the transport of Ca^{2+} in promoting bone formation and in the inflammatory response [15-18]. However, the cells reaction depends on cells line, field parameters and time of exposition [19, 20]. The actuator functioning will depend on the momentarily application of the magnetic field, meaning, that an external magnetic field generator device (*e.g.* magnetic field handheld emitting apparatus) must be present every time the mechanical stimulus is needed [13, 21, 22]. This feature also allows the stimulus to be applied to the fracture site during patient rest periods - when there is no load applied to the fixation devices - and the stimulus generation is not limited to patient motion periods and does not require patient motion. Hence, if a portable magnetic field generator device is to be considered, patients will be able to develop their everyday tasks without interference. Another important feature of the bone healing enhancement device actuator is that the physicians have total control of the stimulus applied allowing them to define patient-specify and healing-stage specific therapeutic protocols based on the progression of the fracture healing. The monitoring of the magnetic field is possible, for example information on the magnetic field strength generated can be obtained through Hall Effect sensor. This simple magnetic sensor is based on

the Hall Effect where a magnetic field placed perpendicular/right angle to a hall transducer (conductive material such as copper) which carries a current flow, will force the charge carriers to one side of the hall transducer. This will cause excess concentration of charges to one side and depletion on the other, which will give rise to an electric field across the transducer and consequently voltage that can be measured across the plate. An equilibrium develops when the magnetic force pushing the charge carriers aside is balanced out by the electric force trying to push them back towards the middle. Hence, the voltage is proportional to the current flowing in the conductor (known parameter) and the magnetic flux density [23-25]. In terms of the bone enhancement actuator device range of application by considering that the actuator will be associated with the intramedullary nail fixation method, its range of application can be considered the same as that of the fixation device which it is associated with. Hence, this strategy takes advantage of the fracture site mechanical stimulus already generated from the orthopedic trauma fixation devices alone and provides additional stimulus which is considered safe, do not interfere negatively in the biological process of bone healing and do not represent any risk for the stabilization method. Although, in the principle demonstration concept model a tube ferrite actuator was fixed to the exterior wall of a intramedullary nail, the wide range of ferromagnetic actuators sizes and dimensions, allow their incorporation into different sites in the tight design of the intramedullary nail (*e.g.* it can be placed along the intramedullary nail cannulated interior after the fixation device is correctly positioned in the bone medullary canal), and still allow the development of vibration at significant forces to be applied. Hence, this bone healing enhancement device also allows the fixation device's implantation procedures and correspondent surgical instrumentation to be maintained, as well as the duration of the fixation device implantation procedure and stipulated remaining time for intramedullary nail inside the patient's body. This characteristic will avoid an additional time consuming learning phase and will help the physicians to feel more comfortable and confident in using this device. The previously mentioned device characteristic guarantees the additional advantage to this invention when compared to other in development or commercially established interfragmentary motion generation devices [26-30].

6.3. Conclusion

In this chapter, an actuator for bone healing enhancement through mechanical stimulus was proposed considering the use of intramedullary nail fixation system. The bioimplantable actuator was required to possess a set of skills to realize the ambitious goal of enhancing the bone fracture healing process in a way that it satisfies the medical community expectations and still tries to keep up with the next generation of intramedullary nails. The proposed technique is

simple and requires minimal equipment. The system comprises a ferromagnetic actuator coupled to the fixation device and controlled through a magnetic field. The flexibility of the invention allows its performance to be customized in order to keep up with and adapt to the optimum mechanical healing stimulus concept evolution and therefore to properly enhance the healing process. Besides all the mentioned advantages, there is still a need for a prototype development and *in vivo* experimentation in order to solidify all the statements presented in this chapter. The developed study will hopefully also draw attention to the range of biomedical applications of ferromagnetic materials and their potential, as well as the need for more studies to consolidate their use.

6.4. References

1. Dengler, S. and B. Farmer. *US Dollar to Euro currency converter*. 2016; Available from: <http://www.xe.com/>.
2. Transparency Market Research, *Orthopedic Trauma Fixation Devices Market - Global Forecast, Share, Size, Growth and Industry Analysis 2014 - 2020*, 2014: New York, USA.
3. Gao, J., et al., *Multi-level assessment of fracture calluses in rats subjected to low-magnitude high-frequency vibration with different rest periods*. *Annals of Biomedical Engineering*, 2016. **44**(8): p. 2489-2504.
4. Aranzulla, P.J., D.S. Muckle, and J.L. Cunningham, *A portable monitoring system for measuring weight-bearing during tibial fracture healing*. *Medical Engineering and Physics*, 1998. **20**: p. 543-548.
5. Reinhardt, B., B. Hency, and M. Peck, *Characterization of Eddy Currents for Space Actuation*, in *AIAA/AAS Astrodynamics Specialist Conference 2012*, American Institute of Aeronautics and Astronautics: Minnesota, USA.
6. Sodano, H.A. and D.J. Inman, *Non-contact vibration control system employing an active eddy current damper*. *Journal of Sound and Vibration*, 2007. **305**(4-5): p. 596-613.
7. de Silva, C.W., *Vibration: Fundamentals and practice*. 2nd ed 2007, Florida, USA: CRC Press.
8. Sodano, H.A. and D.J. Inman, *Modeling of a new active eddy current vibration control system*. *Journal of Dynamic Systems, Measurement, and Control*, 2008. **130**(2): p. 1-11.
9. Zimmer, *Интрамедуллярные гвозди Zimmer Natural Nail, trauma-1*, Editor 2016: Zimmer.
10. Kimball, M., *Stress fracture*, 2011: In[®] SlideShare.
11. Sujatha, C., *Vibration and acoustics - Measurement and signal analysis 2010*, New Delhi, India: Tata McGraw-Hill Education.
12. Konno, K.-I., T.N. Kowasada, and Z. Feng. *Piezoelectric micro device for mechanical stimulation and its detection for living cells*. in *6th World Congress of Biomechanics*. 2010. Singapore: Springer.
13. Weintraub, M.I., R. Mamtani, and M.S. Micozzi, *Complementary and integrative medicine in pain management 2008*, New York, USA: Springer Publishing Company.
14. Biggane, P., X. Jackson, and A. Nazarian, *Bone composition and healing: open electromagnetic and biomechanical problems*, in *38th Annual International Conference of the IEEE Engineering in Medicine and Biology Society (EMBC) 2016*: Florida, USA.
15. Ross, C.L. and B.S. Harrison, *Effect of time-varied magnetic field on inflammatory response in macrophage cell line RAW 264.7*. *Electromagnetic Biology and Medicine* 2013. **32**(1): p. 59-69.

16. Koch, C.L.M.B., et al., *Interaction between weak low frequency magnetic fields and cell membranes*. Bioelectromagnetics, 2003. **24**(6): p. 395–402.
17. Rahbek, U.L., K. Tritsarlis, and S. Dissing, *Interactions of low-frequency, pulsed electromagnetic fields with Living Tissue: Biochemical responses and clinical result*. Oral Biosciences and Medicine, 2005. **2**(1): p. 1-12.
18. D'Amora, U., *A novel route towards the design of 3D morphologically controlled magnetic scaffolds for advanced bone tissue engineering*, in *Department of Chemical, Materials and Industrial Production Engineering* 2013, University of Naples "Federico II": Naples, Italy. p. 1-151.
19. Rusak, A. and Z. Rybak, *Does magnetic stimulation affect wound healing? In vitro studies*. Polimery w Medycynie, 2013. **43**(3): p. 147-152.
20. Sollazzo, V., et al., *Responses of Human MG-63 osteosarcoma cell line and Human osteoblast-like cells to pulsed electromagnetic fields*. Bioelectromagnetics, 1997. **18**: p. 541-547.
21. Morais, R., et al., *An activation circuit for battery-powered biomedical implantable systems*. Sensors and Actuators A: Physical, 2009. **156**: p. 229-236.
22. Heinilä, H., et al., *Low cost miniaturization of an implantable prototype*. Circuit World, 2009. **35**(1): p. 34-40.
23. Ball, S.R., *Analog interfacing to embedded microprocessors: Real world design*. 2nd ed. Embedded technology series 2004, London, UK: Elsevier.
24. Wade, A., *Hall-Effect Sensors: Theory and Application* 2004, Minnesota, USA: MotorBooks International.
25. Ramsden, E., *Hall-effect sensors: Theory and application*. 2nd ed 2011, London, UK: Newnes.
26. Deng, C.-G., et al., *Intramedullary fixing device capable of effectively promoting fracture healing*, 2016: China.
27. Ziran, N., *Dynamic axial nail for intramedullary treatment of long bone fractures*, 2016.
28. Doherty, W., P. O'Conner, and J. Harty, *Intramedullary nails for long bone fracture setting* 2012, Cork Institute Of Technology.
29. Gall, K.A., J.A. Tyber, and D. Pacaccio, *Osteosynthetic implants and methods of use and manufacture*, 2008, Medshape Solutions, Inc.
30. Goodship, A.E., T.J. Lawes, and C.T. Rubin, *Low-magnitude high-frequency mechanical signals accelerate and augment endochondral bone repair: Preliminary evidence of efficacy*. Journal of Orthopaedic Research, 2009. **27**(7): p. 922–930.

“The purpose of science is to develop, without prejudice or preconception of any kind a knowledge of the fact, the laws, and the processes of nature”

Robert A. Millikan

7. General conclusion and future work

As stated by Alton Ochsner in *Thoughts on the Human Body*, “When we arrive on this earth we are endowed with the most perfect, the most efficient, and the best constructed machine ever devised - our body”, still similar to any other engine and independently of the quality of the materials used, accidental damage sometimes occur. In these occurrences, such as bone fractures cases, the engineer’s role is to develop the tools that can allow the system recovery in the minimum necessary time and aiming to a full restoration of its functions.

The level of complexity and multidisciplinary involved in the bone fracture healing process is entirely differently from man-constructed machines intelligible organization. Furthermore, its relation to the intramedullary nail fixation method, issue addressed in this PhD, required, besides a literature review, a complementary study with mechanical experimentation and finite element simulation, in order to gain a better sensibility on this subject. In this study, the contribution of the bone-intramedullary nail system stability and - more important - its dependence on the mechanical properties of the fixation method and on the fracture site mechanical environment during the post-operative period, was demonstrated. In addition, the urgent need for a profound understanding of the relation between the fracture recovery biology and the biomechanical stimulus at the fracture site, was highlighted. This knowledge will be determinant in the development of improved and more reliable fixation technology methods.

In this PhD thesis, a new approach to enhance the bone fracture healing process was presented. This innovative idea is easy to apply and can be considered a low-cost strategy to accelerate and improve the quality of fracture healing. Hence, the project goals were successfully achieved, since the invention reflects the clinician's needs and respects the human body biology. However, the actuator device was developed based on studies claiming the potential of micromotion combined with different frequencies as mechanical stimulus capable of enhancing bone-healing, and there is no practical demonstration of the clinical impact of the developed device. The challenge of adapting a concept to an already existing designed structure, such as the

intramedullary nail, restricted the progress to the development of a conceptual demonstration model. This model allows for demonstrating the main principles, as well as its uniqueness and utility. Thus, future work will focus on the evolution of the actuator device from the laboratory bench stage to a final reliable product with reproducible results *in vivo* in a tightly controlled environment. This path, however, is very demanding, and requires a set of stages such as the development of a prototype for *in vitro* testing and biomechanical analysis followed by *in vivo* testing in small and/or large animals, which could hardly be encompassed in any PhD program. A description of the work developed during the PhD for the preparation of future work is presented in Appendix C. Forthcoming work will be oriented towards an investigation on the market potential, to identify potential risk associated with the device and to develop designs conforming to user needs and intended use.

Overall, this project has proposed a novel method to physiologically align bone with a considerable level of precision between the *in vitro* and *in silico* study. Also, strong evidences pointing towards the selected ferromagnetic materials cytocompatibility not only positively supports their use as actuator in the developed device but also suggests the potential range of application of these materials in the biomedical field. Hopefully, the knowledge gained in this study and the developed actuator device will in the future help to obtain a better understanding of the biomechanics of bone healing, and as stated by Bob Peterhans (President of Zimmer trauma company) the ultimate surgeons goals to have access to options which ensure the best possible fixation for all patient types could be achieved.

8. Appendix

A

The intramedullary nail implantation in the SawBones composite tibia was performed by Professor Miguel Marta, an experienced orthopedic surgeon from the *Centro Hospitalar de São João*. The intramedullary nail and screws as well as full tool set for a realistic implantation procedure to be adopted (instruments are specific for a given nail), followed the ACCU-Nail technical procedure from the L.A. Medicals instrumentation company (Albergaria-a-Velha, Portugal). The fixator and respective instrumentation was provided by *Artur Salgado S.A.*. The proceeding was developed in the *Laboratório de Ensaios Tecnológicos* (translated as Technology Testing Laboratory) at the Mechanical Engineering Department of the Faculty of Engineering of the University of Porto.

After the tibia was correctly positioned and fixed in a bench vice, the preparation procedure for the implant insertion was initiated. It started with the opening of the “cortex” to access the medullary canal through the alternately use of a curved entry site awl (model M507412) and a 6.35-mm-diameter drill, as can be seen in Figure 8.1.(A) and 8.1.(B), respectively. The entry point was on the central line, directly anterior to the articulating surface, between the tibial medial and lateral condyle. According to the manufacture this entry site causes less stress to the proximal tibia and reduces the probability of nail posterior penetration during its implantation. To accommodate the larger proximal portion of the intramedullary nail, 60 mm of the proximal metaphysis was reamed with a 12.7 mm in diameter drill. After the nail entry site was enlarged, a 2.8 mm in diameter per 800 mm length ball-tip guide wire (model M502724) was passed down the medullary canal until it was visible from the opposite end of the tibia. This allowed the initiation of the medullary canal reaming, in sequential steps by increments of 0.5 mm up to a diameter of 10 mm using the flexible intramedullary reamer (see Figure 8.1.(C)). The ball-tip guide wire was replaced by a 2.8 mm in diameter per 800 mm length guide wire with no ball-tip (model M502744), so it could later be removed through the inserted cannulated intramedullary nail. Prior to its insertion in the bone, the intramedullary nail was attached to a combined system: distal aiming device (model M507416)

fixed to the insertion handle (model M507400). The distal aiming device will allow the distal screws to be placement without image intensification. Since the success in the drilling for distal locking screws relied on the alignment between the nail distal screw holes and the distal aiming device, these points were visually lined up and only afterwards the intramedullary nail attached to the insertion handle was inserted through the guide wire into the medullary canal. The nail insertion was performed manually through axial movements to avoid its rotational and consequently misalignment with the distal aiming device (see Figure 8.1.(D.1)). The fixation implant used was a 9 mm in diameter per 345 mm length, cannulated AISI 316L ASTM F318 stainless steel intramedullary nail (model M596222 AB0366 T). After the intramedullary nail was correctly inserted the guide wire was remove and the nail was first locked distally than proximally. The assembly protection sleeve (model M507421) accommodating the drill guide sleeves, where the 8 mm in diameter is placed inside the 10 mm in diameter one (model M507420 and M507418, respectively), was inserted in the holes of the aiming device for drilling guidance to be assured. A 4.0 mm drill (model NBODB) was used for all the 4.8 mm in diameter locking screws (model M 596248) at the proximal and distal portions of the tibia. The length of the screw varied to ensure bicortical penetration. The screws length was determined with the use of the depth gauge (model M507414). The screws were inserted with a 3.5 mm hexagonal driver (model M507422) until they were engaged far in the tibia “cortex”. For best comparability with the finite element model, the nails were locked with two screws distally and two proximally. The upper and lower distal locking screws were placed from lateral direction, as demonstrated in Figure 8.1.(D.2.) For the proximal screws to be placed the distal aiming device was removed and the insertion handle was used for drilling correct position identification. The two proximal locking screws were placed perpendicular to each other from the anterior-medial and the anterior-lateral direction. See Figure 8.1.(E). After the static locked intramedullary nail was correctly implanted and the insertion handle removed, a fracture at the center of the tibial mid-shaft was created. Around 182 mm upwards from the tibial platform, two transverse osteotomies were performed with an oscillating saw (Dremel® Multi-Max™, Wisconsin, USA), creating an 11 mm osteotomy gap, as illustrated in Figure 8.1.(F).

To finalize the proceeding and for future reference, a two plane (frontal and lateral) full length x-rays of the bone-implant construct was taken. The x-ray image is presented in Figure 8.2.

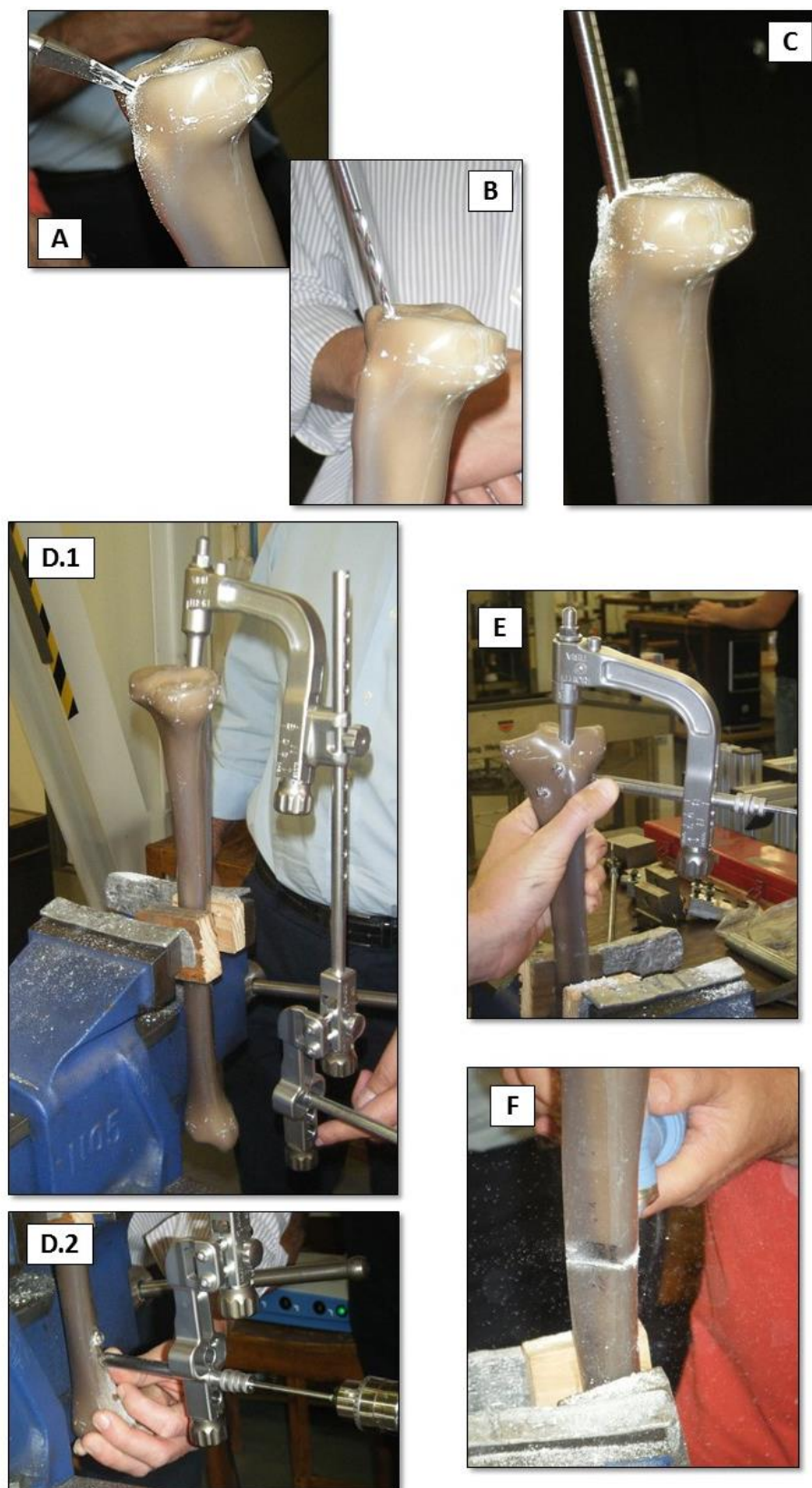


Figure 8.1 - Photographic registers from the intramedullary nail implantation process

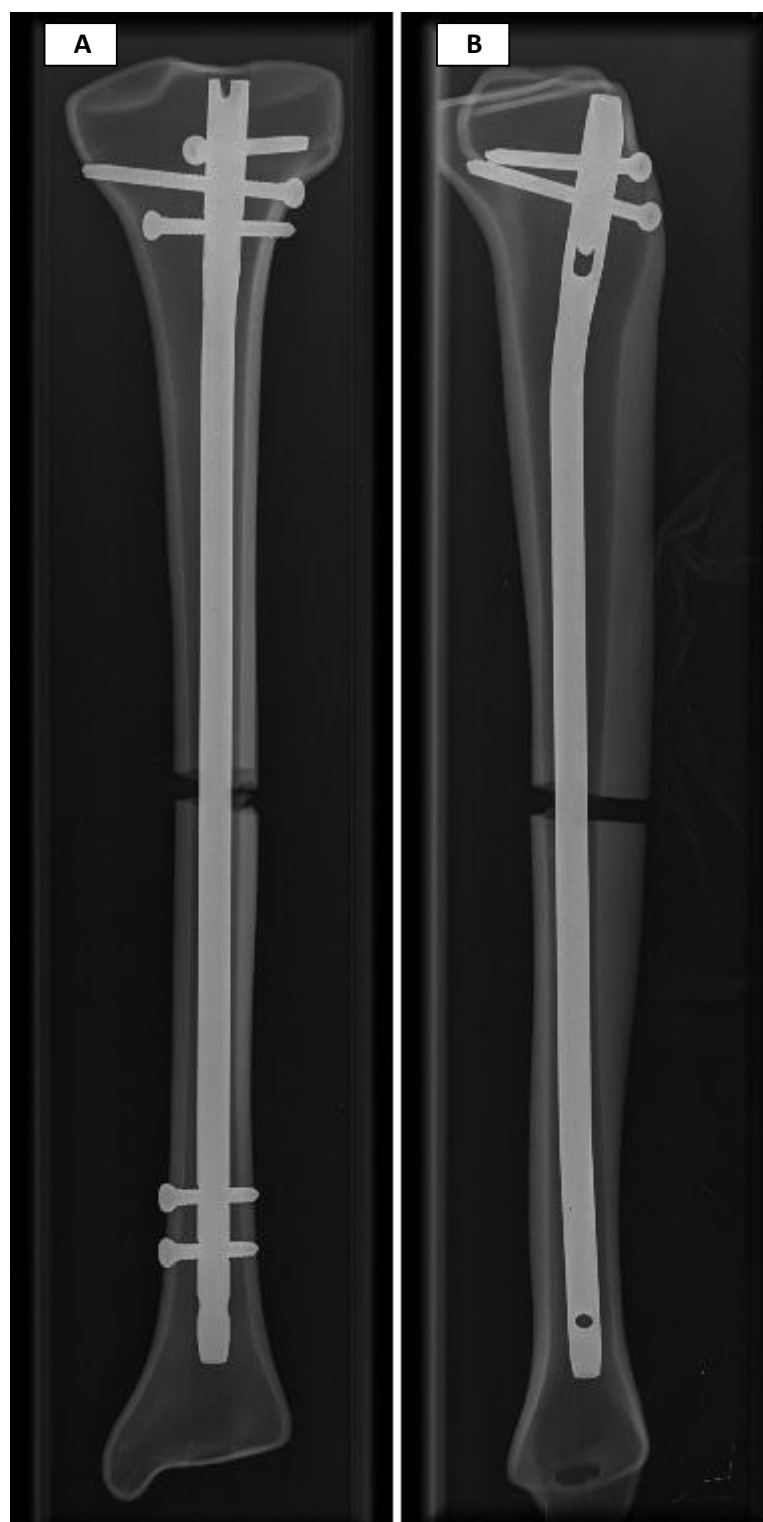


Figure 8.2 - X-ray from the tibia composite with the intramedullary nail implanted from the (A) frontal and (B) medial view

B

Table 8.1 - Properties of some different types of actuators. The two test samples are highlighted in dark grey

| Design | Company | Product reference | Dimensions (mm) | | | Maximum voltage (V) | Free stroke (μm) | Blocking force (N) | Resonant frequency (kHz) |
|-------------|---------------------------------|-------------------|-----------------|-------|--------|---------------------|-------------------------------|--------------------|--------------------------|
| | | | Length | Width | Height | | | | |
| Bender-type | Face® International Corporation | PAB-4010 | 40 | 10 | 0.55 | 100 | 500 | 0.8 | - |
| | Piezomechanik GmbH | BM/ML 60/50/450 | 50 | 14 | 1 | 60 | 450 | 0.5 | 200 |
| | | BM 300/50/800 | 51 | 5 | 0.7 | 100 | 800 | 0.3 | 150 |
| | | BM 70/25/200 M | 25 | 7.5 | 0.4 | 70 | 200 | 0.15 | 300 |
| | PiezoDrive | BA4510 | 45 | 10 | 0.5 | 100 | 30 | 2 | 170 |
| | Johnson Matthey Piezo Products | 1 | 50 | 7.2 | 0.8 | 230 | 2000 | 0.45 | - |
| | | 2 | 50 | 2.1 | 0.9 | 230 | 2000 | 0.15 | - |
| | | 3 | 47.4 | 1.9 | 0.8 | 230 | 2200 | 0.18 | - |
| | | 4 | 47.4 | 1.5 | 0.8 | 230 | 1800 | 0.1 | - |
| | | 5 | 47 | 5.9 | 0.8 | 230 | 2800 | 0.5 | - |
| | | 6 | 36 | 2.1 | 0.67 | 230 | 1400 | 0.15 | - |
| | | 7 | 32.5 | 1.9 | 0.7 | 230 | 1400 | 0.18 | - |
| | | 8 | 25 | 7.2 | 0.48 | 24 | 50 | 0.05 | - |
| | Noliac | CMBP 01 | 21 | 7.8 | 0.7 | 200 | 195 | 1.20 | - |
| | | CMBP 02 | 21 | 7.8 | 1.25 | 200 | 120 | 3.70 | - |
| | | CMBP 03 | 21 | 7.8 | 1.8 | 200 | 85 | 5.50 | - |
| | | CMBP 04 | 32 | 7.8 | 0.7 | 200 | 475 | 0.75 | - |
| | | CMBP 05 | 32 | 7.8 | 1.25 | 200 | 345 | 2.25 | - |
| | | CMBP 06 | 32 | 7.8 | 1.8 | 200 | 210 | 4.30 | - |
| | | CMBP 07 | 50 | 7.8 | 0.7 | 200 | 1270 | 0.40 | - |

| | | | | | | | | | |
|------------|-------------------------------|-------------------|------|------|------|----------|-------|------|------|
| | | CMBP 08 | 50 | 7.8 | 1.25 | 200 | 850 | 1.60 | - |
| | PI Ceramic Piezotechnology | PL112.10 | 17.8 | 9.6 | 0.65 | 60 | 12000 | 2.0 | - |
| | | PL122.10 | 25.0 | 9.6 | 0.56 | 60 | 22000 | 1.1 | - |
| | | PL127.10 | 31.0 | 9.6 | 0.56 | 60 | 27000 | 1.0 | - |
| | | PL128.10 | 35.5 | 6.3 | 0.75 | 60 | 28000 | 0.5 | - |
| | | PL140.10 | 45.0 | 11.0 | 0.6 | 60 | 40000 | 0.5 | - |
| Shear-type | PI Ceramic Piezotechnology | P-141.10 | 12 | 10 | 10 | 250 | 10 | 300 | 100 |
| | | P-141.05 | 7.5 | 10 | 10 | 250 | 5 | 200 | 163 |
| | | P-111.05 | 7.5 | 3 | 3 | 250 | 5 | 20 | 153 |
| | | P-121.05 | 7.5 | 5 | 5 | 250 | 5 | 40 | 153 |
| | | P-151.10 | 12 | 16 | 16 | 250 | 10 | 300 | 100 |
| Plate | Noliac | CMA01 | 3 | 3 | 2 | 60 | 2.2 | 360 | - |
| | | CMA02 | 5 | 5 | 2 | 60 | 2.6 | 1000 | - |
| | | CMA03 | 3 | 3 | 3 | 150 | 4.4 | 360 | - |
| | | CMA04 | 5 | 5 | 3 | 150 | 4.8 | 1000 | - |
| | | CMA05 | 7 | 7 | 2 | 150 | 3.1 | 1960 | - |
| | | CMA06 | 3 | 3 | 2 | 200 | 2.9 | 360 | - |
| | | CMA07 | 5 | 5 | 2 | 200 | 3.1 | 1000 | - |
| | | CMA08 | 7 | 7 | 2 | 200 | 3.2 | 1960 | - |
| | | CMA09 | 10 | 10 | 2 | 200 | 3.2 | 4000 | - |
| | | CMA10 | 3 | 3 | 2 | 200 | 1.8 | 290 | - |
| | | CMA11 | 5 | 5 | 2 | 200 | 2.0 | 800 | - |
| Stack | Piezomechanik GmbH | PSt 150/2x3/5 | 5 | 2 | 3 | -30/+150 | 6.5/5 | 300 | 150 |
| | | PSt 150/2x3/7 | 9 | 2 | 3 | -30/+150 | 13/9 | 300 | 100 |
| | | PSt 150/3.5x3.5/7 | 9 | 3.5 | 3.5 | -30/+152 | 13/9 | 800 | 100 |
| | | PCh 50/5x5/2 | 2 | 5 | 5 | 50 | >3/>2 | 1500 | >500 |
| | NEC/TOKIN | AE0203D04 | 5 | 2 | 3 | 150 | 4.6 | 200 | 261 |
| | PiezoDrive | SA030305 | 5 | 3 | 3 | 150 | 5.6 | 330 | - |
| | | | | | | | | | |

C

The *in vitro* biomechanical analysis by using animal cadaveric bones can provide essential information as a preliminary risk study and will allow to adjust the design to animal experimentation conforms and needs. This step will also allow inferring on the implant potential for bone regeneration. However, the truly assessment of its bone regenerative capabilities, and the immune response associated with implantation, will require *in vivo* experimentation in animal models [13, 14]. Few details relating future work have been addressed during the PhD study period, namely, the selection of the type of animal model for the pilot study, the preparation of the animal model cadaveric bone for the implant prototype adjustments and for biomechanical analysis as well as the elaboration of the permission requirements from local ethical review committee animal experimentation approval.

Biomechanical analysis *in vitro*

Animal model selection

Besides the challenge it represents, a careful election of the animal model and specie, is essential for an efficient research to be conducted [15, 16]. A proper selection may also minimize the number of variables in the experiment and the number of animals needed. This choice is based on the objectives of the research and/or the hypotheses to be tested, availability, regulatory requirements and ensured analogy with human [17, 18]. In the orthopedic implant trauma research field, there is an increased preference in the use of larger animals in detriment of small ones (e.g. small rodents). The larger animals' asset in new implants and biomechanical stability studies is based on the fact that: 1) they present a bone metabolism and postoperative behavior similar to humans (e.g. propensity for immediate weight-bearing), 2) the larger bone size of these animals facilitate the intramedullary nails implantation procedure, 3) mechanical testing is also easier when compared to rodents and 4) the larger animals weight more closely resembles the one in humans. Therefore, it is easier to extrapolate conclusions based on the results obtained in large animals compared to rodents with regard to human's orthopedic implant cases [19, 20]. Although, there is no ideal animal bone model to be used for orthopedic studies [18], from all the large animal models available, the sheep has been used in a number of previous studies [21-34] where intramedullary tibial nail was tested *in vivo* and provided the basis for comparison with human cases (see Table 8.1). According to literature [12, 19, 20, 35], the advantage in the use of sheep models are the high availability, easy housing and handling in the experimental set-up, low cost and acceptance to society as a research animal. The extrapolation of results from sheep experiment to human patients requires caution and it is important to be

aware of the differences between the specimens [28]. In terms of anatomy, as stated by Osterhoff *et al.* [35] the stifle joint was very similar to that of the human knee joint. Also the ovine stifle can be considered as a human knee scaled down by one third. In terms of the peak mechanical forces acting on this joint, according to the study developed by Taylor *et al.* [12], it was determined an average axial tibial-femoral contact forces of 2.12 BW, an averaged 0.7 BW shear loads from the anterior to posterior direction and only small medial to lateral forces. Through a *in vivo*, *ex vivo* and finite simulation study, Duda *et al.* [36] determined even lower axial and shear knee contact forces for the merino sheep's. The loading determined in these studies is somewhat lower than that seen in the human knee (see sub-chapter 2.1.). The difference in force magnitude between the specimens is most probably due to the human's plantigrade bipedal and sheep unguligrade quadrupedal nature. The higher ratio of shear to axial loading in the sheep was explained by its higher knee flexion angles – of over 50 degrees – compared to the human case where the lower limb remains relatively straight during loaded gait (although up to approximately 40 degrees during swing phase). There are also differences in the tibia geometry between sheep and humans which should be taking in consideration when intramedullary implants are to be tested [12]. As described by Osterhoff *et al.* [35], one of the difference is in the proximal end of the ovine tibia which as an upside down triangular pyramided-like shape in contrary to the human tibia proximal end which quickly tapers into a shaft short below the plateau. Also the ovine tibial inner diameter is lower which leads to a cortical index 1.4 times higher than in the humans. The sheep tibia plateau and the proximal tibial shaft are also characterized by a remarkable thick cortical bone. One of the main drawbacks of using sheep for this type of studies are the high amount of bone ingrowth when compared to humans and their age-dependent bone remodeling [37]. Considering that the sheep stifle has similar geometric proportions to the human knee and that although there is no direct comparison of load-bearing patterns in sheep with humans, the similar body weight with humans makes it adequate to apply the same instrumentation as that used in humans. Additionally, the sheep also has a bone healing rate which approximates the human one. Hence, the sheep appears to be a suitable model for the evaluation the potential in bone fractures enhancement conferred by the device developed during this PhD [18, 19, 38].

Table 8.2 - Few parameters adopted in the studies where sheep was used for the evaluation of intramedullary nail fixation device. OD – outer diameter, L- length

| Intramedullary Nail | OD (mm) | L (mm) | Alterations | In vivo models | Age | Weight (Kg) | Procedure | Duration (weeks) | Fracture healing Simulation model | Reference |
|--|---------|--------|-------------|------------------------------------|----------|-------------|--------------------------------|------------------|-----------------------------------|-----------|
| - | - | - | - | Sheep | - | 33-40 | Reamed vs non-reamed | 12 | Fracture ¹ | [21] |
| AO unreamed tibial rod (Synthes) | 7 | - | Custom-made | Female Columbia sheep | Juvenile | 33-38 | Reamed (8.5 mm) vs non-reamed | 12 | Fracture ¹ | [22] |
| - | - | - | - | Sheep | - | 33-40 | Reamed vs non-reamed | 12 | Fracture ¹ | [23] |
| - | - | - | - | Sheep | - | 40-50 | - | - | Transverse osteotomy | [24] |
| - | - | - | - | Sheep | - | 33-40 | Reamed vs non-reamed | 12 | Fracture ¹ | [25] |
| - | - | - | - | Sheep | - | 30-47 | Reamed | - | Transverse osteotomy | [26] |
| Non-reaming commercially available titanium nail (Synthes) | 9 | - | Shortened | Merino-mix sheep (hind limb femur) | 2-3 | - | Non-reamed | 9 | Transverse osteotomy (3 mm) | [39] |
| Seidel (Stryker) humeral nail | 8 | - | - | Scottish Blackface sheep | 21 | 35-50 | Reamed | 5 hours | Fracture ¹ | [40] |
| New design test | 8 | 185 | - | Mature female sheep | - | 70-76 | Non-reamed | 12 | Transverse osteotomy | [29] |
| AO/ASIF nail | 9.5/7.5 | - | - | Swiss mountain sheep | - | - | Reamed vs RIA | - | Fracture ¹ | [30] |
| Standard TriGen META Nail (Smith & Nephew) | 10 | 180 | - | cross Suffolk | 2-3 | 90 | Reamed | 24 | Transverse osteotomy (1 mm) | [31] |
| Solid nail (UHN, Synthes) | 7.5 | 190 | Shortened | Swiss mountain sheep | 5 | 65-70 | Reamed (+1.5 mm) vs non-reamed | 10 | Fracture ¹ | [32] |
| Engineered by MORE Medical Solutions (Rostock, Germany) | 8 | 200 | Custom-made | German black sheep | - | 69 | Minimal reaming (8 mm) | 10 | Transverse osteotomy (0.7 mm) | [33] |

¹Bending technique

Sheep cadaveric bones preparation

Considering the above mentioned geometric differences and based on the information presented in Table 8.2 the intramedullary nail designs used in humans appear to be suitable for implantation in sheep models if the length of the nails is adjusted to fit the sheep tibia. Also the nail diameter should be selected taking in consideration the narrower medullary canal of the animals. If the available nails diameters are not suitable for implantation it is possible to proceed to the enlargement of the medullary canal. However, the reaming procedure should always be avoided. For the intramedullary nails proper adjustment to take place it is necessary to have sheep cadaveric bone available. Hence, during this PhD, sheep bone samples were prepared from cadaveric specimens. There are several methods used in bone preparation, including, enzymatic maceration (*e.g.* trypsin, prepsin, or papain), insect consumption, boiling in water and also the used of techniques to fasten the removal of the attached soft tissues through the use of chemicals [41-43]. From the available bone cleaning procedures, the method suggested by Onwuama *et al.* [42] was adopted since it was classified as reduce time consuming, reduce released of odor and at the same time caused reduce bone damaging effect. By considering this method sheep bone tibiae preparation involve bone cleaning by soft tissue removal followed by bone bleaching.

Material and methods

Two tibiae from one 7 years old euthanized Merino sheep, kindly provided by the Department of Veterinary Medicine at the University of Évora, were dissected and the maximum amount of soft tissue removed. The partially cleaned bones were immersed in a plastic bucket containing 3% solution of sodium hydroxide (pallets, 97%, Sigma-Aldrich, Missouri, USA) in distilled water. To avoid bone crack development, reduce chemical concentration and time exposure, as well as temperature, was adopted. The tibiae where checked every 60 minutes to avoid bones digestion by sodium hydroxide. After the adhering tissue and periosteum was released, the bones were washed in distilled water and dried at room temperature. Since bones after-cleaning presented a creamy appearance, there was no need to adopt a whitening technique (*e.g.* bleaching hydrogen peroxide).

The intramedullary nail adjustment procedure was studied using a finite element model. This process started with a 3D scan (ATOS Triple Scan from GOM, Braunschweig, Germany) of a realistic computational external surface from one of the cleaned cadaveric Merino sheep tibia. The data obtained was imported into SolidWorks (Dassault Systèmes, Concord, MA, USA) using stereolithography file format. SolidWorks software was used for surface preparation (*e.g.*

topographic cleanup of surface) and solid model construction. The bone existing microstructure was ignored and was treated as a continuum.

Conclusion

The two cleaned cadaveric tibiae are suitable to be used as the final assessment of the intramedullary nail adaptation. However, before any physical alteration is made the adjustments can be planed and evaluated though computer simulation.

The national ethical committee, the Portuguese National Authority for Animal Health (Direcção-Geral de Alimentação e Veterinária - DGAV), demanded an extensive experimentation of the new device through finite element simulation, cadaveric or *in vitro* testing before the animal studies are carried out. Hence, the remaining sheep cadaveric bone samples provided by Department of Veterinary Medicine at the University of Évora will be used for future intramedullary nail-cadaveric bone system biomechanical experimentations prior to *in vivo* animal study. However, such type of bone samples will be subjected to different cleaning procedure to avoid alteration of the bone mechanical properties.

***In vivo* study**

The use of *in vivo* animal models is an essential step in concept validation of the new intramedullary nail implant before clinical test in humans are made. However, as stated by Russel and Burch [44], when carrying out animal studies the principles of the three R's; Reduction, Refinement and Replacement must be applied. This concept involves the reduction of the total number of laboratory animals required to achieve a valid statistically significant result, the experiment should be refinement (or altered) to reduce animal suffering, and there should be a replacement of animal experimentation with alternative techniques that minimize the animal suffering and sacrifice [14, 16, 20]. Hence, the *in vivo* experiments using laboratory animals should be: optimally planned, experimentally well-designed, carefully equipment selected, efficiently executed, correctly analyzed and interpreted and clearly presented to guarantee scientifically reliable results and excessive use of animal as stated by the principles of the three R's, prevent waste of time, efforts and founding [18, 45]. The detailed planning of the *in vivo* merino sheep study was considered out-of-the-scope of the PhD project work, however the collaboration of experienced veterinary physicians with their in this experiments along with the material supply from *Artur Salgado S.A.*, will greatly contribute for the quality of the experiment planning.

References

1. Dailey, H.L., et al., *A novel intramedullary nail for micromotion stimulation of tibial fractures*. Clinical Biomechanics, 2012. **27**(2): p. 182-188.
2. Rho, J.-Y., L. Kuhn-Spearing, and P. Zioupos, *Mechanical properties and the hierarchical structure of bone*. Medical Engineering and Physics, 1998. **20**(2): p. 92-102.
3. White, T.D., M.T. Black, and P.A. Folkens, *Human osteology* 2012, Oxford, UK: Academic press.
4. Keaveny, T.M., E.F. Morgan, and O.C. Yeh, *Bone mechanics*, in *Standard Handbook of Biomedical Engineering & Design*, M. Kutz, Editor 2003, McGraw-Hill: New York, USA. p. 200-222.
5. Ascenzi, M.-G., et al., *Individual-specific multi-scale finite element simulation of cortical bone of human proximal femur*. Journal of Computational Physics, 2013. **244**: p. 298-311.
6. Morgan, E.F. and T.M. Keaveny, *Dependence of yield strain of human trabecular bone on anatomic site*. Journal of Biomechanics, 2001. **34**(5): p. 569-577.
7. McCalden, R.W., J.A. McGeough, and M.B. Barker, *Age-related changes in the tensile properties of cortical bone. The relative importance of changes in porosity, mineralization, and microstructure*. The Journal of Bone and Joint Surgery, 1993. **75**(8): p. 1193-1205.
8. Fratzl, P., et al., *Structure and mechanical quality of the collagen–mineral nano-composite in bone*. Journal of Materials Chemistry, 2004. **14**(14): p. 2115-2123.
9. Cowin, S.C., *Bone poroelasticity*. Journal of Biomechanics, 1999. **32**(3): p. 217-238.
10. Weinbaum, S., S.C. Cowin, and Y. Zeng, *A model for the excitation of osteocytes by mechanical loading-induced bone fluid shear stresses*. Journal of Biomechanics, 1994. **27**(3): p. 339-360.
11. Minns, R.J., G.R. Bremble, and J. Campbell, *The geometrical properties of the human tibia*. Journal of Biomechanics, 1975. **8**(3): p. 253-255.
12. Taylor, W.R., et al., *Tibio-femoral joint contact forces in sheep*. Journal of Biomechanics, 2006. **39**(5): p. 791-798.
13. Ferrara, L.A. and D. Dobrea, *Workshop: Designing and evaluating protective gear and implants for safety and effectiveness*, in *International Conference and Expo on Biomechanics and Implant Design* 2015, OMICS International Conferences: Orlando, USA.
14. Moran, C.J., et al., *The benefits and limitations of animal models for translational research in cartilage repair*. Journal of Experimental Orthopaedics, 2016. **3**(1): p. 1-12.
15. Festing, M.F.W., *The choice of animal model and reduction*. Alternatives to Laboratory Animals: ATLA, 2004. **32**(2): p. 59-64.
16. Wood, M.W. and L.A. Hart. *Selecting appropriate animal models and strains: Making the best use of research, information and outreach*. in *6th World Congress on Alternatives and Animal Use in the Life Sciences*. 2007. Tokyo, Japan: AATEX 14.
17. The Three Rs, *Species and Model Selection*, 2015: Ontario, Canada.
18. Martini, L., et al., *Sheep model in orthopedic research: A literature*. Comparative Medicine, 2001. **51**(4): p. 292-299.
19. Potes, J.C., et al., *The sheep as an animal model in orthopaedic research*. Experimental Pathology and Health Science, 2008. **2**(1): p. 29-32.
20. Decker, S., et al., *Non-osteotomy and osteotomy large animal fracture models in orthopedic trauma research*. Orthopedic Reviews, 2014. **6**(4): p. 168-174.
21. Schemitsch, E.H., et al., *Cortical bone blood flow in reamed and unreamed locked intramedullary nailing: a fractured tibia model in sheep*. Journal of orthopaedic trauma, 1994. **8**(5): p. 373-382.

22. Schemitsch, E.H., et al., *Comparison of the effect of reamed and unreamed locked intramedullary nailing on blood flow in the callus and strength of union following fracture of the sheep tibia*. Journal of orthopaedic research, 1995. **13**(3): p. 382-389.
23. Schemitsch, E., M. Kowalski, and M. Swiontkowski, *Soft-tissue blood flow following reamed versus unreamed locked intramedullary nailing: a fractured sheep tibia model*. Annals of plastic surgery, 1996. **36**(1): p. 70-75.
24. Aguilar, M.M., et al., *Posttraumatic lymphocyte response: a comparison between peripheral blood T cells and tissue T cells*. Journal of Trauma and Acute Care Surgery, 1998. **45**(1): p. 14-18.
25. Schemitsch, E.H., et al., *Quantitative assessment of bone injury and repair after reamed and unreamed locked intramedullary nailing*. Journal of Trauma and Acute Care Surgery, 1998. **45**(2): p. 250-255.
26. Mousavi, M., et al., *Influence of controlled reaming on fat intravasation after femoral osteotomy in sheep*. Clinical orthopaedics and related research, 2002. **394**: p. 263-270.
27. Kaspar, K., et al., *Angle stable locking reduces interfragmentary movements and promotes healing after unreamed nailing*. Journal of Bone and Joint Surgery. American Volume, 2005. **87**(9): p. 2028-2037.
28. White, T.O., et al., *The early response to major trauma and intramedullary nailing*. Bone and Joint Journal, , British Volume, 2006. **88**(6): p. 823-827.
29. Lu, Y., et al., *Comparison of a new braid fixation system to an interlocking intramedullary nail for tibial osteotomy repair in an ovine model*. Veterinary Surgery, 2009. **38**(4): p. 467-476.
30. Klein, C., et al., *Unreamed or RIA reamed nailing: an experimental sheep study using comparative histological assessment of affected bone tissue in an acute fracture model*. Injury, 2010. **41**: p. S32-S37.
31. Wilson, D.J., et al. *Development of an ovine instrumented tibial nail model for investigating healing status in ORS 2011 Annual Meeting*. 2011. Long Beach, California.
32. Högel, F., et al., *Fracture healing after reamed and unreamed intramedullary nailing in sheep tibia*. Injury, 2011. **42**(7): p. 667-674.
33. Gradl, G., et al., *Fracture near press-on interlocking enhances callus mineralisation in a sheep midshaft tibia osteotomy model*. Injury, 2014. **45**: p. S66-S70.
34. Rossig, C., et al., *Magnesium-based intramedullary nailing system in a sheep model: Biomechanic evaluation and first in vivo results*. Journal of Veterinary Science and Medical Diagnosis Research Article, 2014. **4**(1).
35. Osterhoff, G., et al., *Comparative anatomical measurements of osseous structures in the ovine and human knee*. The Knee, 2011. **18**(2): p. 98-103.
36. Duda, G.N., et al., *Analysis of inter-fragmentary movement as a fuction of musculoskeletal loading conditions in sheep*. Journal of Biomechanics, 1998. **31**: p. 201-210.
37. Jewell, E., et al., *Surgical fixation hardware for regeneration of long bone segmental defects: Translating large animal model and human experiences*. Clinical Reviews in Bone and Mineral Metabolism, 2015. **13**(4): p. 222–231.
38. Gao, J., et al., *Relationship between microstructure, material distribution, and mechancial properties of sheep tibia during fracture healing process*. International Journal of Medical Sciences, 2013. **10**(11): p. 1560-1569.
39. Kaspar, K., et al., *Angle stable locking reduces interfragmentary movements and promotes healing after unreamed nailing*. The Journal of Bone & Joint Surgery, 2005. **87**(9): p. 2028-2037.
40. White, T.O., et al., *The early response to major trauma and intramedullary nailing*. Journal of Bone & Joint Surgery, British Volume, 2006. **88**(6): p. 823-827.
41. Rennick, S.L., et al., *The effects of skeletal preparation techniques on DNA from human and non-human bone*. Journal of Forensic Science, 2005. **50**(5): p. 1-4.

42. Onwuama, K.T., et al., *Effect of different methods of bone preparation on the skeleton of the african giant pouched rat (Cricetomys gambianus)*. International Journal of Morphology, 2012. **30**(2): p. 425-427.
43. Searfoss, G., *Bone preparation and cleaning*, in *Skulls and Bones: A Guide to the Skeletal Structures and Behavior of North American Mammals*, G. Searfoss, Editor 1995, Stackpole Books: Pennsylvania, USA. p. 215-227.
44. Russell, W.M.S. and R.L. Burch, *The principles of humane experimental technique* 1959, London, UK: Methuen.
45. Festing, M.F.W. and D.G. Altman, *Guidelines for the design and statistical analysis of experiments using laboratory animals*. ILAR Journal, 2002. **43**(4): p. 244-258.